Program
Summaries of SURF Seminar Presentations

SUMMER UNDERGRADUATE RESEARCH FELLOWSHIP

CALIFORNIA INSTITUTE OF TECHNOLOGY

Pasadena, California

SURF Seminar Day
October 9, 1982

TABLE OF CONTENTS

Brief Background of SURF

The Summer Undergraduate Research Fellowship program at Caltech began in 1979 to encourage creative research, promote interaction between undergraduates and faculty, and improve the undergraduate program. This program was the brainchild of Dr. Fredrick H. Shair, Professor of Chemical Engineering, and Dr. Harold Zirin, Professor of Astrophysics and Director of Big Bear Solar Observatory. In four years the program has grown from 18 students in 1979 to 73 students in 1982. President Goldberger has continuously given his enthusiastic support to the program. In 1982 nearly one-third of all faculty in science and in engineering participated as faculty sponsors.

A student applies for a fellowship by developing a research proposal in collaboration with a faculty member who has agreed to sponsor him or her. The proposals are reviewed by a committee of faculty members familiar with the fields represented. Fellowships are awarded on the basis of perceived merit. This year the faculty coordinators were Dr. Fredrick H. Shair; Dr. William Bridges, Professor of Electrical Engineering and Applied Physics; the late Dr. William H. Corcoran, Institute Professor of Chemical Engineering; Dr. Paul Dimotakis, Associate Professor of Aeronautics and Applied Physics; Dr. John Richards, Professor of Organic Chemistry; Dr. Thomas Tombrello, Professor of Physics; and Dr. Harold Zirin. Others who helped administer the program were Carolyn Merkel, Chris Wood, Penny Stephens, Theresa Meisling and Suzanne Rudolph.

SURF students are expected to work full time for ten weeks during the summer to complete the projects, and at the end of the ten weeks, each student submits a report of his or her work. In addition to providing an enjoyable learning opportunity, the tutorial relationship aids in the development of judgment. The program culminates in SURF Seminar Day when each student has the opportunity to present a fifteen minute oral summary of his or her work to other students, faculty and visitors.

In 1982, a stipend of $2400 was paid each SURF student. Student stipends constitute over 95% of the total annual expenditures in the program. Cost of supplies, equipment, computing, travel, etc., are raised by the individual faculty sponsors; this action on the part of Caltech faculty is another indication of their commitment to the training and development of young scientists and engineers.

Initial sponsors of the program are Mr. and Mrs. Samuel P. Krown, Mr. and Mrs. Douglas B. Nickerson, IBM, the Caltech Prize Scholarship Fund, the Paul K. and Evalyn Elizabeth Cook Richter Memorial Funds, Mr. and Mrs. George Tooby, Mr. and Mrs. William Lang, Mrs. Downie Muir III, and Dr. W. Phelps Freeborn. The SURF Executive Committee, Mr. Samuel P. Krown, Chairman; Dr. Marcella Bonsall; Mr. Theodore C. Coleman; Mr. Joseph B. Earl; Mr. Douglas B. Nickerson; Mr. Loyd C. Sigmon, is working with Elba Smith, Ed Baum and Susan Pearce of the Caltech Administration in order to raise enough money to endow the SURF program and thus to ensure its continuation and growth as the integral and important part of the undergraduate program it has proven to be.

Contained in this document are 1) the schedule for the 1982 SURF Seminar Day; 2) the extended abstracts of the students' projects; 3) summaries of the Summer SURF Seminar Series; 4) some publications which have been initiated by SURF projects.

SURF Seminar Day
Saturday, October 9, 1982

Session I: Spalding Labortory, Room 102
Dr. Terrence Collins Presiding
Assistant Professor of Chemistry

9:55	Introduction	Dr. Terrence Collins		
10:00-10:20	Salicylaldimine Complexes of Osmium (Sponsor: Dr. Terrence Collins)	Steven Baxter	Jr	Chemistry
10:20-10:40	Electrodynamic Suspension of Micro-particles for Mass Determination (Sponsor: Dr. Jesse Beauchamp)	Anirvan Ghosh	So	Physics
10:40-11:00	Mechanistic Studies of Addition to d^0 Transition Metal Centers (Sponsor: Dr. John Bercaw)	Pui Tong Ho	Sr	Chemistry
11:00-11:20	A Study of Perflourodecalin as a Medium for Catalytic Oxidation of Organic Compounds (Sponsor: Dr. Michael Hoffman)	Richard Honrath	Jr	Environmental Engineering
11:20-11:40	Organo Metal Research (Sponsor: Dr. Terrence Collins)	Chris Hull	So	EE/Chemistry
11:40-12:00	Cloning and DNA Sequencing of the Genes for the Subunits of the Acetylcholine Receptor (Sponsor: Dr. Norman Davidson)	Tze Kin Ip	Sr	EAS
12:00-1:00	Lunch - Dabney Garden			
1:00-1:20	Reactivity of Bis-Pentamethylcyclo-pentadienyl Zirconium Dihydride with Transition Metal Alkylidene Complexes (Sponsor: Dr. John Bercaw)	Andy Liu	Sr	Chemistry
1:20-1:40	Development of a Computer Program for Multireaction Chemical Equilibria (Sponsor: Dr. George Gavalas)	Tarik Naheiri	Jr	Chemical Engineering
1:40-2:00	New DNA-Cleaving Molecules (Sponsor: Dr. Peter Dervan)	Vincent Powers	Sr	Chemistry
2:00-2:20	RNA Polymerase II Research (Sponsor: Dr. Carl Parker)	Douglas Ruden	Jr	Biochemistry
2:20-2:40	Interhelical DNA-DNA Crosslinking in Intact and T7 Bacteriophage (Sponsor: Dr. Peter Dervan)	Eliza Sutton	Jr	Chemistry/ Biology
2:40-3:00	Progress Towards the Study of Protein Mechanism Via Site-Specific Mutagenesis (Sponsor: Dr. John Richards)	Arlene Keller	Sr	Chemistry
3:00-3:20	The Production of Revertant Beta-Lactamase Under Various Conditions (Sponsor: Dr. John Richards)	Minami Yoda	So	EAS
5:00-6:30	Informal Reception in the President's Garden 415 South Hill, Pasadena Hosted by Dr. and Mrs. Goldberger			

SURF Seminar Day
Saturday, October 9, 1982

Session II: Spalding Labortory, Room 104
Dr. Masakazu Konishi Presiding
Bing Professor of Behavioral Biology

9:55 AM	Introduction	Dr. Masakazu Konishi		
10:00-10:20	Somatic Hypermutation (Sponsor: Dr. Leroy Hood)	Lisa Flitz	Sr	Biology
10:20-10:40	The Structure of Sea Urchin Maternal RNA (Sponsor: Dr. Eric Davidson Dr. Howard Jacobs)	Tracy Furutani	Jr	Chemistry
10:40-11:00	Studies of Promotion of Human Mitochondrial DNA (Sponsor: Dr. Giuseppe Attardi)	George Gibbs	So	Chemical Engineering
11:00-11:20	Electron Microscopy of Gap Junctions (Sponsor: Dr. Jean-Paul Revel)	Scott Gordon	Jr	Biochemistry
11:20-11:40	Spider Brain and Behavior (Sponsor: Dr. John Allman)	Cecile Huling	Sr	EAS
11:40-12:00	A Photochemical Means for the Control of Intracellular Calcium Concentration (Sponsor: Dr. Jeanne Nerbonne)	Donald Lo	Sr	Biology
12:00-1:00	Lunch - Dabney Garden			
1:00-1:20	Search for Sequence Homologies Between a Baboon Endogenous Virus and the Human Genome (Sponsor: Dr. William Dreyer)	David Marvit	Jr	Biology
1:20-1:40	Preparation and Analysis of a Gene Specific Subclone for Actin Gene J in Sea Urchin Strongylocentrotus Purpuratus (Sponsor: Dr. Eric Davidson)	Gary Mockli	Sr	Biology
1:40-2:00	Structural Analysis of a Gene Expressed Only at Embryonic Stages of the Sea Urchin Stronglyocentrotus Purpuratus (Sponsor: Dr. Eric Davidson Dr. Konstantinos Flytzanis)	Glenn Nakamura	Sr	Biology
2:00-2:20	The Neural Control of Birdsong (Sponsor: Dr. Masakazu Konishi)	Dean Shibata	Sr	Biology
2:20-2:40	Regulation of DNA Replication (Sponsor: Dr. Judith Campbell)	Eric Sinn	Sr	Biology
2:40-3:00	New Method of Investigating Gap Junctions Using Flourescent Materials (Sponsor: Dr. Jean-Paul Revel)	Sung J. Yoo	Sr	Biochemistry
	The Design and Implementation of Object Orientated Languages (Sponsor: Dr. James Kajiya)	Keith Hughes*	Jr	Mathematics
5:00-6:30	Informal Reception in President's Garden 415 South Hill, Pasadena Hosted by Dr. and Mrs. Goldberger			

* Unable to participate in SURF Seminar Day

SURF Seminar Day
Saturday, October 9, 1982

Session III: Spalding Laboratory, Room 106
Dr. William Bridges Presiding
Professor of Electrical Engineering and Applied Physics

9:55 AM	Introduction	Dr. William Bridges
10:00-10:20	The Action of Ozone in the Deterioration of Works of Art (Sponsor: Dr. Glen Cass)	Kaitlin Drisko Sr EAS
10:20-10:40	Periodic Solutions to the Truncated Navier-Stokes Equations (Sponsor: Dr. Mark McGuinness)	Edward Felten So Physics
10:40-11:00	Numerical Grain Flow Problems (Sponsor: Dr. Peter Haff)	Kenneth Hui+ Jr Physics
11:00-11:20	Chemical Analysis and Flame Geometry of Fire Plumes (Sponsor: Dr. Edward Zukoski Dr. Richard Flagan)	Hamid Johari Sr EAS
11:20-11:40	Driving Model Piles in the Centrifuge (Sponsor: Dr. Ronald Scott)	Michael Kilby Sr Mechanical Engineering
11:40-12:00	Flow Patterns and Wall Effects of Ciliary Propulsion (Sponsor: Dr. Theodore Wu Dr. George Yates)	Young Soo Lee Sr EAS
12:00-1:00	Lunch - Dabney Garden	
1:00-1:20	Preliminary Studies of Mixed Cultures (Sponsor: Dr. Gregory Stephanopoulos)	Gregory Sayles Sr Chemical Engineering
1:20-1:40	Visualization for Three-Dimensional Turbulent Jet Flow (Sponsor: Dr. Paul Dimotakis)	Kelley Scott Jr EAS
1:40-2:00	A Study of Airborne Transportation in the Santa Barbara County Area (Sponsor: Dr. Fredrick Shair)	Lee Sunderlin Jr Chemical Engineering
2:00-2:20	Mount St. Helens and Fluid Flows (Sponsor: Dr. Bradford Sturtevant)	Matthew Swass Jr Aeronautics
	Separation of Viscous and Elastic Effects in Viscoelastic Fluids (Sponsor: Dr. Gary Leal)	Chris McKinnon* Sr Chemical Engineering
	Modeling of Nonlinear Systems with Iterated Maps (Sponsor: Dr. Donald Cohen)	William Polson* Jr Applied Physics
5:00-6:30	Informal Reception in President's Garden 415 South Hill, Pasadena Hosted by Dr. and Mrs. Goldberger	

\+ Richter/SURF Fellow
* Unable to participate in SURF Seminar Day

SURF Seminar Day
Saturday, October 9, 1982

Session IV: Thomas Laboratory, Room 210
Dr. Thad Vreeland Presiding
Professor of Materials Science

9:55 AM	Introduction	Dr. Thad Vreeland	
10:00-10:20	Level Populations in an FE-AR Hollow-Cathode Discharge (Sponsor: Dr. Ward Whaling)	John Humphrey Sr	Physics
10:20-10:40	Measurement of the Ion and Electron Energy Distribution Function in a Tokamak Plasma (Sponsor: Dr. Stewart Zweben)	Leif Bennett Sr	Applied Physics
10:40-11:00	Field Work in Namibia (Sponsor: Dr. Edwin Munger)	Johanne Bolduc Jr	Geology
11:00-11:20	The Holography of Moving Objects (Sponsor: Dr. William Bridges)	Kirk Haselton Jr	Applied Physics
11:20-11:40	The Oxidation Effects on the Electrical Properties of $NiSi_2$ and $CoSi_2$ on Si and SiO_2 Substrates (Sponsor: Dr. Marc-Aurele Nicolet)	Sung Joon Kim Sr	Electrical Engineering
11:40-12:00	Shock Compaction of Metal Powders (Sponsor: Dr. Thad Vreeland)	Daniel Kostka Sr	Mechanical Engineering
12:00-1:00	Lunch - Dabney Garden		
1:00-1:20	Study of Ni-Nb System by Ion Mixing (Sponsor: Dr. Marc-Aurele Nicolet)	Kenneth Kung Sr	Electrical Engineering
1:20-1:40	Phase Transition of Amorphous $(Zr_{.667}\ Ni_{.333})_{1-x}\ B_x$ (Sponsor: Dr. William Johnson)	Alan Yu Lai Mak Jr	Applied Physics
1:40-2:00	Dichromated Gelatin Holograms (Sponsor: Dr. William Bridges)	Sergay Mnatzakanian Jr	Applied Physics
2:00-2:20	Design and Testing of Thermal Control Systems for a Space Shuttle Payload (Sponsor: Dr. Thomas Caughey)	Norman Princen Jr	EAS
2:20-2:40	Diffusion Limited Unidirectional Crystal Growth from Solution (Sponsor: Dr. David Wood	Darrell Schlom Jr	Materials Science
2:40-3:00	The Supercritical Extraction of Coal (Sponsor: Dr. William Corcoran)	Jen Shu Jr	Chemical Engineering
5:00-6:30	Informal Reception in President's Garden 415 South Hill, Pasadena Hosted by Dr. and Mrs. Goldberger		

SURF Seminar Day
Saturday, October 9, 1982

Session V: Thomas Laboratory, Room 206
Dr. Thomas Tombrello Presiding
Professor of Physics

9:55 AM	Introduction	Dr. Thomas Tombrello
10:00-10:20	Elastic Scattering of Protons by Carbon 12 (Sponsor: Dr. Charles Barnes)	Joe Chang+ Jr Physics
10:20-10:40	Maximum Likelihood Method in Track Reconstruction for the IMB Proton Decay Experiment (Sponsor: Dr. John LoSecco)	Ming-Chung Chu+ Sr Physics
10:40-11:00	Four Jet Events at Petra e^+e^- Physics (Sponsor: Dr. Harvey Newman)	Dave LePoire+ Sr Physics
11:00-11:20	A Gridded Gas Ionization Chamber (Sponsor: Dr. Robert McKeown)	Wuwell Liao+ Jr Physics
11:20-11:40	Let the Chips Fall... (Sponsor: Dr. Thomas Tombrello)	Maclen Marvit+ Sr Physics
11:40-12:00	The Contact Resistivities of Amorphous Fe-W Diffusion Barriers on N^+ and P^+ Silicon (Sponsor: Dr. Marc-Aurele Nicolet)	Eric Pan Jr Applied Physics
12:00-1:00	Lunch - Dabney Garden	
1:00-1:20	Embeddings of SL(2,5) or A_5 as Maximal Subgroups in Various Linear Groupings (Sponsor: Dr. Michael Aschbacher)	Vipul Periwal Jr Physics/ Mathematics
1:20-1:40	Phase Conjugate Optics (Sponsor: Dr. Amnon Yariv)	Harold Weiser Jr EAS
1:40-2:00	The Reaction $\pi^- p \rightarrow \pi^{\pm} K^{\pm} K^o X$ (Sponsor: Dr. Geoffrey Fox)	Julian West So Mathematics
2:00-2:20	Run Away Electrons in a Weakly Coupled Gas (Sponsor: Dr. Noel Corngold)	Walter Wuensch+ Sr Physics
2:20-2:40	Magneto Optic Devices Uses in Optical Signal Processing (Sponsor: Dr. Dimitri Psaltis)	Jeffrey Yu Sr Electrical Engineering
	Beta Decay Phenomenology in Nuclear Fission Products (Sponsor: Dr. Petr Vogel)	John Behr+* Sr Physics
5:00-6:30	Informal Reception in President's Garden 415 South Hill, Pasadena Hosted by Dr. and Mrs. Goldberger	

\+ Richter/SURF Fellow
* Unable to participate in SURF Seminar Day

SURF Seminar Day
Saturday, October 9, 1982

Session VI: Thomas Laboratory, Room 010
Dr. David Stevenson Presiding
Associate Professor of Planetary Science

9:55 AM	Introduction	Dr. David Stevenson		
10:00-10:20	Very-Long-Baseline Interferometry Observations of the Galactic Center (Sponsor: Dr. Kwok-Yung Lo)	Andrew Berkin	Sr	Physics
10:20-10:40	On the "Equivalence" of Various Second Order Ordinary Differential Equations (Sponsor: Dr. Paco Lagerstrom)	Sekhar Chivukula	Sr	Physics
10:40-11:00	The Relationship Between X-Ray and Microwave Bursts from Solar Flares (Sponsor: Dr. Harold Zirin)	Mark Cornell	Sr	Astronomy
11:00-11:20	Erosion of Ice by Ultra Violet Light (Sponsor: Dr. Thomas Tombrello)	John Eng+	So	Electrical Engineering
11:20-11:40	New Understanding of Molecular Hydrogen in the EUV Region (Sponsor: Dr. Yuk Yung)	Tak Leuk Kwok	Jr	Physics
11:40-12:00	Trough Shaped Features on Saturnian Satellites (Sponsor: Dr. David Stevenson)	Mark Marley	Jr	Geophysics
12:00-1:00	Lunch - Dabney Garden			
1:00-1:20	Calibration of the Kitt Peak National Observatory Transform Spectrometer in 2000-3500 A Range (Sponsor: Dr. Ward Whaling)	Edward Miles	Sr	Applied Physics
1:20-1:40	Defining the Source of the Blue Continuum in Whitelight Solar Flares (Sponsor: Dr. Harold Zirin)	Steven Penn	So	Physics
1:40-2:00	VLBI Observations of the Galactic Center (Sponsor: Dr. Marshall Cohen)	Paul Ste. Marie	Jr	Physics
2:00-2:20	A Secenario for the Origin of the Moon (Sponsor: Dr. David Stevenson)	Chris Thompson	Sr	Physics
2:20-2:40	Infrared Photometry of Cepheid Variable Stars (Sponsor: Dr. Gerry Neugebauer)	Fred Wieland	Sr	Astronomy
5:00-6:30	Informal Reception in President's Garden 415 South Hill, Pasadena Hosted by Dr. and Mrs. Goldberger			

+ Richter/SURF Fellow

Steve Baxter
SURF Report
Sponsor: T. Collins

SALICYLALDIMINE COMPLEXES OF OSMIUM

A family of salicylaldimine (or salen) ligands has been synthesized. An unusual complex with a chlorinated salen ligand in a nonplanar configuration on osmium (II) has been prepared. This would be the first such salen complex where a bidentate β-diketonate ligand, such as acetylacetone, was not present.

Recently, J. Christie has synthesized and structurally characterized $K_2\{[Os(\eta^4\text{-}N_2,O_2\text{-}CHBA\text{-}Et)(PPh_3O)]_2O\}$ where CHBA-Et is a tetradentate, tetraanionic ligand (Fig. 1a).[1] The crystal structure (Fig. 1b) of this dimer shows that the two ligands are totally eclipsed, which is rather astonishing considering the large steric interactions between them.

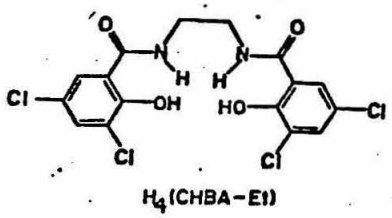

H_4(CHBA-Et)

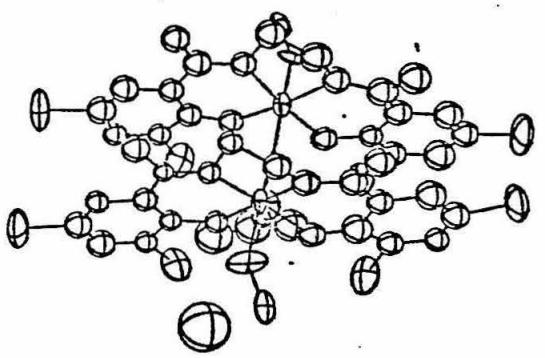

Figure 1. (a) CHBA-Et (b) Crystal structure of $K_2\{[Os(\eta^4\text{-}N_2,O_2\text{-}CHBA\text{-}Et)(PPh_3O)]_2O\}$. (Phenyl rings have been omitted.)

The initial goal of this project was to synthesize an analogous molecule, $[OsLX]_2O$, where L is a tetradentate, binegative ligand and X is, for example, a halide. Such a compound would be neutral, and thus the effect of the potassium ions would be eliminated. Both

x-ray diffraction studies and low temperature NMR could be used to determine any rotational barriers in the molecule and its preferred configuration.

An ideal ligand for the job seemed to be the commonly used salen ligand 1. We chose however to modify salen to provide ligands with a variety of chemical properties. Figure 2 shows a family of salicylaldimine ligands. In 2, 3, and 4, the oxidatively sensitive positions of the phenol rings are blocked with either chlorines or t-butyl groups.

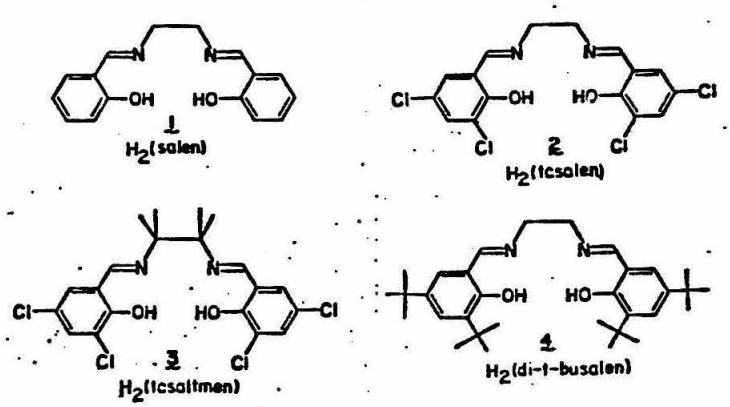

Figure 2. A family of salicylaldimine ligands.

These ligands have been prepared and fully characterized by IR, NMR, and elemental analysis.

The task of making high valent osmium complexes has, however, proven more difficult. Our first approach was the direct reaction of the ligands with high valent osmium starting materials. A variety of these were used, including $K_2OsO_2(OH)_4$, $(NH_4)_2OsCl_6$, $(NBu_4)_2OsCl_6$, and OsO_4. All of these attempts failed to give clean complexes.

Our emphasis then turned to the synthesis of low valent complexes, which we later hoped to oxidize. Although the results from reactions

using $Os_3(CO)_{12}$ and $OsCl_2(PPh_3)_3$ were not encouraging, a reaction involving $OsCl_3$ (Fig. 3) proved quite interesting. After 20 hours

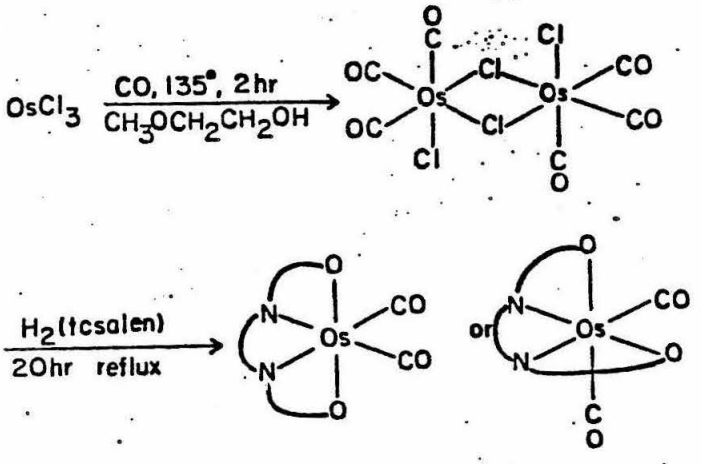

Figure 3. A low valent osmium complex.

reflux in 2-methoxyethanol, the reaction yielded a yellow solid with two C-O stretching bands in its infrared spectrum. This suggests that the compound is a cis-dicarbonyl complex, quite surprising considering that salen is planar in nearly all of its transition metal complexes. Notable exceptions are complexes of the type M(salen)(acac), where acac is acetylacetone, a bidentate ligand.[2,3] In these complexes, the acac ligand, which must occupy two adjacent coordination sites, forces the salen ligand to be nonplanar.

We have synthesized the first salicylaldimine complex of osmium, which we believe to be cis-$Os(CO)_2$(tcsalen). In this compound, the tcsalen ligand takes an unusual nonplanar configuration for reasons which are not yet understood. Our future work will attempt to better

characterize this compound and investigate its reactivity. Once the complex has been fully characterized, we will try to oxidize it to a high valent osmium complex.

References:

1. J. Christie, private communication.

2. M. Calligaris, et.al., J. Chem. Soc., Dalton Trans. (1972), 543-7.

3. N.K. Dutt and K. Nag, J. Inorg. Nucl. Chem., 30, 2779-2783.

BETA DECAY PHENOMENOLOGY IN NUCLEAR FISSION PRODUCTS

John Behr
SURF '82

Phenomenology of beta decay of nuclei produced in fission reactors is examined, using different sources of decay data. Data based upon standard gamma-ray spectra do not vary in average properties. Data based upon a different experimental technique (integrated gamma energies) reveals substantial differences in the dispersion of final decay states.

INTRODUCTION

In order to interpret the current experiments searching for evidence of oscillations of the antineutrinos ($\bar{\nu}_e$'s) emitted by a nuclear fission reactor, the energy spectrum of those $\bar{\nu}_e$'s must be calculated. The existing calculations made by several different groups of this spectrum conflict.[1]

The standard method of calculation is to obtain the individual neutrino spectra of the ~1000 beta-decaying nuclei that are products of fission, and simply sum them. A typical nucleus will decay through several different branches, with different endpoint energies Eend and different probabilities of decay (see Fig. 1). A nucleus' individual spectrum can be obtained directly from this information. However, detailed information on the possible branches is only available for ~200 of these nuclei. These known decay schemes are usually used as a basis for a phenomenological model of the unknown nuclei; thus data for the known decays becomes doubly important.

Prof. F. Boehm's Caltech group has made calculations based primarily on the data in two files put out by Brookhaven National Laboratory— Evaluated Nuclear Data File IV and its more recent successor ENDF/B-V. The two spectra calculated separately from these two files have substantial differences, particularly at the high energies of greatest interest (as much as 15% difference between 5 and 6 Mev).[2,3] Experimental measurements of the electron (β) spectrum from fission tend to support the older calculation.

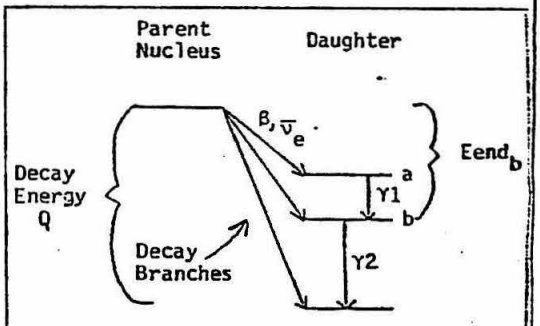

Fig.1 Energy level diagram of typical β decay.

From general principles, these data files may both be suspect. The standard technique for determining decay level schemes is to study the subsequent γ-rays emitted by the excited daughter nucleus. It has been suggested that for very complex level schemes (corresponding to large total decay energies Q), many γ-rays are lost in backround, and thus level schemes are incomplete; this is the so-called "Pandemonium" effect.[4] (E.g., Fig. 1; if γ1 is not observed, decays to level a are mistaken for decays to level b.)

These problems provided the impetus for this summer's work. Evidence was sought

for Pandemonium effects. Also, systematic differences between ENDF/B-V and IV that might explain the spectrum discrepancies were explored.

RESULTS

The present work compared general phenomenological features of β decay determined from four separate sources of data for the nuclei with known decay schemes. The two Brookhaven files used for the Caltech spectra were studied; ENDF/B-IV contains 162 known nuclei; ENDF/B-V contains these nuclei with ~70 others. Recent measurements made by several different groups of some 23 nuclei are gathered in "File 4"; these also used the standard technique of interpreting γ spectra. The other data file, prepared by a group at the Studsvik Science Research Laboratory in Sweden[5], was based upon a different experimental technique. This technique summed the energies of all γ-rays that coincided with a particular electron, thus eliminating Pandemonium effects. This Studsvik file, containing 63 nuclei, was used as a check for Pandemonium effects in the Brookhaven files.

The chief bulk property chosen for study was the fraction of the total available decay energy Q that went into β and $\bar{\nu}_e$ energy, rather than exciting the daughter state. This quantity, denoted by Eend/Q, and its root-mean-square deviation ("ds") are given for a particular nucleus by

$$\text{Eend/Q} = \sum_i (\text{Eend}_i/\text{Q})\text{Pend}_i \quad , \quad \text{ds} = \sqrt{\sum_i (\text{Eend}_i/\text{Q})^2 \text{Pend}_i - \left(\sum_i \text{Eend}_i \text{Pend}_i/\text{Q}\right)^2}$$

where Eend is equal to Q minus the excitation energy, Pend is the probability of decaying to a level Eend, and $\sum_i$ denotes summation over the number of branches.

For a given nucleus, Eend/Q would decrease if more higher-lying daughter states were found. The quantity ds is a measure of the spread of decay energies; it would tend to increase with the complexity of the decay scheme found. In turn, the complexity of decay schemes will generally increase with larger Q.

To observe the variation of these quantities with level-scheme complexity, they were averaged over the nuclei of a given Q, and these averages were then studied as a function of Q. The results are listed in Table 1 for the four sets of data studied. The average fraction of Q going to β kinetic energy alone, $\overline{(E_\beta/Q)}$, is also tabulated.

A general trend in $\overline{(\text{Eend/Q})}$ for Q ≥ 3 Mev was observed in each set of data. Parameters for linear fits to these trends are also listed in Table 1.

The quantity $\overline{(\text{Eend/Q})}$ is similar in the two Brookhaven files. This is true despite the fact that ENDF/B-V contains more branches than ENDF/B-IV (the average number of branches per nucleus in V is 12.2, in IV 9.8). So although the more recent level schemes are apparently much more complete, the new branches added evidently have small decay probabilities. The quantity ds, the dispersion of the decay energies around their mean, is also very similar throughout these two files.

Thus there are no obvious differences in the bulk properties of the two Brookhaven fi[illegible]

There is a substantial difference between the Studsvik and Brookhaven data in $\overline{Eend/Q}$; however, this is due mainly to the different sets of nuclei considered (nuclei common to ENDF/B-V and Studsvik have similar $\overline{Eend/Q}$). The difference in ds, however, is marked and not explainable in such fashion. The spread of endpoint energies is definitely greater in the Studsvik data than in the data based on standard γ spectra.

Q (Mev)	$\overline{(E_\beta/Q)}$ ENDF B-IV	ENDF B-V	Stud-svik	File 4	$\overline{(Eend/Q)}$ ENDF B-IV	ENDF B-V	Stud-svik	File 4	$\overline{ds}$ ENDF B-IV	ENDF B-V	Stud-svik	File 4
.5	.25	.24			.93	.89			.05	.02		
1.0	.24	.26			.76	.81			.08	.09		
1.5	.26	.28			.75	.79			.10	.08		
2.0	.28	.28			.75	.76			.08	.10		
2.5	.29	.28			.73	.72			.15	.14		
3.0	.22	.23	.41	.35	.57	.58	.97	.89	.15	.16	.13	.11
3.5	.26	.23	.30		.66	.58	.75		.13	.11	.12	
4.0	.27	.24	.34		.66	.58	.80		.13	.15	.19	
4.5	.29	.29	.36		.68	.69	.83		.13	.13	.19	
5.0	.29	.27	.32	.37	.68	.64	.75	.86	.15	.14	.24	.08
5.5	.28	.30	.34		.65	.71	.78		.10	.12	.23	
6.0	.34	.34	.36	.34	.77	.77	.81	.78	.10	.14	.25	.10
6.5	.29	.33	.35		.66	.75	.78		.13	.19	.24	
7.0	.32	.29	.32	.31	.71	.65	.72	.70	.26	.15	.25	.15
7.5	.31	.33	.34		.69	.73	.75		.15	.15	.23	
8.0	.45	.38	.37	.31	.97	.84	.81	.70	.13	.18	.21	.10
8.5	.40	.39	.34		.88	.87	.76		.02	.05	.23	
9.0		.32	.25	.36		.70	.56	.80		.26	.30	.11
9.5			.29				.64				.23	
10.0								.67				.16
Linear fit to $\overline{(Eend/Q)}$, for Q ≥ 3 Mev: Slope					.031 ±.003	.028 ±.002	−.018 ±.002	−.031 ±.001				
Y-intercept					.52 ±.02	.54 ±.01	.89 ±.01	.98 ±.01				

Table 1. Average properties of β decays as a function of Q.

CONCLUSIONS

This difference in the dispersion of the endpoint energies of the Studsvik data indicates that this data contains branching to a greater variety of endpoint energies than data based on traditional γ spectra. This suggests that the Pandemonium effect is present in the Brookhaven files.

There were no obvious overall differences found between the Brookhaven files that would explain the discrepancies in the calculated neutrino spectra. Although there are many individual nuclei which have different decay schemes in V and IV, these differences do not appear in any systematic way. The spectra discrepancies may be due to differences in individual nuclei; a list of likely nuclei, based on Eend/Q differences, will appear in a more detailed internal report for the Caltech group.

The present work has had considerable difficulty in discovering meaningful overall trends. Fluctuations among individual nuclei seem to be of more practical importance than average properties; the appearance of Pandemonium may have little practical consequence. It appears that calculations based on current β decay data, rather than relying on finding errors through studying overall decay phenomenology, must examine carefully the data given for the more important individual nuclei.

1. P.H.Frampton and P.Vogel, Phys. Reports 82 (1982) 342.
2. B.R.Davis et.al., Phys. Rev. 19C (1979) 2259.
3. P.Vogel et.al., Phys. Rev. 24C (1981) 1543.
4. J.C.Hardy et.al., Phys. Lett. 71B (1977) 307.
5. K.Aleklett et.al., Nucl. Phys. 246A (1975) 425.

Measurement of the Electron And Ion Energy Distribution Function in a Tokamak Plasma

Leif Bennett

California Institute of Technology, Pasadena, California, USA

ABSTRACT

A repelling field energy analyzer is used to measure the electron and ion distribution functions in the edge region of the Caltech Research Tokamak (B_T = 3.5Kg, $T_e \leq 30$ eV, $n_e \leq 10^{12}cm^{-3}$, R = 45 cm, a = 15 cm). It was found that this method will obtain a consistent electron energy distribution, but will not correctly determine the ion distribution.

Supported by a 1982 Caltech SURF Grant

September 20, 1982

Measurement of the Electron And Ion Energy Distribution Function in a Tokamak Plasma

Leif Bennett

California Institute of Technology, Pasadena, California, USA

1. Introduction

In order to build a working fusion reactor, it is necessary to control the level of impurities in the plasma. The release of impurities from the wall of a tokamak depends strongly on the plasma parameters, including the particle temperatures (T_e, T_i) in the region touching the wall. One device for measuring the temperatures is a retarding field energy analyzer.

A major problem associated with the measurement of ion characteristics is the difference in thermal velocity between ions and electrons. As electrons move about 40 times faster ($\sqrt{m_i/m_e}$) they form about 40 times the flux to a surface ($\gamma = nv$A), and tend to cause a much larger signal than the ions. In addition, the ion gyroradius is of the same order as the probe dimensions; two-dimensional flow of ions must be taken into account. The electron gyroradius is much smaller than the probe dimensions.

2. Apparatus

Figure 1 shows the energy analyzer. The external jacket, collector plate, and grid were all made of stainless steel. The grid mesh is of 50 μm wire, having a transmission coefficient of .75. The grid and collector potentials can be varied with respect to the jacket, which is at the potential of the vacuum vessel. The front aperture is a .34 mm diameter hole (#80 drill) in a .281 mm thick plate.

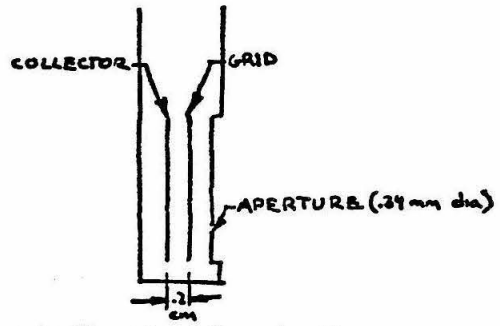

Figure 1: Drawing of probe tip.

The grid and collector were biased with dc power supplies(figure 2). The collector current was measured as the voltage across a known resistor on the grounded side of the collector power supply.

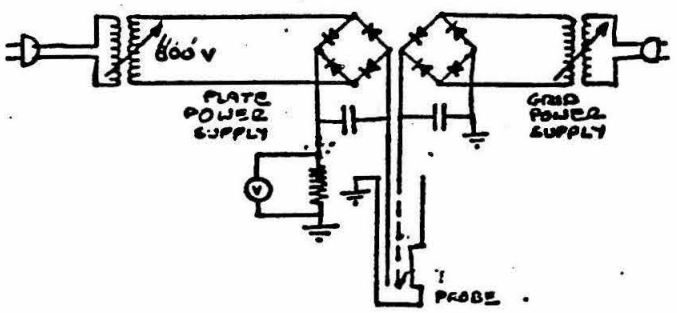

Figure 2: Circuit diagram of power supply and detector.

3. Experiment

3.1. Theory

A calculation of the electron thermal velocity v_τ and the electron drift velocity v_d gives $v_\tau/v_d=200$; in calculating the distribution, drift velocity can be ignored. Thus, the energy distribution function outside the probe (region I) is given by the Maxwellian:

$$n(\varepsilon) = 4\left[\frac{m}{2\pi kT}\right]^{\frac{1}{2}}\varepsilon e^{-\varepsilon} \tag{3.1}$$

where

$$\varepsilon = \frac{E}{kT} = \frac{\frac{1}{2}mv^2}{kT} = \text{dimensionless particle energy}$$

T = average temperature

The debye length λ_d is .036 mm, as compared to the entrance aperture size of .34 mm; shielding does not interfere significantly with the flow of the plasma through the entrance. The flux of particles through the aperture is given by:

$$\gamma(v) = n(v)vA$$

which, combined with (3.1), becomes

$$\gamma(\varepsilon) = 4\frac{A}{\sqrt{\pi}}\varepsilon^{\frac{3}{2}}e^{-\varepsilon} \tag{3.2}$$

The electron gyroradius is .05 mm, which is small compared to the entrance aperature; gyroradial effects can be ignored. For ions, the gyroradius is 1.5 mm. This does not change the number of ions that are incident on the aperature; however, the aperture and grid will stop ions based on the ion angle of incidence. The dependence of this on angle of incidence Θ is given by a transmission factor:

$$\gamma(v_a,v_e) = n(v_a,v_e)v_aAT \tag{3.3}$$

which expands to

$$\gamma(v_a,v_e) = n(v_a,v_e)v_aA\left[1-\left[\frac{t_1}{a_1}+\frac{t_2}{a_2}\right]\left[\frac{v_a}{v_e}\right]+\frac{t_1t_2}{a_1a_2}\left[\frac{v_a}{v_e}\right]^2\right] \tag{3.3a}$$

where

$$\tan\Theta = \frac{v_B}{v_p}$$

v_B = velocity parallel to the magnetic field

v_p = velocity perpendicular to the magnetic field

t_n = thickness of the blocking item

a_n = hole diameter of the blocking item

Thus, as the transmission function depends only on the relative velocities, the grid and entrance aperture have no effect on the energy distribution functions; they simply attenuate the signal.

Only those particles with sufficient energy to overcome the grid potential barrier φ will pass the grid. If the grid is charged with the opposite sign from the particles, essentially all the particles will be transmitted (subject to the transmission factor in 3.3). If the grid is biased to the same sign as the particles, the number of particles per unit time that will reach the region between the grid and collector will be given by:

$$\Gamma(\varphi) = \int_{\varphi}^{\infty} \gamma(\varepsilon)\, d\varepsilon$$

$$\Gamma(\varphi) = \int_{\varphi}^{\infty} 4\frac{A}{\sqrt{\pi}} T\varepsilon^{\frac{3}{2}} e^{-\varepsilon}\, d\varepsilon \qquad (3.4)$$

where T is the transmission factor ($0 < T < 1$) in (3.3).

If the collector is biased to the opposite sign of the grid, all the particles of higher energy than the grid will be attracted to the collector, while the particles having opposite sign than the grid will be repelled by the collector. Thus, to collect electrons, the grid is biased negative, repelling low-energy electrons, and the collector is strongly biased positive, repelling all ions and collecting all electrons that pass the grid.

The sheath thickness of the grid and collector are calculated by

$$d^2 = 5.4\times10^{-8}\, v^{\frac{3}{2}} j^{-1}$$

and ranged from .05 mm for 50 V to .25 mm for 400 V. The distance between the grid and collector, and grid and front end, was 2.3 mm. Particles passing the grid were therefore accelerated and deccelerated equal amounts before entering the collector field. The number of particles per unit time that reach the collector is given by eq 3.4, with φ interpreted as the retarding potential of either the grid or collector, and the current to the collector at a any phi is given by $I = q\Gamma(\varphi)$.

3.2. Results

The analyzer was placed in the tokamak with the entrance aperture about 1.2 cm from the wall. A plot of particles detected against angle of incidence showed that, as expected, the signal was at a maximum when the probe was oriented along the field lines (figure 3). The toroidal field was set at 3.5 kG; n_e at the edge was about $1\times10^{12}\text{cm}^{-3}$.

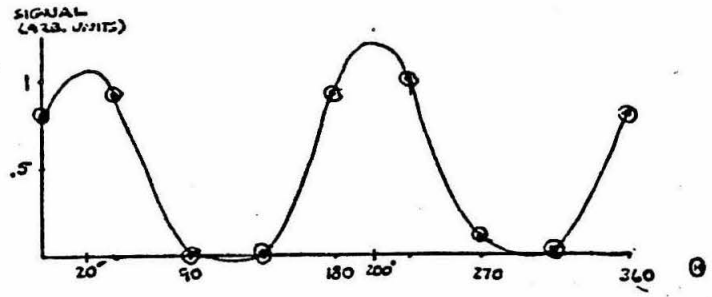

Figure 3: Angular distribution of signal.

3.2.1. Electron distribution function

For the determination of the electron distribution function, the collector plate was biased to +250 volts and the grid bias was varied from 0 to -100 volts between shots; in order to repel both electrons with energy less than the grid potential and all ions. The shots were reproducible to within 10 percent.

Figure 4 shows the current-time plots for various grid biases. The zero grid bias value agrees well with the theoretical current collected (corresponding to an n_e of $4\times10^{11}cm^{-3}$). The calculated electron temperature was 23±5 electron volts, using the best fit to the theoretical curve. The zero bias plot does not correspond to the number of electrons that enter a neutral probe, as the outer shell is at vacuum vessel potential (50 - 100 volts below plasma potential) and therefore changes the electron velocities before they reach the grid. To compesate for this, the current collected was matched with the theoretical curve, allowing for this potential difference (figure 5).

3.2.2. Ion distribution function

For the determination of the ion distribution function, the collector plate was biased to -100 volts and the grid bias was varied from 0 to +300 volts between shots. The shots were again reproducible to within 10 percent.

Figure 6 shows the voltage-time plots for various grid biases. The calculated ion temperature was 160±70 electron volts, again using the best fit to the theoretical curve. This is significantly different from the expected value of 20-30 eV. The difference can be explained as a result of secondary electron emission and front aperature bias. The secondary electrons caused by the ions and electrons hitting the grid and aperature would tend to decrease the grid potential barrier by increasing the density of electrons in the grid sheath. The front end, at vacuum vessel potential, is biased negatively with respect to the plasma. This bias causes the ions to undergo significant accelerations away from their original trajectories, resulting in an increased signal from higher-energy ions.

4. Conclusion

The analyzer was partially successful in measuring the energy distribution functions. The electron energy distribution was determined to be consistent with theory. The ion energy distribution function was not found with any success, although many associated problems were discovered. Further experiments to determine the ion energy distribution should be done.

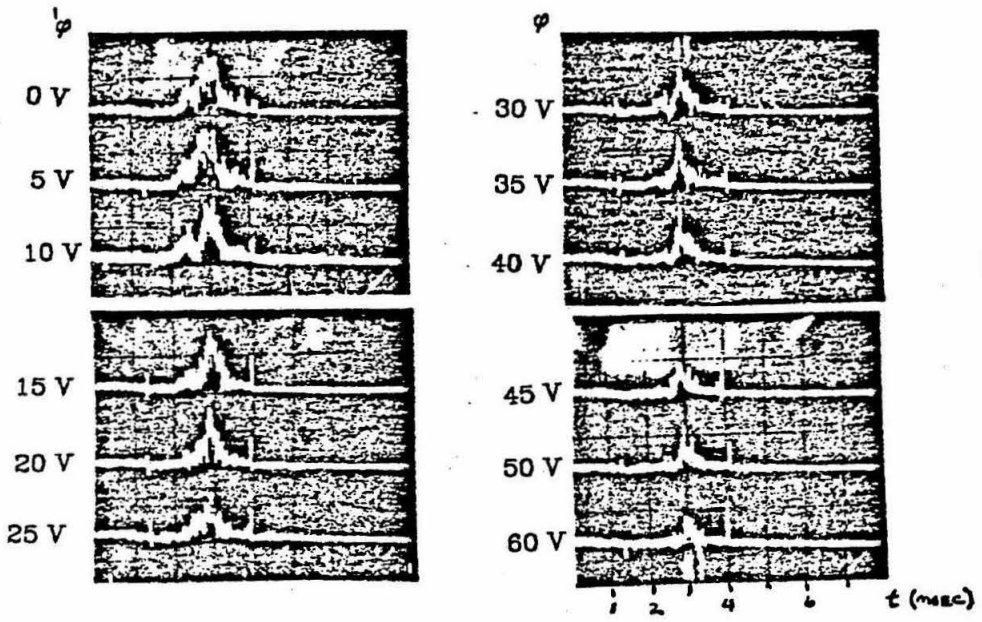

Figure 4 Electron signal at various grid potentials.

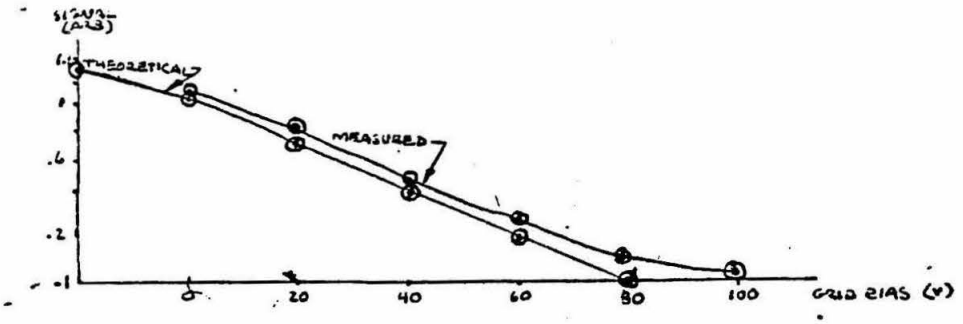

Figure 5 Electron distribution function matched to theoretical curve.

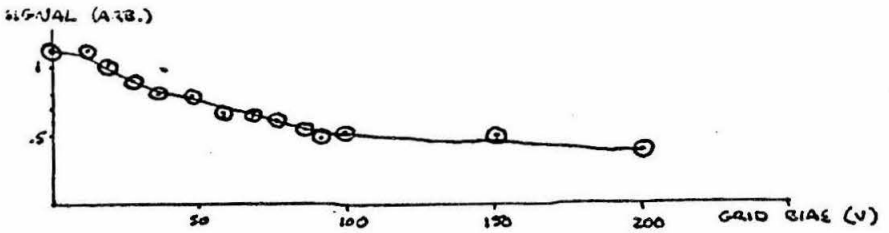

Figure 6 Ion distribution function.

References

1) H. Kimura, K. Odajima, T. Sugie, and H. Maeda: Jpn. J. Appl. Phys. 18 12, (1979) 2275.

2) S. Yamamoto, S. Sengoku, H. Kimura, Y. Shimomura, H. Maeda, H. Ohtsuka, K. Odajima, M. Nagami, and N. Ueda: Nucl. Fusion 18 2 (1978) 205.

3) S. Zweben, P. C. Liewer, and R. W. Gould; presented at Fifth International Conference on Plasma Surface Interactions, Gatlingburg, 1982.

4) A. W. Molvik, Rev. Sci. Instrum. 52 (5) May 1981 704.

5) G. Staudenmaier, P. Staid, and W. Poschenrieder: Journal of Nuclear Materials, 93 (1980) 121.

6) D. D. Neiswender and F. C. Kohout: Rev. Sci. Instrum. 43 (1972) 1475.

7) H. Kimura, H. Maeda, N. Ueda, M. Seki, H. Kawamura, S. Yamamoto, M. Nagami, K. Odajima, S. Sengoku, Y. Shimomura: Nuclear Fusion 18 9 (1978) 1195.

Very-Long-Baseline Interferometry Observations of the Galactic Center

Andrew L. Berkin
Summer Undergraduate Research Fellowship Report
California Institute of Technology
Pasadena, California 91125
September 20, 1982

ABSTRACT

The compact radio source at the Galactic Center was observed using very-long-baseline interferometry at λ=3.6 cm. The results indicate that the closure phase is non-zero, implying asymmetric source structure, and that within the errors, the scale size is the same as previously measured.

INTRODUCTION

The compact source at the Galactic Center is especially interesting because of its close proximity and possible similarities to the stronger compact sources in quasars and active galaxies (Ref 1). The Galactic Center radio source diameter varies as λ^2, which has been interpreted as being due to scattering by a dense surrounding ionized cloud (Ref 2). If true, this means that the intrinsic structure of the source is obscured, much as a star's light is obscured by the Earth's atmosphere, causing a "twinkle". Previous observations have found evidence of an unresolved core of 1 milliarc-second at 3.6 cm., in addition to a larger component of 15 milliarc-seconds (Ref 3).

However, all previous very-long-baseline interferometry (VLBI) observations were based on visibilities obtained on a single interferometer baseline. Our observations were made on three baselines,yielding visibilities measured over an interesting range of baseline lengths for checking the proposed model of the Galactic Center. In addition, closure phase was derived for the first time, providing strong constraints on source structure. Also, our data can be compared to previous observations.

OBSERVATIONS

The observations were made during the nights of July 19 and 20, 1982, using the 40 meter telescope at OVRO and the 26 meter telescopes at Goldstone (DSS1) and Hat Creek (HCRK). The Galactic Center was observed for six hours, with pointing corrections made by observing NRAO530 every hour. Several hours of calibration scans were made before and after the Galactic Center observations.

DATA REDUCTION

The data were recorded on videotapes and cross-correlated using facilities at the Caltech Astronomy department. Next, this data was integrated over time to obtain the uncalibrated visibility phase and amplitude. Integration times of between seven and ten minutes for the Galactic Center and one minute for the calibrators were used to obtain optimal signal to noise ratio without losing coherence.

Calibration of the flux is calculated from

$$S_T = b\rho \sqrt{T_{s1} \cdot T_{s2}} \cdot \frac{1}{\sqrt{g_1 g_2}} \cdot D$$

where S_T is the correlated flux density, S_c is the total flux density, T_s is the total system temperature, g is the antenna gain, and D is the factor Kelvin-per-Jansky (Jy). ρ is the correlation coefficient, and b and D are experimentally determined (Ref 4). The system temperature was measured hourly at each telescope for the Galactic Center and NRAO530; additional measurements were made on NRAO530 during the calibrator scans.

At OVRO, 3C273 was observed over a range of zenith angles to get a rough gain curve. This curve justified the use of a similarly shaped curve obtained by John Marcaide (Ref 5), which had the advantage of being less irregular. Because NRAO530 should be a point source on the baselines used, its amplitude should remain constant over a night's observations. By using the OVRO curve we were able to synthesize gain curves for HCRK and DSS1 by flattening the correlated flux of NRAO530. This data were then used to calibrate the Galactic Center.

RESULTS

Plots of flux density and closure phase versus time were made and compared to the models: a gaussian source of 0.8 Jy peak flux and ".015 FWHM with a 0.2 Jy peak flux spike in the center. Letting these parameters vary, an optimal model of 0.4 Jy peak flux and ".011 FWHM with a .17 Jy spike was fit to the data.

Figures 1-3 show the measured visibility amplitudes versus Greenwich Sidereal Time (GST) on the three baselines and the amplitudes expected from the model that was fit. Figure 4 shows the closure phase versus GST and the fit model. Within errors, the scale size of the Galactic Center is similar to that observed previously. The closure phase is significantly above zero. Thus, evidence exists for a non-zero closure phase, implying an asymmetrical source.

CONCLUSIONS

Due to limited data, previous modelling of the Galactic Center used the simplest models, such as symmetric gaussian brightness distributions. Our observations indicate that asymmetric structure may exist. Thus, the λ^2 dependence of the radius may not be due to interstellar scattering, because this generally implies symmetric structure. This result is important because it implies that any brightness distribution maps of the Galactic Center radio source refer to the intrinsic source structure.

REFERENCES

1. Brown, R.L., Lo, K.Y., and Johnston, K.J. Ap. J. 83, 1594, 1978.

2. Backer, D.C., Ap. J. Letters, 222, L9, 1978

3. Kellerman, K.I., Shaffer, D.B., Clark, B.G., and Geldzahler, B.J., Ap. J. Letters, 214, L61, 1977.

4. Cohen, M.J., et al, Ap. J. 201, 249, 1975.

5. Marcaide, J., memo to OVRO, Sept. 10, 1980.

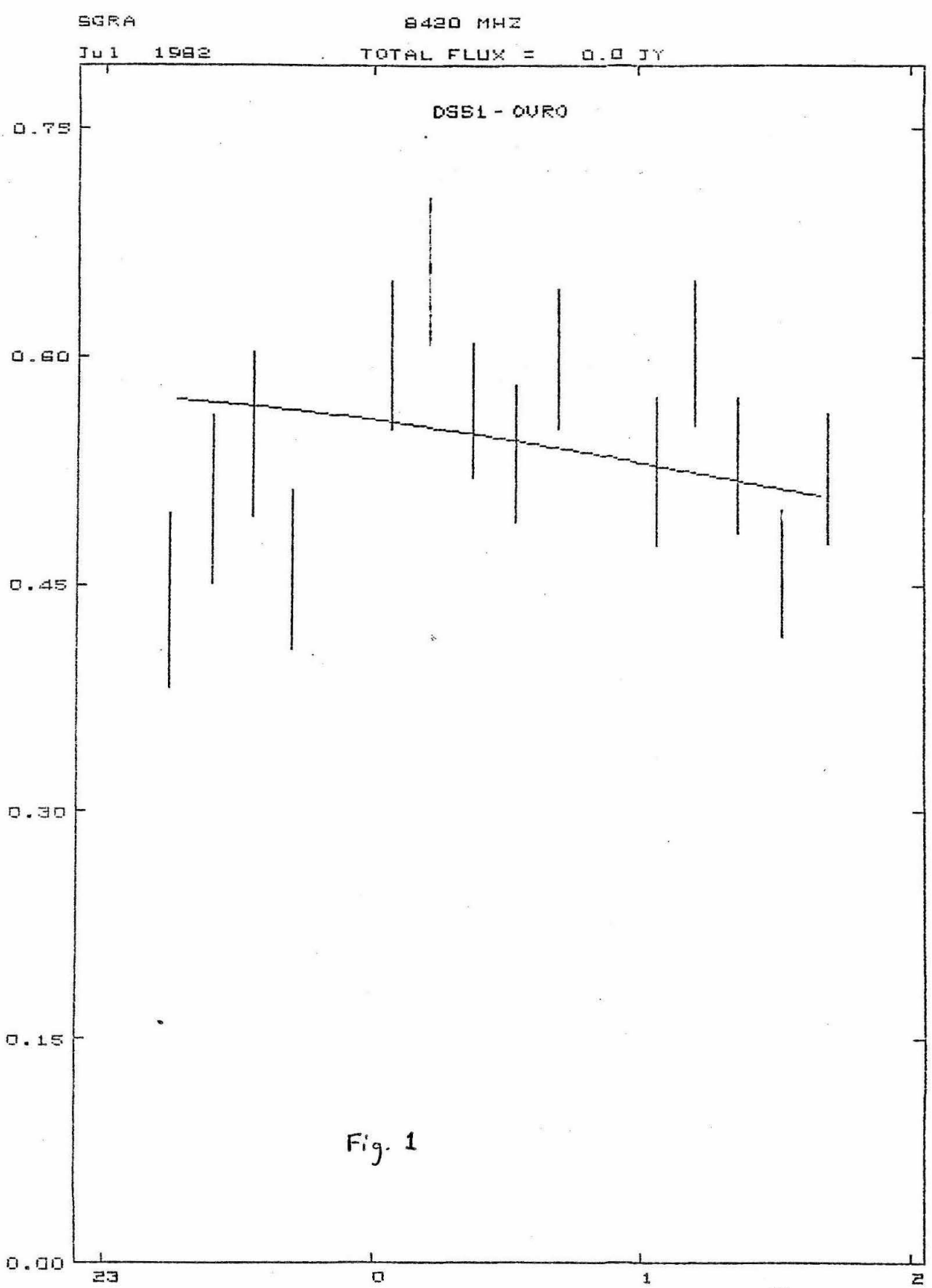
SGRA
8420 MHZ
Jul 1982
TOTAL FLUX = 0.0 JY
DSS1 - OVRO
0.75
0.60
0.45
0.30
0.15
0.00
CORRELATED FLUX (JY)
23
0
1
2
GREENWICH SIDEREAL TIME

Fig. 1

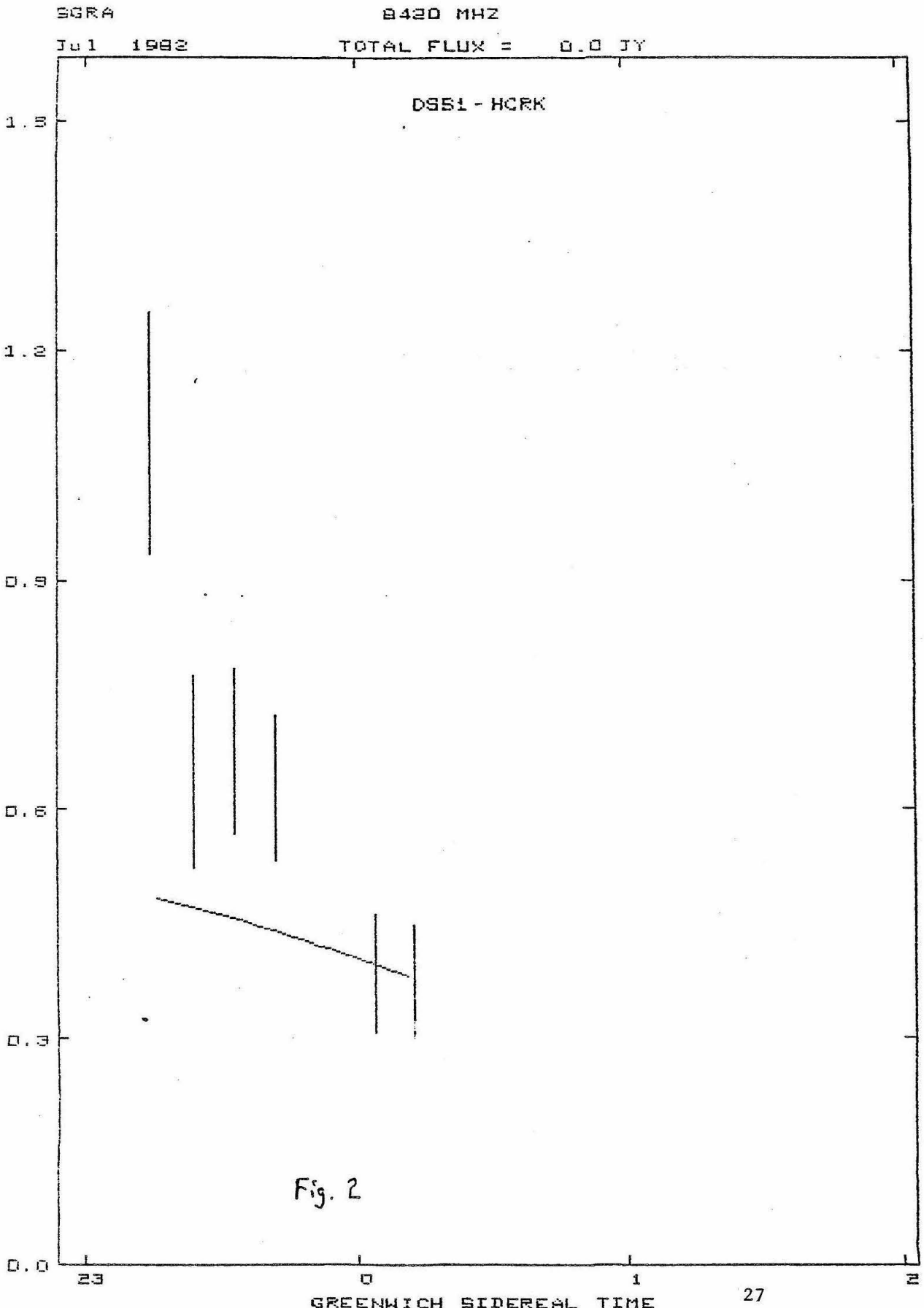
SGRA
8420 MHZ
Jul 1982
TOTAL FLUX = 0.0 JY
DSS1 - HCRK
1.5
1.2
0.9
0.6
0.3
0.0
23
0
1
2
GREENWICH SIDEREAL TIME

Fig. 2

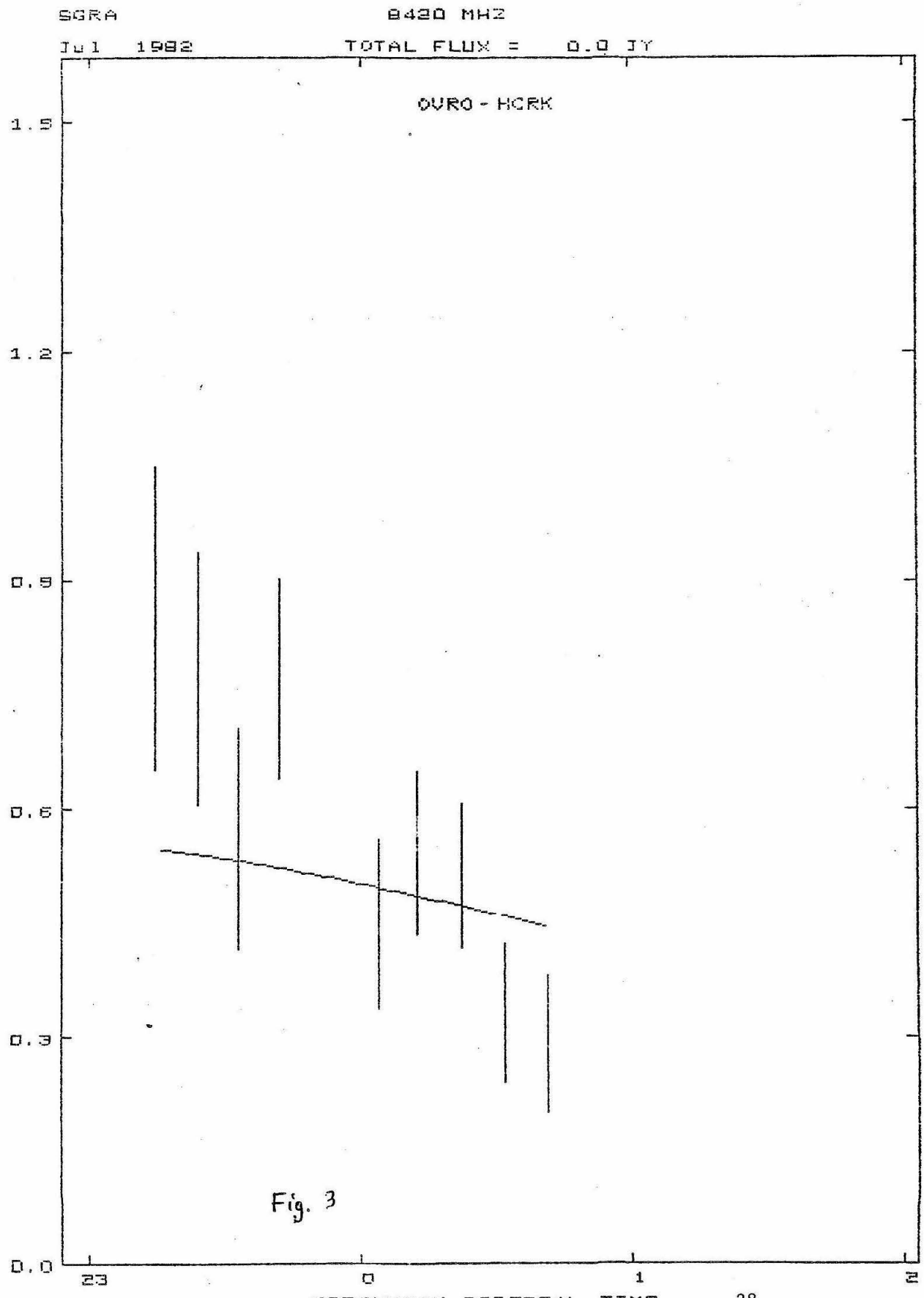
SGRA
8420 MHZ
Jul 1982
TOTAL FLUX = 0.0 JY
OVRO - HCRK
1.5
1.2
0.9
0.6
0.3
0.0
23
0
1
2
GREENWICH SIDEREAL TIME

Fig. 3

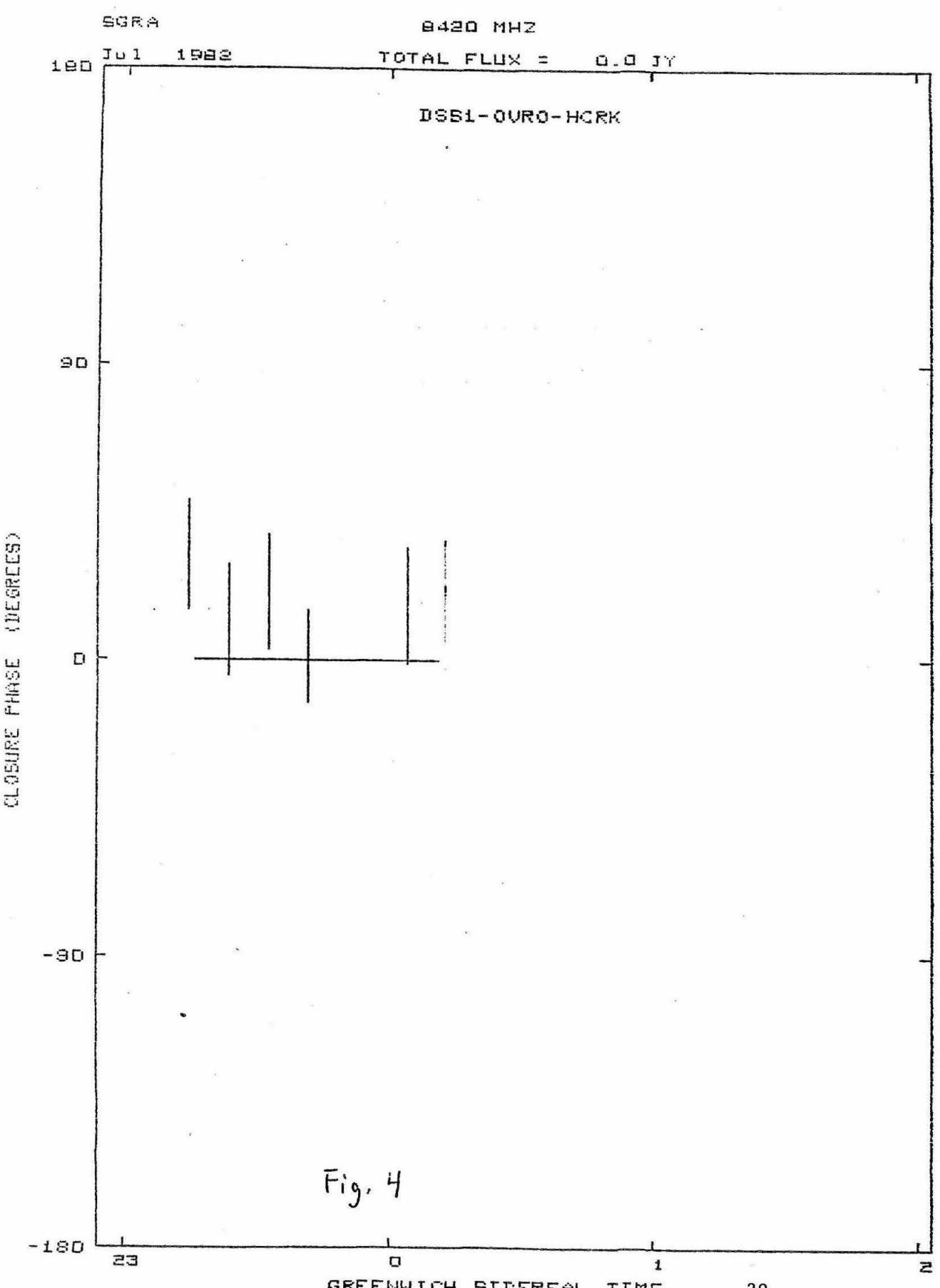
SGRA
8420 MHZ
Jul 1982
TOTAL FLUX = 0.0 JY
DSS1-OVRO-HCRK
180
90
0
-90
-180
CLOSURE PHASE (DEGREES)
23
0
1
2
GREENWICH SIDEREAL TIME

Fig. 4

Field Work in Namibia

Johanne Bolduc, Geology
sponsor: Dr. Ned Munger

My summer research took place in Namibia (South West Africa). There, I accompanied archaeologists and geologists on field expeditions. At the same time, I had the rare opportunity to acquire vast knowledge of a country on the threshold of independence.

My major reason for traveling to this land was to have first-hand experience on archaeological projects with Dr. Beatrice Sandelowsky (PhD., Berkeley) and Dr. Myra Shackley, of the University of Leicester. Also, I planned to assist Dr. Zed Ngavuire (PhD., Oxford) and Dr. Sandelowsky in a program of oral history. Finally, I expected that some of the greatest knowledge and experience I was to acquire would be serendipitouus.

I came across many unexpected difficulties which affected my plans: Dr. Shackley cancelled her trip to Namibia. Dr. Sandelowsky had a two week expedition planned for the northern Kaokoveld, the area bordering on Angola. The war and frequent land mine and terrorist incidents made me decide not to go. Furthermore, there is a personal animosity amongst the archaeologists in Namibia. I was not able to participate much in the oral history project due to my inability to speak the tribal languages, and because Dr. Ngavuire and Dr. Sandelowsky were not fully prepared for my assistance. I thus had to revise my plans.

With Dr. Sandelowsky, I went to the Rehoboth district to look at some Bushmen living sites and graves. There we found many stone tools and a pot. I also helped her and her assistant prepare for the oral history they were to do on their trip to the border.

With Harold Pager, a world-known expert on rock art, I spent many hours learning about rock art work that he is currently doing in the Brandberg, Namibia's tallest mountain. Rock art is a major part of Namibia's archaeology.

With Christine Sievers, archaeologist from the state museum, I spent nearly two weeks among Solitaire, Naukluft, Sesriem, and Sossusvlei, looking at old Bushmen sites. These weeks were most instructive as Christine explained to me all that she knew about excavating, Bushmen traits and habits, etc. In the caves, also, were many rock paintings.

I spent a few days at the Namib Desert Research Station at Gobabeb, which is headed by Dr. Mary Seely. It is a small research station situated amongst sand dunes and gravel plains in the world's oldest desert, the Namib. There, a geomorphologist from Oxford University explained to me the phenomena of sand dunes; I saw a field of Welwitschia (plants found exclusively in the Namib, and as old as 2000 years); and I saw a little of the fascinating beetle and insect work being done by the biologists there.

The South West Africa Geological Survey often invited me to join them on their field trips. The most memorable of them was the week-long trip headed by Dr. Von Knorring (Professor of Mineralogy, Emeritus,

Leeds University, England, now with the South West Africa Geological Survey), to Karabib, Usakos, Omaruru, Uis, Khorixas, and the Brandberg. For seven days we wandered amongst pegmatetic dikes. I had the opportunity to search for, see, and collect many, many minerals, some of which are rare. This week was perhaps the most instructive for me as a geologist, giving me knowledge and enthusiasm for the field of mineralogy.

I also went to a mineral-rich mountain, the Spitzkoppe and to the Skeleton Coastal Park with mining geologists. They shared with me their enthusiasm for the economics of ore bodies, how they discovered ore bodies, how they try to determine how the bodies were formed, and how they try to deduce which way the bodies twist, turn, and plunge.

I went on numerous other one or two day field trips in related areas. With each day out in the field, I also discovered the secrets of the land, the plants, the birds and animals. Namibia is a different and beautiful place, and I find myself most fortunate to have spent time there.

When I was in the city (Windhoek), I met people of all colors, all economic and educational backgrounds, and of all political views. My eyes and ears were opened to the racial problems, the fight for independence, the situation of drought, the reality of war, and cultures totally different to my own.

I cannot put into words all that I experienced this summer. I am still thinking about those things that I have learned, and I will continue discussing my experiences with Dr. Munger. I am most grateful to have had the opportunity to spend my summer in the manner which I did, in Namibia.

My Conclusions

There is a vast difference between black tribal culture and Western culture. The Westernization that Namibians are experiencing contributes to most racial problems. Basically, the racial situation at present seems to be almost hopeless, and it will take decades to reach some form of equilibrium.

I feel that Namibia will experience a period of tragedy and/or war before reaching peaceful independence.

I feel as if most Namibians are not (or do not seem to be) aware or concerned that there is a war in their country.

Namibia is not one country united, but rather it consists of (a minimum of) eleven indigenous tribes, whites, and Asians. People are more concerned with the survival of their group, than that of their country.

My trip has been an invaluable experience.

I realized how much the rest of the world is affected by American economy and politics. Also, I was/am most proud to be an American.

I thoroughly enjoyed being out in the field. My decision to be a geologist was confirmed.

ELASTIC SCATTERING OF PROTONS BY CARBON 12

A measurement of the differential cross section for the elastic scattering of protons by carbon twelve at six angles has been made about the 460 keV resonance in $C^{12}(p,\gamma)$. An extraction of the experimental S wave phase shift is planned. Three groups[1,2,3] have made similar measurements before with an accuracy of about 5% claimed. Due to the availibility of carbon foil targets and solid barrier detectors I expect to improve on the accuracy. In this experiment a beam of H^{2+} was obtained from the JN accelerator and passes through a 90 degree magnet for energy measurement. After passing through the exit slit of the magnet the beam passes through two focusing slits which reduces the beam to a ½x½ mm square striking the target. The solid angle of the detector is approximately $1x10^{-4}$ steradian. The target density was on the order 10 micrograms per square centimeter. Two detectors were used at all times, one held at a standard angle and the other at the angle which one wanted values for. In this manner the cross section at one angle could be extracted relative to the cross section at the standard angle at any particular energy. To measure the cross section at the standard angle a carbon foil was coated with a thin layer of gold and put in place of the carbon only target. With this method we can obtain the cross section of proton-carbon scattering at the standard angle relative to the cross section of proton-gold scattering which is well predicted by Rutherford's formula in this energy range. The ratio of the density of gold to that of carbon on the foil is the only major concern. Since helium-carbon and helium-gold scattering are both well predicted by Rutherford's formula at a common energy range we can measure the ratio of densities of the gold and carbon foil accurately by using a beam of alpha particles in place of H_2^+. From the data that has been analyzed at the time of this report there appears to be some discrepancy with the results of previous works at large angles.

References

1. Thesis by Milne, Caltech 1953
2. G. Goldhaber and R. M. Williamsom, 1951, Phys. Rev. 82, 495
3. Jackson et ale, 1952, Phys.Rev. 89, 365

August 28, 1982

On the "Equivalence" of Various Second Order Ordinary Differential Equations

R. Sekhar Chivukula
Summer Undergraduate Research Fellowship Report
California Institute of Technology (217-50)
Pasadena, CA 91025

Abstract

Using a simple topological argument in Cartan space (the space (x,t,dx/dt)) the "equivalence" of various second order ordinary differential equations is discussed. It is shown that the anharmonic oscillator is equivalent to the simple harmonic oscillator (i.e., an exact linearization is achieved) and that the nonautonomous harmonic oscillator is also equivalent to the simple harmonic oscillator, via an exact invariant. These arguments can be related to perturbation methods and should generalize.

Introduction

We consider the properties of a second order ordinary differential equation:

(1) $L(u,\dot{u},\ddot{u},t) = 0$ where $\dot{u} = \frac{du}{dt}$, $\ddot{u} = \frac{d^2u}{dt^2}$. We view solutions of this equation as paths in Cartan space; Cartan space is the space with coordinates $(u,\dot{u},t)$. From the theory of differential equations it is clear that each solution corresponds to one and only one path. We will also assume that the set of all paths (corresponding to all solutions) is complete, i.e. every point in Cartan Space has one and only one path through it.

Consider a smooth deformation of Cartan space or, equivalently, a smooth invertible mapping of the original Cartan space onto a new Cartan space. The paths in the (original) Cartan space are transformed as well. If, viewed in this deformed or new Cartan Space, the paths represent the solutions of a new differential equation:

(2) $\mathscr{L}(U,U',U'',T) = 0$ where $U' = \frac{dU}{dT}$, $U'' = \frac{d^2U}{dT^2}$,

then the differential equations $L = 0$ and $\mathscr{L} = 0$ are equivalent in the sense that they are related by a smooth, invertible, coordinate trans-

formation of Cartan space. Consequently, there is a relationship between the properties of the solutions of the two equations arising from the one to one correspondence between their solutions. This is particularly interesting when the solutions of one equation are known and the solutions of the other are desired.

We consider two examples in detail, the anharmonic oscillator and the nonautonomous harmonic oscillator and show that they are equivalent to the simple harmonic oscillator. In the first case we obtain the equivalence of a nonlinear equation and a linear one and in the second we find a simple, geometric, argument for the existence of the so-called adiabatic invariant.

Anharmonic Oscillator

Consider the system defined by the following Hamiltonian:

$$(3)\quad H = \frac{p^2}{2} + \frac{q^2}{2} + \frac{kq^4}{4} \qquad k > 0$$

and the corresponding equations of motion:

$$(4)\quad \dot{p} = -q - kq^3 \ , \quad \dot{q} = p$$

which is equivalent to:

$$(5)\quad \ddot{q} + q + kq^3 = 0 \qquad k > 0$$

The curves H = constant are closed "ellipses" in the phase space (p,q) and the paths of solutions in Cartan space are distorted helices. Along each solution the energy $E = p^2/2 + q^2/2 + kq^4/4$ is constant. The period of motion of the anharmonic oscillator is a function of energy.

Consider the following transformation: (1) rescale time (as a function of energy) such that every solution has the same period, (2) distort the coordinates in every constant time slice of Cartan

space such that the radius (in the $(\dot{q},q)$ plane) is equal to the energy of the solutions, and (3) distort the coordinates in every constant time slice such that the angle (in the $(q,\dot{q})$ plane) changes linearly in time along each solution. This transformation takes the paths representing solutions of the anharmonic oscillator equation onto circular helices with constant pitch. The harmonic oscillator:

$$(6)\quad H = \frac{p^2}{2} + \frac{\omega^2 q^2}{2} \Rightarrow \ddot{q} + \omega^2 q = 0$$

has solutions:

$$(7)\quad p = E'\cos(\omega t + \varphi), \quad q = -E'\sin(\omega t + \varphi)$$

which are circular helices with constant pitch in Cartan space. Hence we have shown the equivalence of the anharmonic oscillator and the simple harmonic oscillator. The transformation described above can be carried out explicitly using elliptic functions and integrals.

We have established the equivalence of a nonlinear differential equation and a linear equation. From this point of view the anharmonic oscillator is an archetype of a class of nonlinear differential equations which are equivalent to the simple harmonic oscillator and hence "linearizable in principle". Among other properties, the anharmonic oscillator must inherit a superposition principle from the harmonic oscillator. The appropriate generalizations of these ideas may explain some of the properties of the exactly integrable equations of the KdV type, which possess soliton solutions. In addition, for certain weakly nonlinear equations (where the nonlinearity can be treated as a perturbation), the appropriate "deformation of Cartan space" can be calculated order by order in perturbation theory using the method of averaging[1]. This geometrical result complements the results obtained by R. L. Anderson[2] et. al.

where many of these problems are treated from a group theoretic point of view. We believe that our geometrical methods will be fruitful in further study.

Nonautonomous Harmonic Oscillator

Consider the system defined by the folowing Hamiltonian:

$$(8)\quad H = p^2/2 + \frac{\omega^2(t)q^2}{2}$$

and the correspoinding equations of motion:

$$(9)\quad \dot{p} = -\omega^2(t)q\ ,\quad q = p \quad \text{or} \quad \ddot{q} + \omega^2(t)q = 0$$

where $\omega^2(t)$ is a nonzero function of time. This equation is a model for an ideal pendulum of small amplitude whose length varies with time, in this case $\omega^2(t) = g/\ell(t)$ where g is the gravitational constant. For an adiabatic variation of ℓ (and hence ω), i.e. when the change in ℓ over one period of oscillation is very small with respect to ℓ, this system has an approximate invariant:

$$(10)\quad E/\omega \tilde{=} \text{constant} \quad \text{where } E = \frac{p^2}{2} + \frac{\omega^2(t)q^2}{2}\ ,$$

this is the adiabatic invariant[3]. The adiabatic requirement can be introduced explicitly by letting $\omega(\tau)$, where $\tau = \varepsilon t$ and $\varepsilon << 1$. Then, the adiabatic invariant can be computed approximately to any order in ε[4].

Using the method outlined in Kruskal (1962, see note 4), Lewis[5] obtained an exact invariant ov (8):

$$(11)\quad I = \frac{1}{2}\left[\frac{q^2}{\rho^2} + (\rho p - \dot{\rho} q)^2\right]$$

where ρ satisfies :

$$(12)\quad \frac{d^2\rho}{dt^2} + \omega^2(t)\rho = 1/\rho^3$$

and is considered to be a given function of time. It can be shown that (11) reduces to (10) in the appropriate limit[6]. In addition Lewis obtains an

explicit transformation from (p,q) to (I,Θ), I given above, which satisfy:

$$(13)\quad \frac{dI}{dt} = 0 \quad \frac{d\Theta}{dt} = \frac{1}{\rho^2}$$

Define:

$$(14)\quad T = \int^t \frac{1}{\rho^2(t')}\, dt'$$

then:

$$(15)\quad \frac{dI}{dT} = 0 \ , \quad \frac{d\Theta}{dT} = 1 \ .$$

I and Θ can be regarded as the familiar "action-angle" coordinates for a simple harmonic oscillator with time T, let:

$$(16)\quad P = I\cos\Theta \ , \ Q = I\sin\Theta \ ,$$

then the paths describing the solutions of (9) are circular helices with constant pitch in the (P,Q,T) Cartan space. Hence, the nonautonomous harmonic oscillator is equivalent to the simple harmonic oscillator.

The nonautonomous harmonic oscillator is a special (linear) case of a nearly periodic system[7]; a nearly periodic system is one in which the curves H(p,q;t) = const are nested simple closed curves for constant t. From the point of view of deformations of Cartan space it is clear that many nearly periodic systems are equivalent to the simple harmonic oscillator. The simple harmonic oscillator possesses a nontrivial, local, isolating[8] invariant; namely energy. Because the transformation corresponding to the deformation is smooth and invertible all nearly periodic systems equivalent to the simple harmonic oscillator must inherit such an invariant; i.e. they must have an exact "adiabatic" invariant. This geometrical argument complements those given in Meyer[9] establishing the approximate

invariance of the action for nearly periodic Hamiltonian systems. The transformation from the nearly periodic system to the simple harmonic oscillator can be calculated, for the adiabatic case, order by order in the slowness parameter using an extension of the canonical perturbation method given by Gardner (see note 4).

Conclusions

In the method introduced here we have considered solutions of second order ordinary differential equations as paths in Cartan space and considered topological deformations of these paths. Two equations are said to be equivalent if their solutions are topologically equivalent. This point of view may unify and extend many previous results. We intend to pursue these ideas further. The nonautonomous nonlinear oscillator (with slowly varying parameters) should be studied using perturbation theory, and a more thorough investigation of the nonautonomous harmonic oscillator should be made in the case of parametric resonance. Further, we hope to investigate the group theoretical implications of these ideas; these considerations will probably involve Lie-Bäcklund Theory[10]. In addition, it should be possible to extend this method to higher order ordinary differential equations.

Basic geometric ideas such as those introduced here should underly the reduction of nonlinear partial differential equations to equivalent linear problems. Many difficulties may be encountered since the space which corresponds to the Cartan space in these examples is infinite dimensional. However, some simplification may result in considering only systems derivable from a Hamiltonian, for instance the KdV equation.

Notes

1. Lagerstrom - Boa, Singular Perturbations: Ideas and Techniques, to be published

2. i) R. L. Anderson, D. Peterson, "Algorithm for Global Linearization and Group Theoretical Equivalence of Completely Integrable 2n-Dimensional Dimensional Dynamical Systems Defined on R^{2n}"; Nonlinear Anal 1 (1976/77) no. 5, pp.481-493.

   ii) R. L. Anderson, J. Harrad, P. Winternitz, "Systems of Ordinary Differential Equations with Nonlinear Superposition Principles"; Physica 4D (1982) pp.164-182.

3. For a general discussion of Adiabatic Invariance see:

   i) Goldstein, Classical Mechanics, 2nd Edition, Addison-Wesley 1980, pp.531-540 .

   ii) L. D. Landou and E. M. Lifshitz, Mechanics, Pergamon Press, 1976, pp.154-157 .

4. i) C.S. Gardner, "Adiabatic Invariants of Periodic Classical Systems"; Phys. Rev., Vol. 115, No. 4, pp.791-794, Aug. 15, 1959 .

   ii) M. Kruskal, "Asymptotic Theory of Hamiltonian and other Systems with all Solutions Nearly Periodic"; J. Math. Phy., Vol. 3, No. 4, July-Aug. 1962, pp.801-828.

5. H. R. Lewis, "Class of Exact Invariants for Classical and Quantum Time Dependent Harmonic Oscillators"; J. Math.Phys. Vol. 9, No. 11, Nov. 1968, pp.1976-1986.

6. Goldstein, op.cit.

7. Gardner, op.cit.

8. Kruskal, op.cit.

9. R. E. Meyer, "Adiabiatic Variation - Part V: Nonlinear Near Periodic Oscillator"; ZAMP Vol. 27, 1976.

10. R. L. Anderson, N. H. Ibragimov, Lie-Bäcklund Transformations in Applications, SIAM, (Philadelphia) 1979.

SURF Final Report

Maximum Likelihood Method In Track Reconstruction For The IMB Proton Decay Experiment

by

Ming-Chung Chu

ABSTRACT

Previous efforts in track reconstruction for the IMB Proton Decay Experiment relied heavily on using Chi-squared as the test of goodness-of-fit. These efforts gave results with averaged errors in x,y,z coordinates of the vertex of the Cerenkoff cone of more than 1 m. We instead approached the problem with a Maximum-likelihood method, and we successfully pushed down the errors to within 30 cm.

1. INTRODUCTION

The basic input to the reconstruction process is the location, pulse height and time of arrival for each phototube that fired above a certain threshold among the 2048 phototubes distributed evenly on the walls of a water Cerenkoff detector in a salt mine in Cleveland,Ohio. If we define a Chi-squared as:

$$\chi^2 = \sum_{\substack{\text{all tubes} \\ \text{fired}}} (t - t_c)^2$$

t = OBSERVED FIRING TIME

t_c = CALCULATED FIRING TIME

then we have a measure of goodness-of-fit. From geometry,

$$t_c = t_0 + r \cos(\theta - \theta_c)$$

with to=time at the vertex of the Cerenkoff cone, in cm, r=distance between the vertex and a particular tube, θ=angle between the vertex and that tube, θ_c= Cerenkoff angle. Therefore, tc, and hence χ^2, depends on six parameters: the coordinates of the vertex (x,y,z), the time at the vertex (to) and the two polar angles defining the direction of the track (θ, ϕ).

These previous efforts assumed that the best set of the six parameters defining the track would minimize chi-squared. However, when tested on Monte Carlo events, these Chi-squared minimization programs obtained answers of more than 1 m off from the right track while giving a smaller Chi-squared than the expected answers. This hinted to us that Chi-squared is not a good model for our purpose. My project is to explore a different approach to the problem - the Maximum-likelihood method.

2. MAXIMUM-LIKELIHOOD METHOD

The basic idea of a Maximum-likelihood fit is to match the peak of the probability distribution of a certain observable with the experimentally observed value. For us, that observable is the time of firing of the tubes. We plotted the actual distribution of firing time and devised the following fitting function:

$$P(t) = \frac{1}{[(t-a)^2+b^2]^{\frac{1}{2}}} \frac{1}{\pi}\left[\frac{\pi}{2} + \tan^{-1}(k(t-a-b))\right]$$

where P(t) is the probability of observing the tube fired at time t, a,b,and k are constants. The peak of this distribution is at very nearly a+b. We therefore have a new measure of goodness-of-fit, defined as

$$Y^2 = -\sum_{\substack{\text{all tubes} \\ \text{fired}}} \ln P(t)$$

Tests on Monte-Carlo Events show that the minimization of Y^2 (with to kept fixed) gives a fit of the track to within 30 cm (averaged error in x,y,z coordinates).

We now understand why the Chi-squared model fails. Chi-squared is actually a special case of the Maximum-likelihood method when the probability distribution is a Gaussian. For our case, the distribution of firing time of a phototube, because of causality, Rayleigh scattering and noise, differs very much from Gaussian. Therefore, it is not fair to use the Chi-squared model any more.

3. CONCLUSIONS

In later development of the reconstruction program, we should use the Maximum-likelihood method. Chi-squared is at best a fast approximation to the solution.

Final SURF Report, Summer 1982

THE RELATIONSHIP BETWEEN X-RAY AND MICROWAVE BURSTS FROM SOLAR FLARES

Mark E. Cornell

SURF Advisor: Dr. Harold Zirin

Solar Astronomy 264-33
California Institute of Technology
Pasadena, CA 91125
(213)356-4011

THE RELATIONSHIP BETWEEN X-RAY AND MICROWAVE BURSTS FROM SOLAR FLARES

Mark E. Cornell

ABSTRACT

X-ray and microwave bursts from solar flares are highly correlated in time and there is a time lag between corresponding peaks in the x-ray and microwave time profiles. High time resolution SMM x-ray data have been analyzed with coincident microwave observations to quantify this time lag. In a preliminary analysis of one flare, an energy-dependent lag has been found, varying from ~ 0.4 sec at 32 KeV to 0.0 sec at 200 KeV. The lag does not depend signifcantly on polarization. One interpretation of this result is that the acceleration time of electrons in solar flares has been measured.

INTRODUCTION

Microwave and x-ray emissions from solar flares are closely related because both are generated by energetic electrons, the x-rays from electron bremsstrahlung and the microwaves from synchrotron radiation. It has been known for some time that x-ray and microwave bursts are correlated in time (Takakura 1975). Further, a time delay has been observed between the maxima of hard x-ray and microwave bursts. This time delay has previously been measured to be on the order of ± 6 sec (Crannell et al. 1978). However, as the instruments used for these observations only had a time resolution of between 1 and 5 sec, the magnitude and even the sign of this time delay was unclear. Time delays of this order are interesting because the propagation time of electrons along the magnetic field lines in flares is of the same order.

This work was inspired by the fact that new x-ray and microwave observations have recently become available, with resolutions better by a factor of ten than those available previously. We have analyzed this new data to determine the time lag between x-ray and microwave time profiles as a function of energy, to a resolution of 100 msec. We did not look merely for a time lag between the maxima of the x-ray and microwave bursts. Instead, the entire time profile was used in the calculation of correlation coefficients between the two data sets.

The microwave observations used for this analysis were made at the Owens Valley Radio Observatory using a two-element interferometer operating at 10.6 Ghz. The interferometer uses switched polarization and has an effective time resolution of 100 msec. Up to this point, the interferometer signal from the two antennas was used to emphasize contributions from small scale sources. The x-ray observations were made by the Hard X-Ray Burst Spectrometer (HXRBS), flown aboard the Solar Maximum Mission (SMM). The spectrometer has been described in detail by Orwig et al. (1980) and the data so obtained by Dennis et al. (1982). Basically, the HXRBS data consists of numbers of counts accumulated in 128 msec intervals for each of 15 energy bins, covering energies ranging from about 30 KeV to 500 KeV.

PROCEDURE

A set of four flares was chosen according to the criteria that each be well-covered by microwave and x-ray observations and that each should demonstrate fast x-ray spike structure. The latter criterion ensures that the x-ray time profile would have many sharp peaks that could be easily assigned to corresponding microwave peaks, aiding in the correlation process. To date, only one of these flares has been analyzed.

The first step in the analysis of a flare was to divide the x-ray count data, which has a time resolution of 128 msec, into 100 msec time bins to match the integration time of the microwave data. Fractional x-ray counts were carried through to avoid rounding errors. Once the two data sets were matched up, correlation coefficients between them could be calculated.

The basic idea was to compute a correlation coefficient between the two time profiles using a trial time delay and then to shift the profiles with respect to one another, creating a new trial time delay, which in turn lead to a new correlation coefficient and so on. The equation to be evaluated was:

$$R_{xyr} = \frac{1}{N-r} \sum_{i=1}^{N-r} x_i y_{i+r} \qquad r = -m,\ldots,-1,0,1,\ldots,m \qquad (1)$$

Here, R is the correlation coefficient, N is the number of data points available, x and y are the data sets to be correlated having been standardized by transforming the original data to unit variance and zero mean, r times the data time resolution is the trial delay time, and m times the data resolution is the maximum delay time to try.

Equation (1) was evaluated for the data sets corresponding to the ten lowest HXRBS energy bins, producing a sequence of correlation coefficients versus delay times for each energy. From this information, it is an easy matter to pick off the delay time that maximizes the correlation coefficient, subject to the constraint that the delay so found must be considered plausible when a visual check of a plot of the data is made.

The only problem with the above procedure was that correlation versus delay time plots made from the data as given would have extremely broad peaks — i.e. it was difficult to choose accurately one specific delay time as the best one. It was found that the peaks could be sharpened up considerably if both the microwave signal and the x-ray count time profiles were put through a highpass filter before the correlation coefficients were computed.

Since it was observed that in the particular flare being analyzed, the microwave and x-ray profiles had peaks with widths on the order of 2 sec, the data sets were sent through a highpass filter that cut out all time structure longer than 2 sec. This effect was produced by sending the data through a lowpass sine-Butterworth filter, shifting it back by the filter's time constant (in this case 2 sec), and subtracting the averaged signal so generated from the original. The algorithm for the lowpass filter has been described by Otnes and Enochson (1972) and Otnes (1968). The effect of this processing was to emphasize small time structure in the microwave and x-ray time profiles and hence sharpen the peaks of the correlation versus delay time plots.

Thus the analysis of a flare consists of correlating each x-ray channel separately with each of the left and right polarization microwave signals to generate a most probable time delay to associate with the energy of each x-ray bin. Because the higher energy bins have fewer and fewer x-ray counts associated with them, a limit on the highest energy for which we can find a time delay is imposed. We think that the time delays determined with the procedure discussed here are good to about the FWHM of the correlation peaks divided by square root of the total number of x-ray counts.

RESULTS AND CONCLUSIONS

From the analysis of a flare observed on 2 February 1980, with a peak time of 23:32:55 UT (HXRBS Flare number 2163), an energy-dependent time delay between the x-ray and microwave time profiles was found. The observed time lag varies from $0.40 \pm .03$ sec at 32 KeV to $0.0 \pm .1$ sec at 200 KeV. There were no significant differences found between right and left polarizations. The remaining flares for which we have data will be analyzed as soon as possible.

One explanation of the observed time delay is that it represents the acceleration time of electrons along the loops in solar flares. First we see x-rays from electrons at 30 KeV and then 0.4 sec later we see the corresponding microwave emission. Under the acceleration interpretation, the fact that the 200 KeV electrons exhibit zero time lag implies that they must be the ones producing the microwaves. Hence the electrons would be accelerated to 200 KeV in 0.4 sec.

ACKNOWLEDGEMENTS

We would like to thank Brian Dennis and Alan Kiplinger at the Goddard Space Flight Center for providing the HXRBS data and Gordon Hurford and Harold Zirin at Caltech for much guidance and advice. This work was carried out under a SURF grant from Caltech and will be continued as a senior thesis.

REFERENCES

Crannell, C. J., Frost, K. J., Matzler, C., Ohki, K., and Saba, J. L. 1978, Ap. J., 223, 620.

Dennis, B. R., Frost, K. J., Orwig, L. E., Kiplinger, A., Chewning, T. O., Dennis, H. E., Gibson, B. R., Kennard, G. S., Tolbert, A. K. 1982, The Hard X-Ray Burst Spectrometer Event Listing 1980 and 1981, NASA Technical Memorandum 83925.

Orwig, L. E., Frost, K. J., and Dennis, B. R. 1980, Solar Physics, 65, 25.

Otnes, R. K. 1968, IEEE Trans. Audio Electoacoustics, AU-16, 330-335.

Otnes, R. K., and Enochson, L. 1972, Digital Time Series Analysis (New York: John Wiley and Sons)

Takakura, T. 1975, in IAU Symposium 68, Solar Gamma-, X-, and EUV Radiation, ed. S. Kane (Dordrecht: Reidal), pp. 299-313.

The Action of Ozone in the Deterioration of Works of Art

by
Kaitlin Drisko

ABSTRACT

The effects of ozone on watercolor pigments have been studied. The results are expected to support findings that certain organic pigments are sensitive to the presence of ozone, especially those of anthraquinone and triphenylmethane structures. Possible mechanisms for the fading of anthraquinone pigments are discussed based on studies of ozone-anthraquinone dye reactions.

Introduction

The Earth's upper atmosphere normally contains ozone generated from oxygen by ultraviolet solar radiation. Ozone is also present in photochemical, or 'Los Angeles' smog, formed when ultravoilet radiation initiates a series of photochemical reactions involving gases present in the atmosphere due to the combustion of organic fuels. The excessive cracking of rubber products was one of the earliest indications of the presence of oxidants in this type of smog and has since been attributed specifically to ozone (1). Atmospheric contaminants, particularly ozone and the oxides of nitrogen, have long been a subject of concern in the textile industry, causing fabric damage and the destruction of dyes in colored fabrics (2). Museum conservation scientists have determined that organic colorants will fade very slowly in the presence of oxygen and methods of protecting museum pieces have been discussed (3). The extent or rate at which ozone may be damaging works of art is not known.

The objective of this study was to determine the effects of ozone in the absence of light on the colorfastness of artist's watercolor pigments. This was accomplished by determining the degree of pigment fading upon exposure to 40 pphm ozone for three months and demonstrating which pigments are most susceptible to color change.

Materials

Watercolor paints were chosen for this study because the pigment particles when applied are not immersed in a heavy binder and hence are exposed directly to the surrounding atmosphere. Twenty-seven Winsor-Newton watercolors were selected for their similarity in chemical composition to those which showed fading in a previous experiment conducted at Caltech by Cass and Shaver (1982). The samples were prepared by making lengthwise strokes with a watercolor wash on presoaked strips of Hunt-Bienfang watercolor paper. Extra strokes with water were sometimes needed to eliminate streaking. The strips were cut in half; one half serving as a control sample to be kept in a dark place for the duration of the experiment and the other to be exposed to ozone. A British Blue Scale was also included with the watercolor samples. The British Blue Scale is a strip of fabric dyed with seven standard blue dyes and is used in many museum displays to detect light fading.

Color Analysis

The color of each sample was defined using the Munsell System of Color Notation measuring each sample's hue, value, and chroma (4). The hue indicates a sample's relation to a visually equally spaced scale of ten major hues. The value is the lightness or darkness of a color in relation to a neutral grey scale. Chroma indicates the departure of a given hue from a neutral grey of the same value. Pigment density was determined using a Macbeth Model RV-517 reflectance densitometer which measures the percent reflectance at three distinct wavelengths. A spectrophotometer was used to measure the percentage of light reflected at each of fifteen wavelengths (5).

Experimental Design

Most pigments are not resistant to light fading, therefore an exposure chamber was designed which excludes as much light as possible. Ozone is introduced to the chamber by passing filtered air under an ultraviolet light source. The filters consist of Purafil to extract much of the sulfur dioxide and oxides of nitrogen, activated carbon to decompose most of the ozone already present in the room air, and a particulate filter. The concentration of ozone inside the chamber is monitored by a REM Ozone Monitor and held at 40 pphm for 90 days, a value comparable to approximately three years exposure to Los Angeles outdoor ozone concentrations. Paper sheets to which the watercolor samples were attached were hung against the walls of the chamber. A fan is located at the bottom to insure good mixture of the ozone. The temperature and humidity inside of the chamber are monitored and controlled by the laboratory air conditioning system.

Anticipated Results

The experiment is still in progress at this writing, with the 90 day exposure period due to be completed on October 13, 1982. Supporting the results of the previous Caltech experiment, those pigments containing Alizarin, Pigment Red 83, are expected to show fading. Alizarin is a precipitated solid pigment with an anthraquinone structure. Although anthraquinones are not simple aromatics, because of the presence of two benzene rings they are known to react similarly. Aromatic compounds are reactive towards ozone; and, in phenols, such electron-attracting substituents as nitro and halogen deactivate the ring, and electron-repelling substituents such as alkyl and hydroxyl activate the ring for ozone attack (6). Salvin and Lebensaft (7) have demonstrated that ozone attacks the anthraquinone dye Disperse Blue 3, forming phthallic acid, evidence for the potential of ozone to cleave polycyclic ring systems which leads to an irreversible destruction of the chromophore and a consequent loss of color. Although Alizarin is a solid, precipitated as a metal complex, its basic structure differs from Disperse Blue 3 only in substituents to the anthraquinone ring system. It is therefore possible that this breakdown in structure is also the cause of color loss in the watercolor pigments exposed to ozone. Mauve, a blend of copper phthallocyanine and Triphenylmethane Lake (a lake of Basic Violet 14), has also shown a marked fading in the presence of ozone in the previous experiments at Caltech. Triphenylmethanes are known to be destroyed under strong oxidizing conditions (8); but, by including six samples containing copper phthallocyanine or its derivatives we would expect our results to show if these structures also react with ozone.

Conclusions

Artists are presently using many pigments commercially abandoned long ago due to the synthesis of more stable and durable pigments. Almost all anthraquinone

dyes have recently fallen to disuse in industrial applications in part because of the destructive effects atmospheric contaminants have on them. Studies are in progress to determine the concentrations of ozone which works of art are being subjected to in the Los Angeles area. Improved filteration in the air conditioning systems of most local museums have brought the indoor concentrations of ozone to almost nothing. But buildings such as art galleries, private residences and smaller museums which do not have elaborate filtering systems could have daily indoor ozone levels as high as half of the outdoor concentration.

References

(1) Newton, R. (1945), "Mechanism of Exposure - Cracking of Rubber" Journal of Rubber Research, 14, 27-39.

(2) Jaffe, L. (1967), "The Effects of Photochemical Oxidants on Materials", Journal of the Air Pollution Control Association, 17, 375-378.

(3) Arney, J., Jacobs, A., Newman, R., (1979), "The Influence of Oxygen on the Fading of Organic Colorants", Journal of the American Institute for Conservation, 18, 108-117.

(4) Munsell Book of Color, 2 vol. Munsell Color, Macbeth Division of Kollmorgan Corporation, Baltimore, Maryland.

(5) Pellicori, S., (1980), "Spectral Properties of the Shroud of Turin", Applied Optics, 19, 1913.

(6) Bailey, P., (1975), "Ozonation of Aromatic Compounds", Ozone Chemistry and Technology, J. Murphy and J. Orr (eds.), The Franklin Institute Press, 1975.

(7) Lebensaft, W. and Salvin, V., (1972), "Ozone Fading of Anthraquinone Dyes on Nylon and Acetate", Textile Chemist and Colorist, 4, 182-186.

(8) Kirk-Othmer Encyclopedia of Chemical Technology, vol. 20, 2nd ed., Interscience Publishers, New York, 1963, p. 693.

EROSION OF ICE BY ULTRA VIOLET LIGHT

By

John E. Eng

SURF Final Report

August 23, 1982

Abstract: I will describe the method that I have used and will continue to use to try and actually measure the very controversial sputtering yield of water ice by ultra violet light.

Are the rings of Saturn constantly being regenerated? How long do the icy ring particles "live?" Is ultraviolet photon sputtering the source of the dense cloud of atomic hydrogen surrounding Saturn? These are some of the questions which can be answered by knowing the sputtering yield of ice by ultraviolet light. Some people claim that the sputtering yield is of the order of one while others claim that it is of the order of 10^{-10}. I will try to solve these problems by actually measuring the sputtering yield of ice by ultraviolet light.

Here is my step by step method for measuring the sputtering yield of ice by UV light:

1). Backscatter a collimated 2 MeV proton beam off of a bare beryllium disk coated with a thin layer of gold. This provides an energy calibration for the detector.

2). Form an ice target (approximately 2000Å thick) on the Au-Be target substrate which is cooled to 10°K with liquid helium.

3). Backscatter a collimated 2MeV proton beam off of the ice target.

4). Photon sputter the ice target with a collimated ultraviolet light source.

5). Backscatter a collimated 2 MeV proton beam off of the photon sputtered target.

Note that all of this is done in an ultra high vacuum (approximately 10^{-9} torr).

From the differences in the energy loss of the beam backscattered off of the unsputtered ice target and the subsequent sputtered ice target, we can calculate the change in thickness of the ice target. Since we know the area defined by the

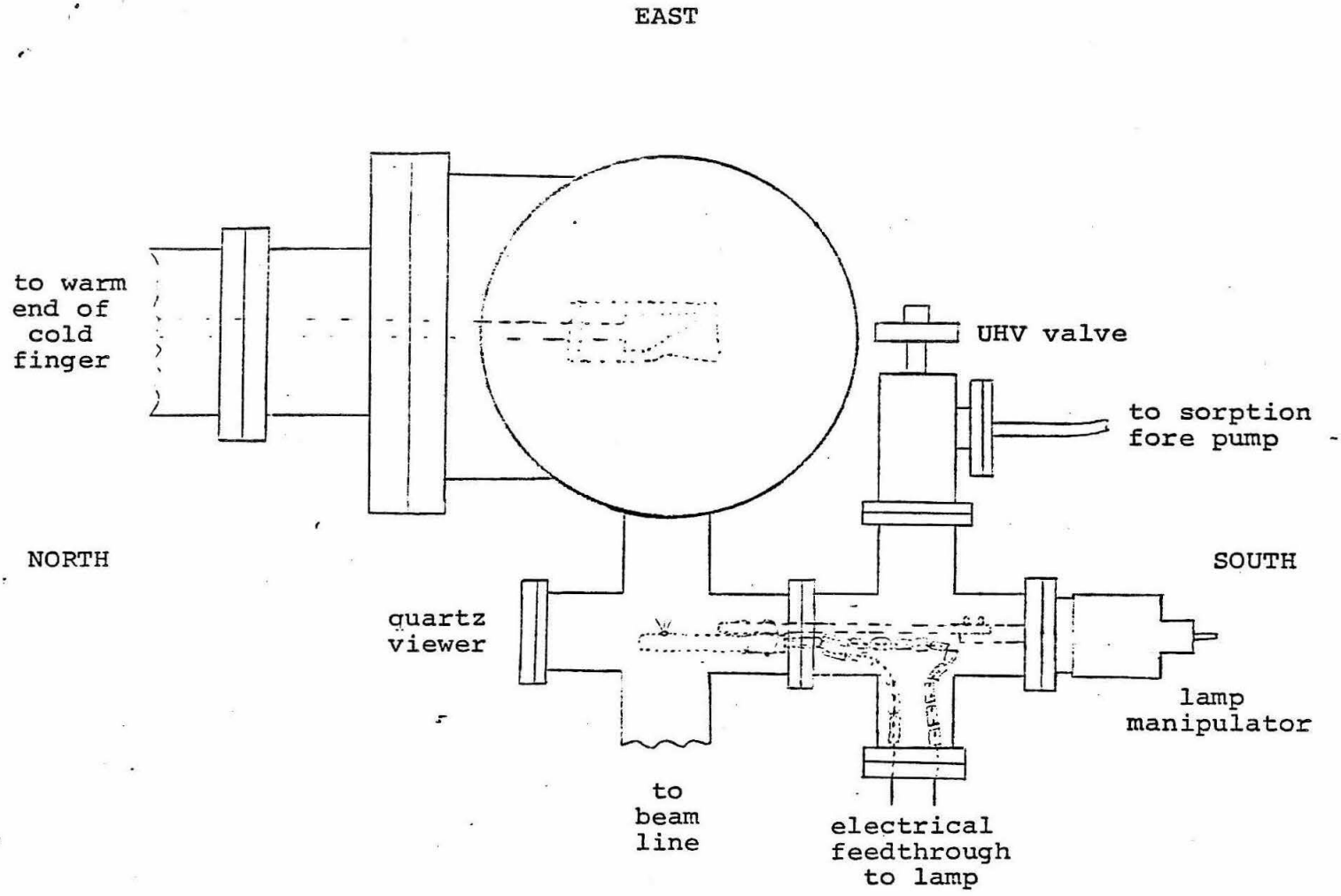

TOP VIEW OF ULTRAHIGH VACUUM CHAMBER

collimators, the photon flux of the ultra violet lamp, and the duration of the exposure, we can calculate the sputtering yield.

Ten weeks is just not enough time to complete most real research projects of any complexity. Ten weeks is usually only enough time to get a good start. I regret that I have not been able to obtain any pertinent data yet.

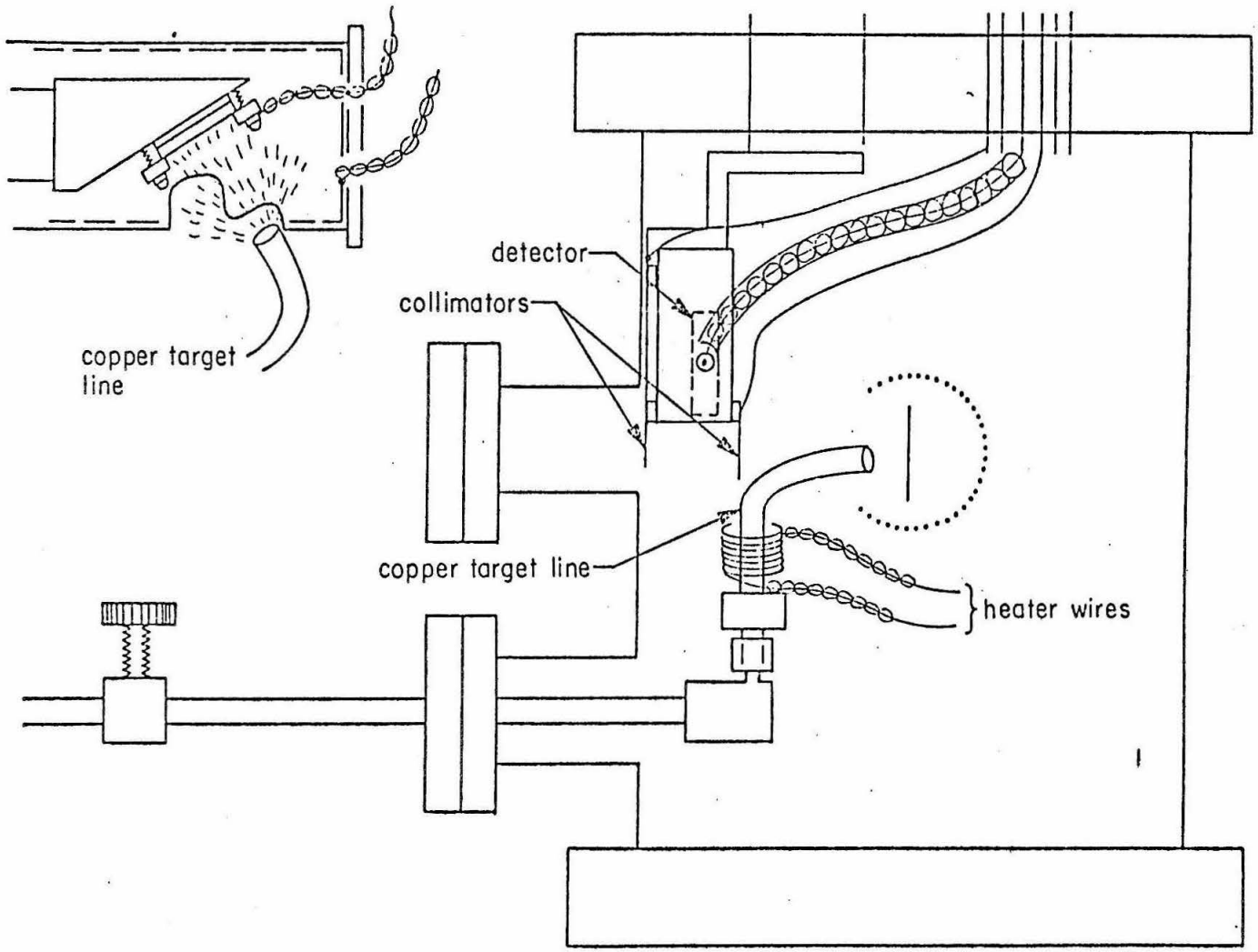

SIDE VIEW OF UHV CHAMBER

Bibliography

1. Borgesen, Peter, Studies on the Bombardment of Condensed Molecular Gases at Liquid-He Temperatures by KeV Electrons and Light Ions, 1982.

2. Carlson, R. W., "Photo-sputtering of Ice and Hydrogen Around Saturn's Rings," Nature, vol.283, 1980.

3. Cooper, Barbara H., Ph.D. Thesis, California Institute of Technology, 1981.

4. Harrison, Halstead and Schoen, R. I., "Evaporation of Ice in Space: Saturn's Rings," 1967.

5. Roberts, Richard W. and Vanderslice, Thomas A., Ultrahigh Vacuum and its Applications (Englewood Cliffs, N.J.: Prentice-Hall, Inc., 1963).

6. Roth, A., Vacuum Technology (Amsterdam: North-Holland Publishing Company, 1976).

7. Sigmund, P., "Sputtering by Particle Bombardment: Theoretical Concepts."

PERIODIC SOLUTIONS TO THE TRUNCATED NAVIER-STOKES EQUATIONS

Edward W. Felten
SURF Project Report
September 3, 1982
Advisor: Dr. Mark McGuinness

ABSTRACT

The results of a numerical study of five coupled nonlinear differential equations are presented. The system is shown to exhibit very complex behavior, including an ordered sequence of periodic solutions. The relevance of such systems of equations to physical problems is discussed.

INTRODUCTION

Most physical systems obey simple mathematical laws; it would seem, therefore, that the behavior of these systems should be simple and predictable. Experience shows that this is not the case. Examples of chaotic or `turbulent' behavior abound. These phenomena have traditionally been studied from a statistical point of view, even though they are governed by strictly deterministic equations.

Recent mathematical advances, however, suggest that certain universal features may govern the route to chaos in physical systems. Results originally derived for simple nonlinear recursion formulas may be extended under some conditions to single- and multi-dimensional differential equations, which are common models for physical phenomena.[1,2] Some of these features have been observed in the transition to turbulence in experimental systems such as nonlinear electrical oscillators,[3,4] convective fluid systems,[5,6] and optically bistable cavities.[7]

The purpose of my work this summer was to conduct a numerical study of a set of differential equations presented by Boldrighini and Franceschini[8] as a loose approximation to the equations of fluid flow. The equations are derived by expanding the Navier-Stokes equation of fluid flow in Fourier series and then solving for the derivatives of the Fourier coefficients. We choose a set of five Fourier coefficients and make the dubious approximation of ignoring the coupling between this set and all of the other modes. We are left with a set of five coupled nonlinear equations which cannot be solved analytically but are not too difficult to study numerically. The equations are:

$$\dot{X}_1 = -2X_1 + 4X_2X_3 + 4X_4X_5$$
$$\dot{X}_2 = -9X_2 + 3X_1X_3$$
$$\dot{X}_3 = -5X_3 - 7X_1X_2 + R$$
$$\dot{X}_4 = -5X_4 - X_1X_5$$
$$\dot{X}_5 = -X_5 - 3X_1X_4$$

where R is the Reynolds number, an adjustable parameter that tells how hard we are driving the system. We study how the behavior of the solutions varies with R.

Franceschini, working with Boldrighini[8] and Tebaldi,[9] conducted two studies of this system, getting an intriguing but incomplete picture of its behavior. The complexity of the situation suggested that more studies needed to be done. Franceschini and his co-workers studied a perturbed version of these equations,[10] a seven-mode truncation (of which this truncation is a subset)[11], and a continuous transition from the five-mode to the seven-mode truncation.[12] They found that the seven-mode truncation exhibited qualitatively different behavior from this system, but were unable to explain exactly why.

RESULTS

My first priority was to confirm the results of Franceschini and coworkers for the original set of equations. I found the phenomenology to be as they had reported it. A summary of the behavior of this model can be found in Figure 1.

I next decided to investigate a perturbed version of the equations. By adding a small constant to the right-hand side of the first and last equations, one may break the symmetry inherent in the original model. Baive and Franceschini investigated this perturbed system with $\epsilon = 1$ and reported behavior rather similar to that of the unperturbed system. As I varied in the range $-1 < \epsilon < 2$, I found that the system usually behaved like the unperturbed one for $R < 35$.

For larger R, the story is different. The unperturbed system contains a stable orbit (`orbit' refers to a periodic motion in phase space) which loops alternately around two unstable fixed points for all $R > 32$. The perturbed system is more complicated. I chose to study the $\epsilon = 1.5$ case in detail.

The evolution of the system for increasing R is in this case rather unusual. As in the other case, the motion consists of loops around two unstable fixed points. However, the pattern of looping varies with R. For $R = 38.0$ there is a stable orbit, looping three times around one fixed point and then twice around the other. As R is increased, this orbit becomes unstable and is replaced by new behavior (either an orbit with a long period or a chaotic `strange attractor'). Soon, a new simple orbit becomes stable. In the same way, a sequence of orbits become stable and then unstable as R is increased. It may be that there is always a stable orbit in existence; to check this conjecture would be a very time-consuming computational task. There does not seem to be any R value in this range for which more than one stable periodic orbit exists.

Recalling that the orbits loop around two fixed points, it seems useful to investigate the duration of the `visit' to each fixed point. Defining the `mean residence time' (MRT) to be the average number of loops (after the first) around a fixed point, we find that the MRT decreases monotonically as we move along the sequence of orbits. In fact, the MRT seems to decay exponentially with increasing R.

Somewhere between R=60 and R=65 this relation breaks down as the MRT becomes zero, signifying that the one-and-one looping orbit (as seen in the unperturbed model) is now stable and globally attracting. As far as I can determine, this situation continues to hold as R becomes arbitrarily large.

In the future I intend to investigate the $40 < R < 60$ regime in greater detail; in particular I would like to determine whether or not a stable periodic orbit is present for all R in this range.

CONCLUSIONS

Sets of coupled nonlinear differential equations exhibit interesting but extremely complicated solutions. Past studies have by no means exhausted the wealth of new information that these models possess. The most fruitful method of investigation continues to be `brute force' numerics rather than theory. I do not believe that this model has direct physical significance in terms of fluid flow, but these systems are an important step on the road to understanding the behavior of real fluid systems. Studies such as this are also intrinsically interesting to mathematicians because of the insight they offer into the dynamics of the transition to chaos.

The behavior of the perturbed system discussed above is intriguing. Previous investigators reported only a few orbits, and were unable to find a pattern in the sequence of orbits. The ordering of orbits observed in this study is apparently a new phenomenon. Further investigations are needed to shed more light on this behavior.

REFERENCES

1. M. Feigenbaum, J. Stat. Phys. 19:1 (1978).
2. M. Feigenbaum, Los Alamos Science, (Summer 1980).
3. P. Linsay, Phys. Rev. Lett. 47:19 (1981).
4. J. Testa, J. Perez, and C. Jeffries, Evidence for Universal Chaotic Behavior of a Driven Nonlinear Oscillator, preprint (1982).
5. A. Libchaber and J. Maurer, J. Phys. Lett. 41:21 (1980).
6. M. Giglio, S. Musazzi, and U. Perini, Phys. Rev. Lett. 47:4 (1981).
7. H. M. Gibbs, F. A. Hopf, D. L. Kaplan, and R. L. Shoemaker, Observation of Chaos in Optical Bistability, preprint (1982).
8. C. Boldrighini and V. Franceschini, Comm. Math. Phys. 64:159 (1979).
9. V. Franceschini and C. Tebaldi, J. Stat. Phys. 21:6 (1979).
10. D. Baive and V. Franceschini, J. Stat. Phys. 26:3 (1981).
11. V. Franceschini and C. Tebaldi, J. Stat. Phys. 25:3 (1981).
12. L. Tedeschini-Lalli, J. Stat. Phys. 27:2 (1982).

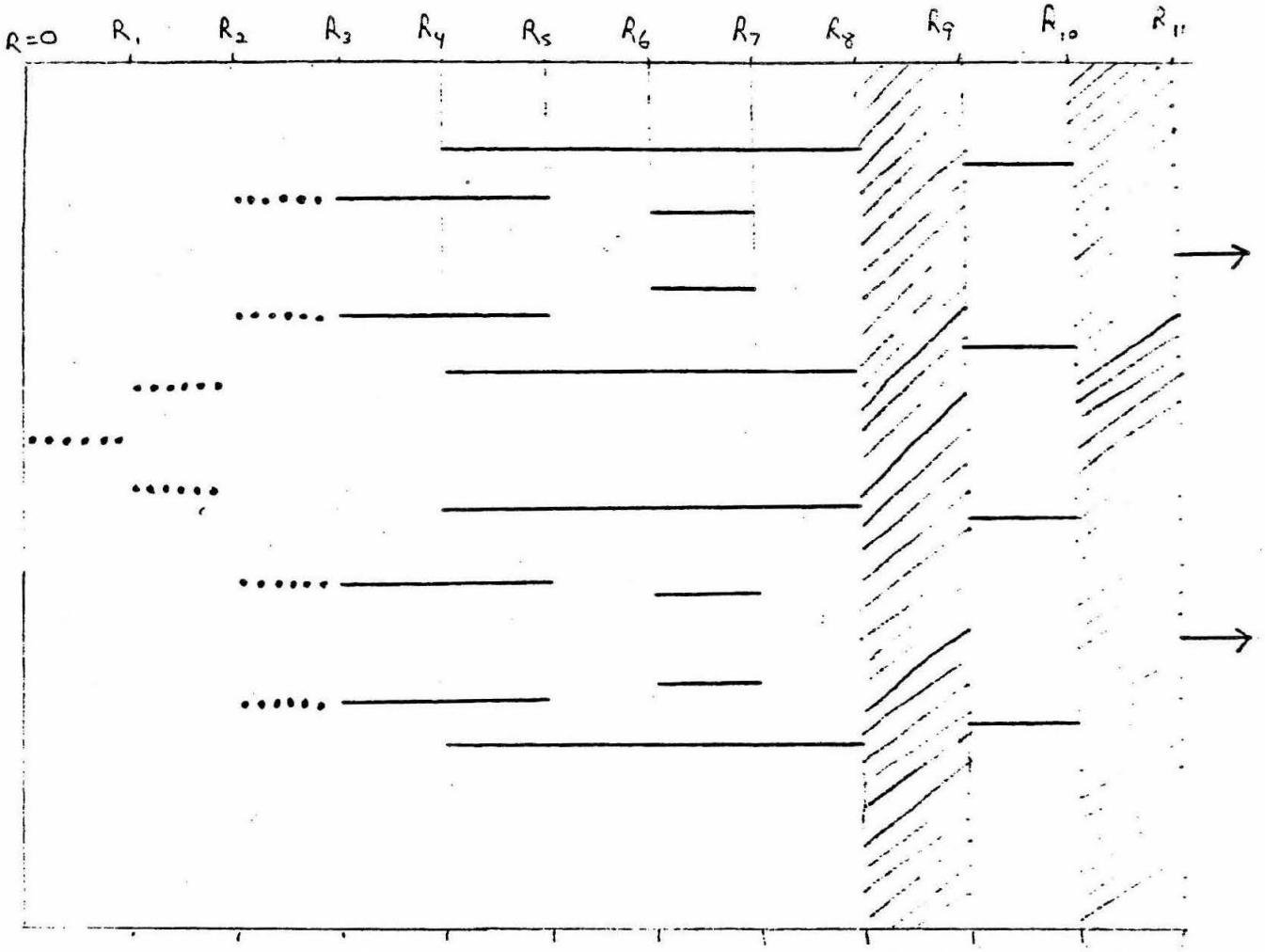

FIGURE 1: Graphical Summary of Behavior of Unperturbed Model. A sequence of spots represents a stable fixed point, a continuous line is used for a stable periodic orbit, and a turbulent regime is indicated by shading.

$R_1 = 5\sqrt{\frac{5}{2}}$, $R_2 = \frac{80}{9}\sqrt{\frac{5}{2}}$, $R_3 \doteq 22.854$, $R_4 \doteq 28.663$,

$R_5 \doteq 28.669$, $R_6 \doteq 28.7033$, $R_7 \doteq 28.7068$, $R_8 \doteq 28.720$,

$R_9 \doteq 30.189$, $R_{10} \doteq 30.543$, $R_{11} \doteq 33.439$.

[copied from reference 10]

SURF REPORT III

SOMATIC HYPERMUTATION

Lisa Flitz

Abstract: It has been found that a somatic mutational mechanism exists for generating variability in rearranged heavy-chain variable (V_H) genes coding for immunoglobulins binding phosphorylcholine in myelomas from BALB/C mice. To determine whether this mechanism has acted during rearrangement, unrearranged V_H genes from these myelomas were to be studied using DNA sequence analysis.

Introduction: The somatic variation of antibody genes is an important element of vertebrates' immune response. A number of mechanisms exist to generate this variability. One of the most recently discovered of these mechanisms is somatic hypermutation. Nucleotide sequence analyses of rearranged V_H genes from myelomas M167 and M603 from BALB/C mice showed extensive localized variation from the germline V_H sequence. The variation rates for these two genes are 3.8% and 1.4%, respectively. This somatic mutation diminishes quickly as one moves away from the gene and is strongly correlated with the class switch. (1) It has been suggested that this somatic mutational mechanism will have only acted on rearranged V_H genes. To substantiate this, it is necessary to sequence unrearranged V_H genes from these same myelomas.

Results and Discussion: In order to isolate the genes we wished to study, a genomic phage library from each of these myelomas was needed. In the case of M603 this library was already in existence, having been constructed by previous workers. The construction of the M167 library has not yet been successful. This is due to difficulties encountered in two areas. First, the preparation of vector Charon 4A DNA has not been productive. Secondly, the efficiency of the packaging extracts used to procuce infective phage has been very low.

The M603 library was screened for unrearranged V_H genes using an E. coli strain containing the plasmid BP21. This plasmid contains the V_3 gene and a supF gene. When the M603 library is allowed to infect this strain, some of the phage containing M603 DNA of sufficient homology to the V_3 gene should undergo recombination with the plasmid. Thus, some of the progeny phage that are closely related to V_3 will contain the plasmid BP21, and be infectious in strains that do not contain the supF gene, while phage that have not undergone recombination will not form plaques. This is the method used to isolate putative V_3 genes. At this time, two distinct clones have been isolated by this method. They are presently being characterized to determine the presence of a V_3-related gene. Nucleotide sequence analysis will then be used to search for evidence of somatic hypermutation. If the proposed mutational mechanism is correct,

the DNA sequence will be nearly identical to the germline sequence - hypermutation will not have occurred.

Conclusions: The sequence data are not yet available from which to draw conclusions. Work in progress includes continuing attempts to construct an M167 library. Clones from the M603 library are being characterized and prepared for sequencing.

Bibliography: Kim,S. et al, Cell, Vol. 27, 573-581, December 1981

Lisa Flitz
Sept. 3, 1982

Structure of Sea Urchin Maternal RNA

by Tracy Furutani

Abstract.

Sea urchin maternal RNA includes transcripts quite different from conventional mRNAs by virtue of their length and their repeat sequence organization. We have investigated the maternal transcripts derived from one particular transcription unit (denoted pP154) of the sea urchin genome, by a combination of blot-hybridizations and nucleotide sequencing. The largest of these transcripts (7.5 kb) is spliced near its 3' end, but still contains a long intervening sequence which is absent from the major short transcripts (1.6 and 1.4 kb). This sequence is blocked in all three translational reading frames, and appears to include a transcribed repeat. We hypothesize that the long transcript is a partially processed mRNA precursor.

Introduction

"Maternal RNA" is the term describing all the RNA present in the sea urchin egg. A large proportion of this RNA has properties which distinguish it from messenger RNA (mRNA). For instance, it is far longer (typically 5 to 10 kilobases) than conventional mRNAs (1,2) and the same piece of single- copy genomic DNA gives rise to several different maternal transcripts(3). Furthermore, this maternal RNA also includes many interspersed genomic repeat sequences (sequences of nucleotides which occur many times in the genome) covalently linked to regions of single-copy sequence (1,2). The transcribed repeats are found in embryonic nuclear RNAs but not in embryonic polysomal mRNAs(4). These "interspersed" transcripts contain almost all the different types of single-copy sequence represented in maternal RNA. We want to know the relationship of this class of maternal RNAs to the genes from which they are transcribed, and to the corresponding functional mRNAs from which cellular proteins are translated. At least some of this maternal RNA cannot be trans- by polysomes as a message for proteins: translational stop signals have been found in all frames in repeat and single-copy portions of maternal trans- cripts(2). In such molecules, the actual message may be interspersed with nonsensical sequences, so to form coding messages from them, some process(such as splicing parts of the RNA structure together, or trimming off sequences at the 5' end) must occur during development to make the message translatable. By studying the structure of maternal RNA, we can see how nonsense sequences and potentially functional sequences are arranged on it.

There are several hypotheses to account for these observations, but the most plausible is that the maternal RNA includes unspliced precursors to mRNA which, like their counterparts in nuclear RNA, contain repeat sequence elements. If these maternal RNAs are spliced during development, the RNA sequence may be expected to contain "splice" signals which direct the removal of intervening sequences, generating the intact message. The disappearence of repeat sequence transcripts from cytoplasmic RNA during development may be synonymous with such functionally significant RNA splicing. Results

SpP154 is a gene of the purple sea urchin (S. Purpuratus). This gene gives rise to multiple transcripts in maternal RNA even though it is represented only once in the sea urchin genome. We know that this gene gives rise to three major maternal transcripts of 7500, 1600 and 1400 nucleotides length. Thus, SpP154 is a good model to study developmental mechanisms in sea urchin maternal RNA.

The gene SpP154 had been derived from a complementary DNA clone (cDNA) found in a pluteus stage embryo cDNA library. λ154A and λ154B are cloned segments of sea urchin genomic DNA which contain the 3' end of the gene; these segments had been isolated by "screening" a genomic lambda phage "library" (explained below) using SpP154 as a probe. The map in Fig 1 shows the important fragments of λ154B and their lengths.

The 5' end of the gene is beyond the end of λ154B. In order to isolate the 5' end, we carried out further screenings of other phage and cosmid libraries which revealed only tentative positive clones. A genomic library is a set of clones constructed by ligating digested or partially digested genomic into a phage or cosmid vector. A sufficient number of recombinants were screened such that there would be a high probability of finding any given single copy fragment. The failure to find a clone containing the 5' end of the SpP154 gene may be due to the fact that for various reasons some DNA sequences are cloned less

efficiently than others.

We have successfully subcloned fragments λ154RH1, λ154RH2 and λ154RH4 into the plasmid cloning vector, pUC8, by sticky-end ligation (confirmed by the Xgal test and mini preps). Thorough restriction mapping was done of each of these fragments. We have located repeat sequence elements in λ154RH1, λ154RH2 and λ154RH4 by genome blots(5), using specific fragment probes labelled by 3' terminal repair synthesis and by "reverse" genome blots ;that is, clone blots reacted with total nick-translated genomic DNA (see Fig 1).

We have also successfully subcloned the Alu I-Bam HI and Bam HI-HindIII fragments of the cDNA into the filamentous, single-stranded DNA phage sequencing vector, M13mp9, and we have sequenced approximately 200 nucleotides on either side of the Bam HI site, using the primer extension method(6,7).

The transcripts derived from various regions of the cDNA and the gene were investigated by RNA blot hybridization, using specific end-labelled fragment probes. In the cDNA clone of SpP154, one region, the BamHI-Hind III fragment, which corresponds to fragment λ154RH3 from the gene, reacted only with the 7.5 kilobase maternal transcript, while another region, between Alu I and the end of the clone, reacted with all three major maternal transcripts (as well as some minor transcripts). We would expect the single copy portion of pλ154RH2 to react with all of the transcripts in an RNA blot-hybridization if all of the transcripts share a common 3' end AND are colinear with the gene but, in fact, we found that only the large transcript is detected. The actual 3' end appears to be located at least 6 kb downstream since it does not lie within λ154A or λ154B. It appears thus that all of the transcripts are spliced near their 3' ends, and that the region represented in the small transcripts is located 3' wards of this splice site. Single-copy fragments from pλ154RH1 reacted in RNA blot-hybridizations with the large (7.5 kb) transcript and with some rarer species (perhaps processing intermediates). From this data, it appears that the SpP154 cDNA is derived from the long transcript, but that it is not colinear with the gene as previously believed. Furthermore, the small transcripts appear to derive from additional splicing, which removes an intervening sequence still contained within the large transcript. The repeat element in λ154RH1 appears, on the basis of RNA blot-hybridizations, to be represented in the 7.5 kb transcript; so this may be an example of a transcribed repeat which is spliced out during processing.

From the sequencing, we were able to detect "stop" signals in every reading frame in the Alu I-Bam HI fragment; thus, the conclusion is that this region is untranslatable. This sequence will not produce a viable message because the "stop" signals will terminate any polypeptide synthesis. Conclusion

In summary, some of the maternal RNA transcripts (in our case, the 7.5 kb SpP154 transcript) appear to be unprocessed or partially processed forms of mRNA and the blot-hybridization data are consistent with the theory that some maternal mRNAs are processed during the development of the embryo. The 1.6 and 1.4 kb transcripts look like further processed versions of the 7.5 kb transcript. These findings are interesting because they raise the possibility that during early development, the levels of abundant mRNAs may be dependent on the presence of these partially processed repeat-containing precursors in the cytoplasm (see ref. 8).

To test these claims, the 3' and 5' ends of the gene must be precisely localized. We know approximately where the 3' end is; further screening of other libraries should show the 5' end.

We need to sequence appropriate fragments of the cDNA and genomic clones to locate splice junctions. The predicted splicing pattern can then be confirmed by S1 mapping. In this way, we can verify our notions that the 7.5 kb fragment is spliced at the 3' end, that the 1.6 and 1.4 kb fragments are spliced versions of the longer transcript, and that all the transcripts share a common 3' end. Subsequently, the questions of "What protein does this gene code for?" and "Is the splicing necessary for the message to be translated into the pro- tein?" will be answered., by the generation of the ccomplete nucleotide sequence.

References

1. Costantini, F.D., Britten,,R.J. and Davidson, E.H. (1980). Nature (London), **287**, 111.

2. Posakony, J.W., Britten, R.J. and Davidson, E.H. (1982). J. Mol. Biol., submitted for publication.

3. Thomas, T.L., Britten, R.J. and Davidson, E.H. (1982). Develop. Biol., in the press.

4. Scheller, R.H., Costantini, F.D., Britten, R.. and Davidson, E.H. (1978). Cell, **15**, 1899.

5. Southern, E.M. (1975). J. Mol. Biol., **98**, 503.

6. Messing, J., Crea, R. and Seeburg, P.H. (1981). Nucl. Acids Res., **9**, 309.

7. Sanger, F., Nickler, S. and Coulsen, A. (1977). Proc. Nat. Acad. Sci. USA, **76**, 5463.

8. Davidson, E.H. and Britten, R.J. (1979). Science, **204**, 1052.

Fig 1 STRUCTURE OF λ154B AND FRAGMENTS THEREIN

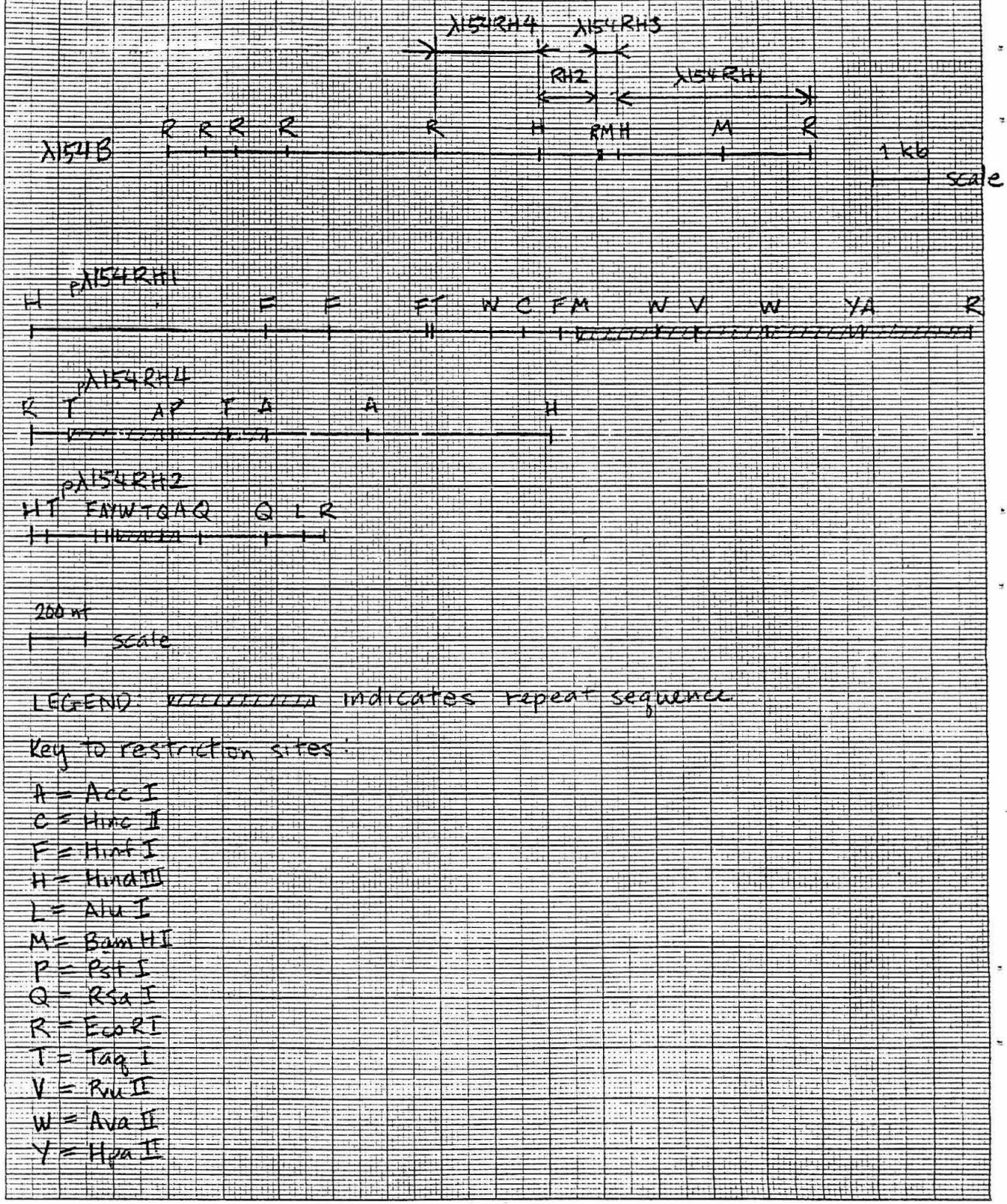

Fig 2 RELATIONSHIP OF Sp?154 WITH THE λ CLONE AND MATERNAL TRANSCRIPTS

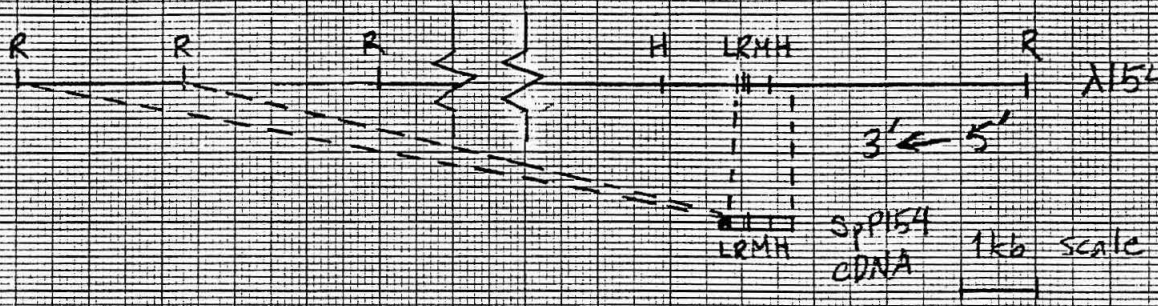

Localization of Sp?154 reaction with genomic DNA. Shaded region does not hybridize with λ154B, but does react with a 2.35 kb EcoRI fragment in a genome blot.

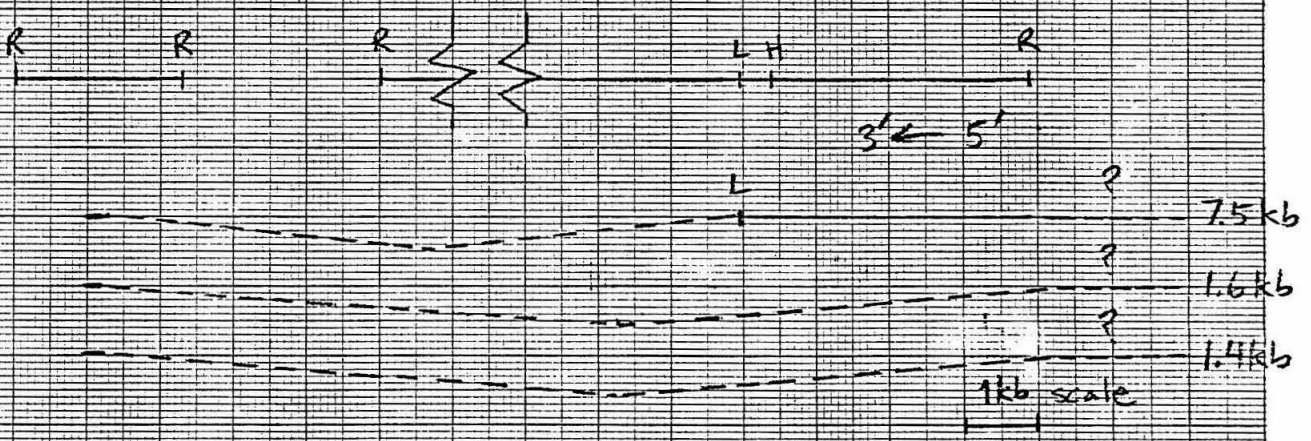

Hypothesized structure of Sp?154 transcripts
diagonal dashes represent hypothesized splices

ELECTRODYNAMIC SUSPENSION OF MICROPARTICLES FOR MASS DETERMINATION

Anirvan Ghosh

Abstract

Modifications are made to the Millikan chamber that make it suitable for microparticle mass measurements and studying catalyst driven reactions in controlled atmospheres. Mass measurements are made on aluminum oxide particles, typically 10 to 100 microns in size. The lowest mass recorded is 1.63×10^{-14} grams.

Introduction

In 1910 Millikan[1] published a paper discussing the experiment to determine the fundamental charge. The apparatus consisted of a pair of capacitor plates giving rise to a uniform electric field in which a charged oil droplet was suspended against gravity. In 1916 Kelly[2] first used the Millikan apparatus to determine the photoemission threshold of negatively charged particles. In 1962 Pope[3] developed a different approach which led to the discovery of a double quantum external photoelectric effect (DQEPE). A modification was made on the Millikan capacitors in 1958 when Wuerker et al.[4] introduced an additional ring electrode carrying an alternating potential to the original apparatus which contained charged particles in a confined region in the chamber. A slight modification of this apparatus was used by Davis and Ray[5] (1980) for mass measurement of aerosol particles. In 1978, Arnold[6,7] followed an alternate approach independent of ring electrodes and used an optical servomechanism to measure masses in the picogram range.

In the present project, a modified Millikan chamber with a stabilizing ring electrode is used to suspend catalyst particles (10-100μ in size) in high vacuum.

Theory

The method used is based on containment of a charged particle at the geometric center of an electrodynamic balance. The focusing of the particle to the center is achieved by balancing the particle against gravity using a vertical electric field and applying an ac voltage to the central ring electrode which produces a time-averaged force on the particle towards the central axis of the

R1 200 K
R2 80 K
C1 0.5 MFD 400 W
C2 0.006 MFD 200 W
Rh 0-0.5 M
B 0-150 V
T 2400 V Power Transformer
Tr LM395K Power Transistor

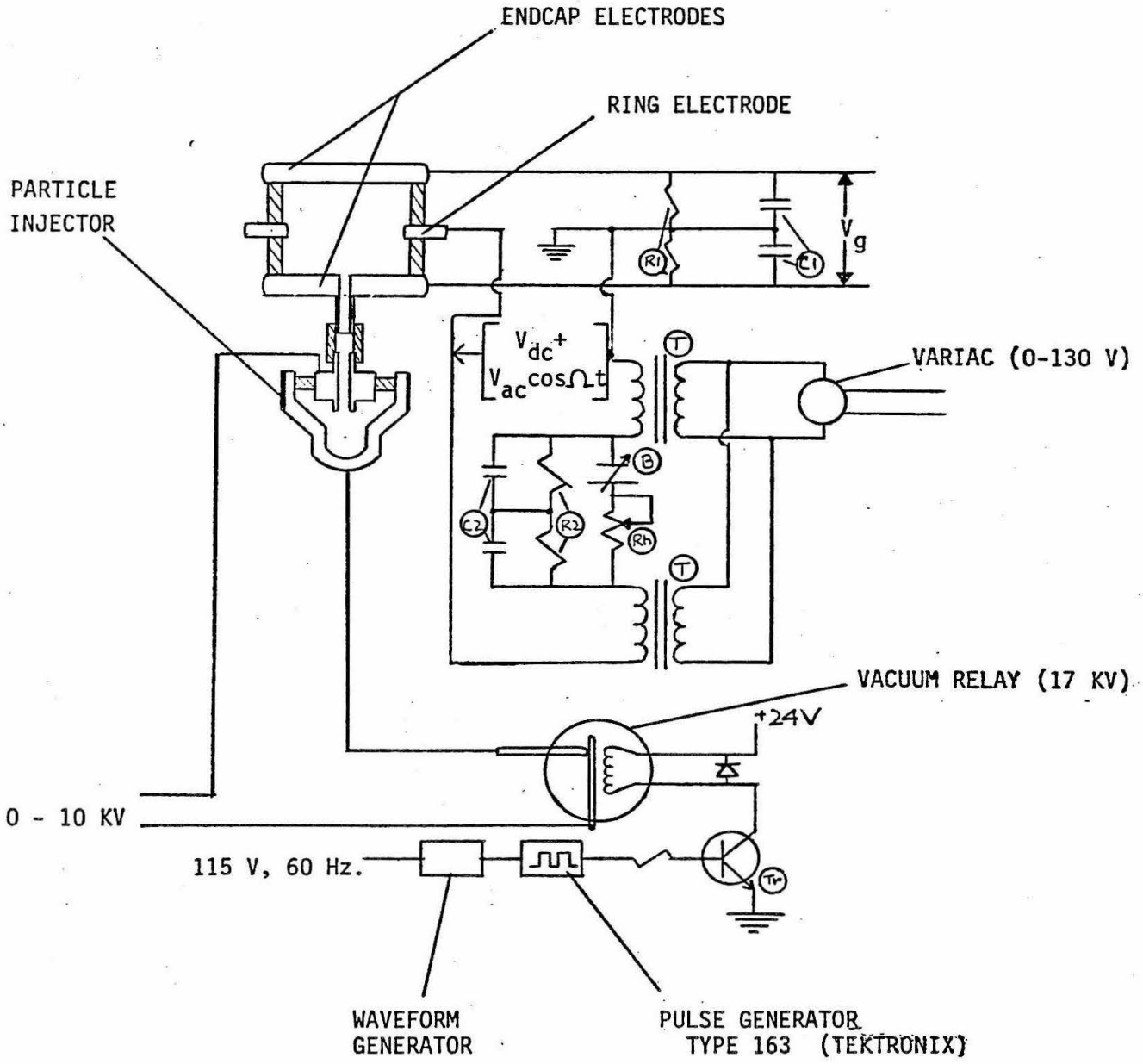

Figure 1 Schematic of the microparticle levitation balance

ring electrode. The particle is held in the plane of the ring by applying an appropriate DC bias to the AC voltage on the ring electrode. The ring electrode produces no net electric field at the center of the chamber. A schematic of the apparatus is shown in Fig. 1.

A necessary condition for this focusing system to work is to find a ring electrode potential configuration which produces a restoring force on the particle proportional to its displacement. A potential of the form

$$V = \left[\frac{V_{dc} - V_{ac} \cos \Omega t}{Z_o^2}\right] [\alpha z^2 - \beta r^2] \qquad (\alpha \text{ and } \beta \text{ are arbitrary constants.})$$

satisfies the condition, where V_{ac} is the peak value of the alternating voltage of frequency Ω with a dc bias V_{dc} . $2Z_o$ is separation of the endcap electrodes. Taking $\alpha = 1$ and $\beta = \frac{1}{2}$ simplifies the particle dynamics. The electric field this ring potential produces has the components

$$E_r = - \frac{dV}{dr} = - (-V_{dc} + V_{ac} \cos \Omega t) \frac{r}{Z_o^2}$$

$$E_z = - \frac{dV}{dz} = 2 (-V_{dc} + V_{ac} \cos \Omega t) \frac{Z}{Z_o^2}$$

Since the electrostatic force acting on a charged particle is qE, in the radial direction V_{ac} has a restoring effect while V_{dc} acts against it. And in the z-direction, V_{dc} has a restoring force and V_{ac} has a destabilizing effect. Also to be noted is that the radial and vertical forces are proportional to the radial and vertical displacements, respectively.

The motion of the particle under these forces can be described by the Mathieu equation:

$$\frac{d^2u}{dx^2} + (a_u - 2q_u \cos 2x)\, u = 0$$

where u can be either r or z to describe radial or vertical motion. The other variables in the equation correspond to

$$x = \Omega t/2$$

$$a_z = -2a_r = 8\left(\frac{q}{m}\right)\left(\frac{V_{dc}}{Z_o^2}\right)\frac{1}{\Omega^2}$$

$$q_z = -2q_r = 4\left(\frac{q}{m}\right)\left(\frac{V_{ac}}{Z_o^2}\right)\frac{1}{\Omega^2}$$

The above equations have been studied elsewhere[4,5] and suggest the following conclusions:

(i) A charged paticle will be bound in a region of stability provided

$$0 < \frac{4}{\Omega^2}\left(\frac{V_{ac}}{Z_o^2}\right)\left(\frac{q}{m}\right) \leq 0.908$$

and $$Z_o > \frac{8(1 + b^2)}{\Omega^2 q_z^2}\left[g - \left(\frac{V_{dc}}{Z_o}\right)\left(\frac{q}{m}\right)\right]$$

where b is the drag parameter:

$$b = \frac{q\mu}{2\rho a^2 \Omega} \quad ;$$

μ = viscosity of gas in chamber

a = effective radius; ρ = particle density

(ii) A charged particle will be stably suspended against gravity in perfect vacuum when

$$qE_z = q\frac{V_g}{2Z_o} = mg$$

V_g is the voltage across the endcap electrodes.

The Apparatus and Its Operation

The endcap electrodes with a diameter of 3.5" have a separation of 0.75". The ring electrode has an inner diameter of 2.5" and an outer diameter of 3.25". The electrostatic particle injector is attached to the bottom plate. The injector consists of a cup and an upper ring which act as two electrodes. These components are supported in a steel base and enclosed within an aluminum vacuum chamber. The chamber has three viewports which are used for the viewing telescope (30-120 X), a xenon UV source for ionizing particles, and a He-Ne laser to illuminate the particle. In addition, there is a gas inlet valve to control the pressure while injecting particles and to act as a monitoring device for future experiments.

The apparatus is operated as follows. First, the chamber is evacuated to a pressure of 10^{-6} torr. Both electrodes of the particle injector are raised to a potential of 10 kV. A pulse is then applied to the cup electrode which instantaneously grounds it for a few microseconds. This is done using a Tektronix 163 pulse generator and a 17 kV vacuum relay. The powder particles shoot up into the chamber where they intercept the UV radiation and get charged to various degrees. Once the particle is charged, the alternating ring potential and the endcap voltages help trap the particle in a confined region. Under the influence of the alternating field, the particle undergoes oscillations about the geometric center. Decreasing V_{ac} causes a rise in amplitude which can be decreased by appropriately monitoring the endcap electrode potential. When the particle reaches electrostatic equilbirum, it does not oscillate and stays at the geometric center even in the absence of an alternating potential. In this equilibrium position,

$$mg - V\rho_m g = qE$$

or $V\rho_p g - V\rho_m g = V(\rho_p - \rho_m)g = qE$

where V is the volume of the particle
ρ_m is density of chamber atmosphere
ρ_p is particle density

$$\frac{m}{\rho_p}(\rho_p - \rho_m)\, g = qE$$

The mass of the particle is then given by

$$m = q\left(\frac{V_g}{2Z_o}\right)\left(\frac{\rho_p}{\rho_p - \rho_m}\right)$$

Knowing the volume of the chamber and the interior pressure, ρ_m can be calculated.

Results

Aluminum oxide particles used as reaction catalysts and having sizes from 10 to 100 microns were suspended in the chamber. The endcap potentials varied from 0.75 kV to 2.0 kV with V_{ac} being 2000 V. The lowest mass measured was $1.63\ \ 10^{-14}$ grams.

In the experiment from which the above data is reported, a mechanical standby particle injector was used due to malfunctioning of the electrostatic injector.

In the mass determining equation, $\left[\frac{\rho_p}{\rho_p - \rho_m}\right] \cong 1$ in vacuum.

Proposed Applications

The present design of the chamber makes it suitable for several studies in physical chemistry. Some possibilities are mentioned below.

In the near future we plan to study the reaction mechanisms at the catalyst surfaces of the Fischer-Tropsch reaction. The suspended particle would be a catalyst, and CO and H_2 would be introduced through the gas monitoring system. A CO_2 laser would activate the catalyst, and accurate mass measurements would enable absorption studies. Additional studies will involve sampling of surface species by thermal desorption.

A suspended particle undergoes a significant increase in temperature due to the laser and may undergo thermionic emission. This would change the balancing potential and provide the rate of electron emission. That in turn would give an accurate measure of the surface area of the particle. There is no other direct method to determine accurately the surface areas of irregular micron size particles.

Acknowledgements

I would like to acknowledge valuable discussions with my supervisor Professor J. L. Beauchamp, and other members of the group and thank the staff of the electronics and machine shops for their cooperation.

This work was supported by the Caltech SURF program.

References

(1) R. A. Millikan, Phil. Mag. S 19(110),209(1910).

(2) M. J. Kelly, Phys. Rev. 16,260(1920).

(3) M. Pope, J. Chem. Phys. 37,1001(1962).

(4) R. F. Wuerker, H. Shelton, and R. V. Langmuir, J. Appl. Phys. 30(3),342(1959).

(5) E. J. Davis and A. K. Ray, J. Colloid Int. Sci. 75(2),566(1980).

(6) S. Arnold, J. Aerosol Sci. 10,49(1979).

(7) L. Altwegg, et al, Rev. Sci. Instrum. 53(3),332(1982).

STUDIES OF PROMOTION OF HUMAN MITOCHONDRIAL DNA

Submitted by
George G. Gibbs
Sponsor: Dr. Giuseppe Attardi
SURF 1982
September 3, 1982

STUDIES OF PROMOTION OF HUMAN MITOCHONDRIAL DNA

ABSTRACT

A 739 base pair human mitochondrial DNA fragment has been isolated and inserted into the plasmid pUC9. This vector was introduced into an in-vitro mitochondrial transcription system in an attempt to identify promoter regions. Preliminary results suggest the addition of ATP is required for transcriptional activity.

THEORY

RNA polymerase molecules begin and terminate transcription at defined sites on the DNA template. To initiate transcription, the polymerase must recognize the proper sequences in the promoter region and catalyze the elongation of the nascent RNA chain. (1)

Dr. Giuseppe Attardi and his colleagues have done extensive research on the organization of the human mitochondrial genome (Figure 1) and mechanisms of its expression. (2) Mapping experiments utilizing "capped" mtRNA molecules and nascent RNA chains have provided evidence that supports Dr. Attardi's hypothesis that the region encompassing the origin of replication contains initiation sites for light (L) and heavy (H) strand transcription. (3-4) I have chosen this region to determine which mtDNA sequences are necessary for the initiation of light and heavy transcription.

Specifically, I have isolated a fragment of mtDNA containing the putative sequence of promotion. Further, this sequence has been tested in the preliminary in-vitro system for transcription activity. Results are now being analyzed and further refinements in the system are being made.

DISCUSSION

My general approach involves isolating a restriction fragment of human mtDNA containing a promoter, introducing it into an in-vitro transcription system,

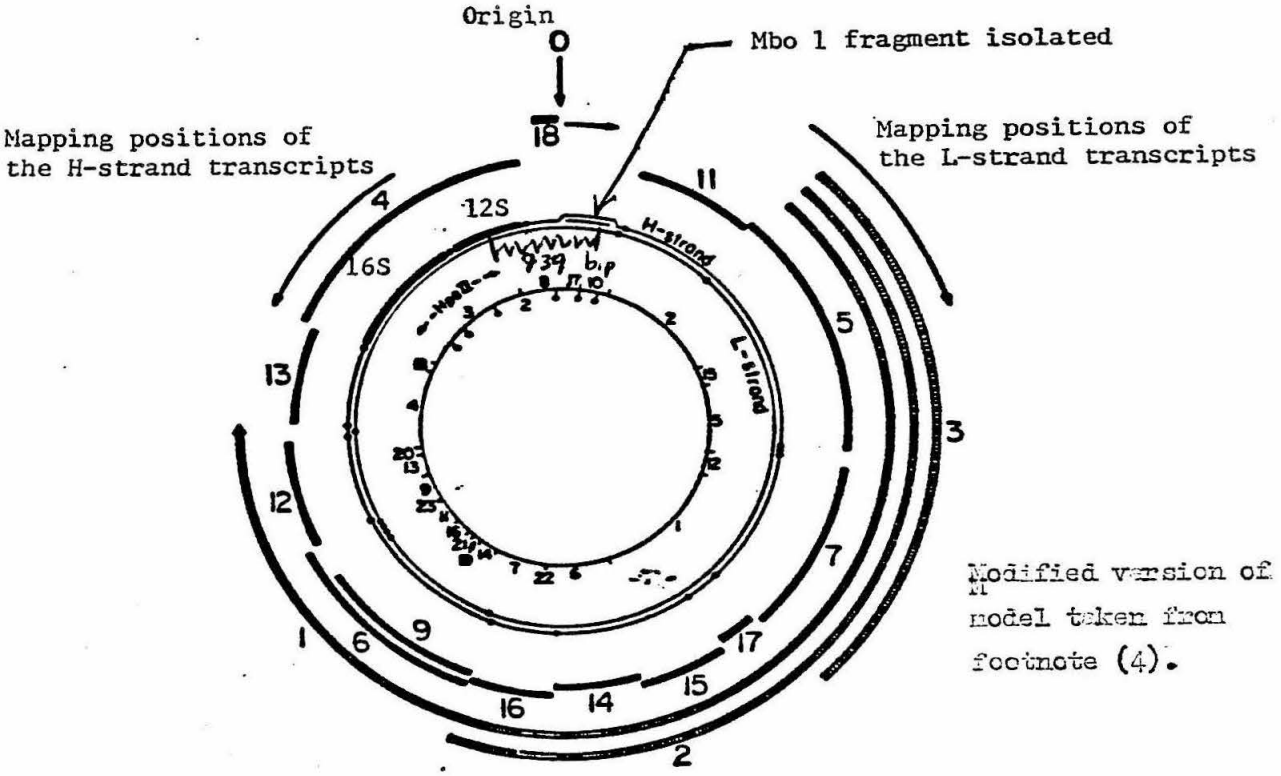

Figure 1: Genetic, transcription, and physical maps of the HeLa cell mitochondrial genome. The two outer circles show the positions of the two rRNA genes and those of the tRNA genes. Left and right arrows indicate the direction of H and L-strand transcription, respectively; the vertical arrow (marked O) indicates the location of the origin. The insert is shown.

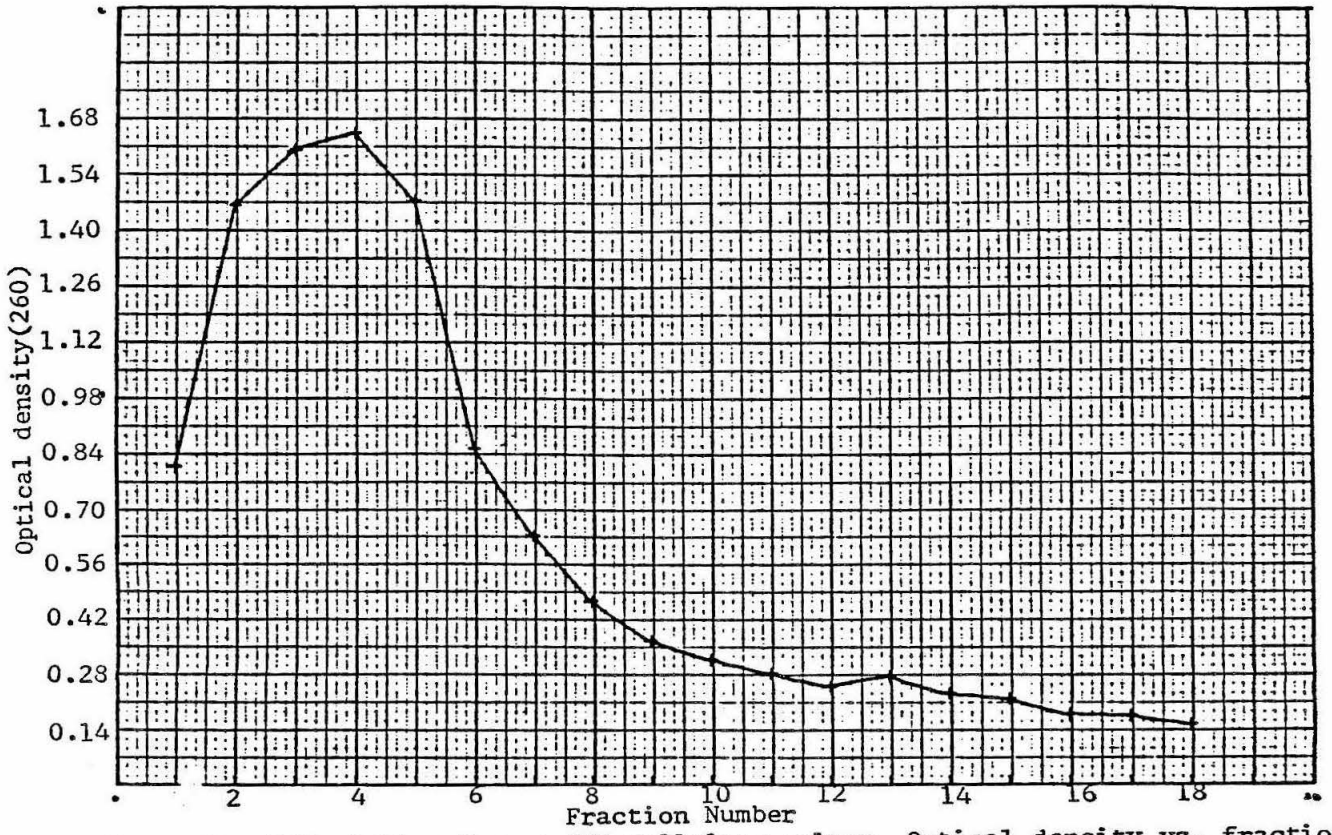

Figure 2: pUC9 elution from a BND cellulose column. Optical density vs. fraction number graphed. Plasmid comes off rather abruptly and gradually tapers off. Fraction

and investigating for any positive activity. Activity will be signified by well-defined bands of rRNA and mRNA on an autoradiograph of a CH_3HgOH 1.4% agarose gel run in borate buffer.

Initially I became directly involved with my advisor in his experiments exploring various optimizing parameters for his in-vitro transcription system. Via direct addition of ^{32}P it was determined that the capacity to synthesize mtRNA is greater in mitochondria isolated from cells currently growing in their exponential phase than from cells in stationary phase. Early experiments also included a comparison of yields of ^{32}P labeled mtRNA from preparations done at both room temperature (25°C) and the standard 0-4°C. SDS-sucrose gradient fraction analysis of transcription complexes isolated after various incubation periods consistently indicated the 0-4°C temperature was necessary to retain activity.

Further, an in-vivo mtRNA preparation with ^{3}H-uridine was compared to a ^{32}P in-vitro preparation for correlation of labeled RNA species. Correlation was found by separation of species by electrophoresis.

Human mtDNA was collected by cell lysis and differential centrifugation. (Appendix A, in office) A suitable DNA fragment encompassing the origin was selected: Mbo 1 fragment 7. (5) Mbo 1 digested mtDNA was screened for the particular fragment on a 0.9% agarose gel. This fragment was subsequently dissected and eluted from the gel and charaterized for proper molecular weight.

Plasmid pUC9 was isolated from E. coli (strain HB101) via alkaline lysis. (Appendix B (in office), Figure 2) With the help of a colleague DNA to be cloned was ligated into a vector molecule; in this case the molecule is pUC9 which carries an amp^R gene. An Mbo 1 digest of mtDNA had been chosen since Mbo 1 generates the same 5'-overhanging single-stranded ends as BamH 1 cut DNA. BamH 1 digested pUC9 was subsequently ligated in-vitro to the Mbo 1 fragment. A similar ligation to BamH 1 cut pBR322 was not successful.

This new plasmid (now termed 9-8) was introduced by transformation into

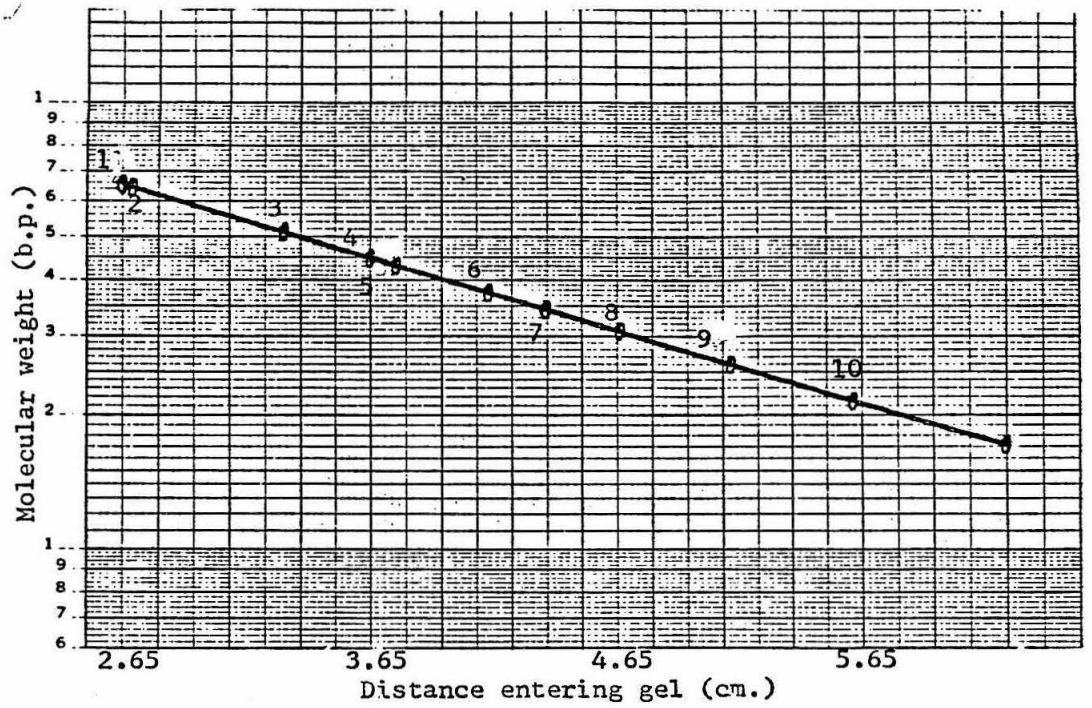

Figure 3: Characterization of 9-8. A 5% acrylamide gel was analyzed for lengths of particular sequences obtained upon numerous restriction digestions. In theory strands will move through gels in a logarithmic fashion according to molecular weight. Of importance are sites 3, 7, and 10. The fact that 3 seems to be the combined sequence 7+10 indicates the identification of an important Hae III site on the pUC9 vector. Further, the cuts all coincide with expected results. The ligation and cloning processes are verified . The orientation of the insert is shown in figure 4.

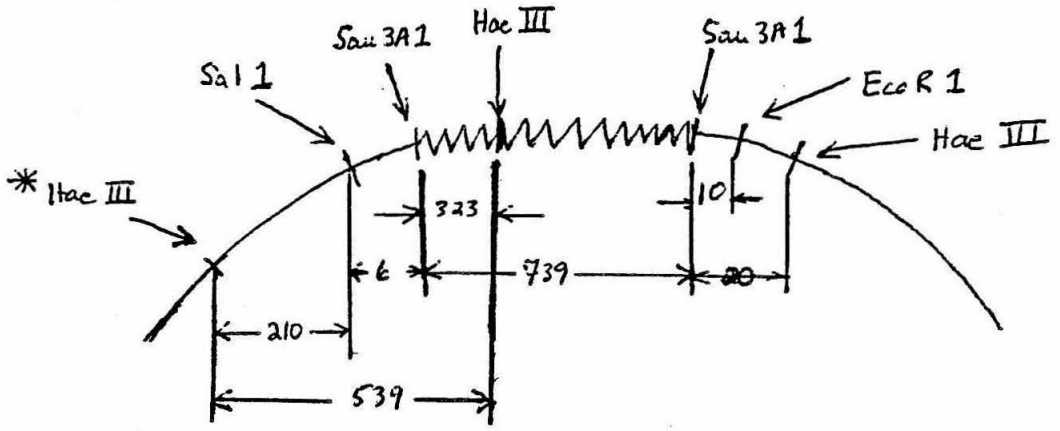

Figure 4: A restriction map of the Mbo 1 fragment ligated into pUC9. Base pair lengths indicated are exact, unlike for figure 3. Note strong correlation between figure 3, though, in lengths of sequences resulting from expected digests. The orientation is as shown because of a 520 b.p. sequence occurring in the 5% acrylamide gel. (actual length is 539 b.p.) *Note position of the Hae III site and number of base pairs from the Sal 1 site. Further, figure 3, point 10, also indicates a 210 b.p. fragment. Plasmid is characterized.

E. coli (strain JM83). Ampicillin resistant beta-galactosidase (-) clones were screened by agarose gel electrophoresis and restriction analysis. Plasmid pUC9 contains a portion of the lac operon which functions as a detection marker for insertion of target DNA when utilized with E. coli (strain JM83). Insertion of a target DNA (the insert isolated) into the cloning site of this vector prevents the synthesis of a functional beta-galactosidase fragment and therefore eliminates the blue colony color produced when cells are plated on medium containing 2% XGAL. (6-7)

Amplification of the plasmid was done in 500 ml. lactose broth; the purified plasmid was again isolated and characterized by restriction analysis. Double digestions Hae III + EcoRl and Hae III + Sal 1, plus the single digest Sau 3Al, all portrayed on a 5% acrylamide gel (Figure 3), proved an acceptable plasmid had been cloned.

Sonicated mitochondria were mixed with either 9-8, pBHK2, or left unmixed. (pBHK2 contains a KPN mtDNA insert slightly longer than the Mbo 1 insert isolated but also contains the origin). These samples were incubated in 75 mM KCl, 7.5 mM $MgCl_2$, 35 mM Tris pH=7.4, 100 mM ATP, CTP, GTP, and tested for transcription activity by measuring incorporation of ^{32}P into RNA species. Two experiments were run, one involving no ATP addition, the other involving addition of ATP pulses at 15 minute intervals for 1 hour. Electrophoretic analysis through a CH_3HgOH 1.4% agarose gel was run with these samples.

CONCLUSIONS

ATP addition seems to have some profound affect on in-vitro transcription activity. An increase of 100% in acid precitable counts occurred with the sample of pBHK2 + sonicated mitochondria compared with 9-8 and the control samples. An autoradiograph of the same pBHK2 mixture gave a faint hint of banding in the 12S rRNA region. This could indicate specific transcription had taken place. 9-8, which contains only a part of the 12S region had no stimulatory effect on in-vitro

transcription. Possible explanations for these effects might be that the 12S rRNA gene must be intact for transcription to occur.

Characterization of the 9-8 plasmid via restriction analysis led to the identification of a Hae III site approximately 210 b.p. from the Sal 1 site on the pUC9 plasmid. (Figure 4) Further, I was able to interpret the orientation of the ligated insert. This information will be vital in future experiments.

Future analysis will involve perfecting the transcription system and obtaining the appropiate sequence whwere promotion occurs.

FOOTNOTES

1) Karp, Gerald, "The Flow of Information Through the Cell, " in Cell Biology, (New York: McGraw-Hill, 1979), pp. 484-485.

2) Attardi, G. (1981), Organization and Expression of Mammalian Mitochondrial Genome: A Lesson in Economy. Trends in Biochemical Sciences, March/April 1981, 86-89, 100-103.

3) Cantatore, P. and Attardi, G., (1980) Mapping of nascent light and heavy strand transcripts in the physical map of HeLa cell mitochondrial DNA. Nucleic Acids Research, 8, 2605-2625.

4) Montoya, J., Christianson, T., Levens, D., Rabinowitz, M., Attardi, G., Identification of initiation sites for heavy strand and light strand transcription in human mitochondrial DNA. Proceedings of the National Academy of Science, submitted for publication.

5) Drouin, J., (1980) Cloning of Human Mitochondrial DNA in Escherichia coli. Journal of Molecular Biology, 140, 15-34.

6) Messing, J., Vieira, J., (1981) Manuscript in preparation.

7) Ruther, U., Koenen, M., Otto, K., Muller-Hill, B., (1981) Nucleic Acids Research, 9, 4087.

REFERENCES

Anderson, W., Diacumakos, A., "Genetic Engineering in Mammalian Cells," Scientific American, 245, 1, pp. 106-121.

Novick, Richard P., "Plasmids," Scientific American, 243, 6, pp. 102-127.

ACKNOWLEDGEMENTS

The author would like to express his heart-felt thanks for the patience and help given to him by George Gaines and Michael King, graduate students in the division of biology. A number of the experiments used their direct assistance.

APPENDIX A

PREPARATION OF MITOCHONDRIAL DNA

I. Procedure: Unless otherwise specified, the operations described below are carried out at 2-4°C.

1) Cells are collected by centrifugation and washed twice in NKM, followed by a final wash in TD.

Note: For large preparations (2 liters of media), initially transfer media to 1-liter plastic bottles. Centrifuge 1300-1400 RPM - 10 minutes. Pellet forms. Draw off most of the supernatant; resuspend pellet in 25 ml. NKM. Rinse with NKM. Transfer suspensions and rinses to 250 ml. glass bottles. Centrifuge 1300 RPM - 7 minutes.

Resuspend cells in TD (buffer) and transfer to 50 ml. conical tubes. Fill tubes to final volume of 40 ml. - TD. Centrifuge at 700 RPM - 5 minutes. Yield: 4-6 ml. packed cells per tube.

2) Homogenization and differential centrifugation.

Resuspend cells in 4-6 volumes RSB-EDTA (approx. 24ml./tube). Incubate on ice for 2 minutes; homogenize with an A.H. Thomas homogenizer until 60-70% of cells are broken (monitor cell breakage by phase contrast microscope). Transfer homogenate to 50 ml. conical tubes containing 4 ml. 2 M Sucrose TE. Suspend well. Put on ice.

Spin at 2300 RPM - 3 minutes. Draw supernatant out - transfer to Sorvall tubes. Respin supernatant at 2300 RPM - 3 minutes. Residual pellet discarded. Transfer supernatant to new tubes. Spin at 9000 RPM - 10 minutes - to pellet mitochondria. Discard supernatant. Suspend pellet in 0.25 M Sucrose TE (½ volume of homogenate). Spin at 2300 RPM - 3 minutes - draw out supernatant. Spin supernatant at 9000 RPM - 10 minutes.

3) Lysis

Resuspend well the pellets in 0.25 M sucrose TE (0.5 to 1.0 ml. per ml. of packed cells harvested. Add 5% SDS to 1.2% final concentration. Leave 10 minutes at room temperature. Add 1/6 volume 7 M CsCl and incubate in ice for 30 minutes. Centrifuge 12,000 RPM - 15 minutes. Draw out supernatant. Respin. Measure volume of supernatant. Add 0.741 g CsCl/ml. of solution. Distribute into Sorvall tubes and incubate on ice - 20 minutes. Centrifuge 17,000 RPM - 20 minutes. Remove solution with pipette, leaving behind "protein skin." Measure volume of solution. Determine refractive index. A R.I. of 1.390 is desired. Add 1/10 volume EtBr/.006 R.I. units above 1.390.

Transfer sample to cellulose nitrate or polyallomer tubes. Add CsCl - EtBr Standardized solution (R.I. = 1.390) to fill tubes, and centrifuge 40 - 48 hours at 20°C in No. 65 rotor.

4) Fractionation

Collect the closed-circular mtDNA (lower band), visualized by U.V. light by puncturing the bottom of the tube and collecting the band.

Reband a second time in CsCl-EB to remove any residual nuclear DNA. Same conditions as first run.

Remove EtBr from the pooled DNA sample by shaking with an equal volume of isoamyl alcohol. Let sit in ice to separate phases, then remove upper alcohol phase. Repeat twice.

Optical density readings will determine concentration of DNA in sample. Use the conversion: 50 micrograms/ml.=1.0 $O.D._{260}$ unit.

II. Reagents

NKM (0.13 M NaCl, 0.005 M KCl, 0.001 M $MgCl_2$)

TD (0.13 M NaCl, 0.005 M KCl, 0.7 mM Na_2HPO_4, 0.25 M Tris pH=7.4)

RSB-EDTA (0.01 M Tris pH=6.7, 0.01 M KCl, 10^{-4} M EDTA)

2 M Sucrose in TE (0.01 M Tris pH=6.7, 10^{-4} M EDTA)

0.25 M Sucrose in TE (0.01 M Tris pH= 7.4, 0.01 M EDTA)

Lysing buffer (0.01 M Tris pH=7.4, 0.01 M EDTA, 2.4% SDS)

Stock buffer for adjusting density (0.01 M Tris pH=7.4, 0.01 M EDTA)

CsCl-EB Buffer (0.01 M Tris pH=7.4. 0.01 M EDTA, CsCL to density of 1.6, 200 micrograms/ml. EB)

EB (10 milligrams EB/ml. 0.01 M Tris pH=7.4, 0.01 M EDTA)

7 M CsCl

Solid CsCl

III. References

1) Hirt, B. (1967) J. Mol. Biol. 26, 365.
2) Hudson, B. and Vinograd, J. (1967) Nature 216, 647.
3) Attardi, B., Cravioto, B., and Attardi, G. (1969) J. Mol. Biol. 44, 47.

APPENDIX B

PLASMID ISOLATION
(This procedure for 1-liter cultures)

1) Grow cells - plasmids may be amplified with chloramphenicol.

2) Harvest cells. Chill on ice - 10 minutes. Pellet at 6000 RPM - 5 minutes. GS3 rotor.

3) Resuspend pellets in 36 ml. 50 mM glucose, 25 mM Tris pH=8.0, 10 mM EDTA. Add 4 ml. 40 mg/ml. lysozyme, room temperature - 10 minutes.

4) Add 80 ml. 0.2 M NaOH 1% SDS (fresh every two weeks)
Swirl, put on ice - 5 minutes

5) Add 40 ml. KOAc solution (3 M KOAc + 2 M glacial acetic acid)

6) Filter supernatant through cheese cloth and put in another GSA bottle.

7) Add90 ml. Isopropanol (0.6 vol), mix well, pellet at 8000 RPM - 10 minutes.

8) Resuspend pellet in 10 ml. 10 mM Tris pH=8, 1mM EDTA.
Add NaCl to 0.1 M. Add RNase A (preheated for inactivating DNase) to 20 micrograms/ml, leave at room temperature 2 hours.
Prepare column. Use 5 g BND/liter culture (column can be a 30-50 ml syringe)

9) Take up cellulose in 0.1 M Tris pH=8, 0.001 M EDTA, o.2 M NaCl, load on column and wash until OD_{260} 0.2. (100 ml.)

10) Add RNased sample to column after adjusting NaCl to 0.2 M . Pass solution through twice. Wash with 0.1 M Tris pH=8, 0.001 M EDTA, 0.2 M NaCl until the OD_{260} 0.2.

11) Wash with 0.1 M Tris pH=8, 0.001 M EDTA, 0.35 M NaCl until OD_{260} 0.2.

12) Elute with 0.1 M Tris pH=8, 0.001 M EDTA, 1 M NaCl. It is good practice to let the column stand in 1 M NaCl Tris buffer solution for 24 hours for high yields of plasmid. DNA comes out reaching a peak rapidly and then gradually decreasing. Collect fractions (1.5 ml each)

13) Then pool fractions, ETOH precipitate, resuspend in TE.

14) Check $OD_{235,240,260,280}$. Run gel to test for purification.

References:

1) Alkaline Lysis: Birnboim, H.C. and Doly, J. (1979) Nucl. Acids Res. 7, 1513-1523.
2) BND: Kiger, J.A. and Sinsheimer, R.L. (1969) J. Mol. Biol. 40, 467-490.

ABSTRACT

Originally interested in freeze cleaving, an investigation of existing freezing techniques convinced me that the apparatus available did not satisfy basic requirements of freeze cleaving or fracture, namely rapid freezing of biological samples to minimize ice crystal damage with little if any stress placed on the sample to be frozen.

INTRODUCTION

Studies on the release of synaptic vesicles[1] (or nerve endings) demonstrated that freeze drying was an effective way of rapidly preserving cells and stopping biologically important events. The work of Heuser and others with an ultra cold metal block apparatus produced first-rate electron micrographs. However, Heuser's techniques have two drawbacks. Firstly, they utilize impact freezing which stresses and possibly distorts structures. Secondly, they are limited to freeze cleaving only.* My work has been concentrated on developing a system for utilizing rapid quenching of materials in liquids. Ideally this system provides stress-free cooling in minimal time between 0 and -130° C, the critical temperatures for starting and stopping ice crystal growth.[2] Both freeze cleaving and freeze fracturing can be performed on samples frozen this way. The use of jets to spray coolant at the sample makes convective as well as conductive cooling possible, hopefully a significant edge on conventional quenching techniques[3] which are limited by conduction in the quenching coolant.

RESULTS AND METHODS

Figure 1: Simpified conventional liquid quenching apparatus (in the vernacular: dunker). A metal rod is held by a solenoid and released to fall a distance of about 6 cm into a liquid coolant. Measurements were made on liquid N2 in a 180 ml styrofoam cup, other coolants were placed in 50 ml Nalgene beakers (to save coolants and avoid solubility problems). For the data shown in Figures 2 and 3 a bare copper constantan thermocouple with 4 twists was run with no standard probe in series. Wire diameter was .013", 4 twists weigh 5.9 mg. *In this context freeze cleaving produces a single replica only while freeze fracturing refers to the production of complementary replicas.

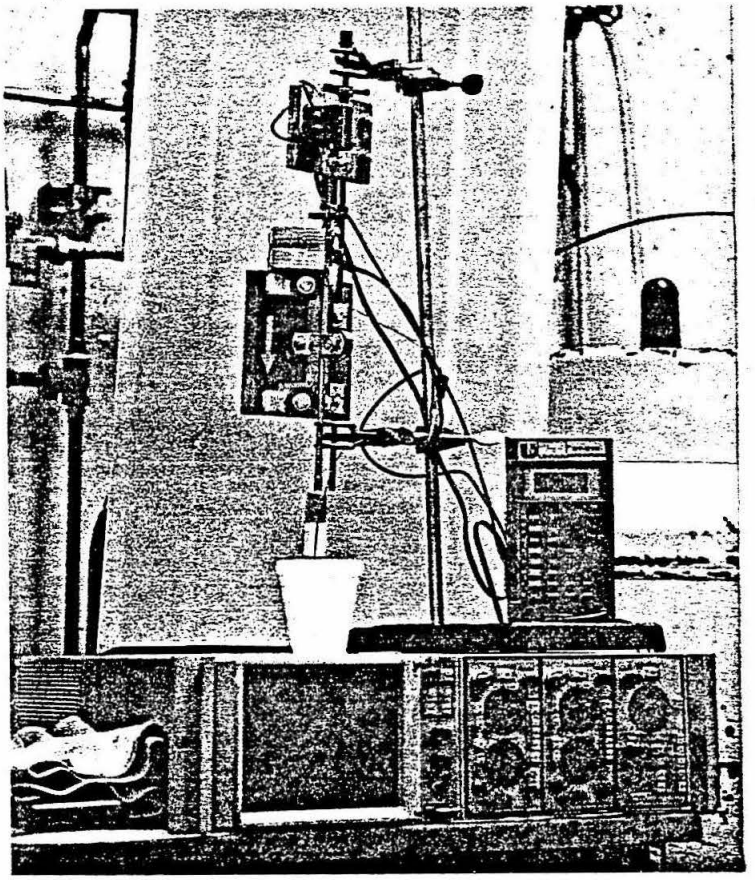

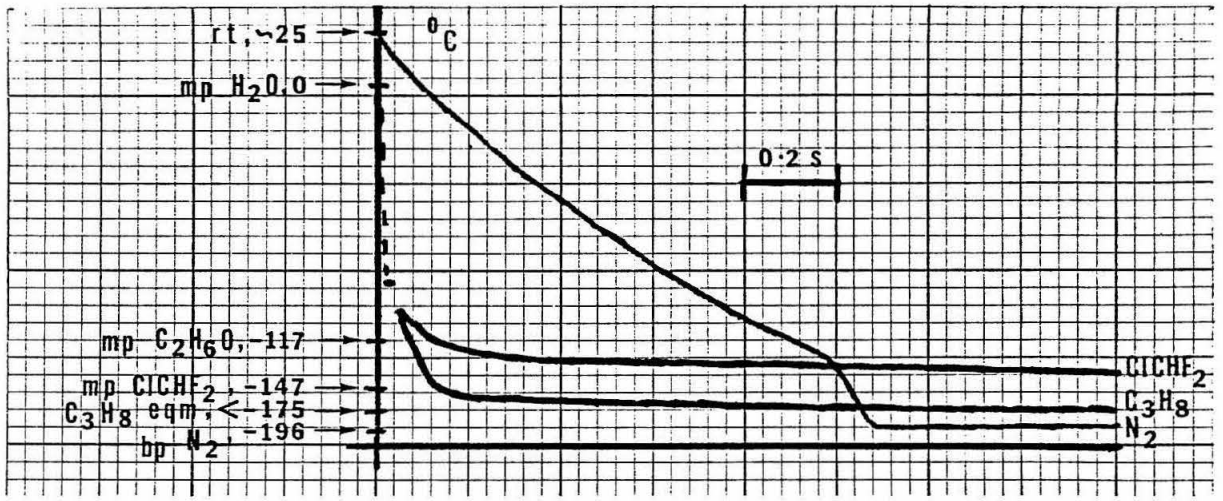

Figure 2: Average cooling curves of two consecutive runs in N2 (nitrogen), ClCHF2 (freon 22) and C3H8 (propane) standardized against equilibrium temperatures of N2, ClCHF2, C3H8, H2O (water) and C2H6O (ethanol). rt, room temperature; mp, melting point; bp, boiling point; eqm, equilibrium.

Notice boundary layer cooling of N2 down to approximately -125°C, at which temperature the gaseous layer of N2 surrounding the probe dissipates. Freon 22 and propane do not exhibit boundary layer cooling.

Under the conditions used -130°C was reached in 100 msec using propane.

Figure 3: Cooling curves of two consecutive runs in ClCHF2 and C3H8 standardized against eqm temperatures of H2O, C2H6O, ClCHF2 and C3H8. From top: a) rt (please note that the tilted line is an artifact of scope used), b) mp H2O, 0, c) mp C2H6O, -117, d) mp ClCHF2, -147, e) C3H8 eqm, <-165. Vertical scale degrees C. Horizontal scale 50 ms/division. With a little interpolation propane can be seen to be a better coolant than freon 22. Cooling rates are critical down to -130°C[4], propane passes this barrier in an estimated .15 s, freon-22 has yet to reach the barrier in an estimated .45 s.

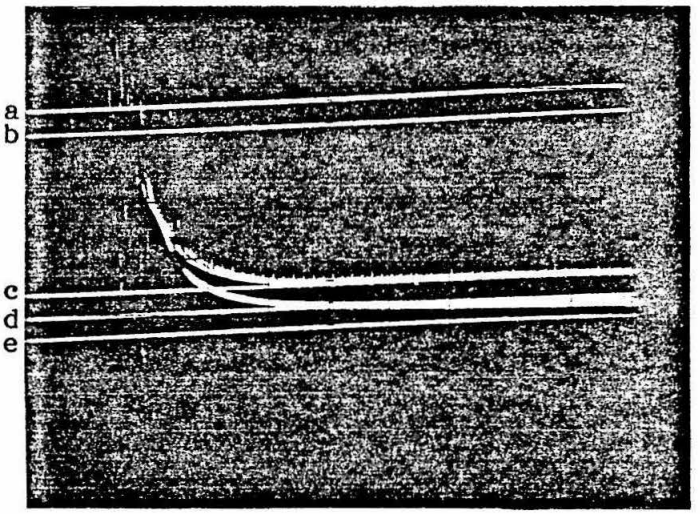

From the data obtained using the "dunker" we concluded that propane is a suitable coolant for rapid cooling to below -130°C; for actual work I constructed a modified version of an existing jet freezing apparatus.

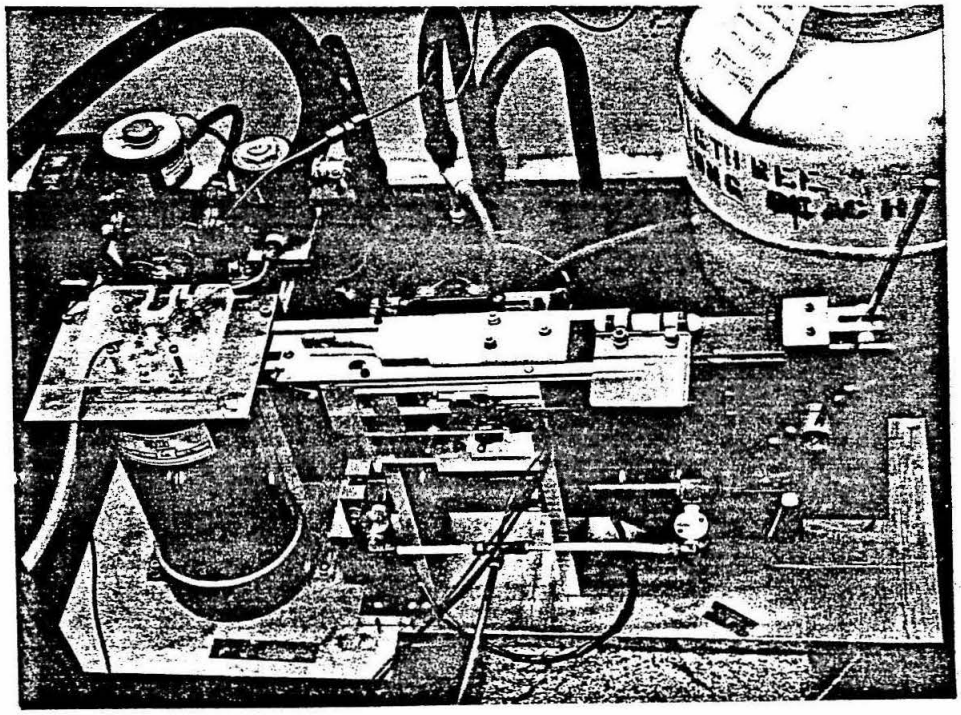

Figure 4: Jet freezing apparatus: a piston propels a slide with specimen into an area in which jets of liquid propane cooled to just above freezing temperature spray the specimen. A system of microswitches and relays determines the relative timing of the propulsion system and the spray of coolant. The spray nozzles can be exchanged and their orientation as well as their height adjusted.

Fig. 4 Schematic: a) A valved supply of dry nitrogen propels the coolant through jet nozzles; b) A supply of propane is fed into a small reservoir cooled by a liquid nitrogen dewar. A one-way valve ensures that cold propane does not leak back into the tank; c) A thermocouple measures the propane temperature; d) A specimen slide holds the sample and is pushed by the piston into the area sprayed by jet nozzles; e) Piston; f) Jets (see diagram).

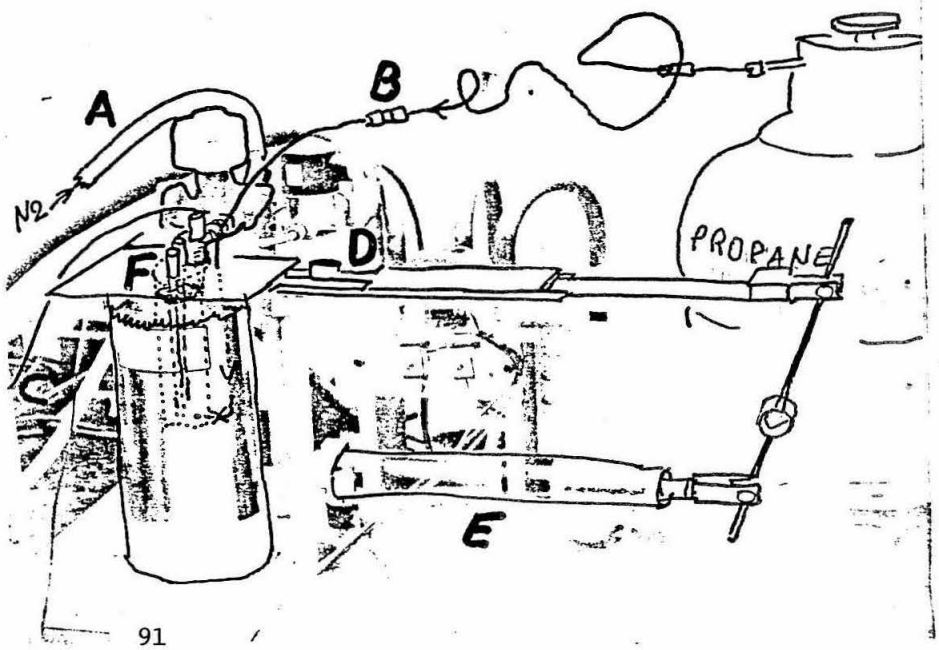

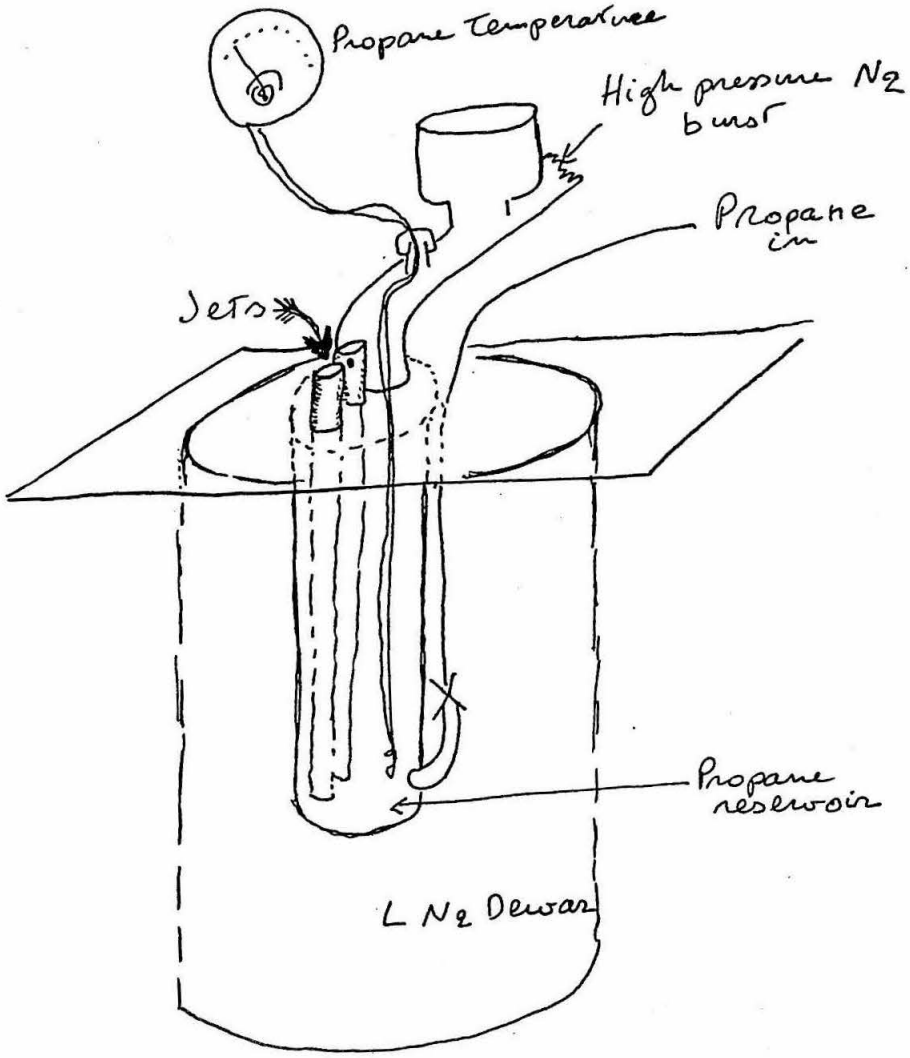
Propane Temperature
High pressure N_2 burst
Propane in
Jets
Propane reservoir
L N_2 Dewar

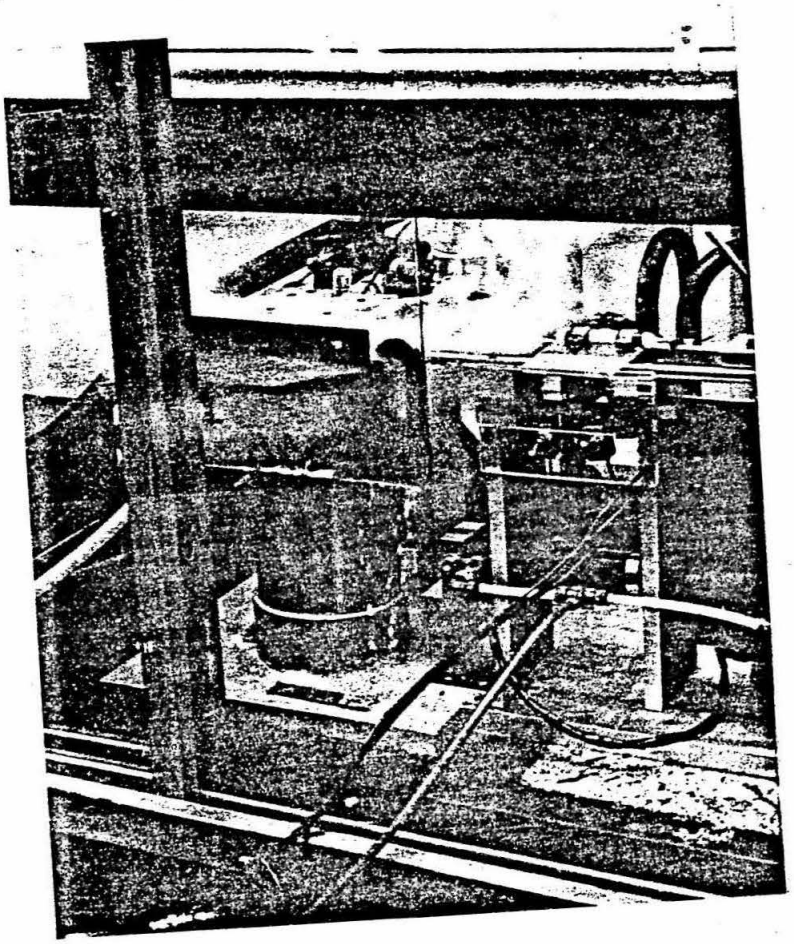

Figure 5: Fun with volatile liquids.

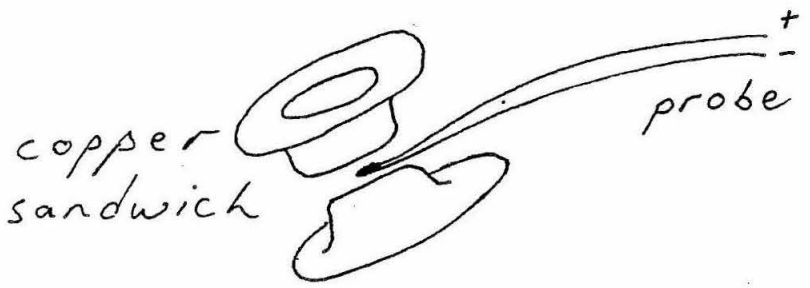

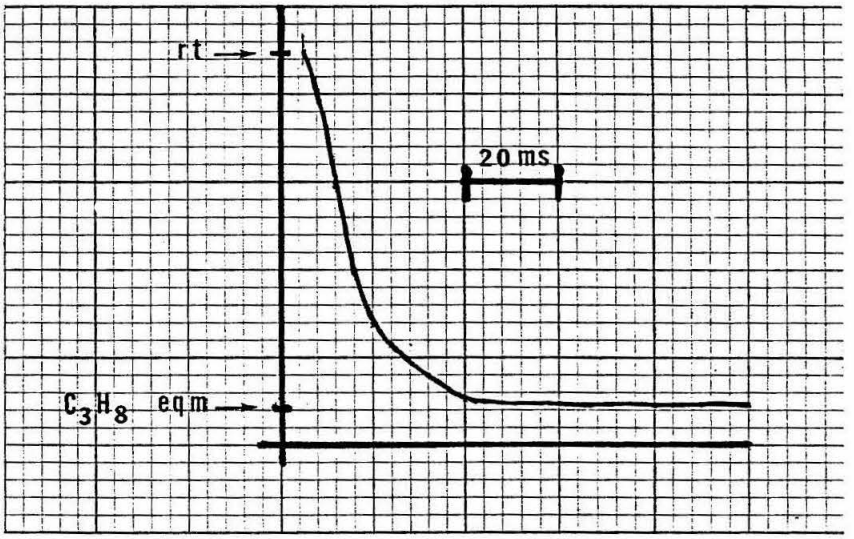

Figure 6: Uncalibrated cooling curve of .001" diameter constantan chromel thermocouple cyanoacrylated in a copper sandwich specimen holder and jet sprayed. Note this is a fine wire probe. Weight of copper sandwich .0079g.

CONCLUSIONS

Electron micrographs (not shown) of biological samples frozen in the uncalibrated, unfinished jet freezer indicate the apparatus is promising but that considerable work in freezing technique and optimization of cooling rates through variation of jet size and jet angle against a standard quenching agent (mp freon 22) remains to be done.[5]

My thanks to those members of Revel's lab who have already spent considerable time on this project and to the Bi/Chem machine shops for the use of their equipment and their help in the construction of the dunker and the specimen slide.

Bibliography

1. Heuser, J. et al. Synaptic vesicle release captured by quick freezing, etc. J. Cell Biol. **81**, 275-300.

   Heuser, J. Quick freeze deep-etch preparation of samples for 3-D electron microscopy. TIBS March 1981.

2. Freeze fracturing and freeze etching in Glauert, A. Practical Methods in Electron Microscopy, Ch. 7 North Holland Publishing Co., Amsterdam/New York/Oxford 1980.

3. Costello, M. J. and Corless, J. M. The direct measurement of temperature changes during rapid quenching. J. Microscopy **112**, 17, 1977.

4. Bank, H. and Mazur, P. Visualization of freezing damage. J. Cell Biol. **57**, 729-742, 1973.

5. Yancey, S. B., Nicholson, B. J., and Revel, J. P. The dynamic state of liver gap junctions. J. Supramolec. Struct. and Cell. Biochem. **16**, 221-232 (1981)

   Cellular Recognition 215-226.

HOLOGRAPHY OF MOVING OBJECTS

Kirk R. Haselton
1982 SURF Report
September 15, 1982

ABSTRACT

An object motion of several wavelengths during a holographic recording can still produce fringes on the recording film of sufficient contrast to reproduce the original object when the recording is played back. This study addresses the quantitative effect of object motion on fringe contrast and thus holographic recording, both in magnitude and direction of the motion.

INTRODUCTION

The construction of a hologram requires recording of the intensity fringe pattern from two interfering fields, one containing the information or signal and the other being a reference field. A change in the relative phase of these two fields causes the intensity pattern to shift over the hologram recording plane. The amplitude transmission factor at any point in the hologram after development is proportional to the integrated intensity present at that point during the exposure. Therefore, a stationary interference pattern will produce the maximum recorded fringe contrast and, in turn, a dimmer holographic image. This is a major difficulty in the holography of moving objects. The exposure time is conventionally thought to be limited in such a way that the fringe pattern moves less than one-half a fringe during exposure. This has resulted in varying "opinions" of how much object motion can be tolerated during exposure.

Randy Bartman, a graduate student at Caltech, has re-examined this theory and concluded that a motion of several wavelengths will not necessarily "wash out" the hologram and that when the object is far from the recording medium and moving parallel to it the object may move several wavelengths before severe fringe shift occurs.

The purpose of the project was to make holographic recordings with both parallel and perpendicular object motion and observe the replayed images, noting their relative intensities and thus confirming or disputing conventional beliefs in limiting object motion during exposure in a holographic recording.

PRESENTATION AND DISCUSSION OF RESULTS

To test this theory, preliminary observations were made by constructing holographic diffraction gratings for a range of displacements of one of the beams. (The holographic diffraction grating is a holographic recording of the interference between two large-diameter, coherent plane waves of equal intensity.) In theory, the fringe contrast is a sinc-squared function where the argument of the sinc is directly related to the amount of fringe motion during exposure (provided the film is actually a linear recording medium). Fringe motion was achieved by shortening the path length of one of the beams by small amounts during exposure and thus inducing a relative phase change between the two beams. Small, accurate displacements of one of the beams was obtained by using a piezoelectric crystal to control the movement of a mirror used to relay that beam to the film plane.

An efficiency of the holographic grating was determined by measuring the intensity of a diffracted beam of light when an incident beam strikes the grating. Gratings were made for a range of fringe shifts up to three fringes. (A relative phase change of 2π contributes a shift of one fringe.) It was expected that grating efficiency would go to zero at odd integral multiples of π in relative phase change and rise back to very low peaks at even multiples of π in relative phase change. The observed data supports these expectations, although for fringe shifts of greater than 1/2 fringe the noise level associated with inaccuracies in both piezoelectric control and the recording film prevented definite confirmation that the fringe contrast followed a sinc-squared function and not another similar function displaying the above characteristics.

Experiments are presently being performed in which spherical objects ranging in size from 5 microns to 2mm in diameter are displaced parallel to the recording plane a few microns to tenths of a millimeter during exposure. When played back, the virtual image is focused onto a light meter and the intensity measured. It is expected that the intensity of the image will drop as 2/N where N is the number of object diameters the object moved during exposure. This, in fact, is the same loss suffered by a time-averaged conventional photograph (within a factor of 2). I hope to determine with these measurements a limit on allowable object motion. For object motion perpendicular to the film plane, the intensity of the virtual image is expected to decrease much more rapidly with motion during exposure.

CONCLUSIONS

It was found that a several-fringe motion during a holographic recording did not completely "wash out" the recording of the fringes; when played back, the reproduced beam was bright enough to be visible to the naked eye, althouth intensity dropped by at least a factor of 100. Overall intensity was, of course, greatly enhanced by bleaching the recording.

No results have yet been attained in the holograms made as described in the latter paragraph above.

REFERENCES

1. Randy Bartman, Private communication, 1982.
2. Hecht, Eugene and Zajac, Robert (1979). Optics. New York: Addison-Wesley.

Mechanistic Studies of Addition to d^0 Transition Metal Centers

Pui Tong Ho

Abstract:

Reactions of bis(η^5-pentamethylcyclopentadienyl)-dimethylzirconium(IV) and bis(η^5-pentamethylcyclopentadienyl)dimethylhafnium(IV) with silane and trimethylsilane were performed and monitored via NMR in order to study the possibility of H, CH_3 exchange via a four centered transition state. The data is inconclusive pending studies now underway.

Introduction:

Hydrogen activation by transition metal centers has long been of interest both synthetically and theoretically. Hydrogen addition to d^0 metal centers is not well understood, however. Because the metal has no available valence electrons, oxidative addition is precluded. Systems composed of Cp_2ZrHR ($Cp=\eta^5-C_5H_5$) or Cp^*_2ZrHR ($Cp^*=\eta^5-C_5Me_5$) with H_2 or D_2 have been studied by Schwartz (1) and Bercaw(2); The products of these reactions are the metal dihydride and the corrosponding hydrocarbon. One postulated mechanism invokes a four-centered transition state(figure 1) (1).

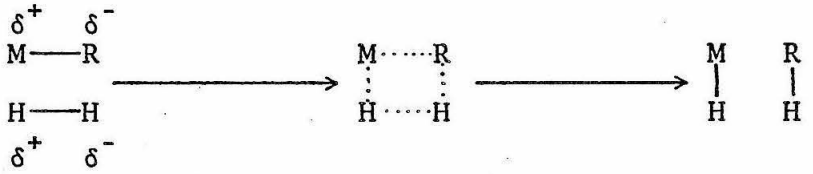

Figure 1

We developed a model system in which the hydrogen is replaced by a substituted silane. Differing the substituents would allow some control over reactivity. $Cp^*_2Zr(CH_3)_2$ and $Cp^*_2Hf(CH_3)_2$ were the metal complexes used; the rections were monitered by NMR.

We are also currently studying the kinetics of a parent system, $Cp^*_2HfH_2$ and H_2, using NMR techniques. By using D_2, we may be able to determine if the hydride ligands are replaced simultaneously(eq. 1) or separately (eq. 2) by monitoring for H_2 and HD.

Eq. 1 $Cp^*_2HfH_2 + D_2 \longrightarrow Cp^*_2HfD_2 + H_2$

Eq. 2 $Cp^*_2HfH_2 + D_2 \longrightarrow Cp^*_2HfHD + HD$

We will also investigate the rate constant for the hydride exchange and solvent effects on the rate by line shape analysis and/or saturation transfer, dynamic NMR techniques.

Results:

$Cp^*_2Zr(CH_3)_2$ and $Cp^*_2Hf(CH_3)_2$ were synthesized from the metal tetrachlorides(eqs. 3 and 4) (3).

Eq. 3 $MCl_4 + 2LiCp^* \longrightarrow Cp^*_2MCl_2 + 2LiCl$ M=Zr or Hf

Eq. 4 $Cp^*_2MCl_2 + 2CH_3Li \longrightarrow Cp^*_2M(CH_3)_2 + 2LiCl$

A new synthesis for HCp* was also investigated.

Both compounds were treated with silane and trimethylsilane in approximately 1:1 mole ratios in benzene-$\underline{d}_6$ in hope of observing a methyl, hydride exchange(eq. 5)

Eq. 5 $Cp^*_2M(CH_3)_2 + HSiR_3 \longrightarrow Cp^*_2M(CH_3)H + CH_3SiR_3$

Silane was consumed rapidly at room temperature in the presence of $Cp^*_2Zr(CH_3)_2$ giving a precipitate that may be polymeric-- the bulk of the metal complex appeared unchanged. Similar results were obtained with silane and $Cp^*_2Hf(CH_3)_2$ after mild heating. Neither metal complex showed any reactivity towards trimethylsilane even after prolonged heating. We are presently studying the behavior of methylsilane and phenylsilane.

Conclusions:

Trimethylsilane's reactivity is low presumably because of its bulkiness and the steric hiderernce in the Cp* wedge. Silane, on the other hand is too reactive. Methylsilane and/or phenylsilane may prove to have reactivities intermediate of silane and trimethylsilane.

References:

1. K. I. Gell and J. Schwartz, J. Am. Chem. Soc., 100, 3246 (1978).

2. D.R. McAlister, D.K. Erwin and J.E. Bercaw, J. Am. Chem. Soc., 100, 5966 (1978).

3. J.M Manriquez, D.R. McAlister, R.D. Sanner and J.E. Bercaw, J. Am. Chem. Soc., 100, 2716, (1978).

A Study of Perfluorodecalin as a Medium for Catalytic Oxidation of Organic Compounds

Richard Honrath

Abstract

The applicability of perfluorodecalin as a medium for oxidation reactions catalyzed by cobalt phthalocyanine was given a preliminary assessment. Rough solubilities of fifteen compounds on an EPA list of priority water pollutants[1] were determined. Cobalt phthalocyanine and perfluorodecalin were purified prior to kinetic and mechanistic studies.

Introduction

The high solubility of oxygen in perfluorocompounds has brought them much attention, mainly as artificial blood substitutes. It has been found that the blood of rats can be totally replaced with an emulsion of perfluorodecalin (F-decalin) without harmful effects[2]. F-decalin was found to have a half-life of about two weeks in the livers of rhesus monkeys, also with no apparent damaging effects[3].

The high oxygen solubility in fluorocarbons and their nontoxicity, coupled with the fact that they are insoluble in water, has led to speculation that they could be part of a liquid waste treatment system. The fluorocarbon would contain an oxidation catalyst, also insoluble in water, and pollutants would diffuse into the fluorocarbon phase where they would be oxidized, creating a continuous concentration gradient. The outgoing water would then be free both of these pollutants and of the oxidation catalyst and fluorocarbon.

The purpose of this study is to begin to determine what pollutants are soluble in F-decalin and to look at the rates and products of oxidation reactions in F-decalin using cobalt phthalocyanine (CoPc) as a catalyst.

Experimental

Solubilities of compounds in F-decalin were found by adding microliter amounts of each compound to five or ten milliliters of F-decalin in a test tube, followed by a sonication bath and/or heating. In some cases a UV/Vis spectraphotometer (HP 8450A) was used to find saturation concentrations.

In addition, a Beckman UD-17 UV/Vis spectraphotometer was used to take spectra over time in order to watch the progress of reactions.

F-decalin was purified by washing with sulfuric acid and water, drying with calcium chloride, and distilling.

CoPc was first washed with 95% ethanol in a Soxhlet extractor for twelve hours. After drying, it was extracted into pyridine using a Soxhlet extractor. It was then crystallized from the pyridine, washed five hours with anhydrous ether to remove combined pyridine, and dried in an evacuated dessicator.

Results and Conclusions

All of the aldehydes tested (5) were found to be solu-

ble in F-decalin in greater than millimolar concentrations after sonication. Of four phenol derivatives, only catechol was not soluble in a concentration of at least one-tenth millimolar. Most of the sulfur and nitrogen compounds were not soluble in the concentrations tested. However, some may be soluble in the less-than-millimolar range. CoPc was found to saturate F-decalin at a concentration of about $7X10^{-5}$ molar.

In a preliminary reaction usin F-decalin saturated with acetaldehyde (0.1M) and CoPc (all unpurified), the absorbance due to acetaldehyde was found to decrease over time. At the start of the reaction, absorbance at 200 nm was 0.528; after five hours it had dropped below 0.225. This would imply a drop in the concentration of acetaldehyde from 0.12M to 0.05M, the remainder presumably having been oxidized to acetic acid.

These results indicate that it may be possible to catalytically oxidize all but the most polar aldehydes and phenols and some less polar sulfur and nitrigen compounds using CoPc in F-decalin. In the next step of this research, the kinetics of some of these reactions will be analyzed using spectraphotometric techniques and the reaction products will be determined by GC, HPLC, and GC/MS.

MAXIMUM SOLUBILITIES IN PERFLUORODECALIN

Aldehydes		
acetaldehyde	CH_3CHO	~0.1 M
acrolein	$CH_2{=}CHCHO$	~0.015
benzaldehyde	C_6H_5CHO	$\geq 0.0096^{s}$
4-chlorobenzaldehyde	$(4\text{-}Cl)C_6H_4CHO$	$\geq 0.005^{s,\ 65}$
crotonaldehyde	$CH_3CH{=}CHCHO$	≥ 0.004
Phenols		
phenol		$\geq 0.02^{50}$
2,4-dichlorophenol	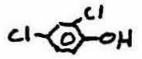	~0.018
2,4-di-tert-butylphenol	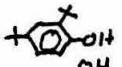	$\geq 0.0009^{40}$
catechol	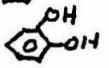	< 0.0001
Nitrogen and Sulfur Compounds		
aniline	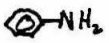	~0.004
hydrazine	H_2NNH_2	< 0.016
dimethyl sulfoxide	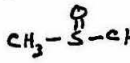	< 0.007
cysteine	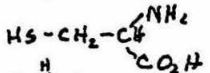	< 0.004
carbazole		< 0.002
diphenyl disulfide	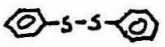	< 0.008
Others		
cobalt phthalocyanine	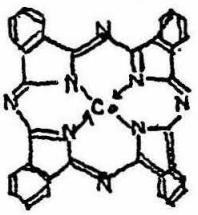	$\sim 7\times10^{-5}$
oxygen[4]		0.03 (40 ml O_2/100 ml)

---

s: sonication bath, n: heated to n C

NOTES

1. Keith, Lawrence, Environmental Science and Technology, Vol. 13, 12 (1979), pp. 1469-1471.

2. R.P. Geyer, N. Engl. J. Med., 289, 1077, (1970).

3. L.C. Clark, E.P. Werseler, S. Kaplan, C. Emory, R. Moore, D. Denson, Biochemistry Involving Carbon-Fluorine Bonds, ACS Symposium Series 28, Washington 1976, p. 135.

4. R.M. Varushchenko et al, Russian Journal of Physical Chemistry, **55** (10), 1981.

August 26, 1982

The Design and Implementation of Object-Orientated Languages

SURF Project, 1982
Keith Hughes
Jim Kajiya, Research Advisor
California Institute of Technology

Abstract

Object-orientated languages (OOL's) are programming systems which work via the metaphor of communicating objects. The purpose of this project was to design and implement a Smalltalk '80 system, such as developed by Xerox's Palo Alto Research Center (PARC), which is an interpretive OOL. A compiler has been nearly completed, and plans are being made for the run-time system.

Introduction

The previous work for this project was begun in my freshman year at Caltech. I had the idea then of writing a FORTH interpreter to help me learn how to write languages. Then the Byte issue about Smalltalk[1] got me interested in a different approach to programming. The FORTH interpreter was modified to handle more complex data structures in an interactive format, thus becoming MPL. MPL was then to have message handling and a Smalltalk compiler patched into it. This was the status as of second term last year. However, after talking to Jim Kajiya, it was decided to start over with a bytecode interpreter like the PARC people did. The project was to bring an entire Smalltalk '80 system up (being the compiler, run-time system, and user-interface); but progress has only created the compiler.

Presentation and Discussion

Those familiar with programming languages are used to the idea of the data in the language being something manipulated by the procedures of the language, but not having any say in the matter. OOL's give the power to manipulate the data structures to the structures themselves using a method called message sending. Each object has what is called a class template, which contains the data structures for the object, and the code for manipulating its various parts. For example, one could have the statement *<some object> + 1*, where *+ 1* is the message and arguments being sent. An instance if class Integer, for example, *'3'*, would return the answer *'4'*; while an instance of class String, say *'foo'*, would return *'foo1'*. In this way, the code becomes less definite, allowing the system to handle complexity much better, due to code controlling flow of information, an idea which may appeal to those who haven't used conventional programming systems.

The storage manager[1,3] was the first module written. An interpreter was then written, based on the Smalltalk '76 system[2]. The compiler was begun as a '76 compiler, but talks with Kajiya convinced the me to go straight for an '80 system. Recursive descent[4] was used as the compiling method, since it was easy to use, and generated code while parsing the statements. A version of the compiler was working by July 15, but all it did was

create the bytecodes without knowing where the variables were stored. Work then was begun to create the necessary symbol tables and other needed run-time information. Work slowed down tremendously here, since the author no longer knew what he was doing. Since Smalltalk '80 allows blocks of code to be passed around as objects in their own right, some method had to be found to allow non-local variable referencing. The idea used by funargs in LISP is to be used when the run-time portion of the code is completed[5,6].

Conclusions

Smalltalk is a non-trivial language to implement, especially when it is one's first language. This was the first and most important thing I learned. OOL's provide elegant methods for generating large application programs in a manner which is easily understood by the computer-novice. The bytecode natureof the compiled code makes efficient use of memory, while the idea of message sending makes for a simple management of complexity. All in all, Smalltalk is a very good language, as are OOL's in general (though Smalltalk and Simula are the only two well-known OOL's at the present time). It is hoped that the entire system will be done and available for distribution very soon.

References

1. Entire issue, *Byte*, August 1981.
2. Daniel H. H. Ingalls, *Proceedings of the Principles of Programming Languages Symposium*, January 1978, pgs 9-15.
3. L. P. Deutsch and D. Brobow, *CACM*, September 1976, pgs 522-526.
4. P. J. Brown, *Writing Interactive Compilers and Interpreters*, John Wiley & Sons, New York.
5. John R. Allen, *Anatomy of LISP*, McGraw-Hill Book Company, New York.
6. Peter Wegner, *Programming Languages, Information Structures, and Machine Organization*, McGraw-Hill Book Company, New York.

Numerical Grain Flow Problems

Kenneth Hui

Abstract

Numerical solutions for three different types of grain flow problems were obtained. The three types were flow between two horizontal moving plates, flow down two vertical plates and flow between two inclined plates. All the plates considered were infinite in dimensions.

Introduction

Not until recently had the subject of grain flow been given serious attention from physicists. Bagnold[1] did some pioneering theoretical work on the symmetries of the flow equations. Most recently, Haff[2] outlined a new approach to the grain flow problem by treating them as continuous matter as in fluid mechanics. The object of the SURF project is to obtain numerical solutions to the grain flow problems taking Haff's point of view since in most cases analytic solutions are not obtainable.

Presentation and Discusson of Results

The equations for the flow equations were constructed as to resemble the fluid flow equations as close as possible. The major differences between the two systems are: 1) Grain size is much greater than molecular size; 2) Grain-grain collisions are inelastic; 3) Grains are irregular in shape; 4) Grain-grain interactions are non-central; 5) the validity of the continuum hypothesis. In order for the continuum hypothesis to hold, the average separation between two grains at any point must be small compared

to the grain diameter. With all the above constraints, one can obtain the continuity equation, the momentum equation and the energy equation for the grain flow system. By introducing some simple but suitable models, one can furthermore obtain the equation of states, the coefficient of viscosity and the coefficient of inelasticity which are needed to solve the grain flow problems. With all these equations, we obtained numerical results for the flow velocity (how fast the grains are flowing), the density and the "thermal velocity" (the magnitude of the random velocity of the grains) for all the three types of flow problems mentioned earlier. The adjustable prarmeters in each of these cases were chosen as realistic as possible. These results matched the expected physical results quite well and it is reasonable to assume that they correspond to some physical phenomenon in nature.

Conclusion

The numerical results obtained give new physical insights to the grain flow problem. It also showed that the approach taken by Haff is highly likely to be a correct description of the grain flow problem. We can also compare these theoretical results with experiment results when they become available in the near future.

Bibliography

1. R.A. Bagnold, The flow of cohesionless grain in fluids, Proc. Roy. Soc. A249, 235-297, 1956.

2. To be published in the J. Fluid Mech.

Spider Brain and Behavior

SURF Final Report

submitted by
Cecile B. Huling

Spider Brain and Behavior

Abstract

The purpose of this project was to study and map the brain of the jumping spider, concentrating on the location and properties of visually stimulated neurons. We found areas of the brain and individual neurons that responded to particular visual stimuli, and other neurons which responded to touch or motion.

Introduction

Previously, studies have been made regarding the visual capabilities of jumping spiders or salticids. Perhaps the best known are those studies by M. F. Land who published several works on the structure and organization of the eyes of salticids and on orientation and pattern recognition in these spiders. The visually directed behavior of jumping spiders has been treated by Forster and Drees, to name just a few. In this project we wanted to concentrate more on the neurological aspect of salticid vision; locating visual pathways in the brain, isolating single neurons and groups of related neurons and identifying their properties.

Presentation and Discussion of Results

We used two types of jumping spiders in this study, the Phidippus johnsoni and an unidentified salticid, both found on campus. We also used the wolf spider (lycosid)

because it too possessed a highly sensitive visual system.

We used two methods to study the spider brain, electrophysiological recording and histology. The electrophysiological experiments consisted of recording from neurons responding to visual and other stimuli. The spider to be studied is first anesthetized, then secured to a platform. An electrode is advanced into the brain of the spider and picks up electrical impulses from the cells it encounters, displaying the signals audibly as pops and clicks and visually as a trace on an oscilloscope. The position and depth of the electrode can be controlled, and the location of interesting cells can be noted.

The histological methods consist of removing the spider's appendages and abdomen, immersing what is left, the prosoma, into a fixative agent to preserve the tissue, embedding the spider in a firmer, supportive substance such as paraffin, sectioning the embedded spider into 10-15 micron sections, and affixing the sections onto a microscope slide. The sections are stained to highlight or contrast types and structures of cells. Unfortunately in this project, none of the sections processed very well, and no information could be obtained from them. However, the electrophysiology experiments did reveal some interesting properties of the jumping spider's brain. We found evoked potentials, indicating areas of visually stimulated neurons, in many of the spiders. These areas were found from 130 microns into a small wolf spider to 2150 microns in larger ones. The most common locations were

posterior to the eyes and close to the midline of the spider's prosoma.

We isolated a single neuron 270 microns into the brain of a salticid. It was behind the posterior lateral eyes of the spider and slightly to the right of the midline. This single cell habituated rapidly and responded to horizontal dark edges moving at about two visual degrees per second against a lighter background. The optimal size for such a stimulus was over three degrees wide. This neuron most probably responded to visual input from the spider's right anterior medial or lateral eye.

In the fifth instar Phidippus johnsoni spiderling reared in the lab, we found single neurons that responded to the motion of the spider's appendages. Very slightly lateral to the midline and on a line between the posterior and anterior eyes of the spider at a depth of approximately 550 microns, signals fired when the left pedipalp (a frontal appendage) was moved.

More medially, almost between the two posterior lateral eyes, we isolated a neuron at 830 microns. This particular neuron fired when the spider moved its chelicerae or jaws.

Conclusion

Single neurons can be isolated in the spider brain and recorded. A neuron responding to distinct visual stimuli, the motion of dark edges on a light background, has been isolated in the brain of a salticid at an approximate depth of 270 microns, slightly lateral to the midline and behind the posterior lateral

eye. Pedipalpal ganglia in fifth instar Phidippus johnsoni may be located in a region 550 microns into the spider, slightly lateral to the midline and between the posterior and anterior lateral eyes. It is also possible that cheliceral ganglia may be located in an area about 300 microns deeper into the spider.

Bibliography

Forster, Lyn, 1982, Vision and Prey-Catching Strategies in Jumping Spiders, American Scientist, Vol. 70, March-April, pp.165-175

Hill, D. E., 1975, The Structure of the Central Nervous System of Jumping Spiders of the Genus Phidippus (Araneae: Salticidae)

CHRIS HULL

No Report Submitted

LEVEL POPULATIONS IN AN FE-AR HOLLOW-CATHODE DISCHARGE

John Humphrey

ABSTRACT

Measurements have been made of the population of the energy levels in an iron-argon hollow-cathode plasma. An attempt has been made to model the populations in the plasma.

INTRODUCTION

The hollow-cathode has been a widely used spectroscopic source for over 50 years. An understanding of the characteristics of its discharge would greatly enhance one's control over the device. A search of the literature revealed papers on the population of ionic levels in a hollow-cathode, but only 2 papers on the population of neutral energy levels. Danzmann and Kock (1981) measured the populations of the energy levels in a titanium-neon and titanium-argon hollow-cathode discharge. The populations followed a Boltzmann distribution. This is in disagreement with our results for an Fe-Ar hollow-cathode discharge. Crosswhite's (1975) results were similar to ours but he measured the populations for fewer energy levels. Also, the transition probabilities he used in calculating the populations were not always accurate enough to reveal the anomalies presented in this report. The purpose of our project was to measure the populations of the energy levels in an Fe-Ar hollow-cathode plasma and then to explain, as well as possible, why the levels have the populations they do.

PRESENTATION AND DISCUSSION OF RESULTS

Spectral data, such as the wavelengths of lines and the areas under them, had been recorded earlier. For an upper level μ, the population N_μ is given by

$$N_\mu = \frac{a_\lambda \lambda^2}{\epsilon_\lambda g_\mu f_{\mu\ell}} \times 1.5 \times 10^{-16}$$

where a_λ is the area under a line, λ is the wavelength (in angstroms), ϵ_λ is the efficiency of the spectrometer, g_μ is the statistical weight of the upper level, and $f_{\mu\ell}$ is the oscillator strength of the transition. This was used whenever accurate (to within 1%) gf-values were known (about 70 lines), and the gf-values were taken from Blackwell et al. (1979). The dominant uncertainty occurs in the measurement of area and is typically 5%. For 12 lines accurate gf-values were not available and N_μ was found from

$$N_\mu = \frac{\tau_R}{g_\mu} \times \sum_\lambda \frac{a_\lambda}{\epsilon_\lambda}$$

where τ_R is the radiative lifetime, and the summation is taken over all possible downward transitions. τ_R contains the dominant uncertainty which is anywhere from 5% for experimental lifetimes to 25% for theoretically derived lifetimes. The experimental lifetimes came from Marek et al. (1979) and the theoretical lifetimes from Kurucz and Peytremann (1975).

Populations were measured in a hollow-cathode of 3 mm inside diameter and 15 mm length. They were measured for an Fe-Ar plasma whose discharge parameters were 400 mA and 244 Volts at a pressure of 1.5 torr. They were also measured in an Fe-Ne plasma run at 202 mA, 260 Volts, and a pressure of 1.2 torr; and an Fe-Ar plasma at 204 mA, 270 Volts, and a pressure of 1.2 torr. No significant differences were noted. The data presented here is for the Fe-Ar plasma at 1.5 torr and 400 mA, 244 Volts. The measured populations are plotted against excitation energy (Fig. 1). It is apparent that the populations do not follow a Boltzmann distribution, which implies that the plasma is not in local thermodynamic equilibrium.

We observed that there was a correlation between population and lifetime. More specifically, for any small range of excitation energies, there is a strong tendency for the higher populations to belong to those levels with longer lifetimes. This is most readily apparent in the $z^3P^o_{0-2}$ levels. We also noted that there was a general exponential decay of population with respect to excitation energy, and that after the lifetimes became long, they ceased to have a definite effect on population. It wasn't discernable when radiative lifetime ceased to be important since the lifetimes we measured tended to be less than 10^{-7} sec or greater than 2×10^{-5} sec, and it was somewhere between these limits that the radiative lifetimes seemed to lose their significance as a mechanism for de-excitation.

A possible model of this process is an excitation term $e^{-\beta E_{ex}}$, where E_{ex} is the excitation energy and β is a positive constant, and de-excitation by radiation and collisional quenching. We estimated a mean collision lifetime of 225 nsec from classical kinetics for a gas at 1.5 torr and our estimated temperature of 400°K. The above model would imply, at balance,

$$A e^{-\beta E_{ex}} = \frac{N_\mu}{\tau_R} + \frac{N_\mu}{\tau_c}$$

where τ_R is the radiative lifetime, τ_c is the collisional lifetime (about 225 nsec), and A is a constant. Thus,

$$(1) \qquad N_\mu = \frac{A e^{-\beta E_{ex}}}{\left(\frac{1}{\tau_R}+\frac{1}{\tau_c}\right)}$$

A shorter collision time (τ_c =100 nsec), and a $\beta = 1.47\times10^{-4}$ cm makes expression (1) fit the observed populations within a factor of 3 over the entire range of τ_R=10 - 10^5 nsec. We can tender no explanation for the regular behavior of population within a term, which is most readily apparent in the z^7D^o, z^7F^o, and z^7P^o terms.

CONCLUSION

Observations of an Fe-Ar hollow-cathode plasma show that the plasma is not in local thermodynamic equilibrium. A significant difference in radiative lifetime between nearby levels can produce anomalous population of those levels, until the lifetime becomes long with respect to collision time. This implies that radiation ia an important de-excitation mechanism in the plasma but there are competing processes which dominate when the lifetimes are long. Further work needs to be done to justify our assumption that the excitation mechanism is proportional to $e^{-\beta E_{ex}}$, and to explain the pattern of population within a term.

BIBLIOGRAPHY

Blackwell, D.E., Ibbetson, P.A., Petford, A.D., and Shallis, M.J., Mon. Not. Royal Astron. Soc. 186 (1979) p.633

Crosswhite, H.M., Jour. of Research of the Nat. Bur. of Standards, 79A (1975) p.17

Danzmann, K., and Kock, M., Jour. Phys. B 14 (1981) p.2989

Kurucz, R.L., and Peytremann, E., "A Table of Semiempirical gf-values," Smithsonian Astrophys. Obs. Spec. Rept. 362 (1975)

Marek, J., Richter, J., and Stahnke, H.-J., Physica Scripta 19 (1979) p.325

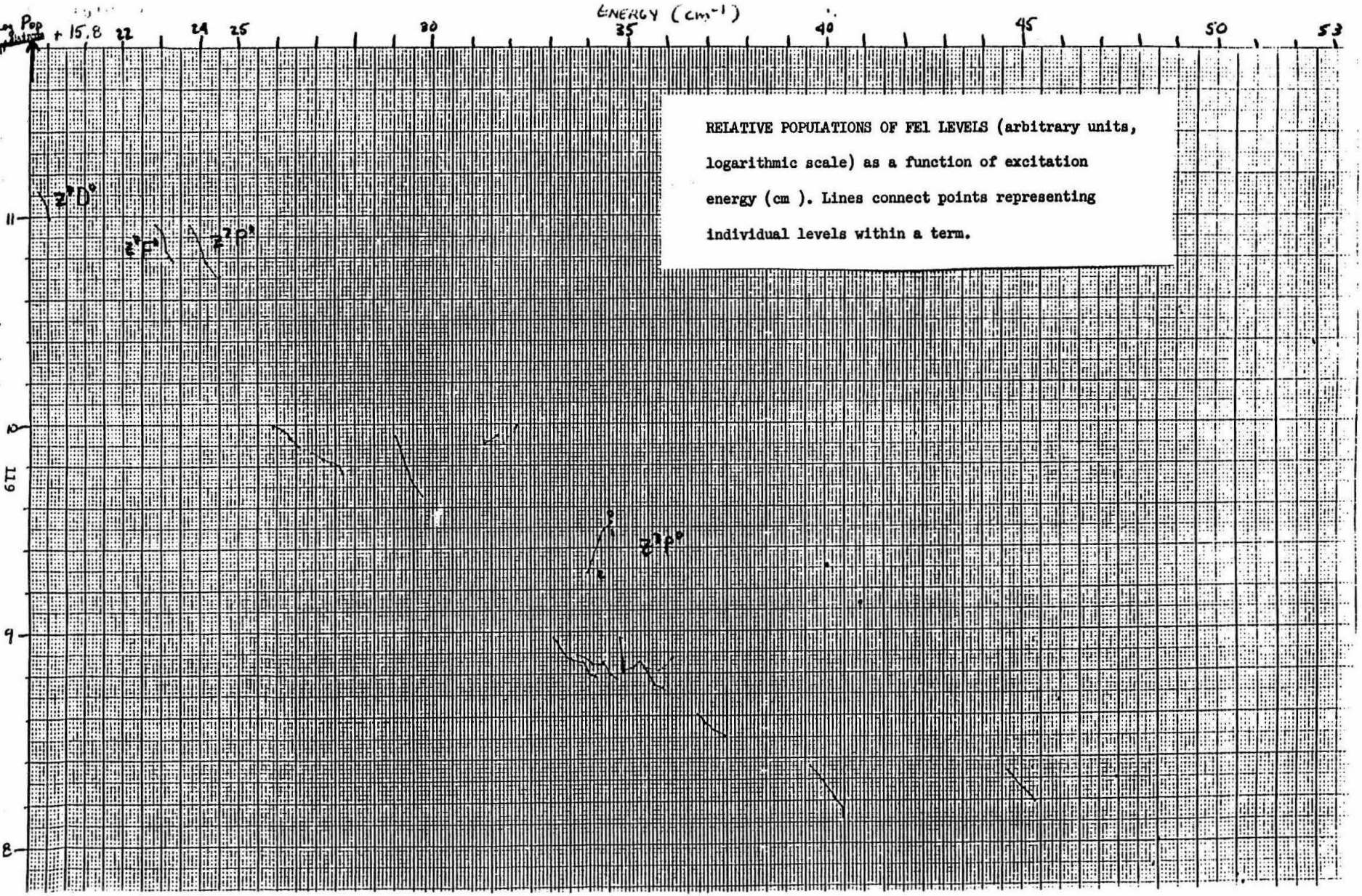

RELATIVE POPULATIONS OF FE1 LEVELS (arbitrary units, logarithmic scale) as a function of excitation energy (cm). Lines connect points representing individual levels within a term.

POPULATIONS FROM Scan 4 12/11/79
LIFETIMES FROM KRRUCZ

p52,53

UPPER LEVEL	J	Energy (cm^{-1})	$\frac{a}{\epsilon}\frac{\lambda^2}{g^0} \propto$ Pop.	τ (ns)
z^7D°	3	19757	1.2871×10^{11}	222837
	2	19913	1.1174×10^{11}	307567
	1	20020	9.9255×10^{10}	423295
z^7F°	5	22846	9.1333×10^{10}	33204
	4	22997	8.5217×10^{10}	28493
	3	23111	6.8049×10^{10}	32556
	2	23193	6.4255×10^{10}	42748
	1	23245	6.2134×10^{10}	58989
z^7P°	4	23711	9.0837×10^{10}	45868
	3	24181	5.9445×10^{10}	84721
	2	24507	5.1637×10^{10}	512092
z^5D°	4	25900	9.7536×10^{9}	80.555
	3	26140	9.3189×10^{9}	85.550
	2	26340	8.4532×10^{9}	85.893
	1	26479	8.1519×10^{9}	80.322
	0	26550	7.8581×10^{9}	89.458
z^5F°	5	26875	7.2663×10^{9}	61.174
	4	27167	6.8878×10^{9}	63.987
	3	27395	6.5746×10^{9}	67.188
	2	27560	6.3344×10^{9}	68.610
	1	27666	5.8058×10^{9}	68.157
z^5P^9	3	29056	8.73×10^{9}	70.769
Taken from Pg 37	2	29469	5.39×10^{9}	52.506
	1	29733	4.55×10^{9}	47.560
z^3F°	4	31307	8.3212×10^{9}	829.993
	3	31805	8.0807×10^{9}	1486.130
	2	32134	9.9102×10^{9}	1860.983
z^3D°	3	31323	8.1146×10^{9}	329.287
	2	31686	8.7747×10^{9}	364.356
y^5D°	4	33096	9.4076×10^{8}	7.823
	3	33507	7.5236×10^{8}	5.875
	2	33802	7.2248×10^{8}	6.457
	1	34017	6.2998×10^{8}	5.916
	0	34122	6.1810×10^{8}	5.928

KT ~ 2900 cm^{-1}
↳ Best Value around 6800 cm^{-1}

UPPER LEVEL	J	Energy(cm^{-1})	$\frac{a}{e}\frac{\lambda^2}{8\pi}$ & Pop.	τ (ns)
y^5F°	5	33.695	7.7440×10^8	8.270
	4	34040	7.1487×10^8	8.081
V	3	34329	7.2199×10^8	7.828
	2	34547	6.3056×10^8	7.885
	1	34692	5.9520×10^8	7.935
z^3P°	2	33947	1.9100×10^9	39.765
	1	34367	3.0622×10^9	100.787
	0	34556	3.3777×10^9	122.693
z^5G°	6	34844	6.4517×10^8	9.814
	5	34782	9.2209×10^8	12.951
	4	35257	7.1899×10^8	11.458
	3	35612	5.6122×10^8	10.357
	2	35856	5.4593×10^8	10.242
z^3G°	5	35379	6.7044×10^8	10.376
	4	35768	6.5531×10^8	11.708
	3	36079	7.4351×10^8	14.354
y^5P°	3	36767	4.0583×10^8	5.458
	2	37158	3.4539×10^8	5.250
	1	37410	3.2454×10^8	5.259
x^5D°	4	39626	2.2976×10^8	2.551
	3	39970	1.9592×10^8	2.607
	2	40231	1.6484×10^8	2.597
	1	40405	1.5109×10^8	2.572
	0	40491	1.3197×10^8	2.422
y^3P°	2	40052	2.0595×10^9	990.885
z^5S°	2	40895	1.3523×10^9	35.558
x^3D°	2	45282	2.2416×10^8	13.441
z^3I°	7	45978	4.6588×10^8	166.188
(1°) z^1D°	2	47420	1.9972×10^8	33.890
x^3P°	1	48586	1.0082×10^8	7.47

TZE KIN IP

No Report Submitted

CALIFORNIA INSTITUTE OF TECHNOLOGY
Daniel and Florence Guggenheim Jet Propulsion Center

CHEMICAL ANALYSIS AND FLAME GEOMETRY OF FIRE PLUMES

by: Hamid Johari

August 1982

Supported Through The Summer
Undergratuate Research Fellowship

ABSTRACT

The main purpose of this research project is to make an accurate mass balance of the chemical species in the ceiling layer gas as a function of temperature and air-fuel ratio of the ceiling layer gas. The most interesting species in the experiment were CO_2 , CO , O_2 , unburnt hydrocarbons, H_2O , N_2 and soot. Some flame geometry data such as eye-averaged flame heights and variations in height are also presented. A methane diffusion flame stabilized on a 0.19 m diameter porous bed burner was the fire.

LIST OF SYMBOLS

D	diameter
M	moles
$\dot{m}$	mass flux
Q	heat release rate in flame based on product of fuel flow rate and heating value
Q^*	dimensionless heat addition parameter, $\dot{Q}/\rho_\infty C_{p_\infty} T_\infty \sqrt{gD}\, D^2$
T	temperature
x	moles of excess air
Y	mole fraction
Z_f	flame height
Z_i	height to the heat source level
ϕ	equivalence ratio

Subscripts:

c	critical
e	entrained
f	flame or fuel
i	interface

Introduction

There has been many attempts for constructing models of fire spread through a room and the most succesful model suggests that two homogeneous layers exist. The upper or ceiling layer contains the hotter gas when a large diffusion flame is the "fire" and when most of the visible flame lies within the ceiling layer. Better understanding of the chemistry would enable us to progress further in the modeling of fire spread through buildings.

Research was done on this project at the Jet Propulsion Center by Professors Zukoski and Kubota and Dr. Cetegen. Their study was mostly concerned with lean fuel-air ratios in the ceiling layer. One exploratory experiment was also done on the fuel rich ceiling layer. The observations revealed that gas temperature stayed almost constant around 850°K and soot was formed when the fuel-air ratio was greater than stoichiometric value. A combustible mixture was formed as soon as the fuel-air ratio was greater than 2 to 2.5 times the stoichiometric ratio.

Experimental Techniques

Since we expected temperatures as high as 1000°C , a small hood; a 2.4 m cube, open on the bottom side, was designed to be used inside the large hood, a 2.4m cube, with mesh screen sides. In order to have a realistic room, all sides of the smaller hood were insulated by Fiberfrax 1.25 cm thick Hot boards. Two 121 sq. in. Pyrex windows were held on one side of the small hood for flame geometry measurements. The small hood along with one of the burners is shown in the Figure 1 .

The small hood is lowered upon the fire by a pulley mechanism and the fires are stabilized by a 0.19 m diameter axisymmetric burner. A gas sample is withdrawn from the hood through a 6 mm diameter stainless-steel tube inserted to various depths in the small hood. An aspirated thermocouple is placed at the entrance of the probe to monitor the gas temperature. The sample was first passed through a cold bath to be dried and then filtered to remove any particulate from the sample stream. The CO_2 and CO content of the sample was measured with an Anard Model 600 Infrared analyzer. The oxygen concenteration was monitored with a Beckman Paramagnetic analyzer and the amount of any remaining unburnt hydrocarbon were measured with a Beckman Model 400 Hydrocarbon analyzer. The location of the hot layer gas interface was determined by a shadow-graph technique and screens surrounding the large hood helped to suppress the disterbances in the ambient air. The large hood was used to remove continuously the hot gases spilled around the edges of the small hood. The experimental set up is shown in the schematic diagram of figure 2.

The fuel used in the experiment was city gas taken without processing from Souther California Gas Company mains. Methane with 0.924 mole fraction is its principle constituent and lower heating value is about 47.5 MJ/Kg. The burner had a diameter of 0.19 m and a 5 cm thick bed of glass beads of diameter 6.3 mm. No floor around the burner was used in this experiment.[1]

[1] B.M. Cetegen, E.E. Zukoski and T. Kubota, Entrainment and Flame Geometry of Fire Plumes, Report, Daniel and Florence Guggenheim Jet Propulsion Center,California Institute of Technology, Pasadena (1982)

Description

If complete combustion of methane into CO_2 and H_2O is achieved, then the measurement of the concentration of either CO_2 or excess O_2 will allow the calculation of the overall air-fuel ratio of the gas in the ceiling layer. The complete combustion of methane in the presence of x moles of excess air can be written as,

$$CH_4 + (2+x)[\ O_2 + 3.76N_2\ ] \longrightarrow CO_2 + 2\ H_2O + xO_2 + (2+x)\ N_2\ ;$$

then for dried products:

$$x = \frac{8.52\ Y_{O2}}{1 - 4.76\ Y_{O2}} \quad \text{or} \quad x = \frac{1 - 8.52\ Y_{CO2}}{4.76\ Y_{CO2}}$$

$$\phi = \frac{\text{Air-Fuel Ratio/ stoi.}}{\text{Air-Fuel Ratio}} = \frac{2}{2 + x}$$

Here Y_{O2} and Y_{CO2} are the measured mole fractions of O_2 and CO_2, respectively. ϕ is the equivalence ratio which represents the stoichiometric Air-Fuel ratio to the experimental value. However, our experiment deals with incomplete combustion in most cases and chemical formula is as following,

$$CH_4 + (2+x)\ [\ O_2 + 3.76\ N_2\ ] \longrightarrow M_{co}\,CO + M_{co_2}CO_2 + M_{o_2}O_2 + M_{H_2O}H_2O + M_{N_2}N_2 + M_c C + M_{H_2}H_2 + \ldots$$

where M is the mole concentration of that specie.
Because accurate quantitative measurements of H_2, N_2 and soot are very difficult, we have assumed that only CO, CO_2, O_2, CH_4 and H_2O can be present in our sample in addition to (2 + x) moles of N_2. Bowman, reference 2, showed that production of any nitric oxide is improbable in our situation. In other words, nitrogen does not enter into any significant chemical reaction.

Mole fractions of oxygen, carbon dioxide, carbon monoxide and unburnt hydrocarbons can be measured accurately in a conditioned, dried sample. Using conservation laws for moles of carbon in the sample, we can conclude that,

[2] G.T.Bowman: Article in Prog. Enrgy. Combust. Sci., 1975

$$\frac{1 - Y_{O2} - 8.52\,[\,Y_{CO2} + Y_{CO} + Y_{CH4}\,]}{3.76\,(\,Y_{CO2} + Y_{CO} + Y_{CH4}\,)} \doteq x$$

By knowing the amount of entrained air, x, equivalence ratio is found easily.

Two sets of experiments were performed and similar results were obtained in both cases. The interface height was fixed at 0.23 m in the first case. Temperature rose from 477°K for a 21 KW fire to 723°K for a 73.5 KW fire while the equivalence ratio increased from 0.21 to 0.75. Hydrocarbon and carbon monoxide mole fractions were negligible up to a 50 KW fire. Carbon dioxide rose continuously to 8.2% and became relatively steady at this level. All the recorded data for this experiment is presented in Table 1. At the same time, the sampling probe was moved up and down inside the hood. Temperature became higher as height increased and a linear profile existed. Ceiling layer gas seemed to be pretty well-mixed because mole fractions of different species stayed the same at various depths. No soot was observed until we reached the 70 KW fire at which point soot started to condense strongly.

For the second experiment, the interface height was reduced to 0.10 m . Because most of the excess air is entrained through the part of the plume which lies below the interface, the mass flux of air was decreased to about one half of the value for the first experiment. Theoretical heat release rates were increased from 10.5 KW to 126 KW, while temperature rose from 420°K to 630°K and became constant thereafter. Oxygen dropped to 0.6% at 84 KW and remained at 0.75% afterwards. Carbon dioxide profile was very similar to the first experiment's. Carbon monoxide and unburnt hydrocarbons' mole fractions had a jump at 35 KW and rose sharply. However, carbon monoxide reached a steady state at 84 KW and we were unable to investigate hydrocarbon levels any further because of our instrument limitation. Soot condensation started at 50 KW and became so dense that covered windows completely. An interesting phenomenon happened after 100KW. Small flamelets were ignited on the thin interface which drifted to the sides before getting extinguished. It reveals that a combustible mixture exists inside the hood and flamelets appear on the interface only, because small amounts of oxygen is mixed

through the interface. Complete data for this experiment is given in Table 2.

For each experiment average flame height and its variation was observed. All observations were made through Pyrex windows and eye estimates. The most significant feature of these flames is a periodic pulsation which consists of a roughly axisymmetric, ring-shaped, vortex like structure which rises through the flame. Eye averaged flame heights agreed closely with data given in reference 1. There is also strong agreement between our $\bar{Z}_{fl}$ vs. $Q_D^* = Q_f/\rho_\infty C_{P\infty} T_\infty \sqrt{gD}\, D^2$ curve and the one given in reference 1. Another feature of flames is that they became very spread out and dark yellow as the equivalence ratio became greater than 0.70. The reason is inefficient combustion and production of dense soot. Table 3 provides important flame geometry data.

Conclusions

We have found that a prominent feature of the flames studied here is the presence of large, regularly vortex-like structures in the flame. Below a critical value of equivalence ratio, $0.7<\phi_c<0.8$, temperature increased steadily with increasing fuel flow rates and soot and unburnt hydrocarbons production stayed at a negligible level. However, for equivalence ratios greater than 80%, soot became increasingly dense. Mole fractions of unburnt hydrocarbons and carbon monoxide rose sharply, too. At approximately stoichiometric ratio, temperature, oxygen level, carbon dioxide and carbon monoxide levels reached a steady state. Combustion is inefficient after $\phi = 0.8$ and a combustible mixture is formed at approximately twice the stoichiometric ratio.

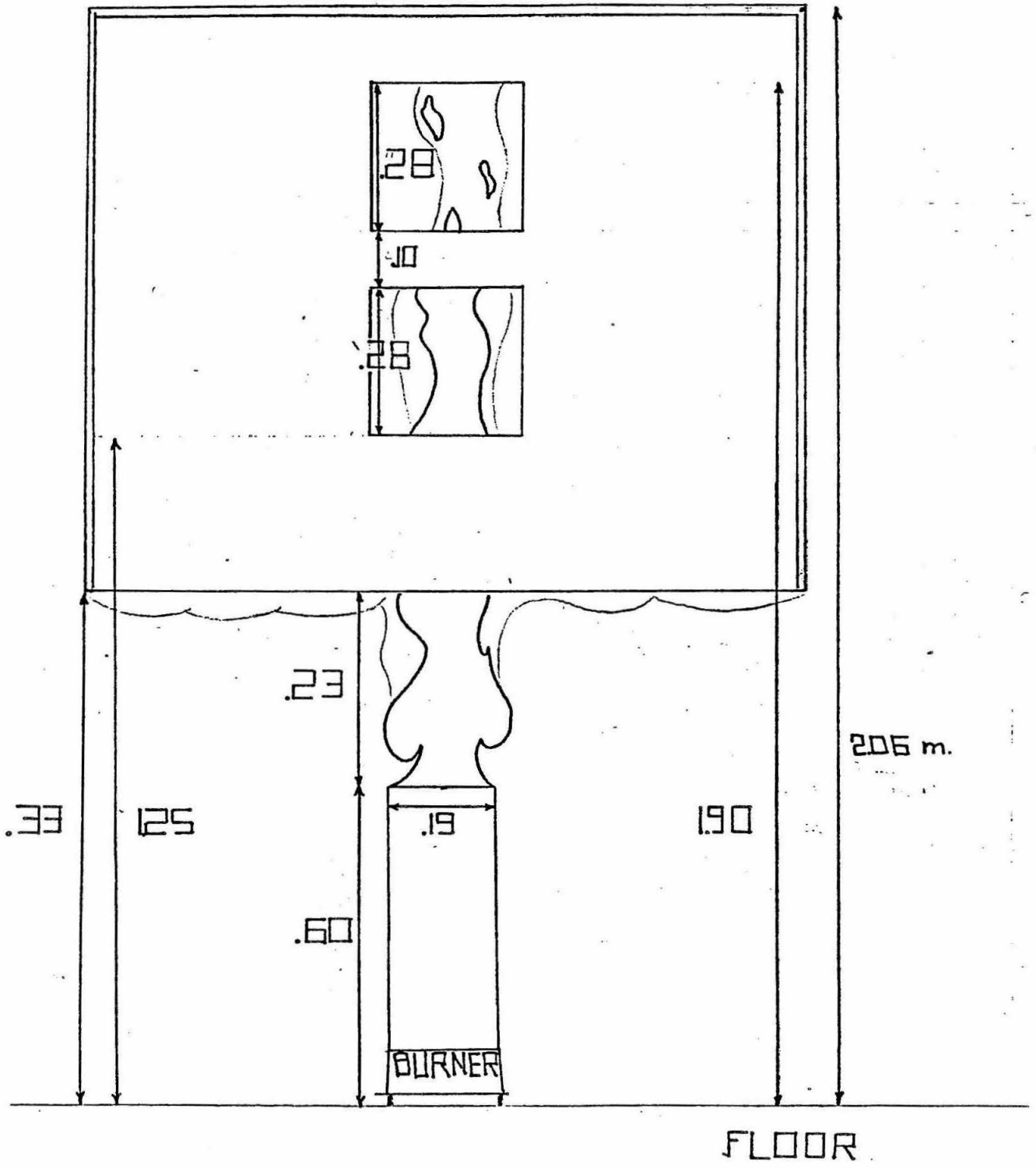

Figure 1

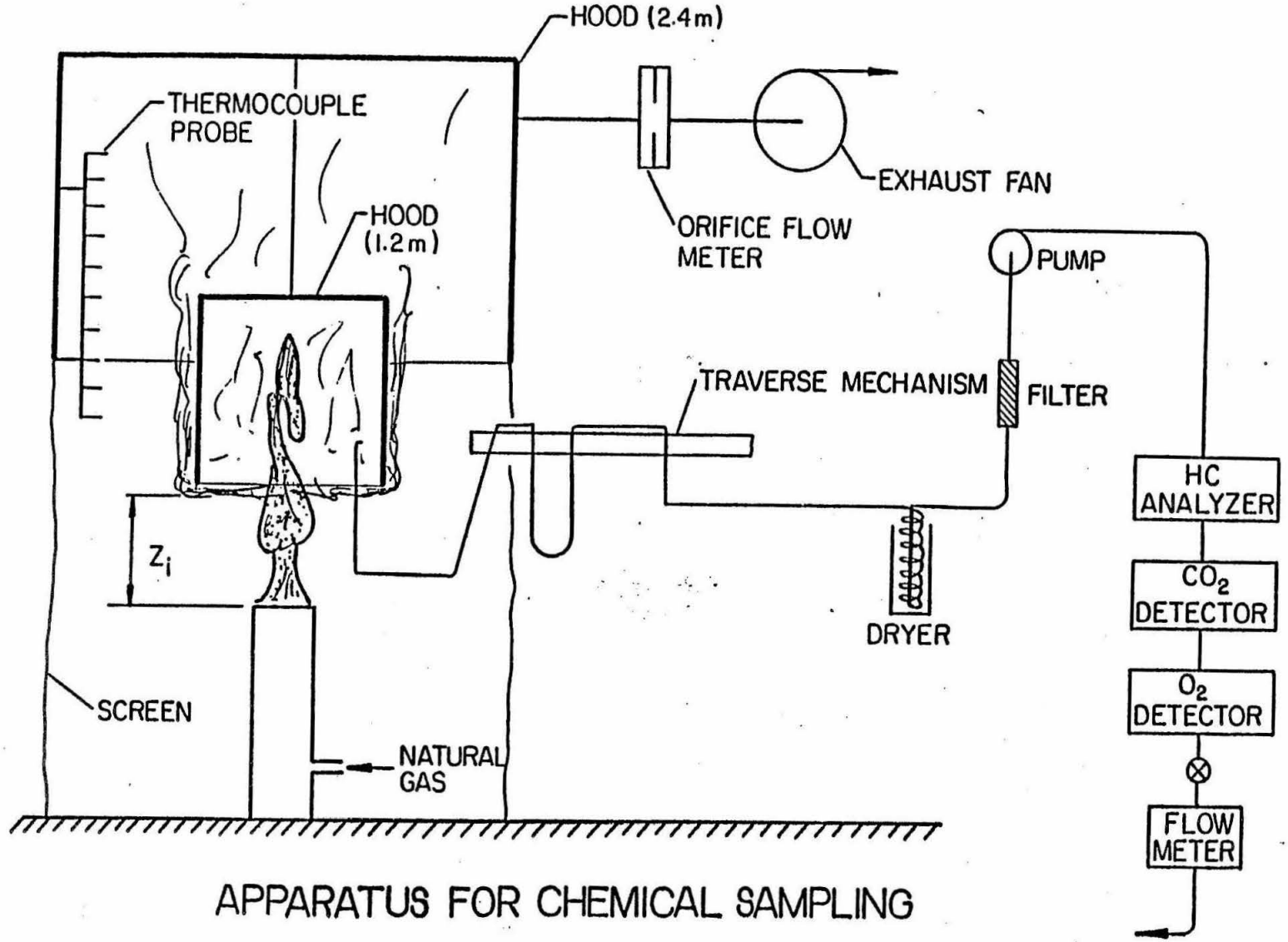

APPARATUS FOR CHEMICAL SAMPLING

Figure 2.

$\dot{Q}_f$ (KW)	T°K	Y_{O2}	Y_{CO2}	Y_{CO}	Y_{CH4}	x	ϕ	$\dot{m}_E$ (gr/sec)
21.0	477	16.8%	2.3%	Neg.	Neg.	7.35	0.21	35.0
42.0	598	12%	4.9%	Neg.	Neg.	2.51	0.44	33.3
52.5	658	9.5%	6.3%	750 PPM	90 PPM	1.50	0.57	32.1
63.0	707	6.8%	7.5%	.23%	200 PPM	0.93	0.68	32.0
73.5	723	4.6%	8.2%	.38%	400 PPM	0.68	0.75	34.0

Table 1. Data for experiment 1

$\dot{Q}_f$ KW	T°K	Y_{O2}	Y_{CO2}	Y_{CO}	Y_{CH4}	x	ϕ	$\dot{m}_E$ gr/sec
10.5	423	0.18	.021	Neg.	Neg.	8.1	.198	18.9
21.0	495	0.14	.038	Neg.	Neg.	3.75	0.35	21.4
31.5	564	0.09	.064	.0024	.002	1.27	0.61	17.9
42.0	606	0.05	.078	.0078	.0065	0.47	0.81	17.9
52.5	617	0.025	.081	.0130	0.030	-0.18	1.10	16.2
63.0	620	0.013	.082	.0155	>0.04	~-0.36	~1.2	~17.4
73.5	615	0.009	.081	.0166	-	-	-	-
84.0	619	0.007	.079	.0175	-	-	-	-
105.0	631	0.008	.078	.0170	-	-	-	-

Table 2. Data for experiment 2

	Exp. 2			Exp. 1			
$\dot{Q}_f$ KW	Z_f m	Z_f/D	Δ	Z_f m	Z_f/D	Δ	Q^*_D
* 10.5	0.44	2.31	0.38	0.21	1.10	-	0.60
21.0	0.55	2.89	0.41	0.41	2.17	0.23	1.20
31.5	0.79	4.16	0.53	0.61	3.24	-	1.80
42.0	0.90	4.74	0.64	0.79	4.16	0.38	2.40
52.5	0.97	5.10	-	0.97	5.11	-	3.0
63.0	1.02	5.37	-	1.10	5.78	0.51	3.60
73.5	1.10	5.79	-	1.23	6.47	-	4.20

Table 3. Flame Geometry Data

[*] Estimated by looking under the hood

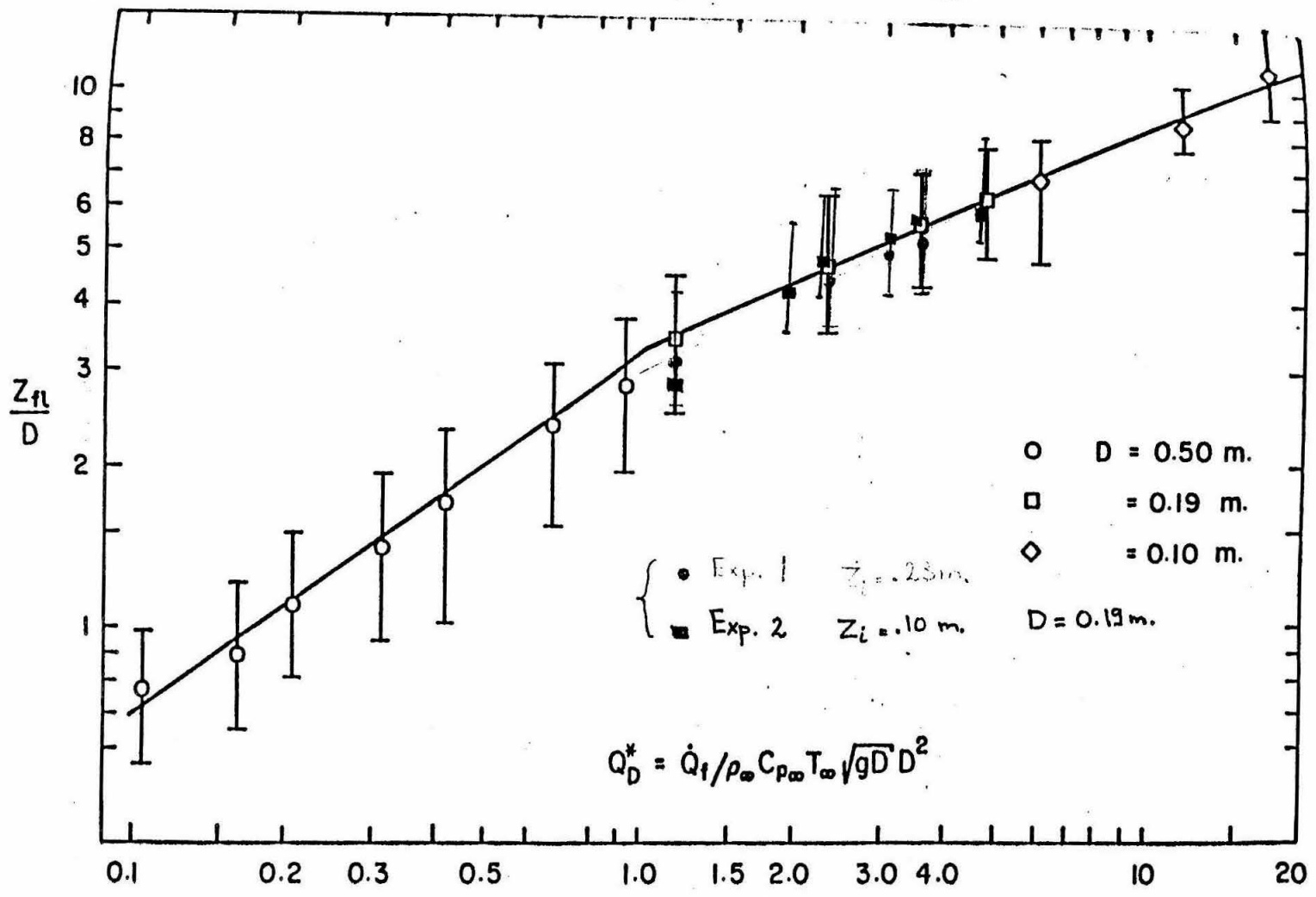

Figure (3.9) **Flame height correlation for 0.10, 0.19 and 0.50 m. diameter burners. The vertical bars indicate the size of the fluctuation heights.**

Taken From Reference 1.

PROGRESS TOWARDS THE STUDY OF PROTEIN MECHANISM VIA SITE-SPECIFIC MUTAGENESIS

Arlene P. Keller
Summer Undergraduate Research Fellowship Report
Summer 1982

Abstract: Specific changes in the beta-lactamase (penicillin-resistant) gene of the plasmid pBR322 have been made possible by site-directed mutagenesis. One mutant beta-lactamase has an inversion of residues 70 and 71, serine-threonine to threonine-serine, and is catalytically inactive. A revertant, with the dyad serine-70 and serine-71, shows a small percentage of the activity of the "wild-type" enzyme. Our efforts have been directed towards purification of the mutant enzymes for kinetic studies of their ability to bind penicillins and cephalosporins.

Introduction

Studies of the relationship between the amino acid sequence and the tertiary structure and function of a protein would be greatly facilitated by the ability to produce specific changes in specific residues of the sequence. Beta-lactamase provides a good system with which to develop this site-directed mutagenesis. Lactamase occurs in bacteria that will grow readily in simple laboratory media. In our case, the vector is E. coli and the enzyme is secreted after synthesis into the periplasmic space. This makes the enzyme relatively easy to isolate. Purification is aided by the simplicity and specificity of the assays available. Another very important reason for studying lactamase is its relevance to medicine.

This enzyme has caused a number of medical problems through its ability to degrade penicillins. Lactamase is known to hydrolyze the lactam ring in penicillin, probably via an acyl-enzyme intermediate, but the mechanism is not yet fully understood. Site-directed mutagenesis may provide some insight into the mechanism.

Three beta-lactamase mutants have been made by the method described by Dalbadie-McFarland et al. The active site of lactamase is thought to contain the conserved residues serine-70 and threonine-71. Alteration of these residues would be a test of their mechanistic role. Accordingly, the two residues were inverted to form a catalytically inactive mutant with thr-70 and ser-71. Two other mutants, one with ser-70-ser-71 and one with thr-70-thr-71, have also been produced. The latter is inactive but the former has a small percentage of the activity of the "wild-type" lactamase. Apparently the secondary hydroxyl group of the thr cannot substitute for the primary hydroxyl group of ser. This may be because of steric hindrance or because of conformational changes within the active site. The latter possibility suggests studies of the penicillin-binding activity of the mutant lactamase. Our efforts this summer have been directed to that end.

Presentation and Discussion of Results

The first step towards penicillin-binding studies was to obtain pure mutant enzyme. The purification of the ser-70-ser-71 mutant could be followed readily by standard assays, since it was catalytically active. However, a different method was needed

for the inactive mutants.

The E. coli strain LS1 with the plasmid pBR322 encoding the "wild-type" beta-lactamase was grown in a large scale (12-liter) fermentor at 37°C. The resulting cells were washed with 50 mM Tris-HCl buffer pH 7.0 and placed in a hyperosmotic sucrose solution. After centrifugation, the pellets were re-suspended in cold de-ionized water, spun down once again and the supernatant retained. The sucrose solution caused the bacterial cell membrane to collapse under osmotic pressure; the de-ionized water then caused the membrane to expand to the cell wall, pushing the periplasmic proteins out of the cell. The cell wall thus acted as a crude filter, letting the lactamase out yet retaining most of the cellular components.

The supernatant was purified by an ammonium sulfate procedure; then the ammonium sulfate was dialyzed out. The resulting solution, now concentrated to 50 ml, was purified further on a 20-cm DEAE-cellulose column. The lactamase was eluted by means of a gradient of increasing buffer concentration, from 25 mM to 200 mM TEA-Cl buffer pH 7.25. The fractions were assayed for activity with a standard assay: 2.0 ml de-ionized water, 0.2 ml 1M potassium-phosphate buffer pH 7.0, and 0.05 ml 50 mM benzyl-penicillin per cuvette, at 30°C and 240 nm. The fractions showed activity, so they will be checked for purity by SDS-acrylamide gel electrophoresis. The fractions will be pooled and concentrated and purified further. The pure "wild-type" beta-lactamase will be injected into rabbits. The resulting antibody,

although directed against the "wild-type" lactamase, should cross-react quite well with the mutant lactamases. Once the antibody-containing serum is obtained, the inactive mutants can be traced throughout the purification procedure.

Purification of the ser-70-ser-71 mutant (R4) would appear to be easier, since the lactamase can be traced directly by its activity. The procedures carried out on R4 have been the same as for the "wild-type" lactamase. E. coli with the mutant plasmid pBR322 was grown in a 1-liter flask at 37°C, from a 0.05 ml inoculum of concentrated freezer stock. The 12-liter fermentor was then inoculated with 30 ml from the 1-liter flask.

The contents of the 1-liter flask were subjected to the osmotic extrusion process described above; and the supernatant displayed activity. We did not have the same success with the large-scale growths, however. A number of the 12-liter growths have been attempted, and only one has shown activity after osmotic extrusion. (That one was lost by accident.) Various conditions have been tried: different growing times, stirring rates, amounts of air, even different 12-liter fermentors, but to no avail. Two of the inactive R4 supernatants have been put through the ammonium sulfate purification, on the chance that an impurity in the supernatant might have been inhibiting the already small activity. But there was still no activity after the purification. One batch was grown with PMSF (phenyl methane sulfonyl fluoride) to discourage any possible proteolysis of the lactamase, but this was unsuccessful as well.

One explanation might be that the mutant enzymes are not

secreted properly into the periplasmic space of the E. coli. If this is so, the osmotic extrusion procedure would not work. Another answer may lie with the temperature at which the bacteria are grown. The usual temperature is 37°C. However, osmotic extrusion of a 1-liter flask of R4 grown at 30°C produced a supernatant which had a significantly higher specifiec activity than one grown at 37°C. This would seem to suggest that the mutant enzyme is less stable than the "wild-type" lactamase.

Conclusions

It is difficult to draw conclusions at this point, since the summer has been devoted to mere purification procedures. The kinetic studies that were the initial aim of the project will have to be done later. The failure of the R4 mutant to produce activity in large-scale growths is a baffling and frustrating puzzle; but temperature-dependence may soon prove to be the answer. The catalytically inactive mutants can be purified by the method described above. The kinetic studies will be done soon enough. Despite some setbacks this summer, the technique of site-directed mutagenesis holds great promise.

References

Dalbadie-McFarland, G.,Cohen, L.W.,Riggs, A.D., Morin, C., Itakura, K., and Richards, J.H. (Unpublished) "Oligonucleotide-Directed Mutagenesis as a General and Powerful Method for Studies of Protein Function".

Dale, J.W. and Ambler, R.P. (1979) Beta-Lactamases, eds. Hamilton-Miller, J.M.T. & Smith, J.T. (Academic Press, London) pp. 73-125.

MICHAEL KILBY

No Report Submitted

THE OXIDATION EFFECTS ON THE ELECTRICAL PROPERTIES OF $NiSi_2$ AND $CoSi_2$ ON Si AND SiO_2 SUBSTRATES

Sung Joon Kim
Electrical Engineering Department
California Institute of Technology
Pasadena, California 91125

Abstract

The oxidation effects on the electrical properties of $NiSi_2$ and $CoSi_2$ on Si and SiO_2 substrates were studied as functions of SiO_2 thickness grown on the silicide, the SiO_2 growth conditions and the types of Si-substrate used to grow the silicides. The resistivity of the silicide changed more drastically for dry oxidized silicide than wet oxidized silicide as the SiO_2 layer grows. For SiO_2 up to 2000 Å on wet oxidized $CoSi_2$ there is no change in resistivity. The carrier type of silicide and resistivity changes as the silicide phase changes when the substrate is SiO_2.

Introduction

Metal silicides are investigated as a possible material for VLSI circuit interconnects. As the silicon integrated circuits packing density increases, the line widths shrink but the total interconnection lengths on a chip grow longer. As a result, the sheet resistance contribution to the RC gate delays increases. Thus it is very important to use low resistivity material for interconnects in IC's. To retain compatibility with existing poly-Si gate technology, the material should be easily oxidized and form an SiO_2 layer. Silicides have shown to meet these requirement. Besides oxidizability, stability during oxidation is also very important.

In this paper, I try to investigate the electrical stability of the silicides as a function of SiO_2 grown on top of it. Specifically, I try to analyse the resistivity and carrier type of $NiSi_2$, $CoSi_2$ and other Co and Ni silicides as a function of SiO_2 thickness grown on it, the SiO_2 growth conditions and the type of substrate used to grow the silicide. I chose $NiSi_2$ and $CoSi_2$ because these silicides have a resistivity of only 40-60 uΩ.cm and 8-15 uΩ.cm respectively compared to 400 uΩ.cm for highly doped-Si as is currently used in the industry. Recently it was found [1,2] that an oxide layer can be thermally grown on these silicides, thus making it very attractive material for VLSI circuit.

When one grows an oxide layer on top of $NiSi_2$ and $CoSi_2$ on a Si substrate, one observes that the growth of the SiO_2 layer is

independent on the crystalline structure (epitaxial or polycrystalline) or the thickness of the $NiSi_2$ and $CoSi_2$ layer, suggesting that the oxidation mechanism is dominated by oxygen diffusion through SiO_2 layer and forming SiO_2 at the $NiSi_2/SiO_2$ and $CoSi_2/SiO_2$ interface [1,2]. New $NiSi_2$ and $CoSi_2$ is continuously formed at the $Si/NiSi_2$ and $Si/CoSi_2$ interface respectively as the SiO_2 layer grows at the surface. It is possible that the changes in the $NiSi_2$ and $CoSi_2$ layer can affect the resistivity of silicide, which is an important factor in IC. The investigation of silicide oxidation when the substrate is inert as a function of SiO_2 thickness is also important one. Since the nature of the silicide compound structure changes as a function of SiO_2 thickness (we deplete the Si content in the SiO_2), its electrical properties such as resistivity and carrier type and its concentration also changes, thus making SiO_2 growth an important factor in changing the silicide structure.

Presentation and Discussion of Results

The samples used for the experiments were N-type (111) silicon wafer of resistivity 5-40 Ωcm and thickness of ~250 um, P-type (111) silicon wafer of 5-30 Ωcm and ~285 um, and N-type (111) silicon wafer with SiO_2 layer grown on top of it. These three types of substrates were ultrasonically cleaned by TCE, acetone and methanol. Then the substrate with SiO_2 layer was blown dried with N_2 and for other substrates the oxide layer were grown

by the solution of $H_2O;H_2O_2;NH_4OH$. Then after etching the oxides in a dilute HF solution, all three types of substrates were introduced to e^- -beam evaporation system.

For N and P types of substrates, thick and thin Ni and Co film of 720 Å$\pm$ 70 Å and 290 Å$\pm$ 30 Å were deposited in each type of substrate in the pressure of the system of $\sim 5\times10^{-8}$ torr. For SiO_2 grown N-type substrate, thick and thin films of Si/Ni and of Si/Co films of 3000 Å/708 Å and 1400 Å/283 Å were deposited in a similar evaporation condition. The substrates deposited with Ni and Si/Ni were gradually annealed from starting temperature of 450°C to a slowly rising temperature of 880°C for 20 minutes at the vacuum of 7×10^{-7} torr, thus forming $NiSi_2$. The substrates with Co and Si/Co were annealed at constant temperature of 850°C for 15 minutes at similar vacuum condition, thus forming $CoSi_2$(see fig. 1). These samples were then all cut into 1 cm by 1 cm. Then all these samples were oxidized for different amount of time for various oxide thickness in wet and dry condition and after that oxide layers were etched off by H_2O;HF (6;1). From previous experience, the oxides with different thickness on substrates were removed by time controlled etching. During etching HF reacted with silicides thus making it hard to make the appropriate electrical measurement. Thus we etched only 4 points in the substrate using mask, decreasing the whole substrate reaction with HF and only exposing minimum silicide area for electrical measurement. Then we soldered these silicide exposed places with indium and applied high electric field using tesla coil for better contact (see fig.2), thus we increased the contact area

in the substrate for better electrical measurement by Van der Pauw method[3], (see fig. 3).

In this experiment, the oxide and silicide thickness and its atomic thickness were measured using 2 Mev alpha particle backscattering spectroscopy. The phase and lattice structure of the silicide compounds were analysed using X-ray diffraction. The Van der Pauw method was used in measuring the sheet resistance,and the carrier type and concentration (see fig. 3).

Experiment #1

N and P type substrates with thick and thin $NiSi_2$ were oxidized in dry condition at 900°C and in wet condition at 1100°C. Since $NiSi_2$ melts at 993°C, in wet oxidation we obtained some other silicide besides $NiSi_2$, thus making irrelevant to make investigation on wet oxidized $NiSi_2$ (see fig. 5).

For dry oxidation, we oxidized the samples for ~1000 Å through 4000 Å. The thickness of the SiO_2 were controlled by fitting the kinetics of the reaction into the following equation; $d^2=K_o \exp(-E_a/kT)t$, where t is the growth time, d is the SiO_2 thickness, E_a is the activation energy, k is the Boltzmann constant, T is the absolute temperature, and K_o is a proportionality constant related to the physical properties of the oxidizing species and the structure of the oxide. In case of $NiSi_2$ dry oxidation K_o is 9.4×10^{11} $Å^2 hr.^{-1}$ and E_a is $1.5 \pm .1$ ev [1].

Virgin $NiSi_2$ on N type substrate shown to have very low resistivity of 4-10 uΩcm, and was constant as SiO_2 layer was grown on it. The carrier was electrons. These facts contradicts with the

known data from literature, where virgin $NiSi_2$ without SiO_2 layer grown on it had resistivity of 30-40 uΩ.cm and the carrier was holes. Thus the electrical properties of $NiSi_2$ on N-type substrate with low resistivity in function of SiO_2 layer grown on it needs further careful investigation (see fig. 6).

$NiSi_2$ on P-type substrate without SiO_2 layer had compatible resistivity of ∿33 uΩ.cm with known data from literature. The carrier was also shown to be holes. The resistivity of thin silicide climbed up immediately but stabilizing after ∿2000 Å of SiO_2. The resistivity of thick silicide also climbed up but it did not rise as much as the thin silicide. We suspect from the data and from backscattering spectroscopy that interface between $NiSi_2$ and Si is not distinct and that especially in thin silicide we do not have all $NiSi_2$ compound but some other mixture of compound (see fig. 7).

Experiment #2

SiO_2 layers were grown on thick and thin $CoSi_2$ on N and P type of substrates in dry and wet conditions. Since the kinetics of SiO_2 growth on $CoSi_2$ is the same as that of SiO_2 growth on $NiSi_2$ the oxide thickness growth were controlled by the following equation; $d^2=K_o\exp(-E_a/kT)t$, where $K_o=2.63\times10^{11}$ $Å^2hr.^{-1}$ and $E_a=1.05\pm.05$ev for wet oxidation and for dry oxidation we used $K_o=3.54\times10^{11}$ $Å^2hr.^{-1}$ and $E_a=1.39\pm.05$ ev[2]. The temperature for dry and wet oxidations were 900° C and 1100° C respectively.

All the $CoSi_2$ without SiO_2 grown on top of it had resistivity of 9-14 uΩ.cm with holes as the carrier type which is compatible with the known $CoSi_2$ resistivity from other literature. In general the resistivity of silicides with SiO_2 grown in wet condi-

tion were much lower and constant than the silicides with SiO_2 grown in dry condition as the SiO_2 thickness grows up. Thick silicide samples had lower resistivity than thin samples, and also in general silicide grown on P-type seemed to have lower resistivity than on N-type as the SiO_2 layer grows up, and it is interesting to note that the carrier type in these silicides were all holes. Thus we suspect that there was a substrate effect in the resistivity measurement, so possibility that we have been measuring parallel resistance of $CoSi_2$ and the substrate needs further investigation (see fig. 8,9).

Experiment #3

On SiO_2 grown N-type substrate, thick and thin films of Si/Ni were deposited and annealed to form initially si-rich $NiSi_2$ (see fig. 1). As we grow SiO_2 layer as in experiment #1 on silicide for up to 4000 Å for thin silicide and 7000 Å for thick silicide, we observed phase changes of silicides accompanied by carrier type and resistivity changes. From X-ray analysis, backscattering spectra and from Si to Ni atomic concentration ratio calculation, we observed that the Si-rich silicide had holes for carrier type while Ni-rich silicide had electrons for carrier. And also resistivity were higher for Si-rich silicide than Ni-rich silicide (see fig. 10, 11).

Experiment #4

Similarly to experiment #3, Co/Si thick and thin films were deposited on SiO_2 grown N-type substrate, then annealed to form initially Si-rich $CoSi_2$ (see fig. 12, 13). As we grew SiO_2 layer as in experiment #2 we observed phase changes of silicides with carrier type and resistivity changes. The thin Si-rich silicide had

low resistivity with holes as the carrier, but as the $CoSi_2$ started to change into CoSi phase, the resistivity started climb up sharply but as the silicide becomes to Co-rich silicide the resistivity went down sharply and the carrier became to electrons. Similar phenomena happened to thick Co-rich silicide but it needs further investigation by growing thicker SiO_2 to insure that the formation of Co-rich silicide will cause lower resistivity.

Conclusions

1. The resistivity of $NiSi_2$ generally increases as SiO_2 layer thickness grown on it increases.
2. The carrier type for all $CoSi_2$ and $NiSi_2$ on P-type substrate remained as holes as the SiO_2 grew up.
3. The carrier type for $NiSi_2$ on N-type (111) silicon wafer of resistivity 5-40 Ω.cm and thickness of $\sim$250 um, was shown to be electrons and had unusually low resistivity compared to known data, thus it needs further investigation.
4. Dry oxidation produced higher and non-constant $CoSi_2$ resistivity than wet oxidation.
5. The phase change of Ni silicides and Co silicides were accompanied by carrier type and resistivity changes.
6. When there was carrier type change accompanied by phase change, there were drastic resistivity changes.

References

[1] M. Bartur and M-A. Nicolet, Appl. Phys. Lett.40(2) (1982).

[2] M. Bartur and M-A. Nicolet, Thermal Oxidation of $CoSi_2$, Appl. Phys. Lett. (accepted 1982).

[3] K. Seeger, Semiconductor Physics, (Springer - Verlag, Wien-New York, 1973), p.485.

[4] W.K.Chu, J.W.Mayer, and M-A. Nicolet, Backscattering Spectroscopy (Academic, New York, 1978).

[5] B.D. Cullity, Elements of X-ray Diffraction (1978).

Figures

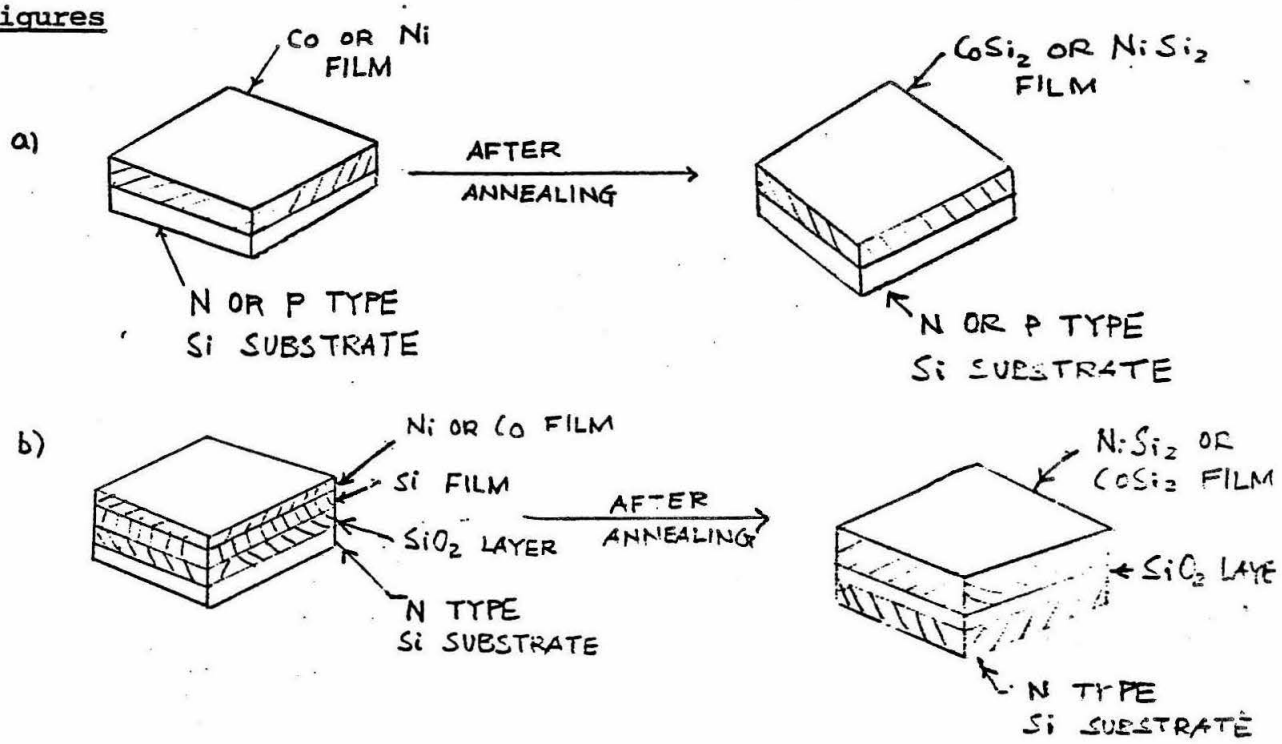

FIG. 1

a) FORMATION OF $CoSi_2$ AND $NiSi_2$ ON N OR P Si SUBSTRATE.

b) FORMATION OF $CoSi_2$ AND $NiSi_2$ ON SiO_2/Si SUBSTRATE

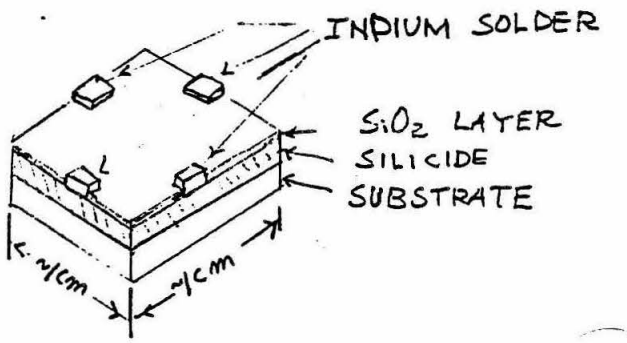

FIG. 2. SAMPLE AFTER OXIDATION, ETCHING AND SOLDERING WITH INDIUM.

Figures

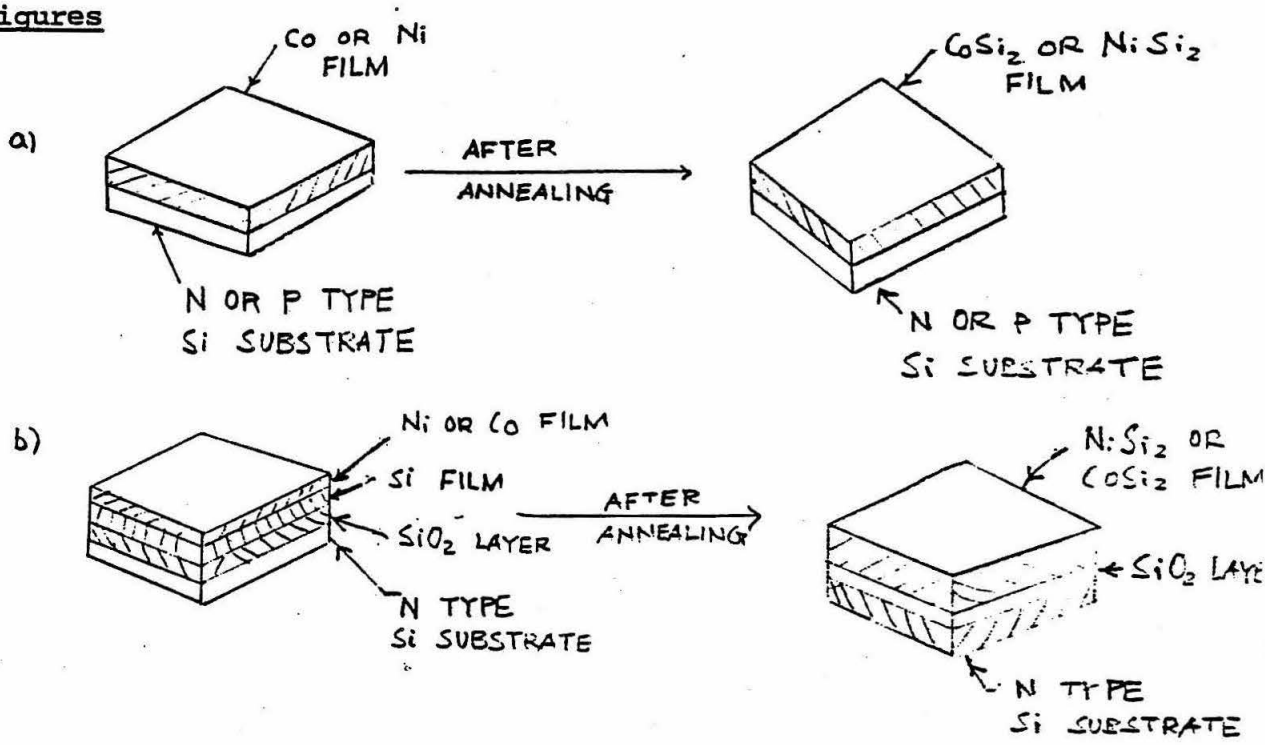

FIG. 1

a) FORMATION OF $CoSi_2$ AND $NiSi_2$ ON N OR P Si SUBSTRATE.

b) FORMATION OF $CoSi_2$ AND $NiSi_2$ ON SiO_2/Si SUBSTRATE

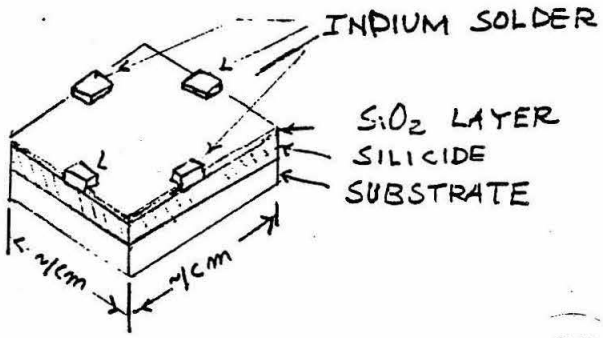

FIG. 2. SAMPLE AFTER OXIDATION, ETCHING AND SOLDERING WITH INDIUM.

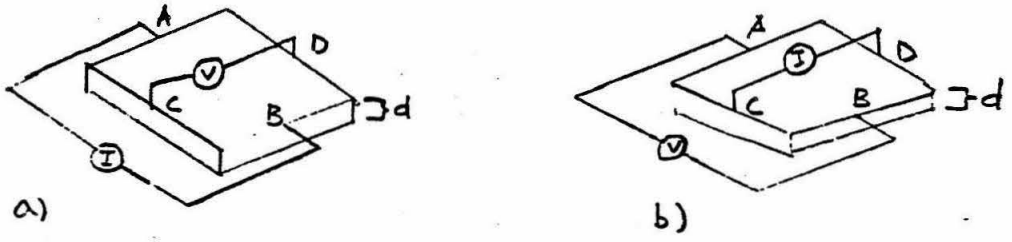

FIG. 3. VAN DER PAUW METHOD FOR RESISTIVITY MEASUREMENT.

FROM a) $R_{AB,CD} = \frac{|V_{CD}|}{I_{AB}}$ FROM b) $R_{BC,DA} = \frac{|V_{DA}|}{I_{BC}}$.

FROM a) AND b) VAN DER PAUW PROVED THAT;

$$\exp\left(-\pi \frac{d}{\rho} R_{AB;CD}\right) + \exp\left(-\pi \frac{d}{\rho} R_{BC;DA}\right) = 1$$

FROM ABOVE WE GET THE RESISTIVITY:

$$\rho = \frac{\pi}{\ln 2} d \cdot \frac{R_{AB,CD} + R_{BC,DA}}{2} f \quad \text{WHERE}$$

f SOLVES THE FOLLOWING TRANSCENDENTAL EQUATION

$$\cosh\left\{\frac{\ln 2}{f} \cdot \frac{(R_{AB,CD}/R_{BC,DA})^{-1}}{(R_{AB,CD}/R_{BC,DA})^{+1}}\right\} = \frac{1}{2}\exp\left(\frac{\ln 2}{f}\right)$$

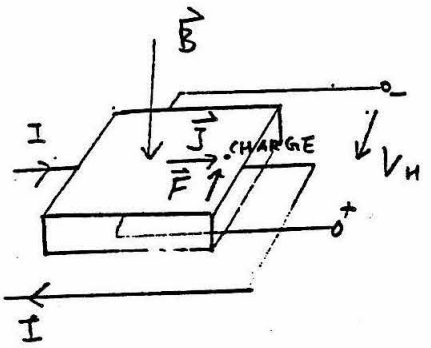

$$\vec{F} = \vec{J} \times \vec{B}$$

FIG 4. PRINCIPLE OF CARRIER TYPE (HALL) MEASUREMENT
IF ELECTRON IS THE CARRIER THEN V_H IS POSITIVE
IF HOLE IS THE CARRIER THEN V_H IS NEGATIVE

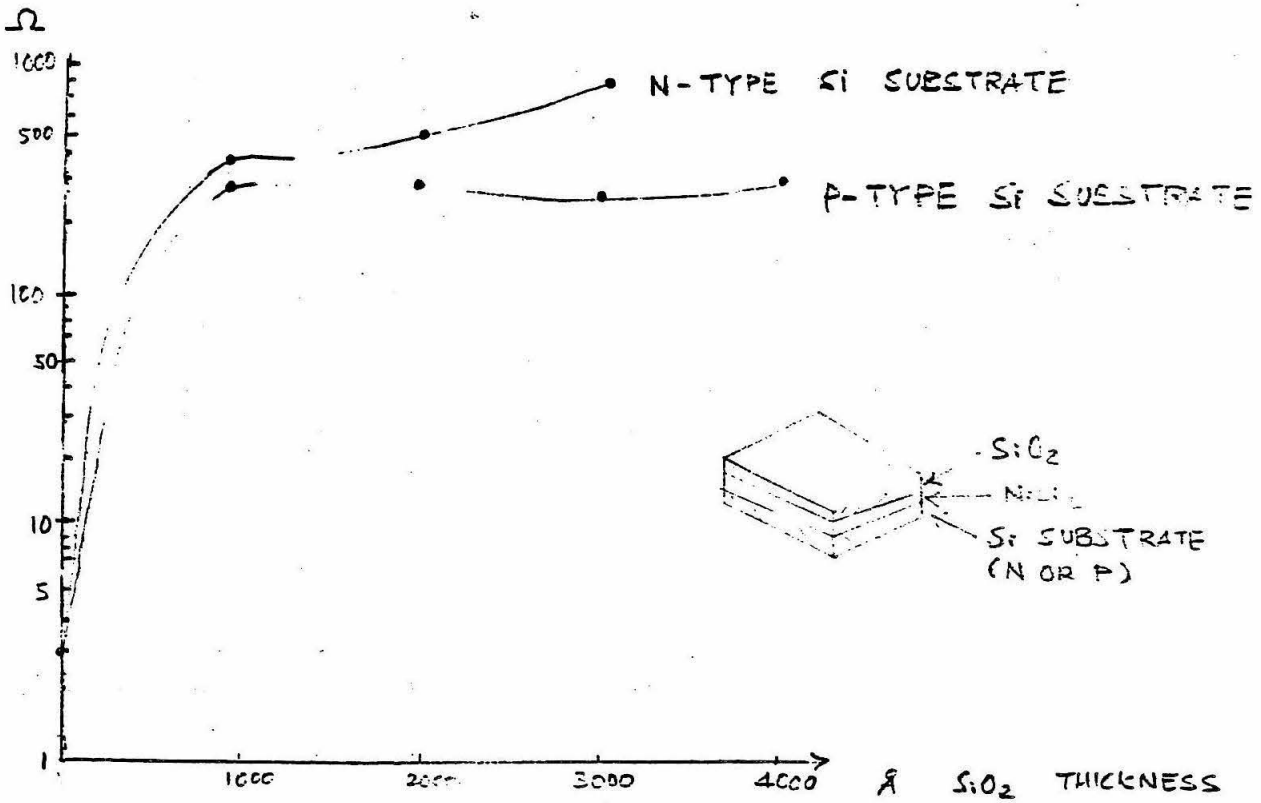

FIG 5. a) SHEET RESISTANCE VS. SiO_2 THICKNESS OF WET OXIDIZED THIN $NiSi_2$

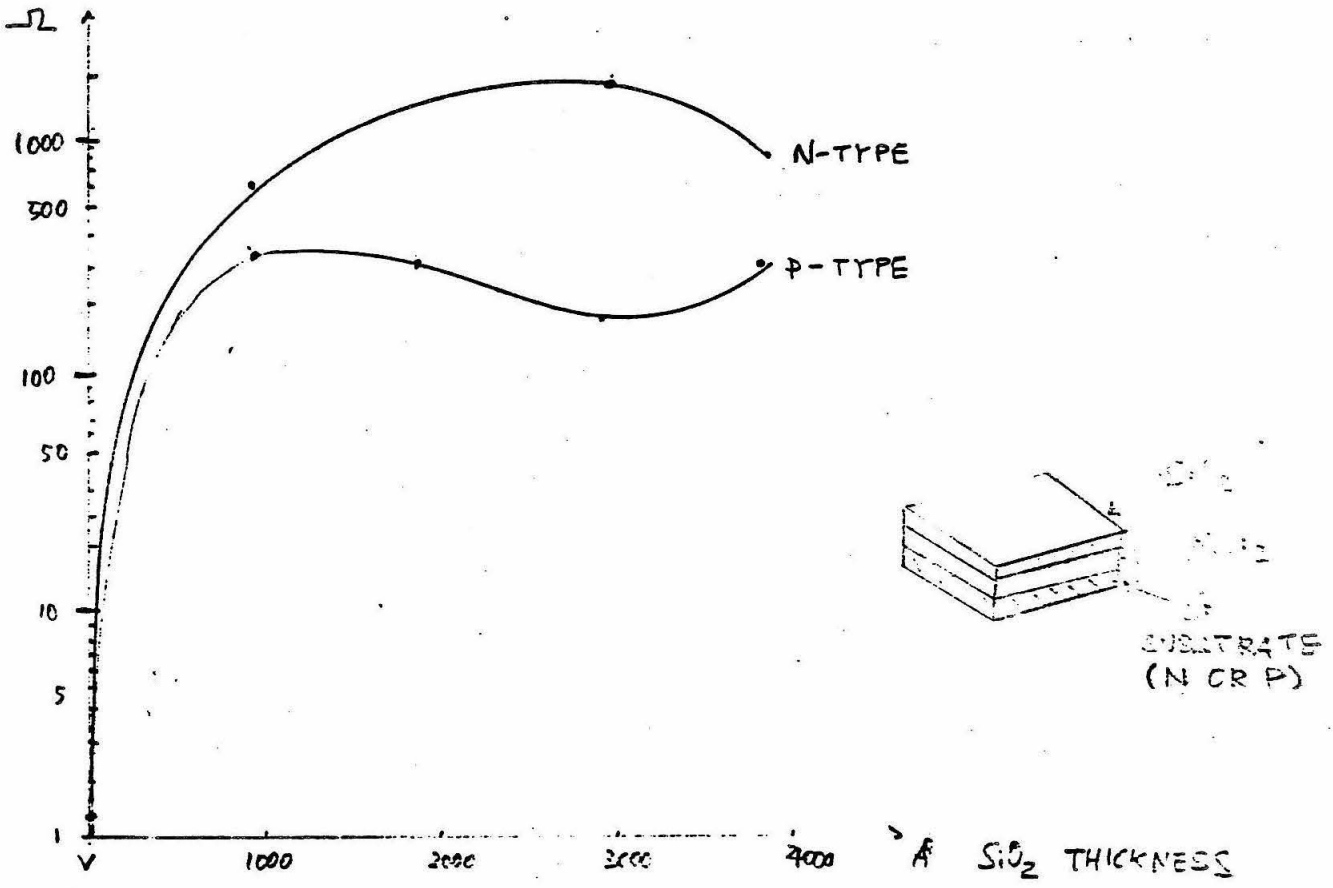

FIG 5. b) SHEET RESISTANCE VS SiO_2 THICKNESS OF WET OXIDIZED THICK Ni_2Si.

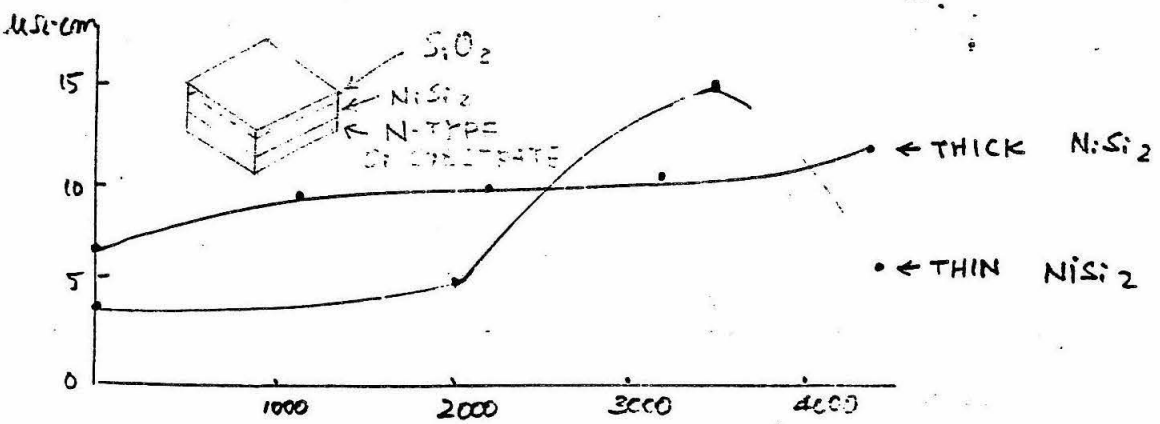

FIG 6. RESISTIVITY VS. SiO_2 THICKNESS OF DRY OXIDIZED Ni_2Si ON N-TYPE Si SUBSTRATE.

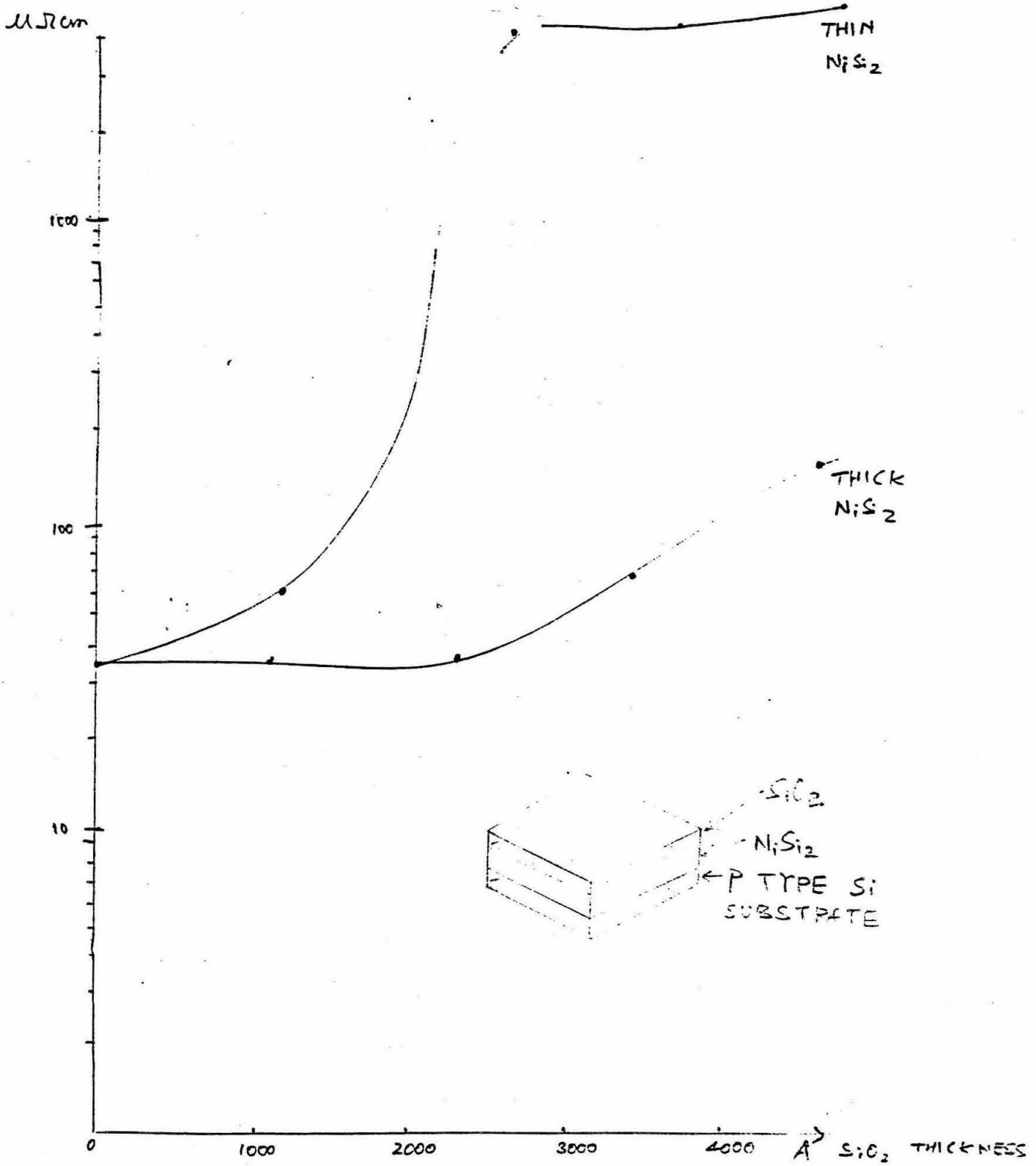

FIG. 7. RESISTIVITY VS. SiO_2 THICKNESS OF DRY OXIDIZED $NiSi_2$ ON P-TYPE Si SUBSTRATE.

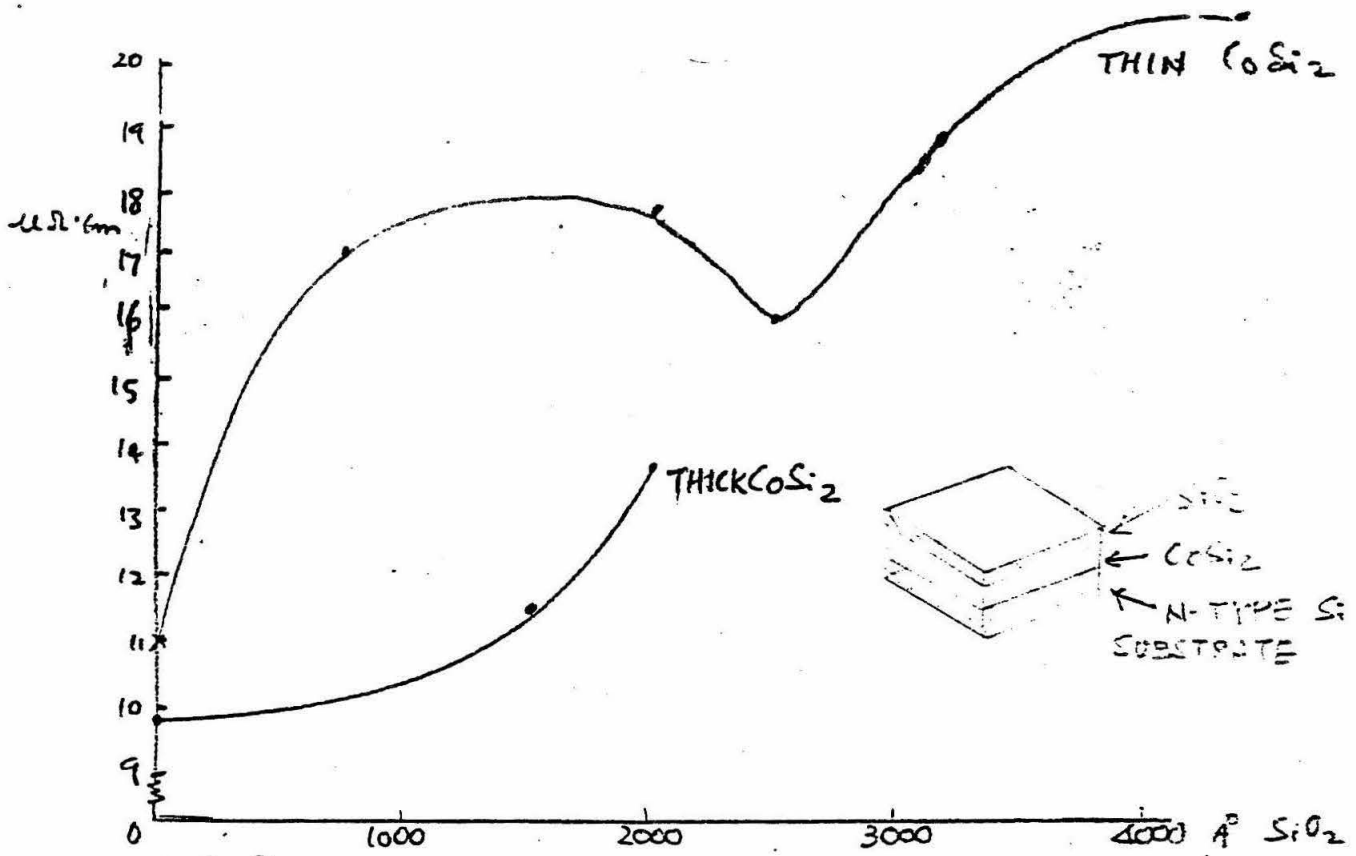

FIG 8. a) RESISTIVITY VS. SiO_2 THICKNESS OF WET OXIDIZED $CoSi_2$ ON N-TYPE Si SUBSTRATE

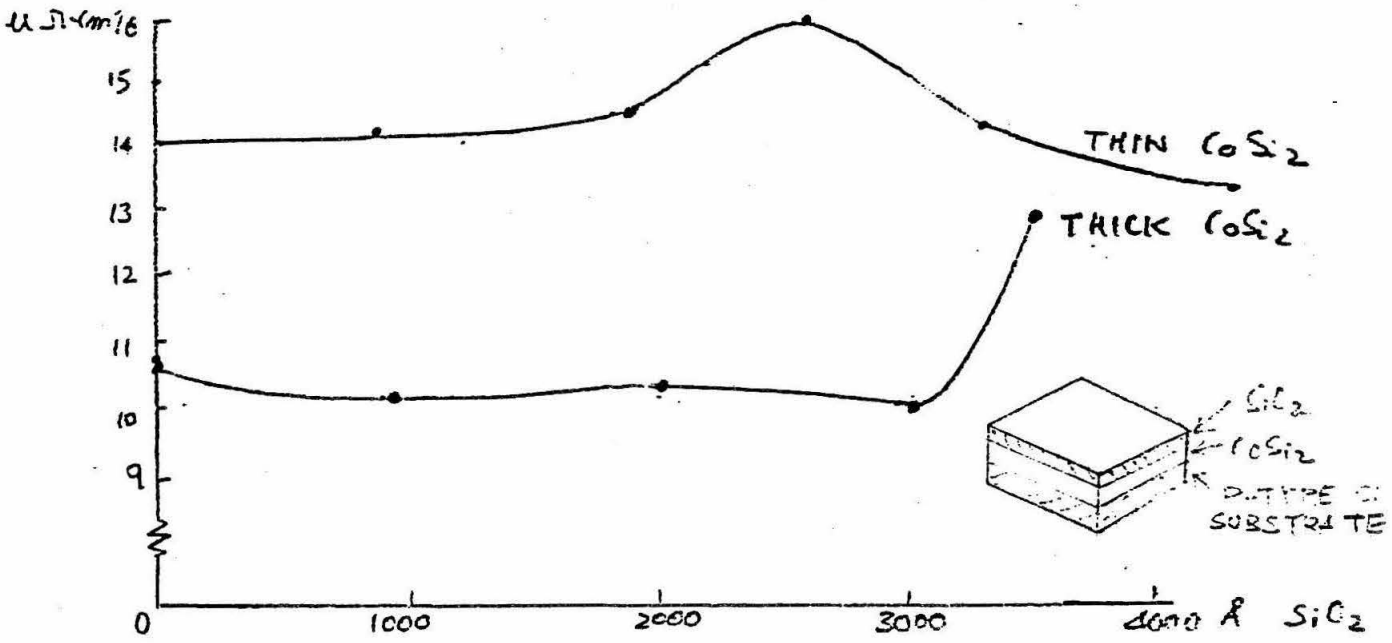

FIG 8. b) RESISTIVITY VS. SiO_2 THICKNESS OF WET OXIDIZED $CoSi_2$ ON P-TYPE Si SUBSTRATE

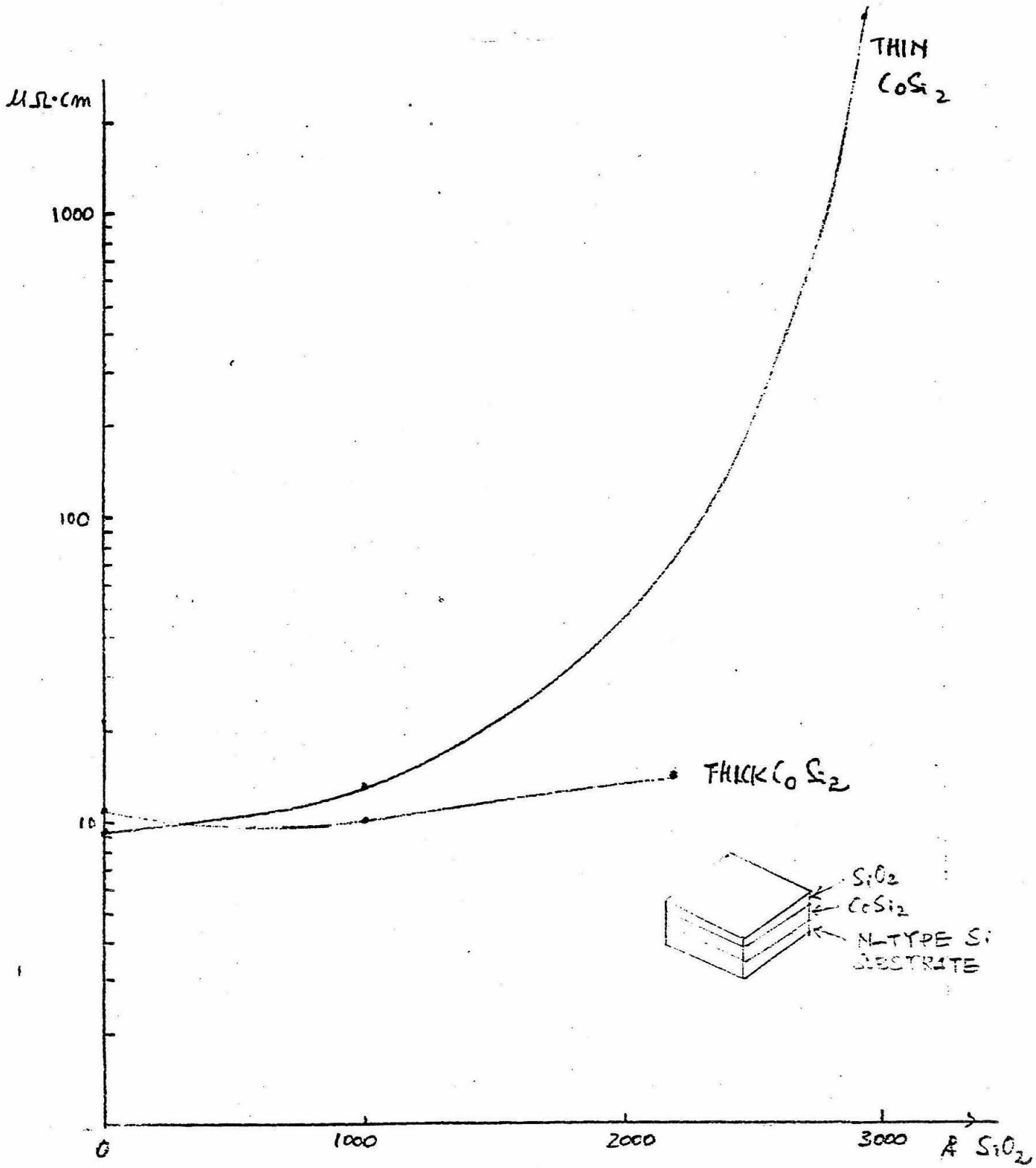

FIG 9.a) RESISTIVITY VS. SiO_2 THICKNESS OF DRY OXIDIZED $CoSi_2$ ON N-TYPE Si SUBSTRATE

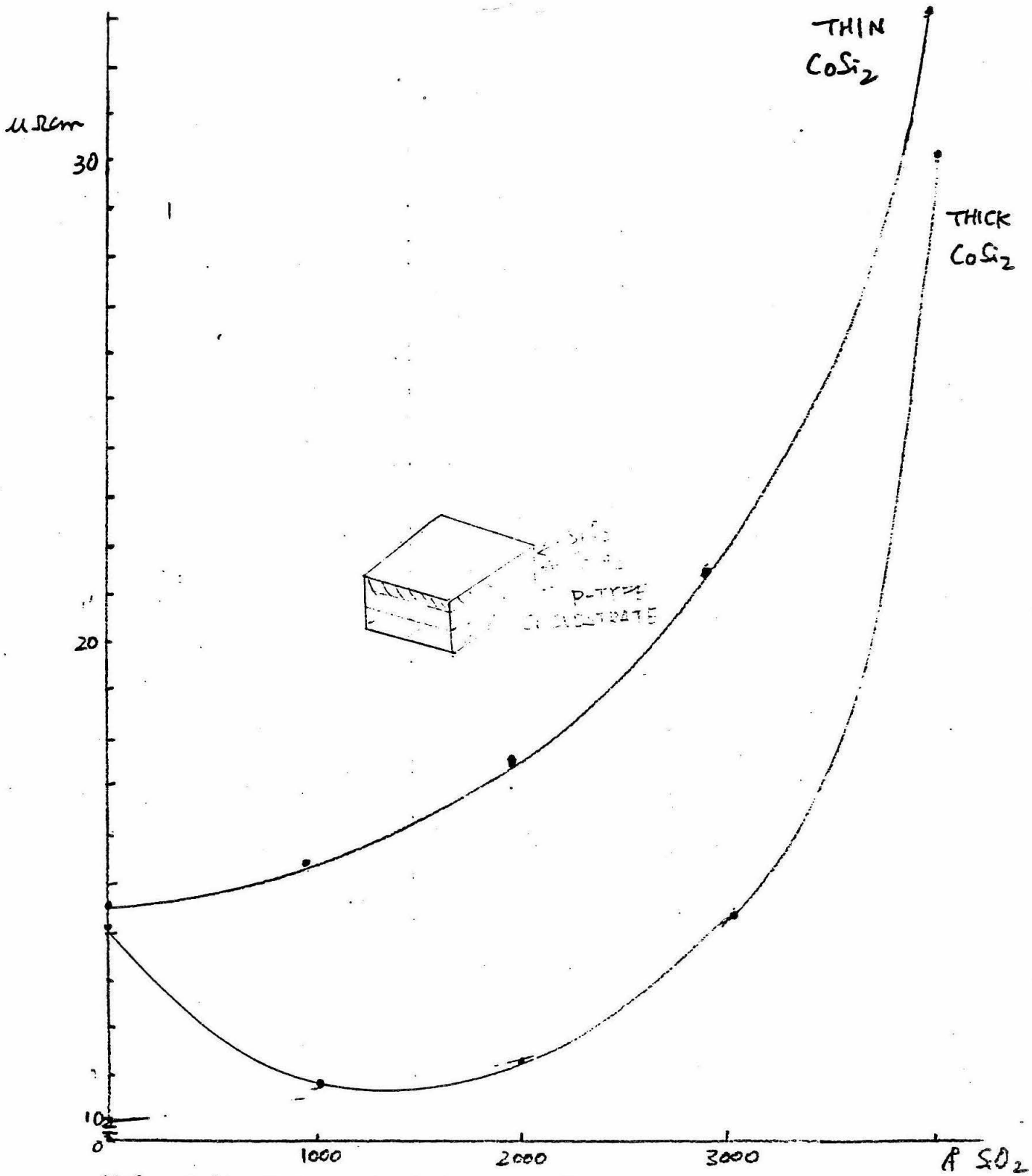

FIG. 9.6) RESISTIVITY VS. SiO_2 THICKNESS OF DRY OXIDIZED $CoSi_2$ ON P-TYPE Si SUBSTRATE

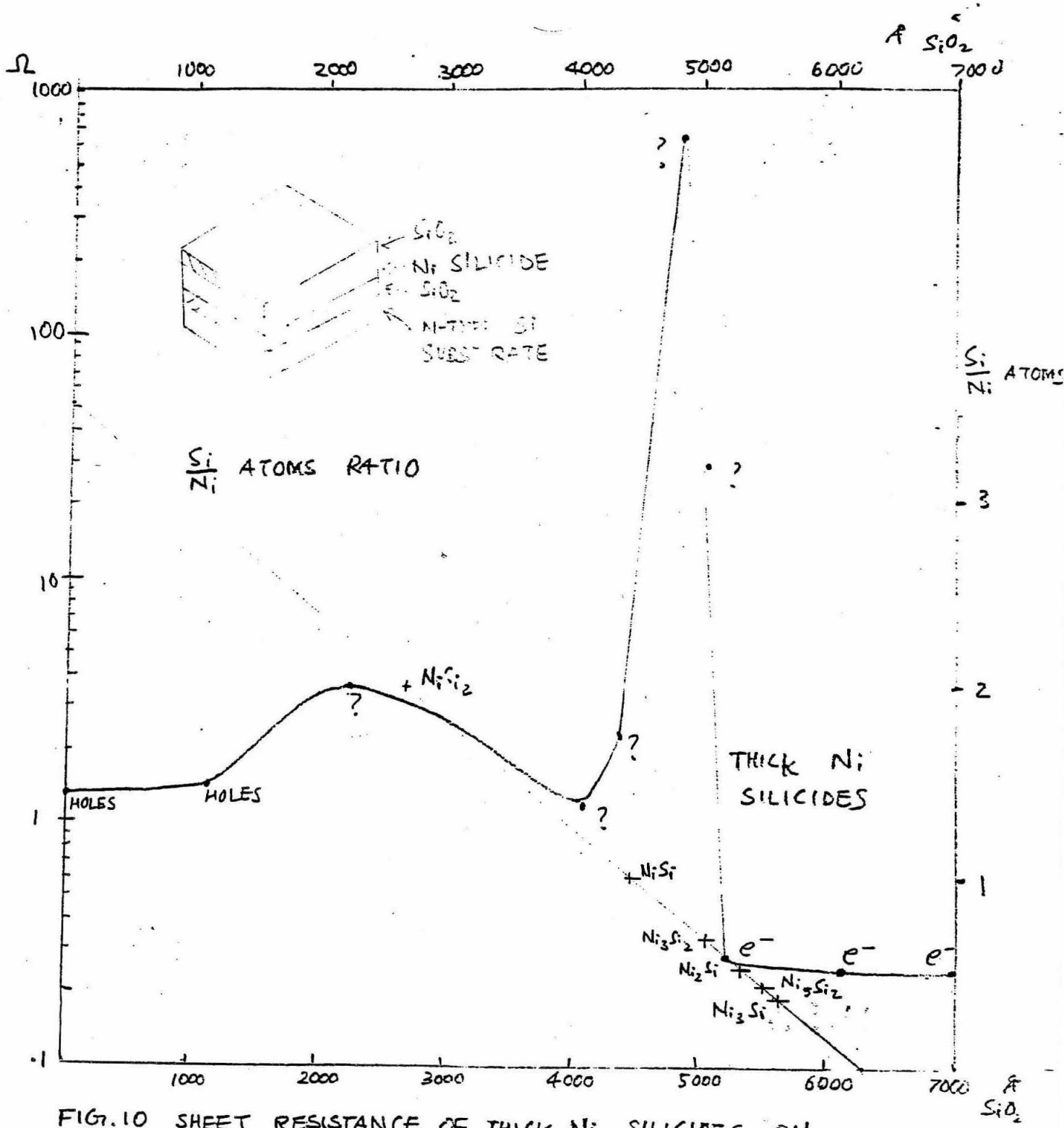

FIG. 10 SHEET RESISTANCE OF THICK Ni SILICIDES ON SiO_2/Si SUBSTRATE VS. SiO_2 THICKNESS AND $\frac{Si}{Ni}$ ATOMS RATIO VS. SiO_2 THICKNESS

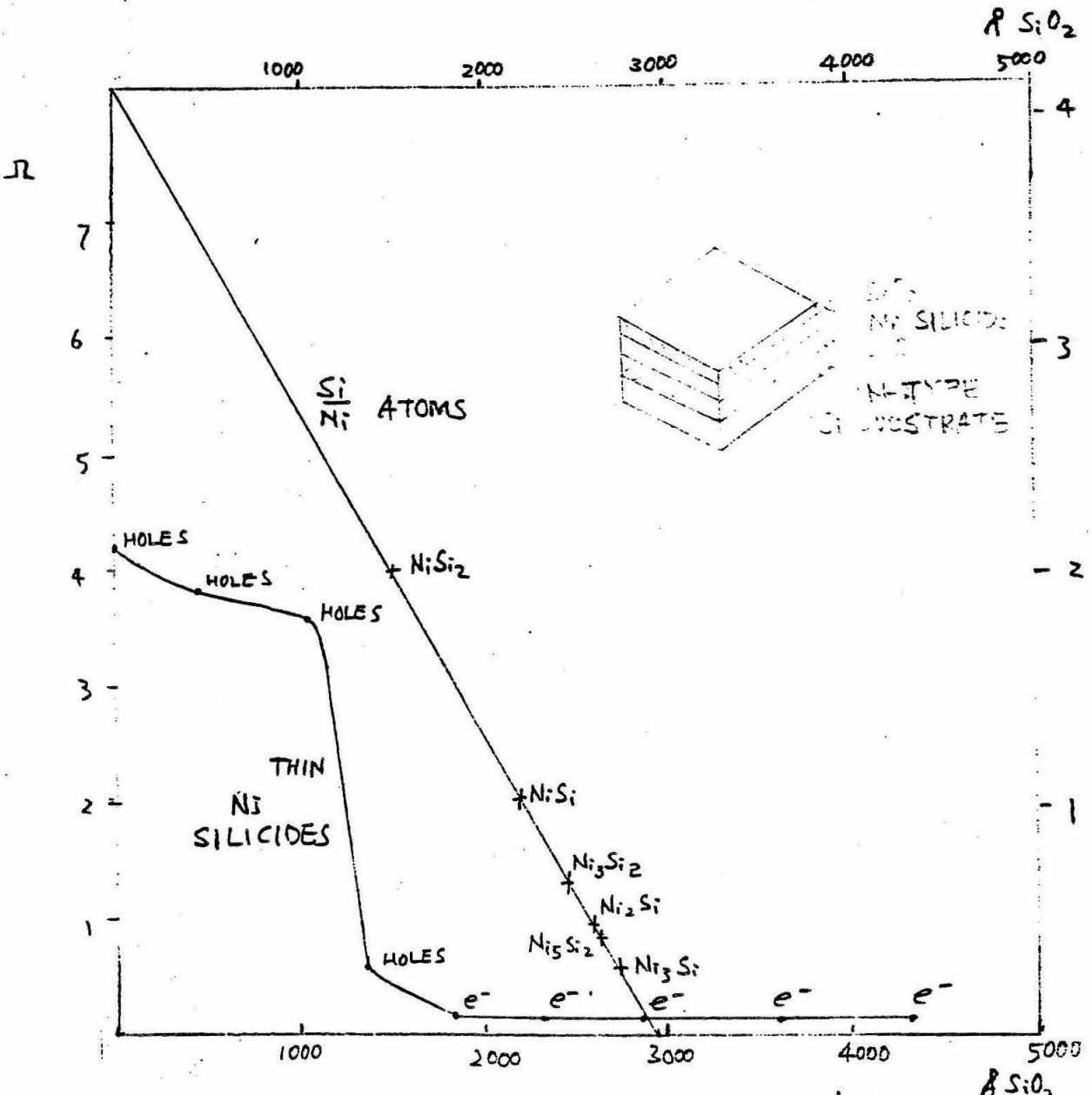

FIG. 11 SHEET RESISTANCE OF THIN Ni SILICIDES ON SiO_2/Si SUBSTRATE VS. SiO_2 THICKNESS AND $\frac{Si}{Ni}$ ATOMS RATIO VS. SiO_2 THICKNESS.

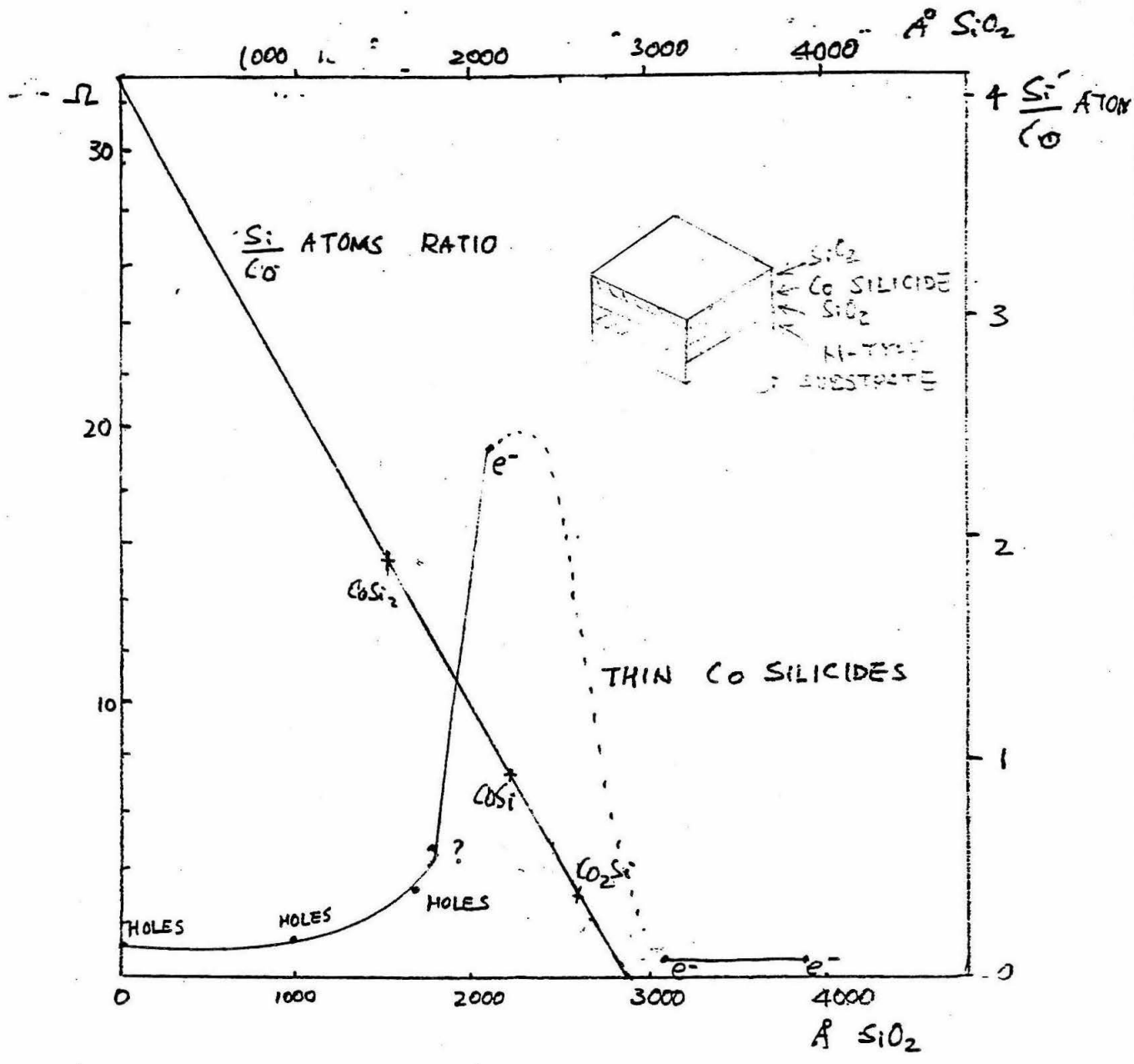

FIG. 1R SHEET RESISTANCE OF THIN Co SILICIDES ON SiO_2/Si SUBSTRATE VS. SiO_2 THICKNESS AND $\frac{Si}{Co}$ ATOMS RATIO VS. SiO_2 THICKNESS.

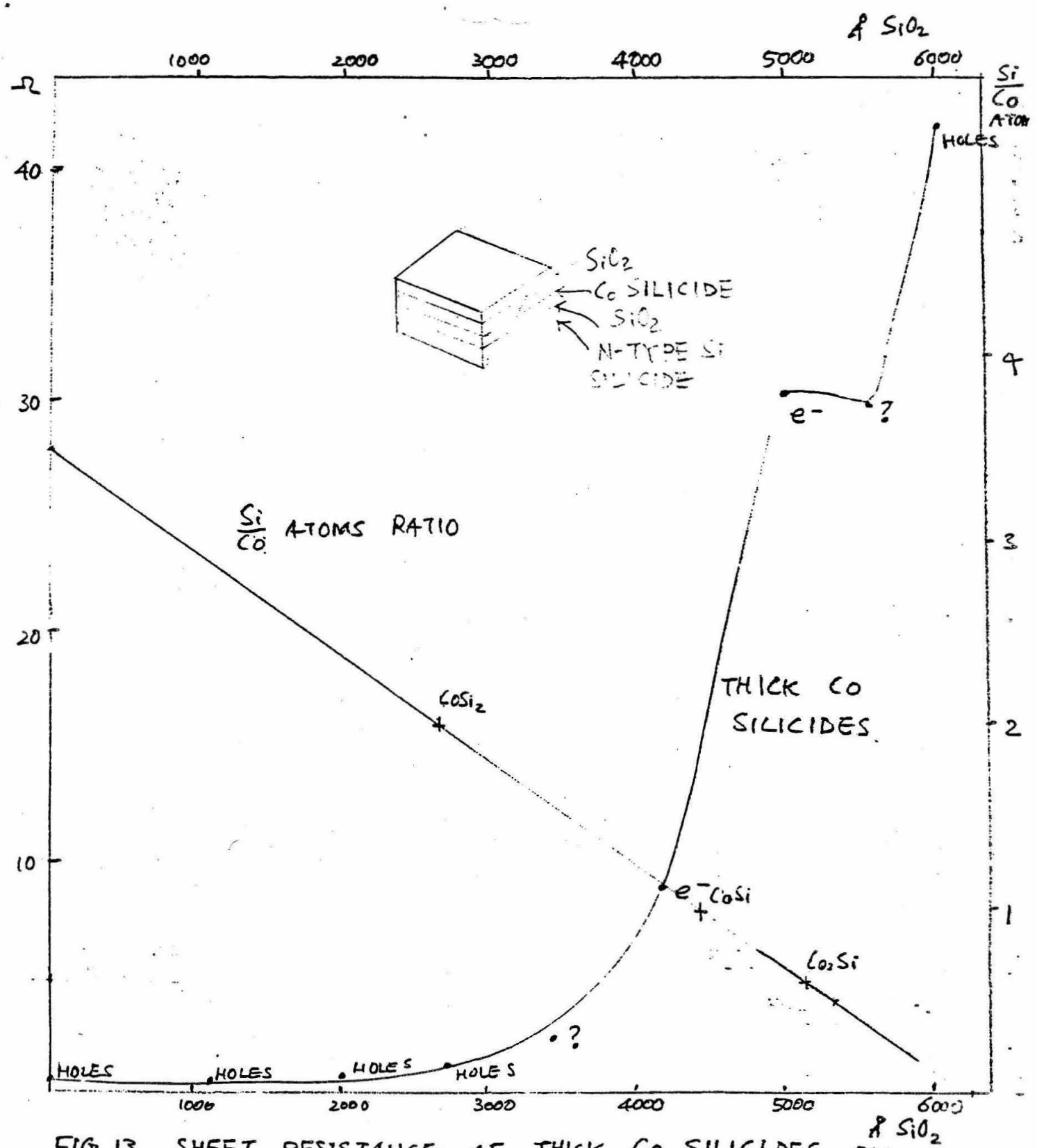

FIG. 13. SHEET RESISTANCE OF THICK Co SILICIDES ON SiO_2/Si SUBSTRATE VS. SiO_2 THICKNESS AND $\frac{Si}{Co}$ ATOMS RATIO VS. SiO_2 THICKNESS.

SHOCK COMPACTION OF METAL POWDERS

by

Dan Kostka

ABSTRACT

Shock compaction is a new and possibly superior method to form metal parts from metal powders without losing desirable but metastable properties. Once the technique is perfected, large-scale metal parts can be produced which are superior to parts presently made by conventional means. We were able to shock compact AISI 9310 powder into a compact with excellent material properties: an ultimate tensile strength of 190,000 psi, and a Vickers diamond pyramid microhardness of 545.

INTRODUCTION

Metal powders can be produced possessing great strength and hardness. However, these properties are metastable. Thus in forming metal parts by sintering, these properties are lost in the extended heating. Shock compaction is one solution to this heat problem. A shock wave of high enough pressure and short enough duration will bond the powder grains together at their boundaries without affecting their interiors. This is because most of the energy is preferentially deposited at the grain boundaries. The fused grain boundaries may be rapidly quenched by the grain interiors, and metastable properties are then preserved. An additional advantage of shock compaction is that parts can be produced with nearly their final shape---reducing the amount of machining required.

The purpose of this research was to optimize the ultimate tensile strength of a specific metal powder, AISI 9310, by varying the pressure amplitude, while keeping the other variables fixed (such as pressure duration, initial temperature, powder size, and initial porosity).

PRACTICE

Each shock compaction, or shot, is done on a 20 mm gun. The metal powder is inside a target assembly attached to the barrel muzzle (see Fig. 1). Firing a shotgun shell (loaded with gunpowder) in the gun breech propels a stainless steel plate (glued to a lexan projectile) into the target assembly. The barrel is vacuum pumped; an axial spall plate is attached to the rear of the target assembly to act as a momentum trap; and the flyer velocity is measured by timing the flyer's interruption of two parallel laser beams of known spacing.

After the shot, the metal compact is studied or tested in three ways. First, it can be polished, chemically etched, and photomicrographed to study grain structure and bonding. Second, its microhardness can be measured. Third, small tensile test pieces can be cut from the sample by electron discharge machining and tested for ultimate tensile strength.

The powder we studied was AISI 9310. It's composition is mainly Fe, with .07-.13% C, .4-.7% Mn, .2-.35% Si, 2.95-3.55% Ni, 1.0-1.45% Gr, and .08-.15% Mo. We held the following parameters fixed: pressure duration (by using flyer plates of constant thickness), initial temperature (room temperature), powder size (42-72 μm size, see Fig. 2), and initial porosity (61% of fully compacted density). The flyer velocity determined the pressure amplitude, which first travels through the powder in the first pressure jump, and then rings up to full pressure.

RESULTS

We obtained the strongest compact on shot 730 (see Fig. 3). It had an UTS of 190,000 psi and a microhardness of 545 (with a 100p indentor). By comparison, 304 stainless steel has the respective values of 80,000 and 400. Examining Fig. 4, UTS goes up with increasing pressure, although it appears to be leveling out. Examining Fig. 5, the microhardness of the shock compacted powder is much higher than the pre-compacted powder, due to work hardening. However, above 110 Kbars, annealing (due to the bulk rise in temperature) begins to bring the microhardness down.

BIBLIOGRAPHY

1. R. R. Boade, "Dynamic Compaction of Porous Tungsten," Journal of Applied Physics, Vol. 40, No. 9, Aug. 1969.

2. Ray Kinslow, High-Velocity Impact Phenomena. New York: Academic Press, 1970.

FIGURE 1 CROSS-SECTIONAL VIEW OF TARGET ASSEMBLY (FULL SCALE)

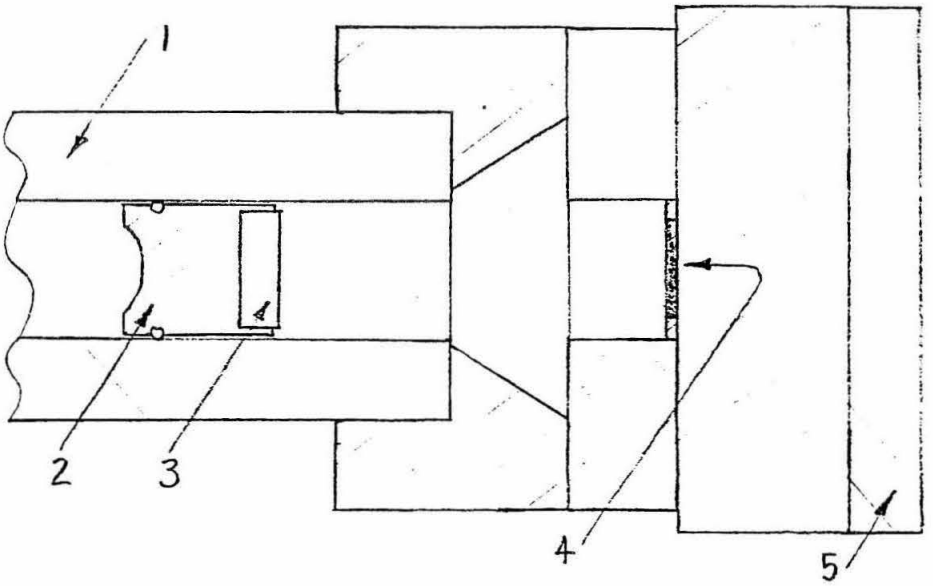

1 BARREL

2 PROJECTILE

3 FLYER

4 9310 POWDER

5 AXIAL SPALL PLATE

FIGURE 2

9310 POWDER IN LUCITE

500 x , NITAL ETCH

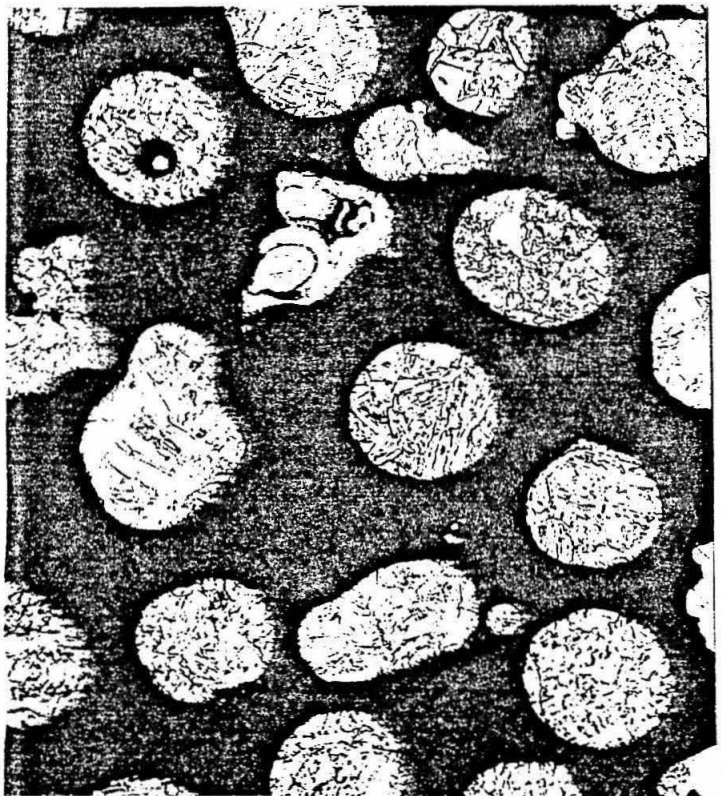

FIGURE 3

SHOCK COMPACTED 9310 POWDER

SHOT 730 , 500 x , NITAL ETCH

1.6 Km/SEC FLYER VELOCITY

190,000 PSI UTS ; 545 MICROHARDNESS

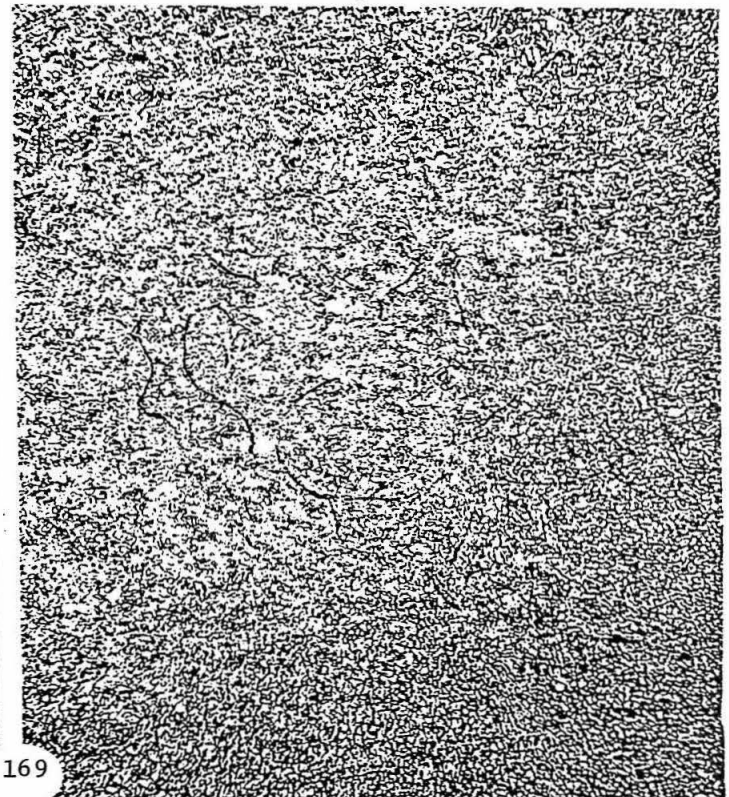

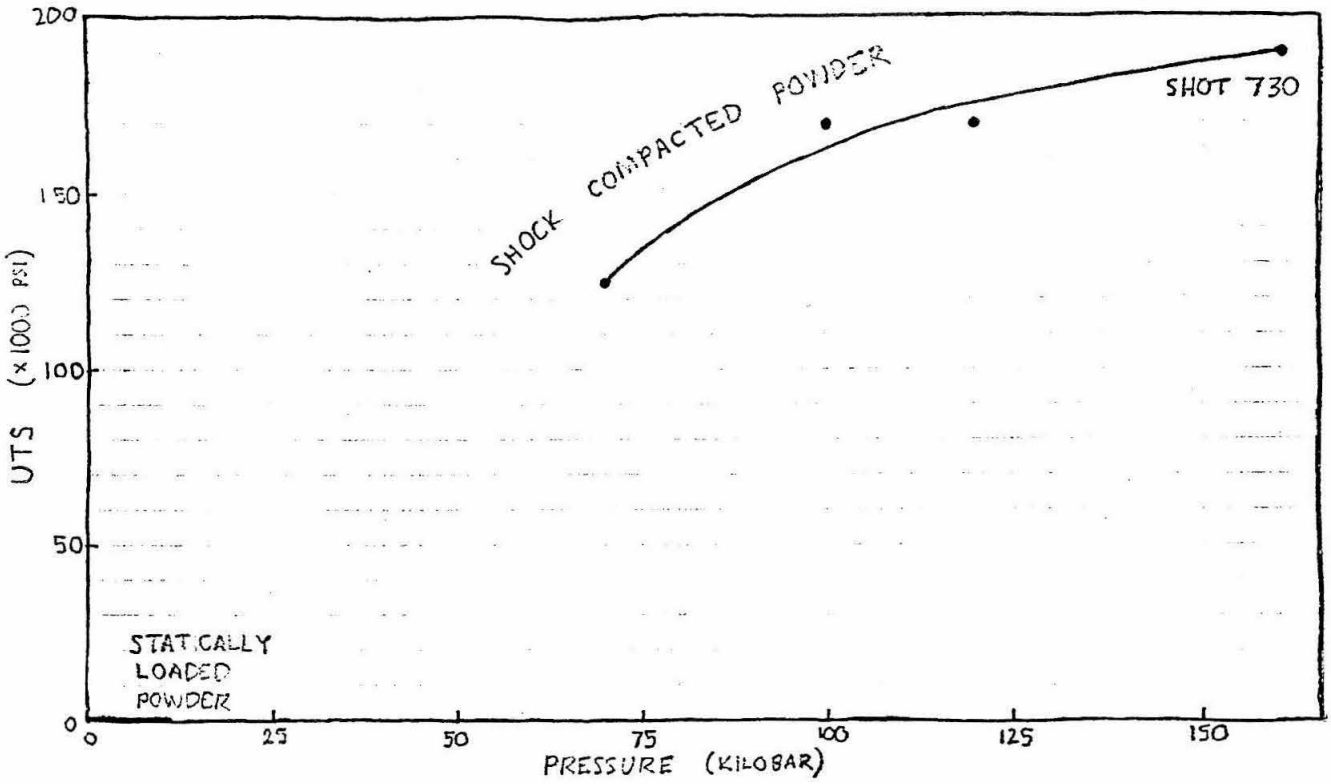

FIGURE 4 UTS vs FIRST PRESSURE JUMP

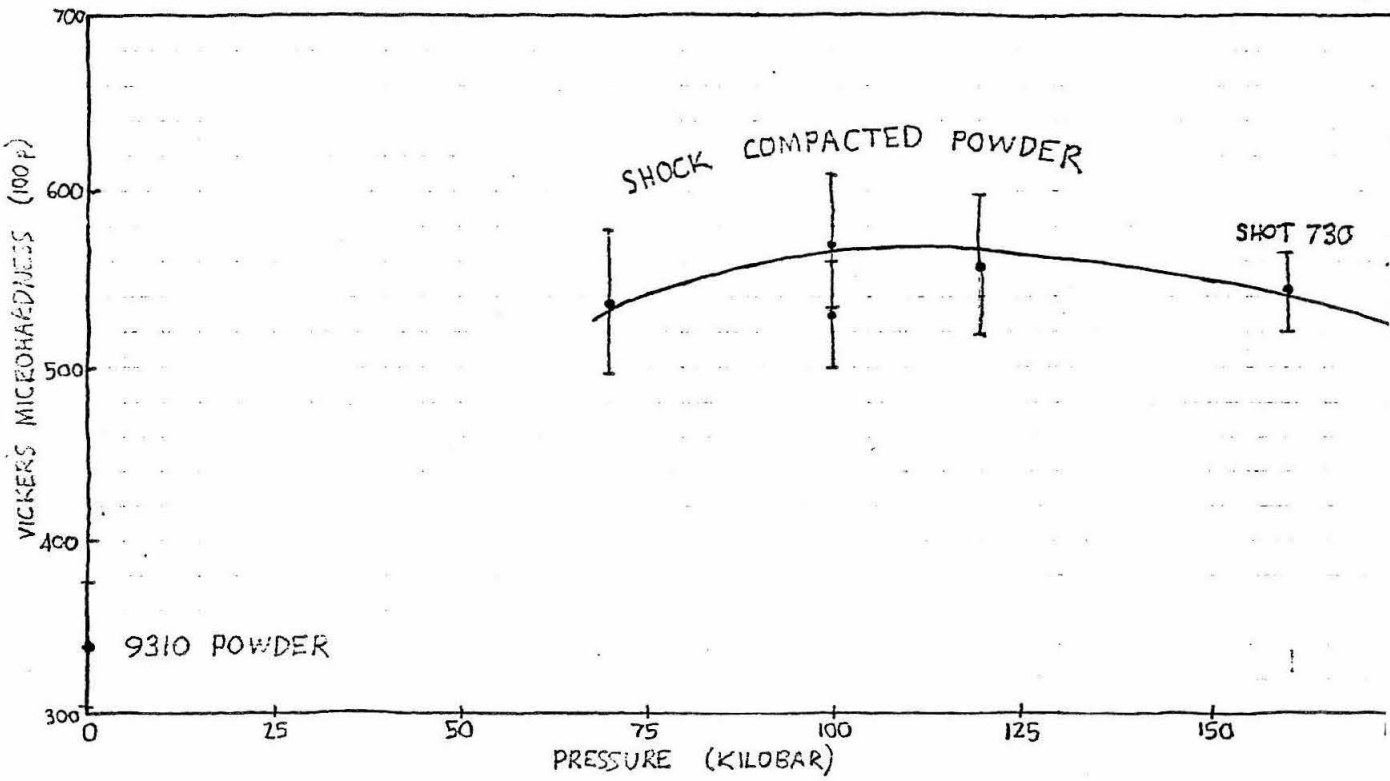

FIGURE 5 MICROHARDNESS vs FIRST PRESSURE JUMP

Study of *Ni-Nb* System by Ion Mixing

Kenneth T.Y. Kung
SURF Final Report
September 3, 1982

ABSTRACT

Amorphous *Ni-Nb* alloy films have been formed from multiple-layered *Ni-Nb* samples of various atomic compositions, by ion mixing (IM) with 300 KeV Xe^+ ions, at doses ranging from 3x to 17x10^{15} *ions / cm*^{2}. The resulting mixed layers were studied with 1.5 MeV He^+ backscattering spectrometry and X-ray diffraction measurements. The recrystalization temperatures of these amorphous alloys, as defined on a practical time scale, were determined to be in the range 450 - 650 °C.

INTRODUCTION

Amorphization of binary metallic systems by IM attracts academic interests and has potentials for practical applications, but so far only a limited number of systems have been studied by IM [1]. This study investigates the ion-mixed amorphous alloys formed from multiple-layered *Ni-Nb* samples of 4 different compositions ($Ni_{35}Nb_{65}$, $Ni_{55}Nb_{45}$, $Ni_{65}Nb_{35}$ and $Ni_{80}Nb_{20}$, chosen to be away from any stable equilibrium compound in the *Ni-Nb* phase diagram [2]), deposited on thick inert (SiO_2) layers. The amorphous structure and compositions of the mixed layers are confirmed by X-ray diffraction measurements (Read Camera) and 1.5 Mev He^+ backscattering spectrometry, respectively.

The recrystalization temperatures of the amorphous alloys (defined as the temperature at which an amorphous structure transforms into crystalline after 1/2 hr thermal annealing) are determined by post annnealing, while the changes in structures and thus in resistivities are determined at room temperature by X-ray diffraction (Read Camera) and Hall 4-point probe

sheet resistivity measurements after each annealing period.

The potential of these amorphous layers to be used as diffusion barriers against metals are investigated by depositing a thin film of *Au* on top of both the amorphous and the recrystalized alloys of the same compositions, and then comparing the extents of *Au* diffusion (under thermal annealing) through the two differently structured layers by backscattering spectrometry.

PRESENTATION AND DISCUSSION OF RESULTS

Ni-Nb multiple-layered thin-film samples were prepared by electron-gun evaporation of high purity *Ni* (99.9% pure) and *Nb* (99.99% pure) in an oil-free evaporation system onto thick SiO_2 layers, about 3000 Å thick, grown on an organically cleaned n-type (*P*-doped) *Si* wafer of <111> orientation. FIGURE I is a scaled schematic representation of the sample. The relative total thicknesses of the *Ni* and the *Nb* films were chosen to fix the 4 desired alloy compositions ($Ni_{35}Nb_{65}$, $Ni_{55}Nb_{45}$, $Ni_{65}Nb_{35}$ and $Ni_{80}Nb_{20}$). The total thicknesses of the *Ni-Nb* samples, in the range 573 - 639 Å, were chosen to equal the Rp+δRp (projected range + projected range straggling) of the 300 KeV Xe^+ ion employed for irradiation [3].

The samples were then irradiated with 300 KeV Xe^+ ions at room temperature for 5 dose levels: 3x, 5x, 7x, 10x and 17×10^{15} *ions* / cm^2.

X-ray diffraction (Read Camera) and electrical sheet resistivity (Hall 4-Point Probe) measurements were then employed to study the structures of the mixed layers, and it was confirmed within the resolution of the X-ray diffraction technique used here that all the mixed layers were completely amorphous, as indicated by the presence of a single diffusion ring (no sharp lines) on the X-ray diffraction patterns and the high sheet resistivities of the mixed layers (about 4 times higher than the virgin layers; see TABLE I). 1.5 Mev He^+

backscattering spectrometry was employed to confirm the chosen compositions of the mixed layers.

The amorphous alloys, which we obtained by irradiation to a dose of $5x10^{15}$ *ions / cm*^{2}, were then post annealed to determine their recrystalization temperatures (defined earlier as the temperatures at which the amorphous structures transform into crystallines after 1/2 hr thermal annealing). X-ray diffraction and Hall 4-point probe sheet resistivity measurements were employed to detect when the structure changes occur. The recrystalization temperatures so determined are tabulated in TABLE II.

To determine the advantage of the amorphous alloys as diffusion barriers against metals (as compared with their recrystalized counterparts), the alloys which we obtained by irradiation to a dose of $7x10^{15}$ *ions / cm*^{2} were chosen as the "amorphous" samples, while those obtained by irradiation to a dose of $10x10^{15}$ *ions / cm*^{2} were thermally annealed and recrystalized and chosen as the "recrystalized" samples. Thin *Au* films, about 300 - 400 Å thick, were then deposited on top of the "amorphous" and the "recrystalized" samples simultaneously in the oil-free electron-gun evaporation system. These samples were then simultaneously thermally annealed and the extents of *Au* diffusion into the alloy layers were checked by backscattering spectrometry. However, due to the difficulty involved in preventing oxidation to occur while thermally annealing the $10x10^{15}$-*ions / cm*^{2} samples for recrystalization (metal oxides in this case are good diffusion barriers themselves), we could not obtain a solid experimental evidence to support the advantage of the amorphous thin films as metal diffusion barriers as compared to their recrystalized counterparts. Further experimentation will be performed after the SURF period to achieve this.

CONCLUSIONS:

1. Amorphous alloys can be formed from multiple-layered *Ni-Nb* systems, of atomic compositions $Ni_{35}Nb_{65}$, $Ni_{55}Nb_{45}$, $Ni_{65}Nb_{35}$ and $Ni_{80}Nb_{20}$ by IM under doses ranging from 3x to $17x10^{15}$ *ions / cm*^{2} (equivalent to a dpa of 30 - 160 [4]).

2. These *Ni-Nb* amorphous alloys are stable upon irradiation since, while a low dose of $3x10^{15}$ *ions / cm*^{2} (equivalent to a dpa of 30) is enough to amorphize the multiple layers, another irradiation dose of $14x10^{15}$ *ions / cm*^{2} (equivalent to a dpa of 130) does not make the amorphous alloys change.

3. These *Ni-Nb* amorphous alloys have recrystalization temperatures in the range 450 - 650 °C, with the one whose atomic composition is closest to the center of the *Ni-Nb* phase diagram (and away from any stable equilibrium compound) having the highest Tc.

BIBLIOGRAPHY

[1] B.X. Liu, W.L. Johnson, M-A. Nicolet and S.S. Lau, "Amorphous Film Formation by Ion Mixing in Binary Metal Systems", (IBMM-82 International Conference, Grenoble, France, September 6-10, 1982).

[2] S.S. Lau, B.X. Liu and M-A. Nicolet, "Ion Mixing and Phase Diagrams", (IBMM-82 International Conference, Grenoble, France, September 6-10, 1982).

[3] G. Dearnaley et al. in "Ion Implantation", (North-Holland, New York, 1973), p.766.

[4] M.W. Thompson in "Defects and Radiation Damage in Metals", (Cambridge at The University Press, 1969), Chapters 4 and 5.

FIGURE I Schematic Representation of the *Ni-Nb* Sample before Irradiation, Drawn Roughly to Scale.

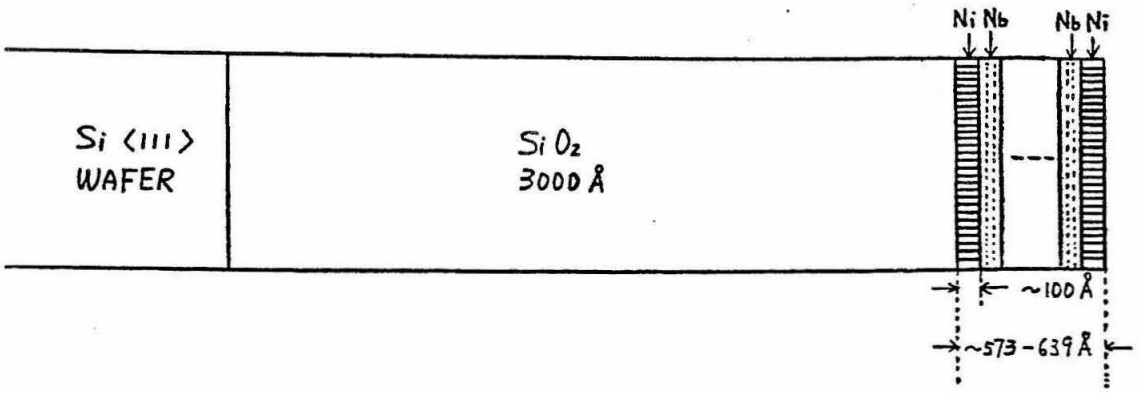

TABLE I Sheet Resistivities of the *Ni-Nb* Samples of Different Atomic Compositions and Doses, Obtained by Hall 4-Point Probe Measurements.

Dose / Composition	virgin	3x	5x	7x	10x	17x	10^{15} *ions / cm²*
$Ni_{35}Nb_{65}$	5.75	23.2	24.7	25.7	26.7	29.6	*ohms / square*
$Ni_{55}Nb_{45}$	4.47	23.3	25.1	27.3	26.9	31.2	*ohms / square*
$Ni_{65}Nb_{35}$	4.94	32.7	34.3	34.2	37.2	40.3	*ohms / square*
$Ni_{80}Nb_{20}$	4.41	27.7	28.7	27.5	29.7	31.6	*ohms / square*

TABLE II Recrystalization Temperatures of the *Ni-Nb* Amorphous Samples (Obtained by Irradiation to a Dose of $5x10^{15}$ *ions / cm²*) as Determined by Post Annealing, with X-ray Diffraction and Hall 4-Point Probe Sheet Resistivity Measurements to Confirm the Structure Changes.

Composition	Recrystalization Temperatures
$Ni_{35}Nb_{65}$	550 - 600 °C
$Ni_{55}Nb_{45}$	600 - 650 °C
$Ni_{65}Nb_{35}$	500 - 550 °C
$Ni_{80}Nb_{20}$	450 - 500 °C

New Understanding of Molecular Hydrogen in the EUV Region

Tak Leuk Kwok

Abstract:

A laboratory measurement of the absolute emission cross-sections of the new band systems, namely the B′-X and D-X bands of H_2 by electron impact has been taken. The emission cross section of the B′-X transition at 100 eV is found out to be 6.7×10^{-18} cm^2 and 8.3×10^{-18} cm^2 for the D-X transition. Both measurements are accurate to within a factor of two. The ratio of these two together to the Werner band cross-section is roughly 1 to 2, in good agreement with theoretical calculation by Shemansky[1].

Introduction:

Spectroscopic calibration in the EUV region has been very difficult for many years and no one has ever done a nice job in that yet. The situation has become more and more intolerable as spacecraft research is making ever rising rate of progress. Spectra obtained by the Voyager from Jupiter show a lot of features in the EUV region. Much of the VUV spectral features of the Jovian atmosphere has been clarified successfully by Yung, et al,[2] and now we understand that the Lyman, Werner and Cascade bands of molecular hydrogen constitute a major portion of the VUV spectra of the Jovian atmosphere. The cross-sections for these three bands has been obtained to excellent agreement with theory. There has been much confusion about the identity of the EUV feature. We speculate that they are mainly due to the B′-X and D-X transitions of molecular hydrogen. Experiment has been carried out and our ideas proven to be correct, that a synthetic

spectrum of H_2 taking into account these two transitions match very well with an experimental electron impact spectrum both in wavelengths and in the relative heights of the peaks. Accurate values of cross-sections can then be easily obtained by doing a nonlinear least square ft between the two; the techniques of which were developed during the VUV study of H_2[3].

Presentation and Discussion of Results:

A detailed description of the experimental apparatus is presented in Ajello and Srivastava's work.[3] The apparatus consists of an electron-impact collision chamber in tandem with a UV spectrometer. A collimated beam of electrons is generated by an electron gun whose kinetic energy can be varied from 1eV to a few keV. This beam of electrons is crossed with a beam of gas formed by a capillary which produces a background gas pressure of the order of 10^{-6} Torr. Inelastic electron molecule collisions lead to emission of photons. The emitted photons enter into a UV spectrometer consisting of an osmium-coated concave grating that can be rotated around a vertical axis, thus a spectral region between 50 and 500 nm can be scanned. The detector used is a channel electron multiplier-channeltron. The usual linearity checks of signal intensity versus current and pressure were made to demonstrate the absence of secondary processes at the energies studied.

The entire optical system was calibrated mainly depending on published cross-sections for Argon by Mental and Morgan[4]. We put in Argon gas and obtain an Argon spectrum between 500 and 1524 Å. By comparing the area under peaks to the cross sections published, we are able to obtain a rough calibration of the system, accurate to within a factor of 2. However the Argon calibration only allows us to go to a wavelength of about 1067 Å -

the Ar I resonance line, since beyond that there aren't any distinct peaks. We thus have to rely on another gas for calibrating the longer wavelength region. Due to the signal intensity, we decide to choose H_2 as the candidate. This is done carefully by sorting out those peaks that we are sure to be due only to the Lyman, Werner or Cascade band emission. In a similar way as before, we find the ratio of area under peaks to total intensity from the three band contribution. In the process, we have used the published cross-sections by Yung, et al, on those three bands. Finally, we normalize the two calibration at 1055 Å. The final calibration curve turns out to have the dominant feature of the channeltron, i.e., its sensitivity drops drastically when reaching beyond Lyman alpha at 1215.7 Å.

With the calibration curve thus obtained, we subtract the background from the experimental spectrum and multiply the entire spectrum with the inverse sensitivity factor to obtain a calibrated spectrum. We first work at 100 eV electron beam energy and using a non linear least square ft program, we obtain the cross sections of B'-X and D-X emisson as 6.7×10^{-18} cm^2 and 8.3×10^{-18} cm^2.

Conclusions:

Compared with theoretical calculation by Shemansky[1], our experimental cross sections for the two new bands are in pretty good agreement. Even though we believe our calibration to be accurate only within a factor of two, we have nevertheless made a successful touch at first doing a calibration for a EUV spectroscopic system and have obtained reasonably consistent values for the cross sections of the new bands. Right now we are trying another method of calibrating the system - namely, the double monochromator

method. So far we have had consistent qualitative matching of the two methods. Hopefully, we will be able to fine tune our instrument and finally both accomplish a better EUV calibration and obtain more accurate values for the new bands cross sections. They will be of great importance to planetary modelling of the Jovian atmosphere in the EUV region.

Bibliography

1. The Saturn Spectrum in the EUV - Electron Excited Hydrogen D.E.Shemansky, J.M.Ajello, Submitted to Journal of Geophysical Research, Feb. 8, 1982.

2. Laboratory studies of UV emissions of H_2 by electron impact, The Werner and Lyman-band systems, J.M. Ajello, S.K. Srivastava, Yuk L. Yung, Physical Review A, Volume 25, No. 5, p. 2485-2498.

3. J.M. Ajello and S.K. Srivastava, J. Chem. Phys. 75, 4454(1981).

4. Mentall and Morgan, Phy. Rev A, Vol. 14, No. 3, 954.

FLOW PATTERNS AND WALL EFFECTS OF CILIARY PROPULSION

by Y. S. Lee
T. Y. Wu & G. Yates (sponsors)

Division of Engineering and Applied Science,
California Institute of Technology

An experimental attempt has been made to verify the theoretical model of ciliary propulsion which predicts a great difference of the streamlines for an inert body and freely swimming microorganism. Moreover, effects of microscopic slide boundaries on the flow field of ciliary propulsion will be discussed.

Introduction

Recently, there have been several theoretical investigations of ciliary locomotion using various geometrically simplified models. Although ciliates have a wide variety of body shapes, a great number of them are approximately axisymmetric and can be suitably represented by a prolate spheroid. Keller and Wu (1977) proposed a simple hydrodynamic model based on this assumption to determine the self-propulsion of ciliated micro-organisms and to examine the effect of body shape upon the velocity of propulsion. Their model predicts a vast difference in the streamlines for the translation of an inert impermeable body and a freely swimming micro-organism of the same shape. They confirmed their theory experimentally using specimens of Paramecium caudatum. In this paper, results of similar experiments conducted on specimens of Paramecium multimicronucleatum using small polystylene latex spheres as markers in the fluid are presented.

In most theoretical investigations, it is generally assumed that wall drag on free-moving, self-propelled moving micro-organisms is not significant under normal observation conditions. However, in a number of applications of low-Reynolds-number flow theory (e. g. the muco-ciliary propulsion system in trachea, spermatozoa transport in ciliated duct and organisms moving in thin slide preparations) the wall is close enough to affect flow motion significantly. In order to investigate wall effects on flow motion of P. multimicronucleatum,

a series of experiments were conducted measuring velocities of swimming ciliates at various distances from the wall using Zeiss light microscope and a video system.

Results and Discussion

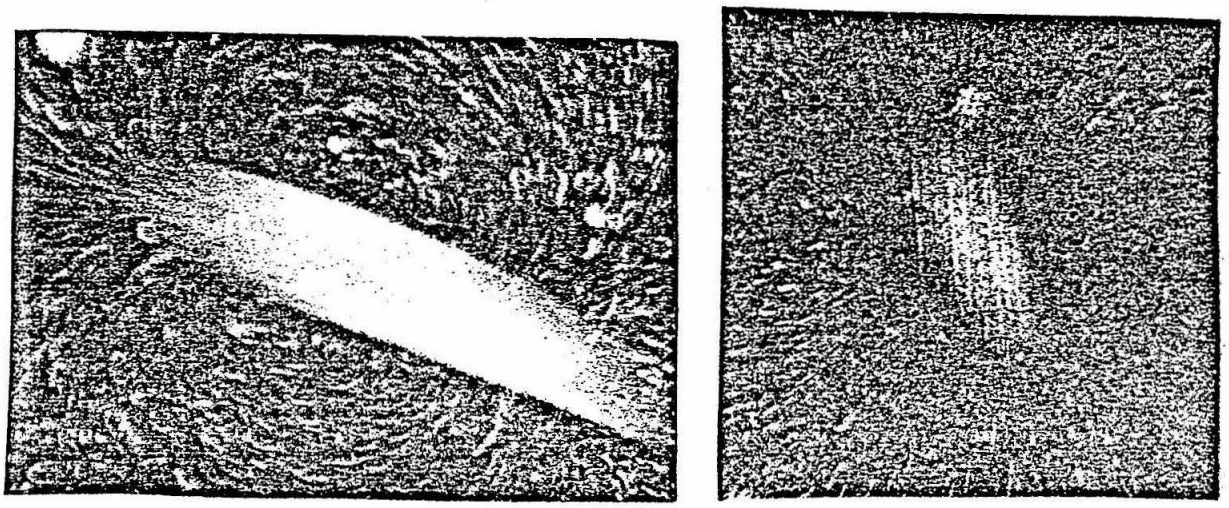

(a) (b)

Figure 1 a, b. Streak photographs of a freely swimming speciment of P. multimicronucleatum (a) and of a dead on sedimenting under gravity (b).

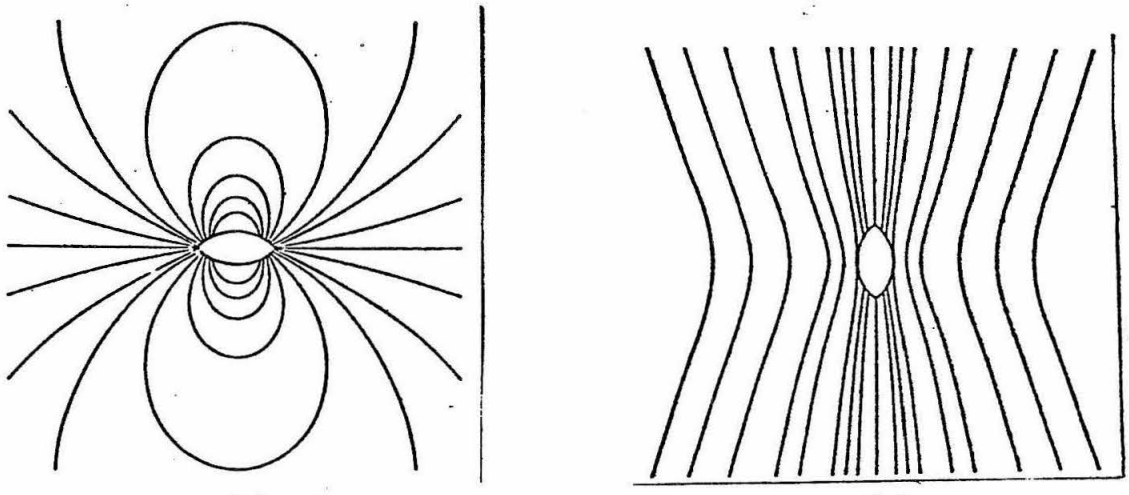

(a) (b)

Figure 2 a, b. The streamlines, in the laboratory frame, of a self-propelling prolate spheroid (a) and of an externally-driven spheroid of the same shape (b) (Keller and Wu, 1977).

Figure 1a is a typical photograph of a freely swimming ciliate (zero total net force acting on an organism). The streak paths of the tracer spheres around the ciliate are seen to be at least qualitatively in agreement with the theoretical streamlines, which resemble those due to a doublet distribution (figure 2a), in the case of free swimming. The streamlines in the second case of sedimenting flow (figure 2b) resemble a set due to a Stokeslet distribution, and again comparison with the particle paths of figure 1b (sedimenting under gravity) indicates a qualitative agreement between theory and experiment. The theory, however, did not take into account the effect of the walls and other flow boundaries that were present in the experiment. This could explain some minor discrepancy between theory and experiment.

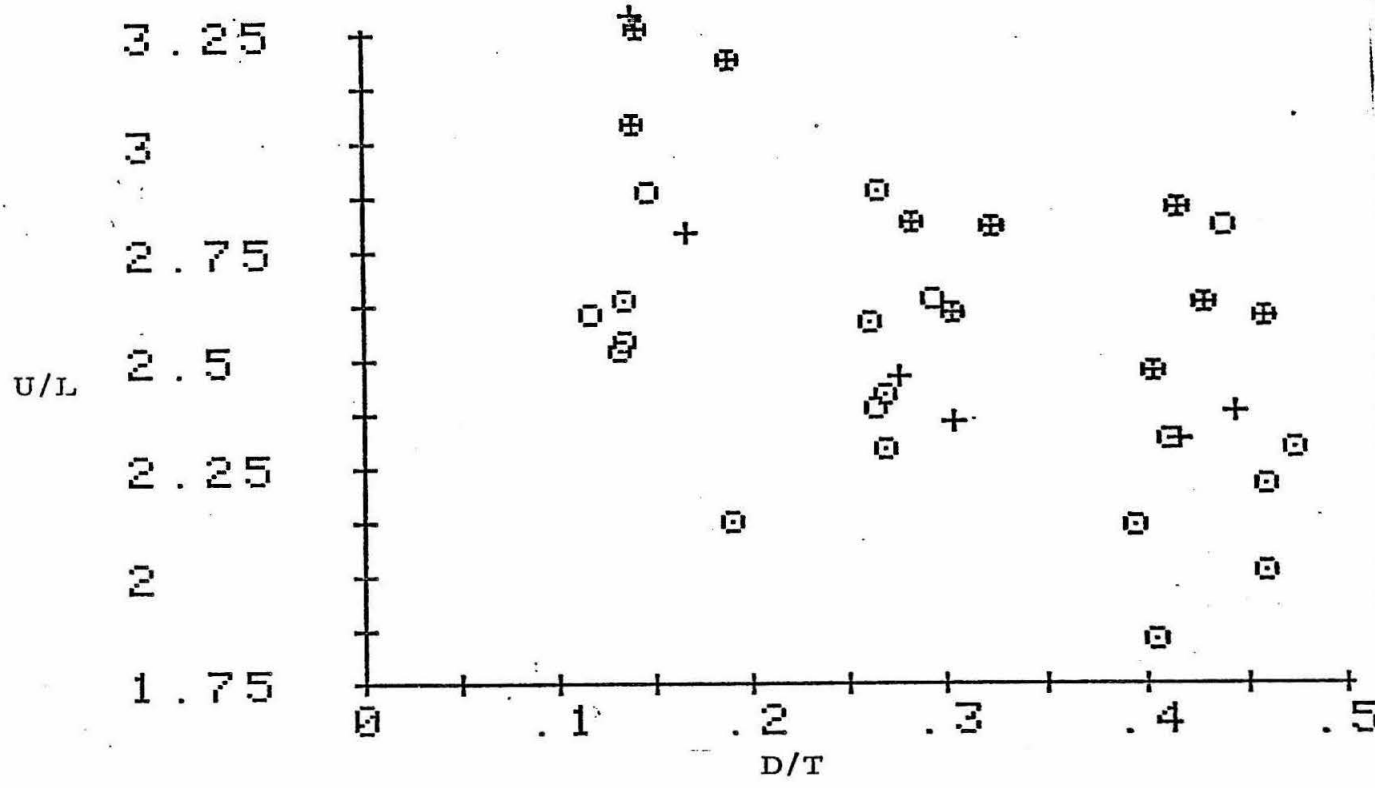

Figure 3. U/L vs. D/T (U=speed of propulsion μm/sec, L=body length μm, D=distance from the ciliate to the closest wall μm, T=distance between microscope slide and coverslip μm. Each symbol represents different culture day of P. multimicronucleatum specimens)..

The specimen preparations for investigating wall effects were made using a glass slide and a modified vaseline mount in which the coverslip was supported by a certain thickness of vaseline around its perimeter with two thin plastic strips inserted between the slide and the coverslip. The average thickness of preparations was 350 μm, and distance from the microscope slide was varied in 50 μm interval. Since exact measurements of the distance between organism and slide were difficult to obtain, care was taken to only measure velocities of organisms that were in sharp focus at each interval. Figure 3 shows results of a series of experiments conducted at four different culture days of micro-organisms. This preliminary data clearly indicate that the velocities of free-swimming ciliates are greater as organisms swim closer to the boundaries. Since a wall affects a nearby body's motion by influencing upon the volume of fluid reacting to the forces exerted by the body, ciliates were expected to swim slower near the wall. Explanation for this contradicting experimental observation will be a subject of further study.

Conclusion

Qualitatively, good agreement is found between the theoretically predicted streamlines by Keller and Wu (1977) and experimental streak photographs of freely swimming and inert-sedimenting P. multimicronucleatum. Although the drag on a body is increased as the wall is approached, preliminary data indicate that free-moving ciliates swim considerably faster near the wall. Further experiments and study on this subject would be of practical value in many applications of low-Reynolds-number flow.

References

Blake, J. R., Liron, W., Aldis, G. K. 1982 Flow patterns around ciliated microorganisms and in ciliated duct. J. Theor. Biol. (in press).

Cheung, A. T. W., Winet, H. 1975 Flow velocity profile over a ciliated surface. eds. T. Y. Wu, C. J. Brokaw, C. Brennen, Swimming and Flying in Nature, Vol. I, Plenum Press: N. Y., 223-34.

Keller, S. R., Wu, T. Y. 1977 A porous prolate spheroidal model for ciliated microorganisms. J. Fluid Mech. 80: 259-78.

Keller, S. R., Wu, T. Y., Brennen, C. 1975 A traction layer model for ciliated propulsion. eds. T. Y. Wu, C. J. Brokaw, C. Brennen, Swimming and Flying in Nature, Vol. I, Plenum Press: N. Y., 253-72.

Winet, H. 1973 Wall drag on free-moving ciliated microorganisms. J. Expt. Biol. 59: 753-66.

FOUR JET EVENTS AT PETRA

Dave LePoire

Advisor: H.Newman

Abstract: It is hoped that the reaction $e^+e^- \rightarrow 4$jets can be used to test theories of the strong interaction. A sample of 4 jet events were identified by a cluster algoritm. The jet algoritm is able to reconstruct the parton energies with an rms error of 25% and the parton directions with an rms of 11°. By additional cuts on the four jet event sample a signal to noise of better than 1:1 was achieved. Background consisted mostly of events with heavy quarks. With this sample the following areas were investigated 1. Four jet resolution, 2.Comparison to the QCD predictions, 3.Comparison to resonance production, and 4. Comparison to Abelian QCD.

QCD is a theory of the strong force. It can be tested at PETRA through the o servation of the production of it fundamental particles quarks and gluons. Most events of this type are quark antiquark events which are seen in the detector as two groups of particles (jets) heading in opposite directions Events with three jets have also been observed. These are believed to be events where an energetic gluon is emitted by a quark. This process is similar to bremsstrahlung in QED.

Programs have been developed by members of the MARK-J collaboration which generate events and simulate the response of the detector. The goal is to find some observables that distinguish between the 4 jet events from $e^+ e^- \to q\bar{q}GG$ and $e^+ e^- \to q\bar{q}q\bar{q}$ from other processes. Measures of success include the following: efficiency (i.e. the number of 4 jet events found divided by the number of four parton final states occuring), the signal to noise ratio, the reconstruction of energy and angle of the jets, and identification of the jets as either quark or gluon.

RESULTS

A Monte Carlo event simualtor was used to find strategies for identifying 4 jet events. The MARK-J jet cluster routine which finds clusters of hits in the detector according to their direction and energy was applied first. The event has to be identified as a 4 jet event by this routine. At near optimal settings, 24% of the true four jet events of the Monte Carlo simulator were accepted. Since the four jet cross section (with the Monte Carlo simulator definition) is approximately 5% of the total hadronic cross section this would mean 125 signal events would be found out of 10,000 hadronic events. The signal to noise ratio at this stage is about 1:2.

No simple distribution could distinguish between the signal and noise in this sample so more complicated cuts were investigated. Two important indications of four jetiness are the acoplanarity (i.e. how much the 4 jets do not lie in a plane) and the minimun opening angle between any two jets. Some cuts were used to remove photons radiated by the beam and others were used to find hits that had been misinterpreted in the detector.

After applying 6 cuts the efficiency was 13% and the signal to noise was 1:1 . The noise events had the following distribution of quarks 34% b, 24% c, 30% u, 5% s, and 2% d. This suggests that weak decay of the heavy quarks may be the major contribution to the noise. The reconstruction of the energy is $\frac{E(\text{jet})-E(\text{parton})}{E(\text{parton})} = 5.1 \pm 25\%$ and that of the angle, $\angle(\text{jet, parton}) = 18^{\circ} \pm 72\%$ of the signal events had both gluons identified correctly as the pair with the lowest invariant mass.

With this sample the following areas were investigated 1. Four jet resolution, 2. Comparison to the QCD predictions, 3. Comparison to resonance production, and 4. Comparison to Abelian QCD.

1. The internal angle is a jet which characterizes its width is defined as

$$\sin\theta_{int} = \frac{\text{invariant mass}}{\text{energy of jet}}$$

The external angle is the angle between the identified momentum axis of jets. With these definitions the average internal angle is 24° and the external angle is 82° showing that all jets are narrow and separated by angles much greater than their width.

Another way to show the resolution is to project the events onto the planes between the jets and plot energy versus momentum.

2. A preliminary comparison of the data with a Monte Carlo QCD simulation (with the strong coupling constant $\alpha_s = .167$ and the characteristic transverse momentum of 300 MeV) shows:

	accepted events
MC	54±5
data	46±6

Without 4 jet events the Monte Carlo would be 27±5. Thus this shows a 4 sigma effect in the existance of 4 jet events.

3. A comparison was made with the decay of a hypothetical $t\bar{t}$ resonance with the top quark mass being 8 GeV. It was found that 4.2% of the events passed the jet assignment and cuts. This would mean in order to explain the data

$$\frac{\sigma_{res}}{\sigma_{QCD}} = \frac{\text{number of resonance events}}{\text{number of regular QCD events}} = .18 \pm .04$$

This is ruled out by distributions such as thrust.

4. There are a few tests for the gluon self coupling. Two of these are being investigated. One is based on the difference of angular distribution of gluons and quarks coming from the decay of the virtual gluon. The other is based on the energy distribution as a result of the different emission properties of quarks and gluons. Both of these await analysis of a QCD simulation without gluon self coupling.

It is probable that the hard cuts that were needed to obtain a clean 4 jet sample, removed most of the gluon self coupling effects since the gluons are preferentially emitted along the axis of the $q\bar{q}$ pair.

CONCLUSIONS

Hadronic events with 4 resolved jets have been found. The jets have been shown to be high energy, narrow and well separated. The rate of production with the value of α_s

obtained by three jet analysis is comparable to that observed although better statistics are required. The analysis method rules out final states not containing 4 narrow jets (such as the production of a new quark flavor) as a possible source of the 4 jet events observed. From Monte Carlo comparison, half of the events accepted are due to four parton processes. Many of the others come from heavy quark production and decay. A high percentage of gluon pairs can be found in the signal events as the pair with the lowest invariant mass. At this energy hard cuts have to be made to ensure good signal to noise. This probably reduces the chance of testing the effects of the gluon self coupling, but efficient identification of the gluons might offset this.

Bibliography

]. MARK-J Collaboration, Physics with High Energy Electron Positron Colliding Beams with the MARK-J Detector , Physics Reports, Sept 1980.

2. The MARK-J programs used included
   ].A Monte Carlo event generator
   2. A detector Simulator
   3. An event selection as done on the data and formatting program
   4. A cluster analysis program which was the first step in choosing events

3.O.Nachtman and A.Reiter, A Test for the Gluon Self Coupling in the Reaction $e^+ e^- \to 4$ jets and $Z^o \to 4$ jets ,HD-THEP-82-9, June 82.

4. K.Koller,K.H.Streng,T.F.Walsh,P.M.Zerwas, Multijet decays of Quarkonia Testing the Three Gluon Vertex , SLAC-PUB-2858, Dec 1981.

Jet Assignments
After Cluster Analysis

Number of partons N_{QG}

Number of Jets N_{Jet}	2	3	4	total
2	90	47	24	73
3	10	47	52	23
4	.5	6	24	4
total	63	32	5	

Read as: Percentage of N_{QG} events identified with N_{Jet} jets

Four Jet Processes

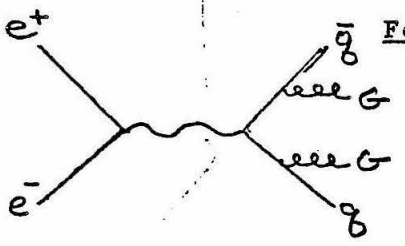

double bremsstrahlung

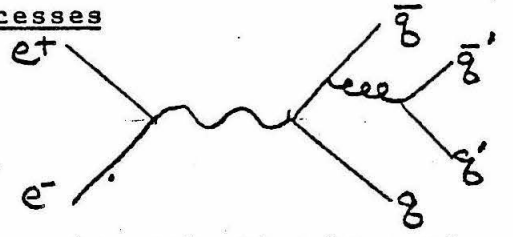

pair production by a gluon

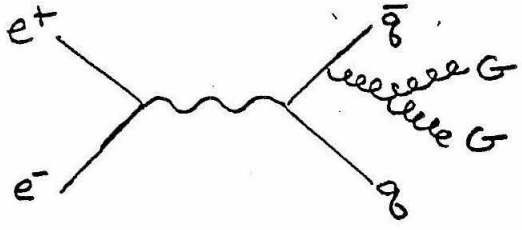

gluon self coupling

Examples of Simulated Events

—— true parton direction - - - jet direction

Signal

$q\bar{q}GG$

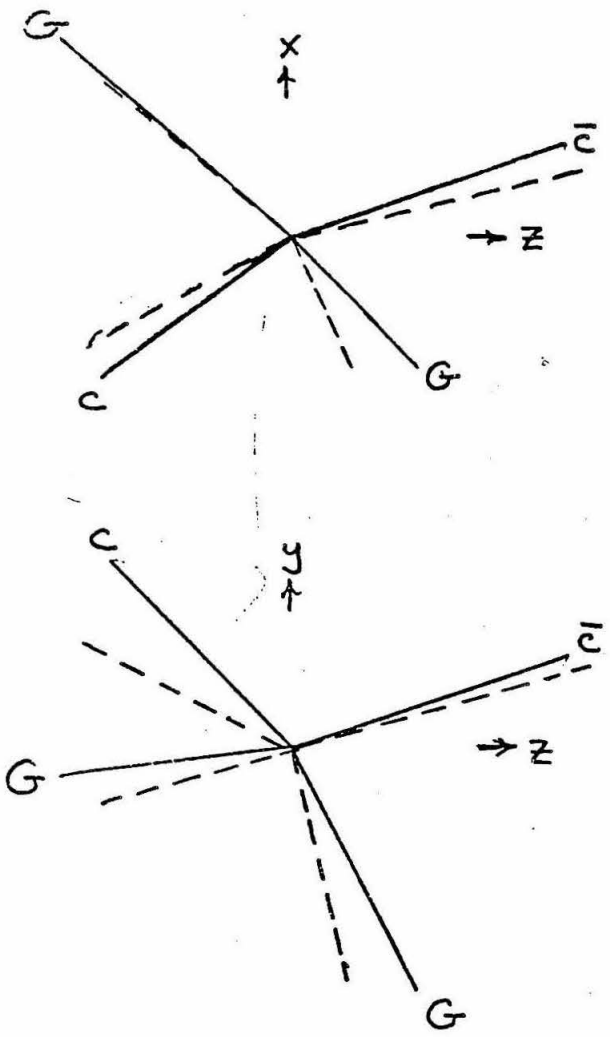

Noise

$q\bar{q}G$

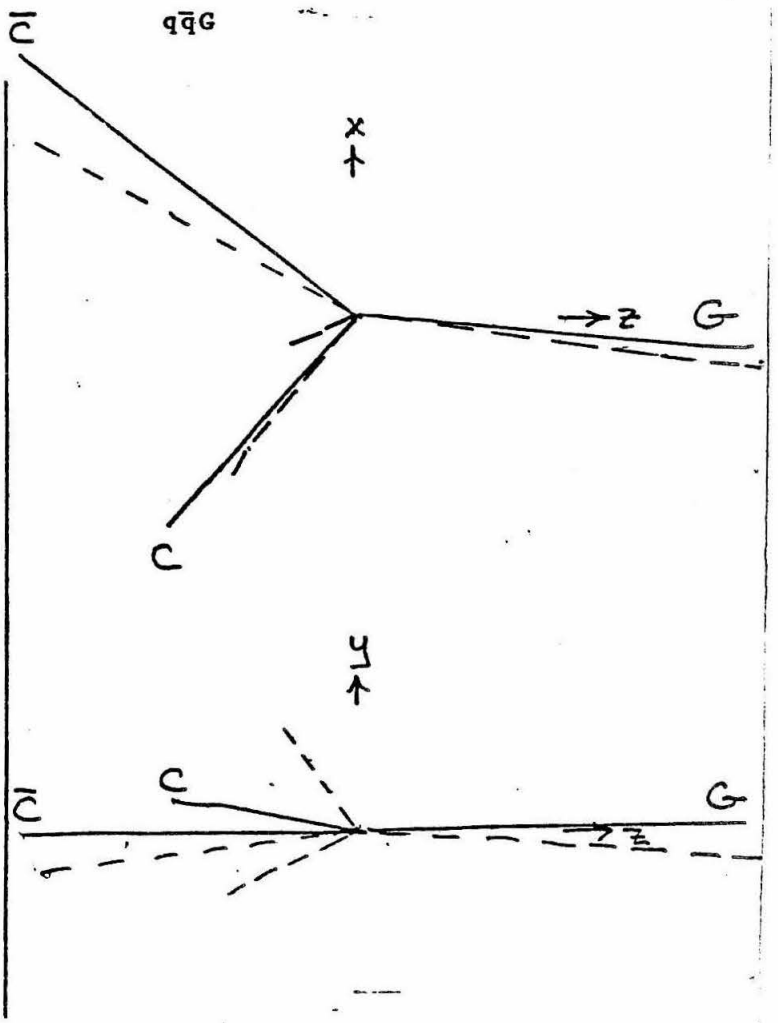

A Gridded Gas Ionization Chamber

by Wuwell Liao

ABSTRACT

A gridded ionization chamber for heavy particle identification in the F.C.P. (Fractionally Charged Particles) search experiment is described which measures the energy E of the detected particle. Preliminary test showed that the resolution (FWHM) of 5.486 Mev alpha particles was about 127 kev. The entrance window is a circular Formvar thin film with the thickness of 40 $\mu g/cm^2$ and the radius of ½ cm.

INTRODUCTION

Gas ionization chamber is one of the oldest and simplest detectors for charged particles. For light particles, its energy resolution is inferior to that of the solid state detector. However, for heavy ions, the energy resolution of gas ionization chamber is comparable to or even better than that of solid state counter. Moreover, there are other limitations, which the ionization chamber is not subject to, to the solid state detectors in heavy-ions detection :

(1) The pulse-height defect becomes important and the response of the detector won't be very linear as the atomic number Z of the ion goes up.
(2) Radiation damage of the crystal by heavy ions deteriorates the performance of the detector.

This gridded ionization chamber is the prototype of the counter that will be used in the F.C.P. search experiment.

The function of the counter is to determine the kinetic energy E of the F.C.P. beam which is accelerated through the Tandem and deflected by electrostatic analyzers. Knowing the angular deflection and the energy E, we can then uniquely determine the charge state of the F.C.P. beam. The first element tested will be Niobium, in which Stanford group claimed they had found F.C.P.

OPERATING SYSTEM OF THE IONIZATION CHAMBER

Figure 1. is the schematic diagram of the gridded ionization chamber. The charged particle, after going through the window, deposits its energy in the gas in the space between aluminum housing (which acts as the cathode) and the Frish grid and thereby leaves a trail of ion pairs. The electrons are pulled toward the anode plate and detected by a charge-sensitive Ge(Li) preamplifier. Since it takes about 30 ev to produce an electron-ion pair in the gas, the pulse height will be directly proportional to the energy deposited in the chamber gas.

The positive ions move about 1000 times slower toward the aluminum housing than electrons. The purpose of the Frish grid is to shield the anode from the field of the positive ions, so that the preamplifier will not detect any charge induced by the positive ions. If the field due to positive ions is not shielded, the pulse coming out of the pre-amp will not be well defined due to long rise-time and variable pulse height.

The grid is a sheet of Nickel mesh of 95% geometrical transparency. It is soldered and glued onto a brass frame which is tightly fixed on the sides by lucite. The anode plate is made of ⅜" thick brass with surface etched and well cleaned. Both the plate and the grid are fixed on the lucite support which is attached to the back plate and firmly fitted in the aluminum housing. This design helps to avoid the problem of microphonics.

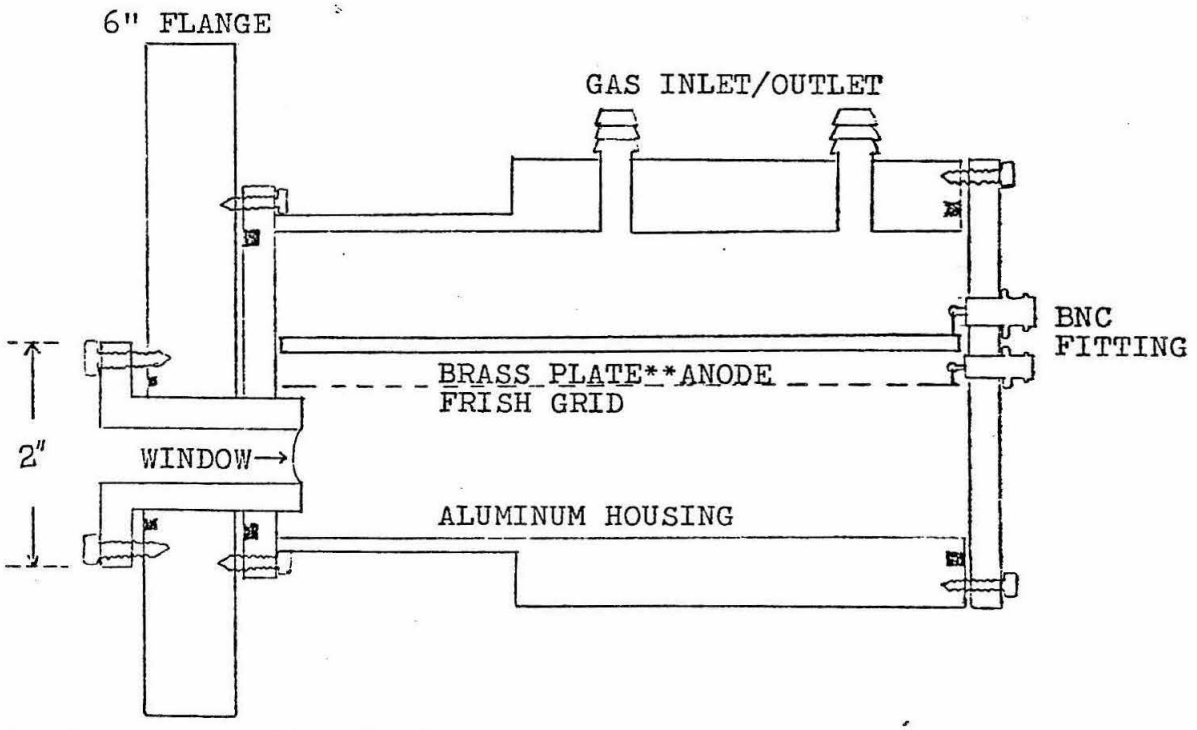

Fig. 1. A cross-sectional view of the cylindrical chamber

Figure 2 is the diagram of the gas supply-regulation system and electronics. The gas in the counter is maintainted at 70±1 torr. Regulation of the pressure in the counter is accomplished by a Cartesian manostat. Counting gas from a gas bottle at high pressure flows through a needle valve, cooled by dry ice in acetone, then through the counter and to the Cartesian manostat, to another needle valve, and finally to a vácuum pump. The use of flowing gas system reduces the probability of the presence of the materials that would normally poison the counting gas.

The pre-amplifier is of the charge-sensitive type. The grid and the anode voltages are supplied from an Ortec detector power supply. The signal from the amplifier is connected to a Multi-channel analyzer and is monitored by an oscillscope. After calibration, we will know the energy deposited in the chamber of the incoming particle by looking at the channel number of the peak on the MCA screen.

PREPARATION OF WINDOW FILMS

Thin Formvar films are used as the window to seal the counting gas in the counter. These films must be very uniform, micro-pinhole free, and easy to reproduce. Two types of Formvar, 15/95E and 12/85, and various solvents were tested. Among those tested solvents, only Cyclohexanone will spread out on the surface of the water. Hence the solution of Formvar 12/85 in Cyclohexanone was used to spray on the surface of the water to form 2-5 $\mu g/cm^2$ thin films for lamination. However, when increasing the concentration to produce thicker films, this

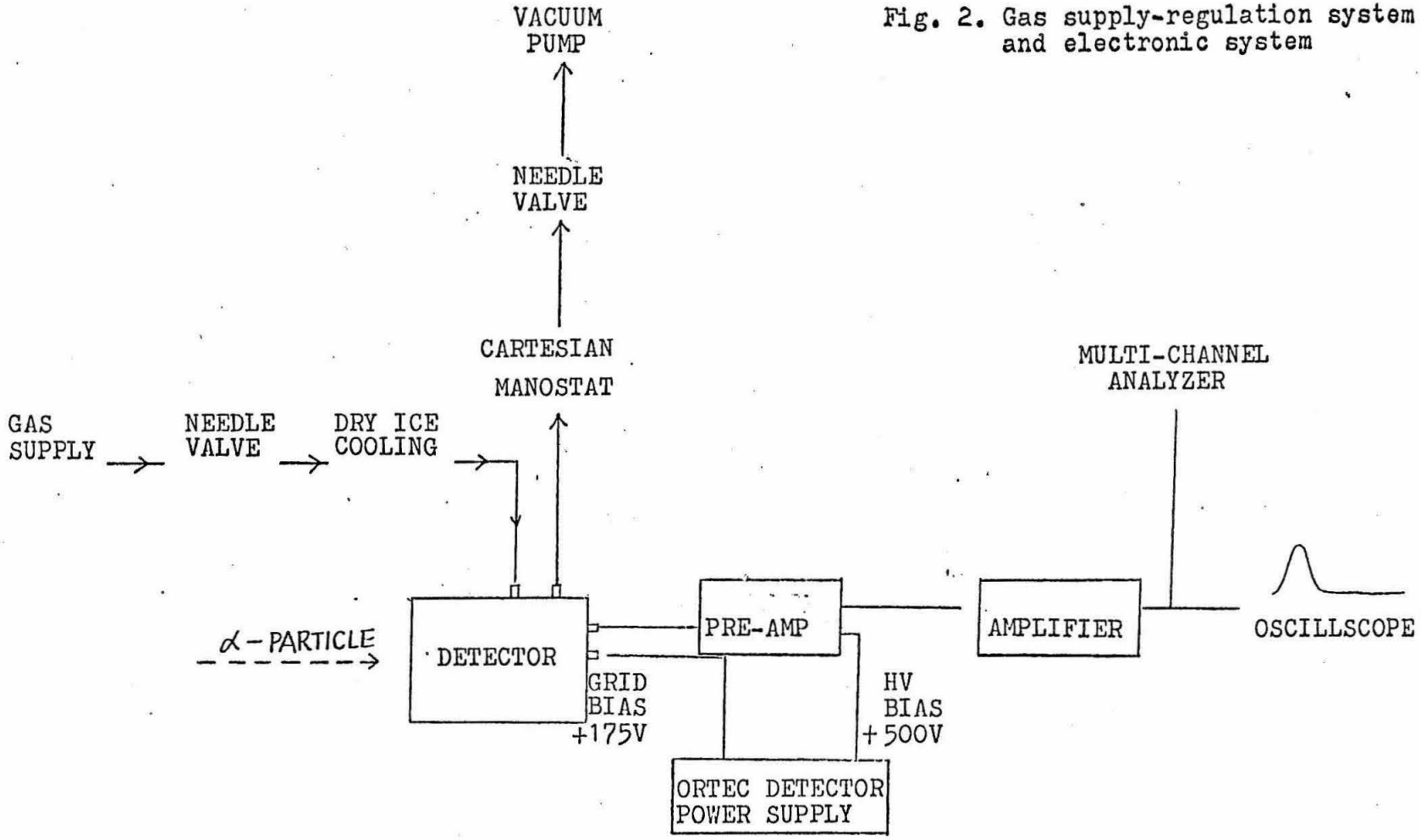

Fig. 2. Gas supply-regulation system and electronic system

method fails to give very uniform films. Often the center part is much thicker than the outer part.

In order to produce uniform thick films (thickness $\geq 20\ \mu g/cm^2$), another method is employed. The Formvar powder is dissolved in Chloroform. A glass microscope slide is then immersed in the Formvar solution in a flow-controlled funnel. After one minute, the solution is drained out at fixed speed. The constancy of the flow rate of the solution is vital to the uniformity of the film casted on the slide. By varying the concentration of the solution, we can make films of any thickness. Once the process is calibrated, it is easy to reproduce films of desired thickness. Furthermore, it is important that the whole process be carried out in the dust free region in order to prevent any micro-pinhole on the films.

After numerous tests, results showed that the above method does give very uniform and reproducible thin films. For our 1 cm diameter window, $40\ \mu g/cm^2$ window films can seal (vacuum side at 100 micron) only up to 30 torr. After that, the stretched films start to leak and finally break at about 40 torr. Hence, either the counter has to be made longer or the window size has to be made smaller.

EXPERIMENTAL RESULTS AND CONCLUSION

Alpha particles from ^{241}Am are used to test the performance of the counter. The counting gas used is CH_4, cooled with dry ice in Acetone. Methane has the good properties of being fast, long mean free path for electrons, good stopping power,

and low electron affinity. The grid and the anode plate is 175 V and 500 V respectively.

With the window of thickness 125 $\mu g/cm^2$, the total resolution (including the straggling in window films) of the detector are the following :

(1) 5.38 MeV at p=355 torr, FWHM=130 keV.
(2) 0.79 MeV at p= 70 torr, FWHM= 63 keV.

Acknowledgment

I would like to thank Jeff Ungar for his zealous helps in designing and testing the chamber. Also, I am grateful to all SURF sponsors and Dr. R.D. Mckeown for giving me this valuable opportunity to carry out this work.

REFERENCES

(1) M.M. Fowler and R.C. Jared, Nucl. Instr. and Meth. 124 (1975) 341-347
(2) R.W.M. Revell and A.W. Agar, British J. Appl. Phys. 6,23 (1955)

Reactivity of Bis-Pentamethylcyclopentadienyl Zirconium Dihydride with Transition Metal Alkylidene Complexes

by Andy Liu

Abstract: $(\eta^5\text{-}C_5Me_5)_2ZrH_2$ reacts with $(\eta^5\text{-}C_5H_5)_2Ta(CH_2)(Me)$ in the presence of PMe_3 to form $(\eta^5\text{-}C_5Me_5)_2Zr(Me)(H)$, $(\eta^5\text{-}C_5Me_5)_2ZrMe_2$, $(\eta^5\text{-}C_5H_5)_2Ta(Me)(PMe_3)$, and methane.

Introduction: The reduction of carbon monoxide by transition metal hydrides is an area of intense current interest. In the investigation of the permethylzirconocene,"$(\eta^5\text{-}C_5Me_5)_2Zr$"(1), system, it was found that dihydrogen reacts with $(\eta^5\text{-}C_5Me_5)_2Zr(CO)_2$(2) to reduce the carbon monoxide on the metal to form $(\eta^5\text{-}C_5Me_5)_2Zr(H)(OCH_3)$(3)[1,2,3] in nearly quantitative yields (eq.1)

eq.1:

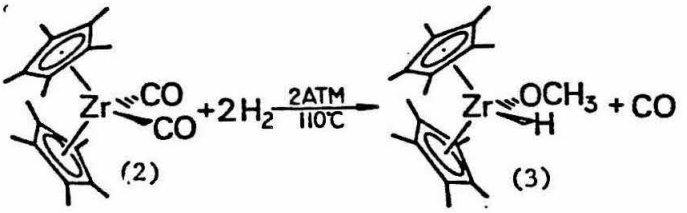

It was also found that the dihydride complex $(\eta^5\text{-}C_5Me_5)_2ZrH_2$(4) also reacts with (2) to form the methoxy hydride complex (3), but the major product of the reaction is the cis dimer, $\{(\eta^5\text{-}C_5Me_5)_2ZrH\}_2(\mu\text{-}OCHCHO)$[2,3,4](eq.2).

eq.2:

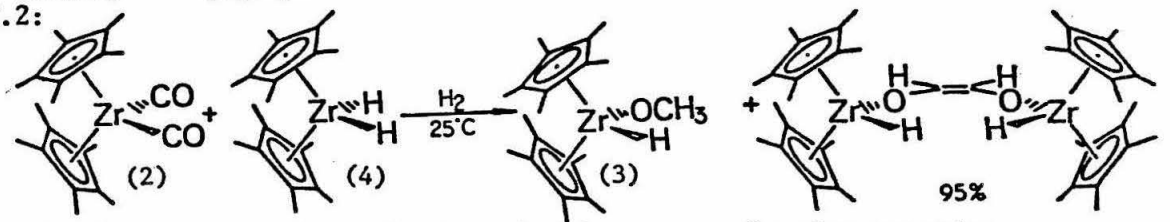

To investigate the mechanism of this stereoselective reaction, the similar but sterically less bulky complex, $(\eta^5\text{-}C_5H_5)_2Zr(CO)_2$(5), was used in place of (2) in the above reaction producing the expected zirconoxycarbene (6)[5,6,7](eq.3). This reaction, however, must be carried

eq.3:

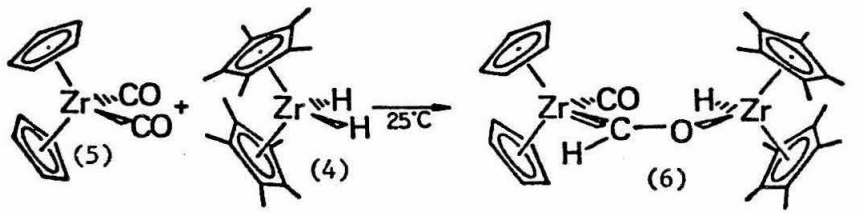

out in small exess of (5) in dilute solutions or a second product is observed. This second product is proposed to result from reaction of a second equivalent of $(\eta^5\text{-}C_5Me_5)_2ZrH_2$(4) with the carbene (6) (eq.4).

eq.4:

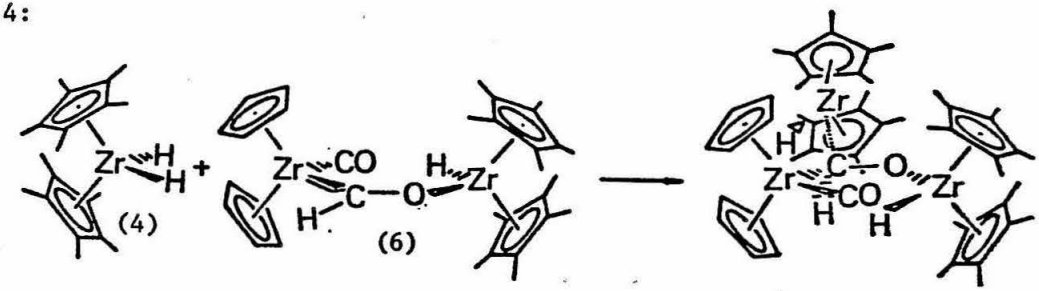

Such an addition of a metal hydride across a metal-carbon double bond had no precedent but is analogous to the insertion of the metal hydride into carbon-carbon double bonds which has been proposed in such processes as olefin isomerization and hydrogenation. To further investigate this process, experiments were carried out studying the reactivity of $(\eta^5\text{-}C_5Me_5)_2ZrH_2$(4) with various transition metal complexes containing metal-carbon multiple bonds.

Results: Permethyl zirconocene-hydrogen bonds as well as the related zirconocene-hydrogen bonds are known to react with carbon-carbon multiple bonds[8,9](eq.5,6).

eq.5:

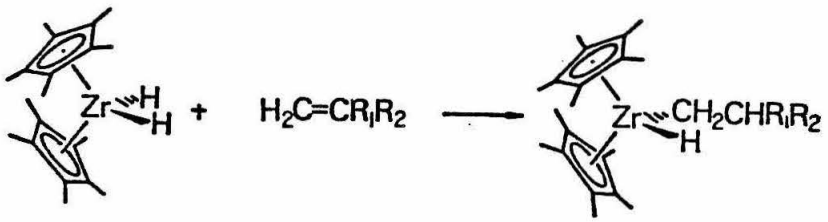

R_1	R_2
H	H
H	Et
Me	Me
H	^{t}Bu
H	Ph

eq.6:

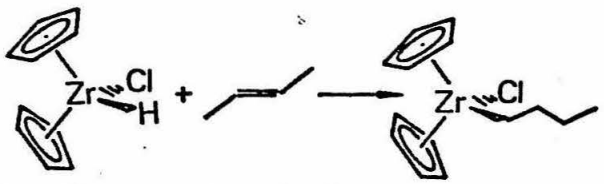

Thus the reaction of (4) with various carbenes was attempted[10,11] (eq.7-9) No reaction was observed by ^{1}H NMR for any of the samples.

eq.7:

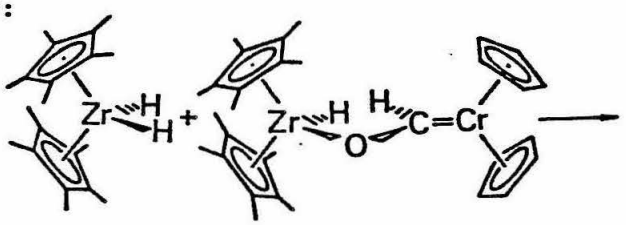

eq.8:

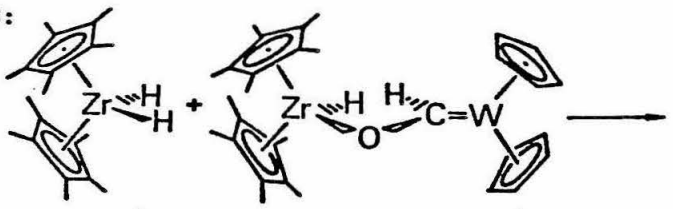

eq.9:

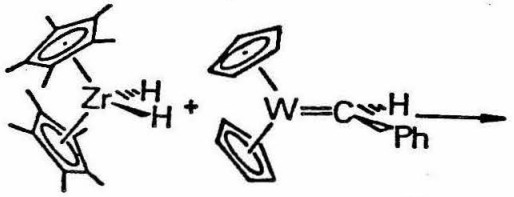

When the samples were heated to 80°C for prolonged periods, the only change observed was that the (η^5-C_5Me_5) peak of (4) (δ2.00) slowly decreased in amplitude while a new peak grew in the same region (δ1.83)- a decomposition that is observed when (4) is heated in solution[12].

Since it is known that (4) will only add to terminal or disubstituted olefins[8,12,13], it would appear that the lack of reactivity is due to adverse steric interactions between the alkylidene and the (η^5-C_5Me_5) ligands of (4). Hence methylidene complexes appear to be the most likely to react with (4). Thus (η^5-$C_5H_5)_2Ta(CH_2)(Me)$(7) was prepared[14] and treated with (4) in benzene. Reaction is immediate as (η^5-$C_5Me_5)_2Zr(H)(Me)$, (η^5-$C_5Me_5)_2ZrMe_2$, CH_4, (η^5-$C_5H_5)_2Ta(C_2H_4)(Me)$ together with various unknown tantalum decomposition products were observed. Over a period of several hours, the reaction was complete (all starting materials were consumed as observed by ^{1}H NMR) with the ratio of (8) to (9) of 8:3. With time, however, the less stable methyl hydride complex (8) appears to convert to the dimethyl complex; at the end of two weeks the ratio of (8) to (9) decreased to 6:5 - a process that would be looked into. To stabilize the (η^5-$C_5H_5)_2Ta(Me)$ fragment that is assumed as the initial tantalum product, one equivalent of PMe_3 was added to the reaction mixture. The expected products (8), (9), (η^5-$C_5H_5)_2Ta(PMe_3)(Me)$(10)[14], methane, and small amounts of unknown tantalum complexes were observed. The gas evolved in the reaction was Toepler pumped off and was identified as methane by infrared spectroscopy. The ratio of (moles of starting material):(moles of methane) was found to be 4.3:1.0.

Other methylidene or methylidene generating species were also treated with (4). {(η^5-$C_5H_5)_2TiCH_2$}$_2$ did not react with (4) in benzene at room temperature. (η^5-$C_5H_5)_2Ti(CH_2)(PMe_2Ph)$(11) appears to react with (4) over a period of an hour to form (η^5-$C_5Me_5)_2Zr(H)(Me)$, methane, and another compound as yet unidentified. It is unclear what the fate of the titanium species is. Unfortunately sufficient amounts of pure (11) are not yet attainable. These experiments will continue when this difficulty is overcome.

Discussion: In the reaction of (η^5-$C_5Me_5)_2ZrH_2$(4) with (η^5-$C_5H_5)_2Ta(CH_2)(Me)$(7), in the presence of PMe_3, (η^5-$C_5Me_5)_2Zr(H)(Me)$(8), (η^5-$C_5H_5)_2Ta(PMe_3)(Me)$(10), and CH_4 were produced. This strongly suggests that the intermediate (η^5-$C_5Me_5)_2(H)Zr(\mu$-$CH_2)Ta(H)(Me)(\eta^5$-$C_5H_5)_2$(12) was first formed (though not observed) followed by rapid reductive elimination at the tantalum center to produce (8) and (10). The methyl hydride complex (8) can then add to a second molecule of (7) to form (η^5-$C_5Me_5)_2(Me)Zr(\mu$-$CH_2)Ta(H)(Me)(\eta^5$-$C_5H_5)_2$(13) which then decomposes to (η^5-$C_5Me_5)_2ZrMe_2$(9) and (10). The methane may be formed by either decomposition of (8) or the reductive elimination of the methyl and hydride ligands on tantalum of the complexes (12) and (13). The two paths may be distinguished by labeling (4) with deuterium - if the former is true then CH_2D_2 will be observed but if the latter is correct then CH_3D will be detected. This experiment will be tried.

Though the existence of the intermediates (12) and (13) is strongly supported by the above experiment, nevertheless, these intermediates are never observed. In attempt to synthesize observable and even isolable intermediates, the following reactions will be tried (eq.10, 11) with less bulky ligands it is our hope that the intermediates

eq.10:

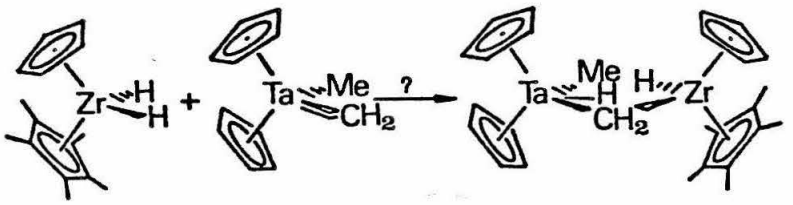

eq.11:

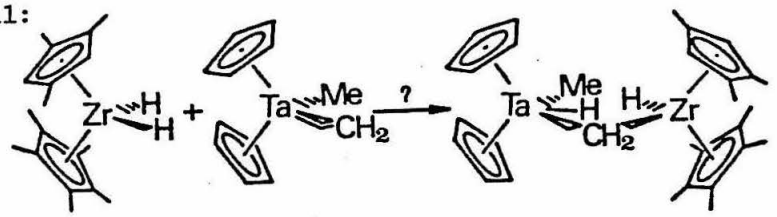

will be formed more rapidly than it decompses.

As a model of alkylidenes, imido complexes will also be tried[15] (eq.12,13).

eq.12:

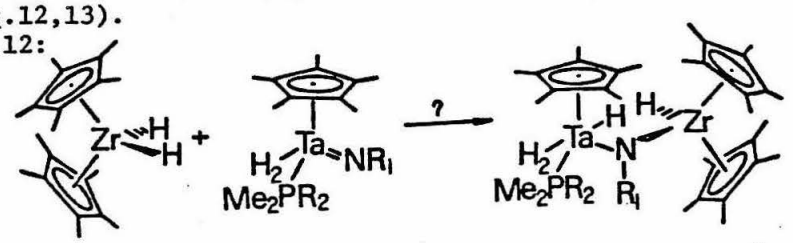

R_1	R_2
CH_2^tBu	Me
^tBu	Ph
CH_2^tBu	Ph

eq.13:

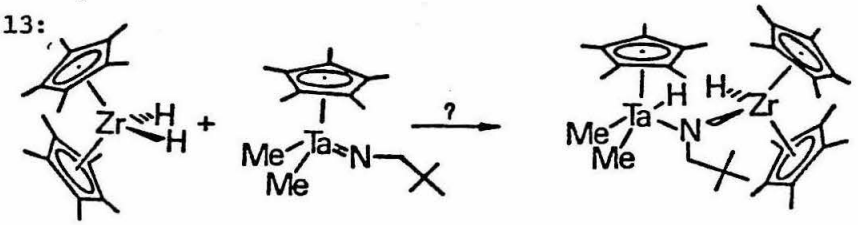

Experimental: All manipulations were preformed by using either glove box or high vacuum techniques. Solvents were purified by first vacuum transfer from $LiAlH_4$ and then from "titanocene"[16]. NMR solvents, toluene-d_8 and benzene-d_6 (stohler, Inc.), were also purified by transfer from "titanocene". Hydrogen and deuterium was passed over MnO on vermiculite and activated 4Å molecular sieves[17].

^1H NMR spectra were obtained on a Varian EM-390 spectrometer and ^2H NMR spectra were recorded with a Bruker WM 500 spectrometer. A Beckman 4240 spectrometer was used for measuring infrared spectra.

Many reactions were carried out in sealed NMR tubes and monitored by ^1H NMR spectroscopy. A typical example is the reaction of $(\eta^5\text{-}C_5H_5)_2Ti(CH_2)(PMe_2Ph)$(4) with $(\eta^5\text{-}C_5Me_5)_2ZrH_2$(4): 18mg(0.055mmol) of (11) and 20mg(0.055mmol) of (4) were transfered to an NMR tube sealed to a ground glass joint to which is fitted a teflon needle valve adapter. benzene-d_6 (0.4ml) was vacuum transferred into the tube at 77K and the tube was sealed with a torch.

$(\eta^5\text{-}C_5Me_5)_2ZrH_2$[2], $(\eta^5\text{-}C_5Me_5)(\eta^5\text{-}C_5H_5)ZrH_2$[18], $(\eta^5\text{-}C_5Me_5)(\eta^5\text{-}C_5$1,2,4 $Me_3H_2)ZrH_2$[18], and $(\eta^5\text{-}C_5H_5)_2Ta(CH_2)(Me)$[14] were prepared via literature procedure. $\{(\eta^5\text{-}C_5H_5)_2TiCH_2\}_2$and $(\eta^5\text{-}C_5H_5)_2Ti(CH_2)(PMe_2Ph)$ were gifts from D. Meinhart, Dr. K. Ott, and Prof. R.H. Grubbs.

1. Manriquez,J.M.; McAlister,D.R.; Sanner,R.D.; Bercaw,J.E. J.Am.Chem. Soc. 98,1976,6733
2. Manriquez,J.M.; McAlister,D.R.; Sanner,R.D.; Bercaw,J.E. J.Am.Chem. Soc. 100,1978,2716
3. Wolczanski,P.T.; Bercaw,J.E. Acc.Chem.Res. 13,1980,121
4. Wolczanski,P.T.; Bercaw,J.E. J.Am.Chem.Soc. 101,1979,6450
5. Wolczanski,P.T.; Threlkel,R.S.; Bercaw,J.E. J.Am.Chem.Soc. 101,1979,218
6. Threlkel,R.S.; Bercaw,J.E. J.Am.Chem.Soc. 103,1981,2650
7. Barger,P.T.; Bercaw,J.E. unpublished results
8. Roddick,D.M.; Bercaw,J.E. unpublished results
9. Hart,D.; Schwartz,J. J.Am.Chem.Soc. 96,1974,8115
10. Prepared via literature. See references 5 and 6.
11. Marsella,J.A.; Folting,K.; Huffman,J.C.; Caulton,K.C. J.Am.Chem.Soc. 103,1981,5596
12. McDade,C.; Bercaw,J.E. unpublished results
13. $(\eta^5\text{-}C_5Me_5)_2ZrH_2$+ 2-methyl-2-butene → reacts but not to form the expected alkyl complex. The complex thus formed is yet unidentified.
14. Schrock,R.R.; Sharp,P.R. J.Am.Chem.Soc. 100,1978,2389
15. Mayer,J.M.; Bercaw,J.E. unpublished results
16. Marvich,R.H.; Brintzinger,H.H. J.Am.Chem.Soc. 93,1971,2046
17. Brown,T.L.; Dickerhoff,D.W.; Bafus,D.A.; Morgan,G.L. Rev.Sci.Instrum. 33,1962,491
18. Wolczanski,P.T.; Bercaw,J.E. Organometallics 1,1982,793

Donald C. Lo
SURF Report
September 16, 1982

A PHOTOCHEMICAL MEANS FOR THE CONTROL OF INTRACELLULAR CALCIUM CONCENTRATION

ABSTRACT -- For the study of calcium-mediated processes we propose to use a calcium chelator whose binding affinity is greatly reduced upon irradiation. We have synthesized a pilot compound that has a binding affinity of 2.2 micromolar, which is reduced ten-fold by irradiation. This suggests that a photolabile chelator effective in the physiological range (~0.1 micromolar) can be constructed.

Intracellular calcium has been found to perform a regulatory function in a variety of cell types. The role it plays may be a primary one, as in certain excitable membranes where it serves as a current carrier, or it may be secondary, serving as a second messenger for other signals. For instance, in the neuromuscular junction, an arriving action potential causes an increase in the calcium concentration inside the nerve terminal; this causes the release of the neurotransmitter acetylcholine. In the muscles themselves, the electrical stimulation effected by the acetylcholine induces the release of calcium stored in the sarcoplasmic reticulum. This calcium in turn interacts with the protein troponin, activating the actin-myosin system responsible for muscle contraction.

In the study of such processes, it is desirable to have a method by which intracellular calcium concentrations can be changed quickly and locally with little interference with the cell's natural physiology. Current methods are very slow in changing intracellular calcium concentration when compared to the time scale of most physiological processes (milliseconds to seconds), and in addition some

involve drastic changes in cell environment.

We have proposed to control intracellular calcium concentration through the use of a calcium chelator whose binding affinity becomes greatly reduced upon exposure to a flash of light. Irradiation of cells that have been loaded with this chelator would cause a virtually instantaneous jump in intracellular calcium concentration. The spatial and temporal resolution thus afforded is unapproached by existing methods; in particular, the extreme speed at which calcium levels may be changed enables the kinetics of calcium-mediated processes to be studied.

Since this compound is to be used in living systems, a number of constraints must be applied to its chemical properties. Foremost, as the internal calcium level of most cells is maintained around 10^{-7} molar, the binding constant of the chelator prior to irradiation should not exceed this level, and should decrease by at least ten-fold after irradiation. Intracellular magnesium concentration is relatively high, some 1-5 millimolar; thus, the chelator must effectively discriminate between calcium and magnesium, preferably by at least a factor of a thousand. Finally, the compound must be stable before and after irradiation, its photoactivation must be rapid and efficient, and it must not have any complicating pharmacology.

In the design of such a molecule, our strategy has been to combine the binding properties of the strong calcium chelators ethyleneglycol-bis-(β-aminoethyl ether)N,N'-tetraacetic acid (EGTA) and ethylenediamine-NNN'N'-tetra-

acetic acid (EDTA) with the photoactivatable properties of azobenzenes or nitroaromatics (Figure 1). The structural

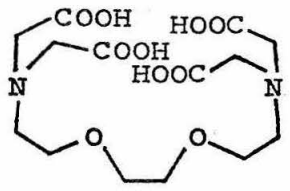

EGTA

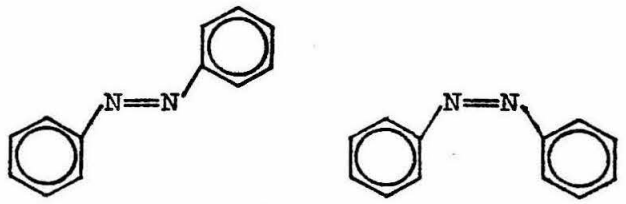

AZOBENZENES

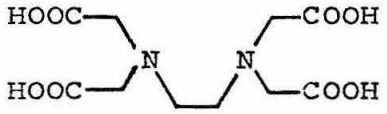

EDTA

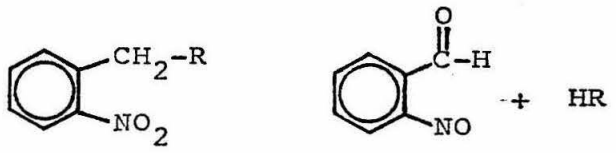

NITROAROMATICS
(Similar reactions occur when the benzylic C is replaced by N or O)

FIGURE 1

rearrangements these molecules undergo upon irradiation should be sufficient to disrupt calcium chelation.

We have synthesized and characterized several such compounds, one of which is shown in Figure 2. Before

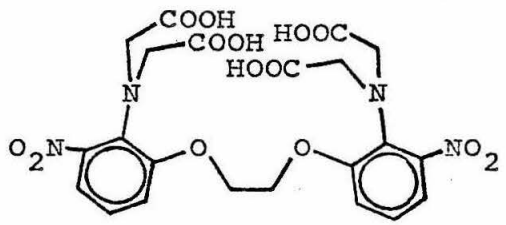

FIGURE 2

exposure to light, this molecule closely resembles EGTA. Upon irradiation, however, the molecule undergoes cleavage

into two to three fragments. We have measured the binding affinity of the intact molecule to be 2.2 micromolar (0.1 micromolar for EGTA), which decreases by approximately ten-fold upon irradiation.

The measurement of calcium binding affinity itself is a nontrivial problem. Whereas changes in UV-visible absorption patterns can yield accurate binding constants through the use of Scatchard and Hill analyses, absorption changes are often small relative to the resolution of spectrophotometers, and the procedure is always quite tedious.

To surmount these problems, we have extended the operating range of a commercially-available calcium-electrode from its rated lower limit of 10^{-5} molar calcium to 10^{-8} molar; this has enabled us to measure binding constants through the titration of our compounds with calcium. Although its precision is inferior to that of absorption analysis, this method is quite useful as a rapid preliminary test for our experimental compounds, and is accurate to within an order of magnitude. Promising compounds are then investigated further through absorption studies.

The performances of our pilot compounds have been highly encouraging, although the binding properties achieved have not been quite optimal. At present we are engaged in the synthesis and characterization of several more compounds which show promise of extending these preliminary results.

Upon completion of a satisfactory compound, we will be initiating experiments to confirm its effectiveness in the

living cell. A well-characterized system such as the snail neuron will be used in conjunction with standard intracellular calcium assays, such as the metallochromic indicator Arsenazo III and the calcium microelectrode, to measure its photolability in a cytoplasmic environment.

PHASE TRANSITION OF AMORPHOUS (Zr.667 Ni.333)1-x Bx

Alan Mak
W.M.Keck Laboratory of Engineering Materials,
California Institute of Technology, Pasadena,
California 91125, USA

ABSTRACT

Amorphous samples of (Zr.667 Ni.333)1-x Bx where $0 \leqslant x \leqslant .25$ were prepared. Their electrical and superconducting properties were measured as a function of boron concentration. The results indicate that phase transition is possible and that for our material it probably occurs when the boron concentration is 4%.

INTRODUCTION

Liquid alloys can solidify without going through crystallization. This is achieved by various quenching or rapid cooling techniques. The resulting amorphous solids formed are catagorized as metallic glass. The study of metallic glass is relatively new. No single model has been established to explain all their properties. Yet their unique characteristics guarantee this class of metals strong potential in industrial applications. Because of the lack of long range order, dramatic changes in atomic structures due to continuous variations in alloy compositions (a kind of phase transition) are believed to be impossible. In this experiment attempts were made to prove the existence of such phase transitions. The strategy was to vary the percentage boron in (Zr.667 Ni.333)1-x Bx and observe the corresponding changes in density, electrical resistivity, critical magnetic field gradient, superconducting transition temperature and the deduced density of electronic states at the Fermi surface.

EXPERIMENTAL

Ingots of the desired compositions were made under an argon atmosphere on the silver boat, a device that employs induction melting and magnetic repulsion. The melt spinner then turned the ingots into amorphous ribbons, some were as thin as 20 microns. The amorphous structures were confirmed by running rough X-ray scans. To measure density with uncertainty less than .5%, the hydrostatic weighing technique[1] was adopted, with toluene as the working fluid. An a.c. bridge was used to measure superconducting transition temperature Tc, and a variable magnetic field was employed to study the critical magnetic field Hc2. The last two measurements required the sample temperature to be below 4°K, and liquid helium was used for that purpose.

RESULTS

The curves of density (fig 1), electrical resistivity ρ (fig 2), critical field gradient (fig 3) and density of states at Fermi surface (fig 5 except for a proportionality constant) all exhibite a sudden change in slope at about 4% boron. On the other hand discontinuity for the superconducting transition temperature occurs at around 12%.

DISCUSSION

The dramatic behavior shown by density, resistivity, critical field and density of states provides strong evidence of a phase transition at 4% boron. It remains to reconcile the "delayed" drop in superconducting transition temperature. To accomplish this task, let us label the structure before the 4% phase transition as phase I and that after as phase II. Let us further suppose that phase I has a higher Tc than phase II. It is very likely that a small portion of phase I remains even when the percentage boron is above 4%. As long as these phase I alloy forms a continuous path, the sample as a whole would have the higher phase I Tc. In this way the transition at 4% boron is concealed. At boron concentration above 10%, the amount of phase I material is not enough to form a continuous path. Hence the sample assumes the phase II Tc.
Computation of density of states at the Fermi surface $D(\epsilon_F)$:

$$Hc2 = \frac{dHc2}{dT}\,(Tc - T)$$

$$\frac{dHc2}{dT} \propto \rho\,\gamma$$

$$D(\epsilon_F) \propto \gamma \propto \frac{dHc2}{dT} \cdot \frac{1}{\rho}$$

CONCLUSION

Our data strongly indicate the existence of a phase transition at about 4% boron concentration. A better confirmation can be obtained by running detailed X-ray scans, specifically studying the radial distribution function RDF.

ACKNOWLEDGEMENT

The author would like to thank Dr. W.L. Johnson and his group for their enlightened guidance and grateful assistance.

BIBLIOGRAPHY

1 H. Berman, Am. Mineralogist 24 (1939) 434.

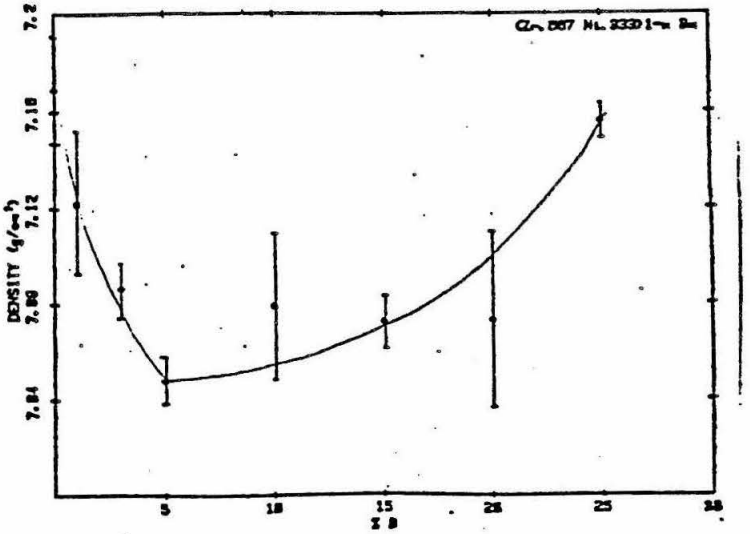

Fig 1

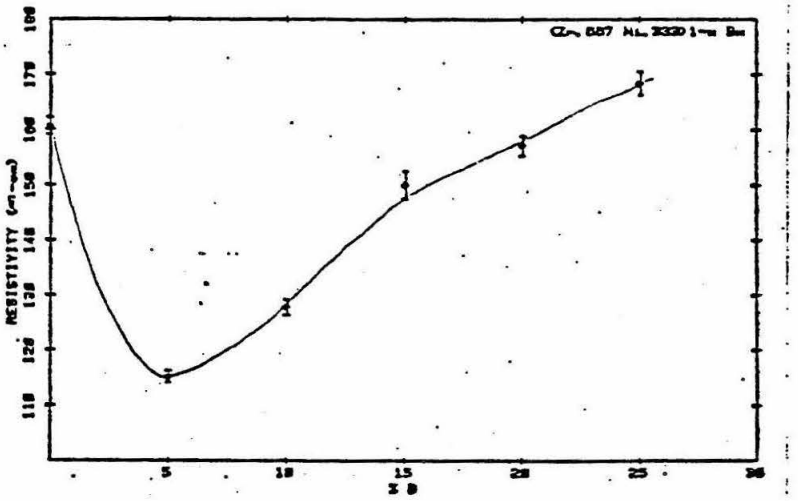

Fig 2

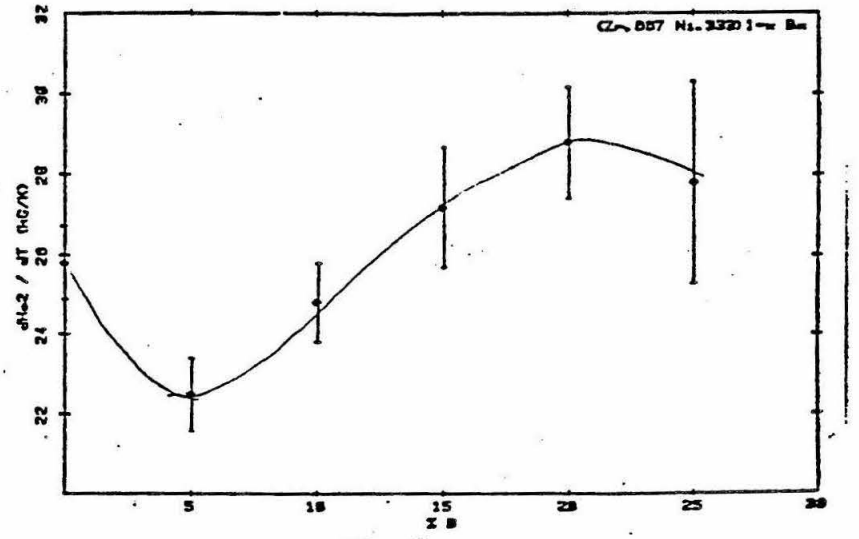

Fig 3

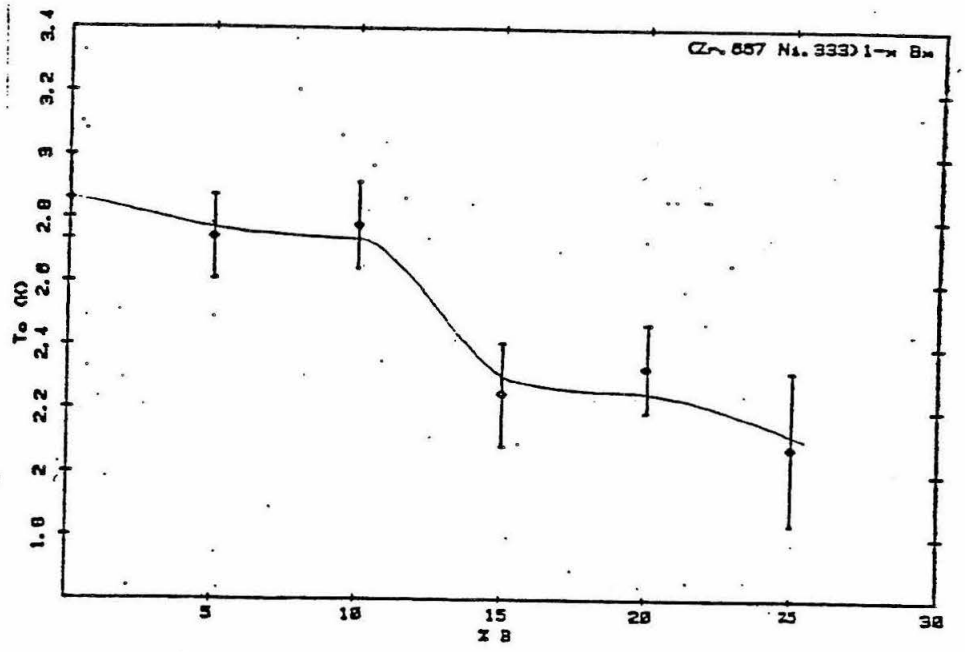
Cz~ 857 Ni. 3330 1-x Bx
To (K)
1.8
2
2.2
2.4
2.6
2.8
3
3.2
3.4
5
10
15
20
25
30
x B

Fig 4

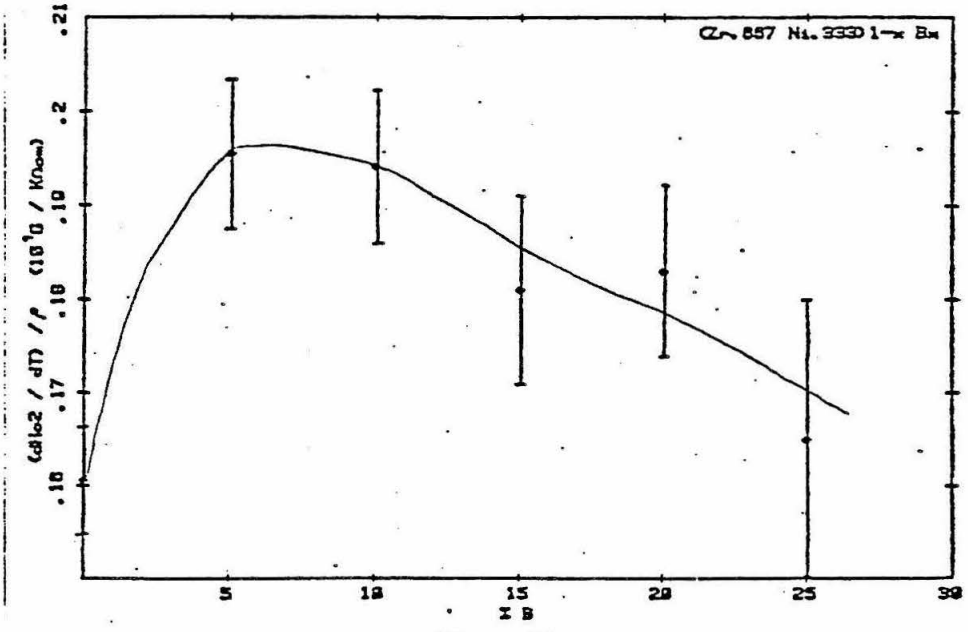
Cz~ 857 Ni. 3330 1-x Bx
(d1n2 / dT) / ρ (10³Ω / KΩcm)
.16
.17
.18
.19
.2
.21
5
10
15
20
25
30
x B

Fig 5

TROUGH SHAPED FEATURES ON SATURNIAN SATELLITES

by Mark Marley

This study was undertaken to characterize and explain the formation of the troughs found on the surfaces of the icy Saturnian satellites by Voyager 1 and 2. Troughs on satellites in the Saturnian system were found to have a remarkably constant size and morphology over the wide range of satellite sizes. Although several mechanisms of trough formation seem likely, no single mechanism adequately explains all of the features observed.

The images of the icy Saturnian satellites returned by the Voyager spacecraft indicated significant modification of the surfaces of the bodies by internal processes.[1-3] The satellites of interest, Mimas, Dione, Enceladus, Rhea, Tethys, and Iapetus are predominantly composed of water-ice. It has been proposed by Stevenson,[4] however, that the presence of NH_3 as a hydrate in the satellites could result in a low melting point magma which may be responsible for much of the surface modification, including the formation of the numerous troughs found on the surfaces of the satellites. These troughs are long, curvilinear features found on all of the icy satellites in the Saturnian system. This investigation attempted to characterize the troughs and identify a mechanism which could result in trough formation.

Topographic information on trough width, depth, and cross-sectional morphology was obtained by photoclinometric analysis of actual Voyager images. Photoclinometry is a process whereby topographic information is inferred from the shading of specific picture elements when compared to surrounding elements. It is a quantitative method that in a sense duplicates the process the human eye and brain do qualitatively when examining shadows to determine relief in an aerial photo. Photoclinometric profiles were generated by a computer program developed and explained by Passey,[5] who estimates that depths determined by the program are within ±25% of the actual depths within a 95% confidence interval.

The photoclinometric data, coupled with direct observation of the Voyager frames and analysis of maps indicated that the trough size and morphology are strikingly uniform from body to body even though the radius of the various satellites (and thus surface gravity) differ almost a factor of 4. Troughs can range in length from 20 to 400 km; the majority of troughs on all the satellites, however, lie in the 30-50 km range. It is trough widths and depths, which ought to be the characteristics most sensitive to local gravity, which are remarkably uniform. The typical trough depth is 0.3 ± 0.1 km (this value is close to the maximum resolution obtainable through photoclinometry). The average trough width is 5 ± 1 km, although Mimas is atypical, having an average trough width of 11 ± 2 km. Most of the troughs studies exhibited a width to depth ratio of ~15.

Troughs generally maintain a constant cross-sectional shape, width, and depth along their length. The typical trough cross-section is a gently sloping U shape. One important aspect of trough morphology is that the great majority of all the troughs have one, and occasionally both, ends associated with a pit crater which may or may not be of impact origin. The crater is usually 2-3 times the width of the trough and occasionally much larger. Such pits generally are only associated with one trough. In localized areas most troughs tend along a single direction and there are global trends which can be recognized as well. On Dione and Tethys trough orientation is generally aligned Northwest to Southeast, while troughs on Rhea are aligned Northeast to Southwest. On Tethys troughs are strongly aligned North to South. These alignments are quite striking and the probability that they are due to random chance is quite small (generally <5%). The alignments may give information about the tensional environment of the satellites when the troughs formed. Each satellite may have undergone a period of radial expansion caused both by thermal expansion and the phase change from ice to a water-ammonia magma. This expansion could have played an important role in trough formation.

In addition to the troughs on the Saturnian satellites there are also trough-shaped features on the Galilean satellite Callisto. The troughs on Callisto are of similar size to the Saturnian troughs but are generally more sinuous and more degraded. It is not clear that troughs on Callisto formed through the same mechanism as the Saturnian troughs.

The troughs of the Saturnian satellites are also similar in some respects to trough-like features elsewhere in the solar system. On Mars there are pit chains which join to form trough like features which may have formed when subsurface magma was removed.[6] On the Moon there are long channels or sinuous rilles which may have formed when surface lava flows thermally eroded away the lunar surface.[7] In the Earth's arctic there is a glacial phenomenon which forms pits similar to those associated with troughs on the satellites. The phenomenon is known as a Jökulhlaup and occurs when water, which had been trapped beneath a glacier, suddenly escapes to the side leaving a large pit on the glacier's surface.[8] These mechanisms along with the global expansion discussed earlier seem to be the most likely candidates for the trough forming mechanism. No single mechanism, however, can adequately explain the observations, especially the tendency for troughs to originate or end in a pit feature. A final conclusion on trough origin probably must await higher resolution images of the satellites' surfaces.

In conclusion the troughs on the various icy satellites of Saturn show a surprising constancy of morphology despite significant differences in the probable formative environments. The troughs, which are generally associated with a pit, show clear global directional trends. There are apparently no features elsewhere in the solar system whose method of formation can adequately explain trough formation. Advanced modelling and better photographs will be needed to explain the trough formative mechanism.

References

1. Smith, B. et al., *Science* **212**, 163 (1981).

2. Smith, B. et al., *Science* **215**, 504 (1982).

3. Plescia, J.B. and Boyce, J.M., *Nature* **295**, 285 (1982).

4. Stevenson, D.J., *Nature* **298**, 142 (1982).

5. Passey, Q.R., Ph.D. thesis, California Institute of Technology (1982).

6. Sharp, R.P. and Malin, M.C., *Geol. Soc. Amer. Bull.* **86**, 593 (1975).

7. Hulme, G., *Geophys. J. Roy. Astron. Soc.* **39**, 361 (1974).

8. Björnsson, H., *Jökull* **25**, 1 (1975).

DAVE MARVIT

No Report Submitted

MACLEN MARVIT

No Report Submitted

Seperation of Viscous and Elastic Effects in Viscoelastic Fluids

Abstract

The non-Newtonian behavior of many polymer solutions is both shear-thinning and elastic(viscoelastic). By utilizing appropriate fluids, however, these effects may be seperated experimentally.

Introduction

The flow characteristics of both Newtonian and viscoelastic fluids are well documented. To date, however, an experimental seperation of viscous and elastic effects has not been done. By comparing a purely elastic(Boger) fluid and a purely shear-thinning(psuedo-plastic) fluid[1] with both a Newtonian and a viscoelastic fluid, a seperation of the two effects is possible.

Presentation

The experimental vehicle for this study was a tethered sphere[2] attached to a ring force transducer(strain guage). The transducer was fixed to a translational system, which raised and lowered the sphere at a constant velocity(.2 to 1 cm/s) through various fluids.[3] Force measurements were taken on a strip chart recorder from the voltage drop across the transducer.[4]

---

[1] Actually, these are viscoelastic fluids where the one effect dominates the other.

[2] Two spheres of 3/4" and 1" diameters and wires of .004"and .008" were used.

[3] Polybutene #16 and corn syrup were the Newtonian fluids. 4ppm of separan added to the corn syrup was the elastic fluid. A .15% solution of Carbopol in water was the psuedo-plastic fluid, and a .8% solution of separan and water was the viscoelastic fluid.

[4] For a more detailed description see Berdan, Ph.D. Thesis, CALIFORNIA

Interpretting the data required several considerations. Since the force measurements were compared with theoretical results for the drag on a sphere alone, the effect of the wire in the experiment had to be accounted for. Fortunately, most of the fluids flowed cleanly off the wire as it left the fluid; by measuring the drag on just a wire, the problem became one of subtraction, with the assumption that the individual drags on the sphere and the wire were additive. Other corrections were the effect of the tank walls[5] on the drag and the buoyancy force due to the changing length of wire.

The results of this experiment are not available at the present time; but a graph of the Reynolds number versus measured drag, non-dimensionalized by Stoke's drag, should seperate the viscous and elastic effects. Another relative graph will be a plot of the non-dimensional drag versus the Weissenburg number. The SURF program will be mentioned in the forthcoming paper and will receive copies of it.

---

[5]The tanks were a 15x15" square tank, and two round tanks of 5½" and 2" diameters.

EDWARD MILES

No Report Submitted

DICHROMATED GELATIN HOLOGRAMS

Sergay Mnatzakanian

SURF 1982

ABSTRACT

One can find various suggested methods and techniques for making dichromated gelatin holograms in different publications. In this experiment commercially available holographic plates (Kodak 649-F) were used as a gelatin base for the holograms. The gelatin plates were then dichromated and exposed, and results studied.

INTRODUCTION

Dichromated gelatin holograms are being used more than ever before, both in making Holographic Optical Elements (HOE's), as well as artistic pictorial holography. The reasons behind this are:

(1) A very large refractive index modulation upto 0.08 .

(2) Very high resolution capacity, upto 5000 lines/mm .

(3) The thickness of the dichromated gelatin hologram can be controlled, mainly by varying the humidity in the procedures.

(4) Dichromated gelatin holograms are environmentally stable as long as they are not exposed to humidity.

(5) Dichromated gelatin holograms have a quite high signal to noise ratio.

The above qualities of dichromated gelatin holograms, specially high resolution and thickness flexibility, make them a very suitable holographic recording medium for Holographic Optical Elements.

PROCEDURE

There are several methods of making dichromated gelatin holograms, one is even indirect -- i.e. first the hologram is recorded on silver halide and then transferred onto the dichromated gelatin. I chose to use direct methods for this project. There are several suggested procedures that follow more or less the same pathes. All the experiments were done using Kodak 649-F holographic plates. First the plates were fixed to get rid of the silver halide, and then they were dichromated and exposed. Then the dichromated plates were developed , which seems to be the most sensitive procedure. There were some variations in the techniques, but a typical procedure is shown in the following tables:

TABLE I Preparing the Dichromated Gelatin Plate:

1 Soak in fixer for 10 minutes.
2 Wash in running water for 5 minutes.
3 Rinse in distilled water for 5 minutes..
4 Soak in Photo-Flo 200 (2 drops/litre) for 30 seconds.
5 Dry the plate at room temprature. (overnight?)
6 Soak in 0.5% amonium dichromate solution for 5 minutes.
7 Dry the plate at room temprature. (overnight?)

TABLE II Developing the Dichromated Gelatin Plate:

1 Soak in 0.5% amonium dichromate for 5 minutes.
2 Soak in fixer for 5 minutes.
3 Wash in running water for 10 minutes.
4 Dip in Photo-Flo for 30 seconds.
5 Soak in distilled water for 2 minutes.
6 Dehydrate in a 50/50 solution of isopropanol and distilled water.for 3 minutes.
7 Dehydrate in 100% solution of isopropanol for 3 minutes.
8 Let the plate dry.

A variety of different times for soaking and drying were tried, specially where it said overnight. Also various exposure times were tried ranging from 10 seconds to 10 minutes. Also the intensity of the laser was varied from 600 $\mu J/cm^2$ to 100 mJ/cm^2. Unfortunately there were no successful results obtained.

CONCLUSION

Considering the wide range of exposure times and various exposure powers, as well as a veriety of developing procedures, it seems wise to deduce that there was a systematic problem. Probably there was a problem with the preparation of the plates, for example the chemicals that were used.

REFERENCES

Chang B. J. & C. D. Leonard, Dichromated Gelatin for fabrication of Holographic Optical Elements, Applied Optics Vol.18 No.14 pp2407-17.

Chang B. J., Post-Processing of Developed Dichromated Gelatin Holograms, Optics Communications Vol.17 No.3 pp270-1.

McCauly D. G. & C. E. Simpson & W. J. Murbach, Holographic Optical Element for Visual Display Applications, Applied Optics Vol.12 No.2 pp232-42.

Preparation and Analysis of a Gene Specific Subclone for Actin Gene J in the Sea Urchin Strongylocentrotus purpuratus

by

Gary Mockli

Abstract

A gene specific subclone for actin gene J from the sea urchin Strongylocentrotus purpuratus has been prepared from its 3' untranslated region. Preliminary analysis show it to be gene specific, existing as a single allelic pair in the sea urchin genome.

Introduction

A number of different actin genes are expressed during the various stages of development as well as in different adult tissues in Strongylocentrotus purpuratus. Approximately eleven nonallelic members of the actin gene family have been found in this sea urchin by screening a lambda library.[1] The 3' untranslated regions of actin transcripts seem to be subfamily specific, i.e., a probe made from this region of an actin gene is homologous with only a subset of the actin gene family. Thus, preparation of subfamily specific clones will allow us to follow the expression of these sea urchin genes throughout early development.

The purpose of this SURF project was to prepare a gene specific subclone for actin gene J. To prepare this subclone, A clone of the entire J gene in pBR322, designated pSpG28, which was prepared by William Crain, was utilized as a starting material (Figure 1)

Results

The gene specific subclone was prepared using the methods of recombinant DNA technology. pSpG28 was grown in E. coli strain HB101.

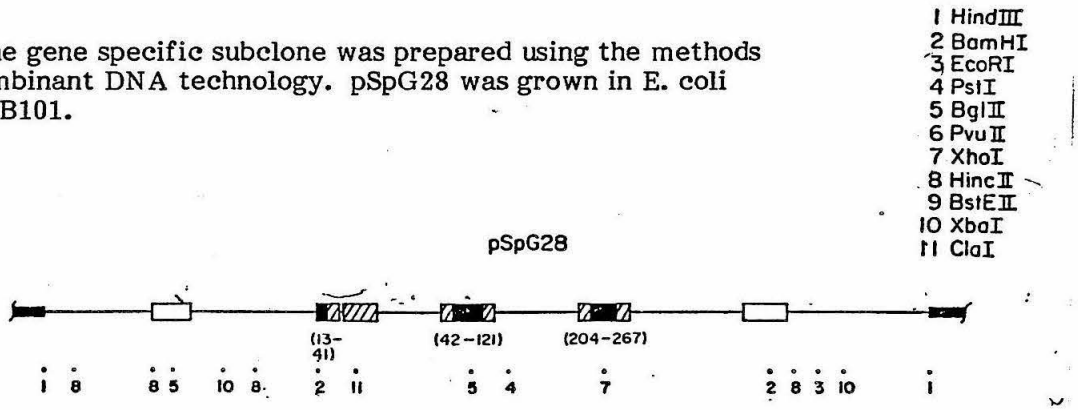

Figure #1

1. Scheller et al. (1918)

Plasmid DNA was isolated via detergent lysis and an ethidium bromide-cesium chloride ultracentrifugation. A BamHI-HindIII restriction digest was used to liberate a probe that is 3' to the last exon, and the desired fragment was isolated on a 1% preparative agarose gel, electroeluted, and purified on a DE 52 ionic exchange column. Vector was prepared from the new recombinant plasmid pUC9, which contains a procaryotic β-galactosidase gene interrupted by a poly linker (this vector was developed by J. Messing of the University of Minnesota). A sticky end ligation was used to unidirectionally insert the desired fragment into the vector. The transformation into HB101 was conducted by the method of Cohen[2] and transformants were identified by means of the β-galactosidase color reaction. Ten of the transformants isolated were then examined via the rapid screen technique of Birnboim.[3]

Figure #2

Figure #3

Figure #4

Plasmid DNA of the specific subclone was also isolated by detergent lysis and ethiduum bromide-cesium chloride ultracentrifugation. Probe was prepared from this subclone by the end fill label method,[4] and the specificity of the subclone was checked on a blot against all the lambdas in our library that contained actin (Figure 2). HindIII and EcoRI genome blots from sperm DNA isolated from one individual, designated Cyril, were then performed (Figures 3 and 4, respectively) to determine the copy number of J-type genes in the sea urchin genome, thus concluding the preliminary analysis of this subclone.

Conclusions

A J-specific subclone has, indeed, been generated. Only J lanes react with probe made from the subclone in the lambda specificity blot. According to the Cyril genome blots there appears to be only a single J-type gene (single band on HindIII genome blot) with two alleles (2 small EcoRI bands) in the S. purpuratus genome.

[2]Cohen et al., PNAS **69**, 989, 1972

[3]H. C. Birboim and J. Doly, PNAS **7**, 1513, 1979

[4]J. W. Posakony et al., submitted

Future Considerations

A J-specific subclone is now available. Subfamily specific subclones for the remaining actin genes are presently being produced. When they are all available, blots against RNAs from a number of early embryological stages and selected adult tissues will be utilized to determine in which stages and tissues the various members of the actin gene family are expressed. Also, intraspecies genome blots will allow us to study the polymorphism in these actin genes, and interspecies genome blots with sea urchins from other genera and species will be performed to study the evolutionary divergence of these genes. Next, titrations will be utilized in order to determine the exact number of copies of these transcripts present in the various embryological stages, while the ultimate goal of this project is to examine the transcriptional kinetics of the various actin genes during development.

DEVELOPMENT OF A COMPUTER PROGRAM FOR MULTIREACTION CHEMICAL EQUILIBRIA

Student: Tarik Naheiri

Sponsor: George R. Gavalas, Ph.D.

Summer Undergraduate Research Fellowship

(SURF)

Summer of 1982

ABSTRACT

The ill effects on our environment of sulfur gas from burning coal are well publicized. Introduction of alkali metal and alkaline earth oxides to remove any sulfur oxides from coal during combustion seems a promising solution. The effectiveness of this method depends on thermodynamic equilibrium considerations. In order to measure the extent of sulfur extraction, we have developped a computer code that incorporates these multireaction chemical equilibria calculations.

INTRODUCTION

The problem of multireaction chemical equilibria can lead to very tedious and complex calculations. Many computer programs have been developped to solve this problem. These computer codes have a major drawback: their generality.

The equilibrium problems that we encounter involve chemical species in the gaseous or solid phases. The need of a specialized and more practical computer program is apparent. The purpose of this project is to derive such an algorithm. We plan to use this as a tool to further our studies in the chemistry of desulfurisation of coal.

PRESENTATION AND DISCUSSION OF RESULTS

A. Theoretical approach.

During any irreversible process, the total Gibbs Free Energy (TGE) of a closed system at constant temperature (T) and pressure (P) drops. When thermodynamic equilibrium is attained TGE assures it's minimum value.

The TGE of a chemical system is a function of the molar amounts of every chemical species present (N(i)), of the pressure P and of temperature T.

$$TGE = \sum_{i=1}^{M} mu(i)*N(i)$$

- mu(i): Chemical potential of species i
- N(i) : Number of moles of species i
- M : Number of species present

Noting that

$$mu(i) = R*T*\ln(f(i))+fct(T)$$

at standard state

$$muo(i) = R*T*\ln(fo(i))+fct(T)$$

$$mu(i) = muo(i)+R*T*\ln(f(i)/fo(i))$$

leading to a definition for mu(i)

$$mu(i) = Gf(i)+R*T*\ln(f(i)/fo(i))$$

combining these two equations, we obtain a general form for TGE.

$$TGE = \sum_{i=1}^{M} N(i)*(Gf(i)+R*T*\ln(f(i)/fo(i)))$$

- f(i) : fugacity of species i in a mixture
- fo(i): pure state fugacity of species i
- Gf(i): Gibbs Free Energy of formation of species i

Since we are dealing with solids and gases only:

solids:

$$f(i) = fp(i)*actcoef(i)*x(i)$$

$$fo(i) = fp(i)$$

$$f(i)/fo(i) = actcoef(i)*x(i) = 1$$

assuming that at equilibrium any solid is pure and unreactive

- actcoef(i): activity coefficient of solid i

- x(i) : molar concentration of solid i

- fp(i): fugacity of solid i at P and T

for all solid phases

$$TGE = \sum_{solids} N(i)*Gf(i)$$

gases:

$$f(i) = p(i) \quad \text{(partial pressure of gas i)}$$

This equality results from ideal gas assumption, since we will be dealing with high temperatures, this assumption is reasonable.

$$fo(i) = \text{constant} = Po \quad \text{(standard state pressure, usually 1 atm)}$$

for all gaseous phases

$$TGE = \sum_{gases} N(i)*(Gf(i)+R*T*\ln(p(i)/Po))$$

In a condensed form

$$(3) \qquad TGE = \sum_{i=1}^{M} N(i)*(Gf(i)+K(i)*R*T*\ln(p(i)/Po))$$

where K(i) is defined to be: 1 if i is a gas

0 if i is a solid

We have now a function of M unknowns that we seek to minimize under two constraints.

These are

a. Conservation of mass

b. All values of N(i) must be greater than zero

This first condition will lead us to N element balances. Where N is the number of elements present. Then we can write N linear equations of the form

$$\sum_{j=NH}^{M} a(j)N(j) = No(i)$$

where No(i) is the original number of moles of element i; (i varies

between 1 and N). If we solve this system of N equations and M unknowns (M greater than N) we will oftain relations of the form:

for each element i:

$$N(i) = \sum_{j=N+1}^{M} a(j)*N(j)+No(i) \quad (4)$$

so that substitution of (4) into (3) will reduce the M variables to M - N. TGE is now a function of M - N variables.

$$TGE = \sum_{j=N+1}^{M} N(j)*(Gf(j)+R*T*\ln(p(i)/Po))+funct(N(j))$$

Where funct(N(j)) expresses N(i) as a linear combination of N(j). (i varies between 1 and N) (j varies between N + 1 and M)

In order to assure that the values of N(i) are positive non zero, we make a change of variables:

ln(N(i)) becomes X(i)

the domain of the natural logarithm function assures us that condition (b) is met.

TGE is now a function of M - N variables X(j). In order to minimize this function we must provide derivative information. The gradient vector will be a very useful tool for the minimization process. The final expression of a gradient component is

$$G(j) = EXP(X(j))*(Gf(j)+R*T*K(j)*(\ln(P/Po)+\ln(EXP(X(j)/GAS)+1) + \sum_{i=1}^{N} B(i,j)*(Gf(i)+K(i)*R*T*(\ln(P/Po)+\ln(E(i)/GAS)+1)) -ZOG(j)/GAS *R*T*(\sum_{i=1}^{N} E(i)*K(i)+ \sum_{i=N+1}^{M} K(j)*EXP(X(j)))$$

- G(j) : partial derivative of TGE with respect to X(j)
- GAS : total amount of gaseous moles
- E(i) : moles of species i, as a function of X(j)
- ZOG(j): partial derivative of GAS with respect to X(j)

- B(i,j): partial derivative of N(i) with respect to N(j)

The function TGE and its gradient vector are defined.

B. Computer.

The program was developped in Fortran. It uses two I.M.S.L.I.B. subroutines.

- LEQTIF: solves a system of N linear equations
- ZXCGR : minimization routine

plus two user supplied subroutines

- DUMMY: calculates values of the Gibbs Free Energy of formation for each species i
- FUNCT: calculates TGE and its gradient for any values of X(j)

CONCLUSION

I am now debugging this program. It will be operational in October of 1982.

I intend to use it as a tool to measure the extent of sulfur extraction from coal.

REFERENCES

Introduction to Chemical Engineering Thermodynamics,
Smith & Van Ness; McGraw Hill.

Process Optimisation,
Ray & Szekely; Wiley Interscience.

SUMMER UNDERGRADUATE RESEARCH
FELLOWSHIP FINAL REPORT

Title: "Structural Analysis of a Gene Expressed Only at Embryonic Stages of the Sea Urchin Stronglyocentrotus Purpuratus"

Student: Glenn Nakamura

Faculty Sponsors: Dr. Constantin Flytzanis
Dr. Eric Davidson

Abstract

From a genomic library of the sea urchin Strongylocentrotus purpuratus, we have isolated three clones carrying a gene which is expressed only during the embryonic stage. We have characterized these clones with restriction enzyme analysis and studied the transcriptional unit on one of the clones. The results are reported herein.

Introduction

The sea urchin embryo is an excellent system for studying the regulation of gene expression during early development. Using eggs and embryos of S. purpuratus, the purple sea urchin, it has been shown that for most poly A$^+$ RNA sequences, the prevalence levels determined during oogenesis are maintained throughout early development. However, a minority of sequences display sharp stage specific changes. A set of clones complementary to poly A$^+$ RNAs that show such stage specific changes has been selected from cDNA libraries of various embryonic stages. Using RNA blots with RNA isolated from embryonic and adult tissues, the developmental pattern of expression of these clones has been investigated[1], and one particular clone has been selected for further study. This cDNA clone (SpP 25) shows a very small number of complementary transcripts, if any, in the egg of S. purpuratus and a dramatic increase in transcripts at gastrula and pluteus stages. A single transcript (1450 bases long) has been identified at these stages. This transcript is absent in intestine poly A$^+$ RNA where the existence of a less prevalent transcript has been shown. To characterize the gene coding for the SpP 25 transcript, a genomic library made from DNA of an individual sea urchin was screened with the cDNA clone, and a set of λclones, λ25.2, λ25.5, λ25.19 have been characterized by restriction digest analysis. Furthermore we subcloned fragments of one of the three genomic cloned segments, and characterized with restriction digest analysis the subclone (called pλ5) that contains sequence homology to the cDNA clone SpP 25. RNA blot hybridizations carried out with radioactively labeled subclones revealed the existence of an intervening sequence. The goal of this investigation is the characterization of the transcripts coming from "gene 25" at different developmental stages and tissues of the sea urchin. The results presented in the following section constitute the basis for further structural analysis needed for a complete understanding of this transcriptional unit.

Results and discussion

Restriction enzyme mapping of the genomic clones.

Figure 1 shows the restriction maps established from single and double digests of the clones λ25.2, λ25.19, and λ25.5. Careful analysis of the maps revealed that λ25.2 and λ25.19 are overlapping fragments coming from the same chromosomal locus. The clone λ25.5 shows an extensive conservation of restriction sites, except for the left end of the insert. The λ25.5 clone was digested with the restriction enzymes Hind III and Eco RI

and the six resulting DNA fragments were labeled and hybridized to blotted restriction digests (using the same enzymes) of the clones λ25.2 and λ25.19. All λ25.5 fragments were homologous to the respective fragments of λ25.2 and λ25.19 except for the two fragments at the left end of the cloned insert, that showed no homology to λ25.19. This result suggests that λ25.5 carries a homologous gene cloned from another chromosomal locus.

Partial characterization of the "gene 25" transcription unit

We analyzed the structure of the genomic clone, λ25.5, in more detail. For this purpose, we subcloned the six fragments that were obtained from a Hind III-Eco RI digest of the DNA into the plasmid vector pBR 322. They were placed either in the Hind III site or the Eco RI, Hind III sites depending on the restriction sites present at the ends of each fragment. Figure 2 (top) shows the subclones obtained. The cDNA clone SpP25 was radioactively labeled and hybridized to the six subclones and only hybridization to subclone pλ5 was obtained. We further characterized pλ5 with restriction digest analysis and a restriction map is presented in figure 2 (middle). When pλ5 was digested with the restriction enzymes Hpa II, Hinc II and Hha I, and blot hybridization carried out using radioactively labeled SpP 25 as a probe, only the Hpa II-Hinc II fragment indicated in figure 2 was positive. This gave us the exact location of the cDNA clone on the genomic subclone. We knew that the cDNA clone represents only a part of the whole mRNA. (The cDNA clone is 320 bases long including the poly d(A-T) tails and the mRNA is 1500 nucleotides long.) The cDNA used to construct the library was primed with oligo dT annealed to the poly A tail the mRNA has on its 3' end. In most of the cDNA clones analyzed so far, the 3' end of the mRNA is included in the cDNA clone. Our experiment suggests that the Hpa II-Hinc II fragment contains the 3' end of the gene. In another experiment, we found the orientation of transcription on the pλ5 subclone. The experiment was designed as follows. We labeled the 3' ends of the Eco RI-Hind III fragment by filling in with Klenow's pol I, digested with Hinc II, then separated the two resulting fragments on an agarose gel. By such a procedure, each fragment has only one 3' end labeled and the label is on different strands. We used these two fragments as probes for RNA blot hybridizations. Only the Eco RI-Hinc II fragment hybridized and consequently the orientation of transcription is from the Eco RI to the Hinc II as noted in figure 2. With the above described experiments, we have localized the 3' end of the gene and found the orientation of transcription. Our next step was to localize the 5' end of the gene (i.e. where transcription starts). We carried out RNA blot hybridizations using all five fragments of pλ5 that result after digestion with Hpa II, Hinc II and Hha I. The five fragments were isolated from an agarose gel and labeled by nick-translation. Two fragments hybridized to the RNA: the Eco RI-Hpa II and the Hpa II-Hinc II. The combined length of the two fragments is about 1,000 base pairs, so the 5' end of the gene was located on another subclone. We labeled the DNA of all six subclones and used them for hybridizations to RNA blots. We found that only two subclones hybridized to

the 1.5 kb RNA, the pλ5 and the pλ6 (see figure 2-top). These two fragments are separated from each other by a 0.6 kb Hind III-Eco RI fragment (pλ2) that did not hybridize to the mature mRNA. This results suggests that at least a 0.6 kb intervening sequence exists at about 1 kb from the 3' end of the gene. More experiments will have to be done to locate the 5' end of the gene and find if it is contained in the pλ6 subclone. If the 5' end is not present in the pλ6 subclone, it will suggest that fragments 1 and 3 are also part of another intervening sequence since these two subclones do not hybridize to the mature mRNA. Also further experimentation will have to be done at the sequence level to find if the RNA corresponding to the cDNA clone SpP 25 actually is transcribed from the gene present in the λ25.5 clone.

Conclusions

We have shown in our analysis that there is more than 1 gene that could have given rise to the transcript of interest. The question of whether λ25.5, λ25.2, or λ25.19 give rise to the transcript or if another gene yet undetermined from our analysis is the actual transcription site is still unknown. However, we have shown evidence of an intervening sequence of at least 0.6 kb, located the gene's 3' end, and determined the direction of transcription. Further experimentation is sure to reveal more about this transcriptional unit.

Bibliography:

Flytzanis, C., Brandhorst, B.P., Britten, R.J., Davidson, E.H. (1981). Developmental Patterns of Cytoplasmic Transcript Prevalence in Sea Urchin Embryos, Develop. Biol.91,27-35

Footnote

1. Flytzanis, C., Brandhorst, B.P., Britten, R.J., Davidson, E.H. (1981). Developmental Patterns of Cytoplasmic Transcript Prevalence in Sea Urchin Embryos, Develop. Biol.91,27-35

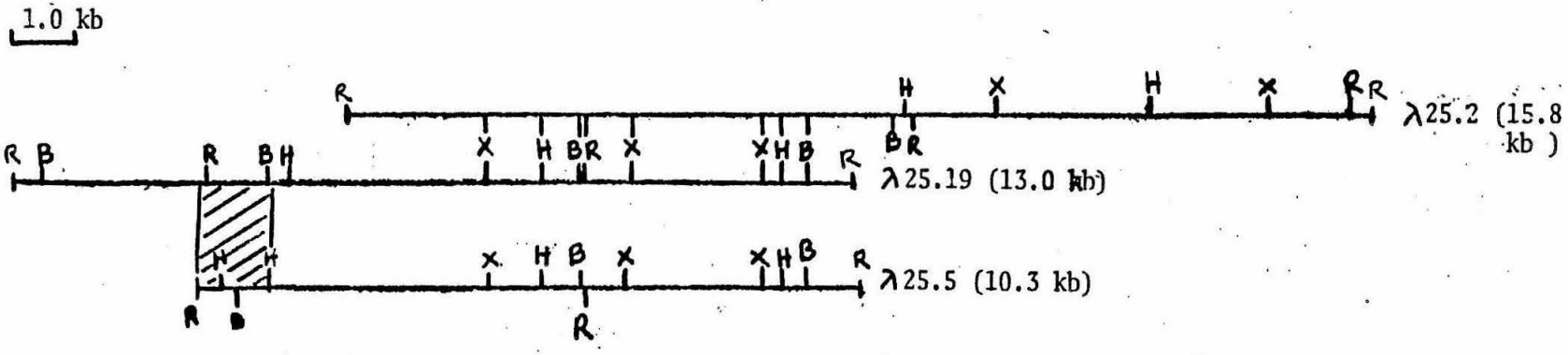

FIGURE 1.

B- Bam HI
H- Hind III
R- Eco RI
X- Xba I

-Region where homology between λ25.5 and λ25.19 diverges.

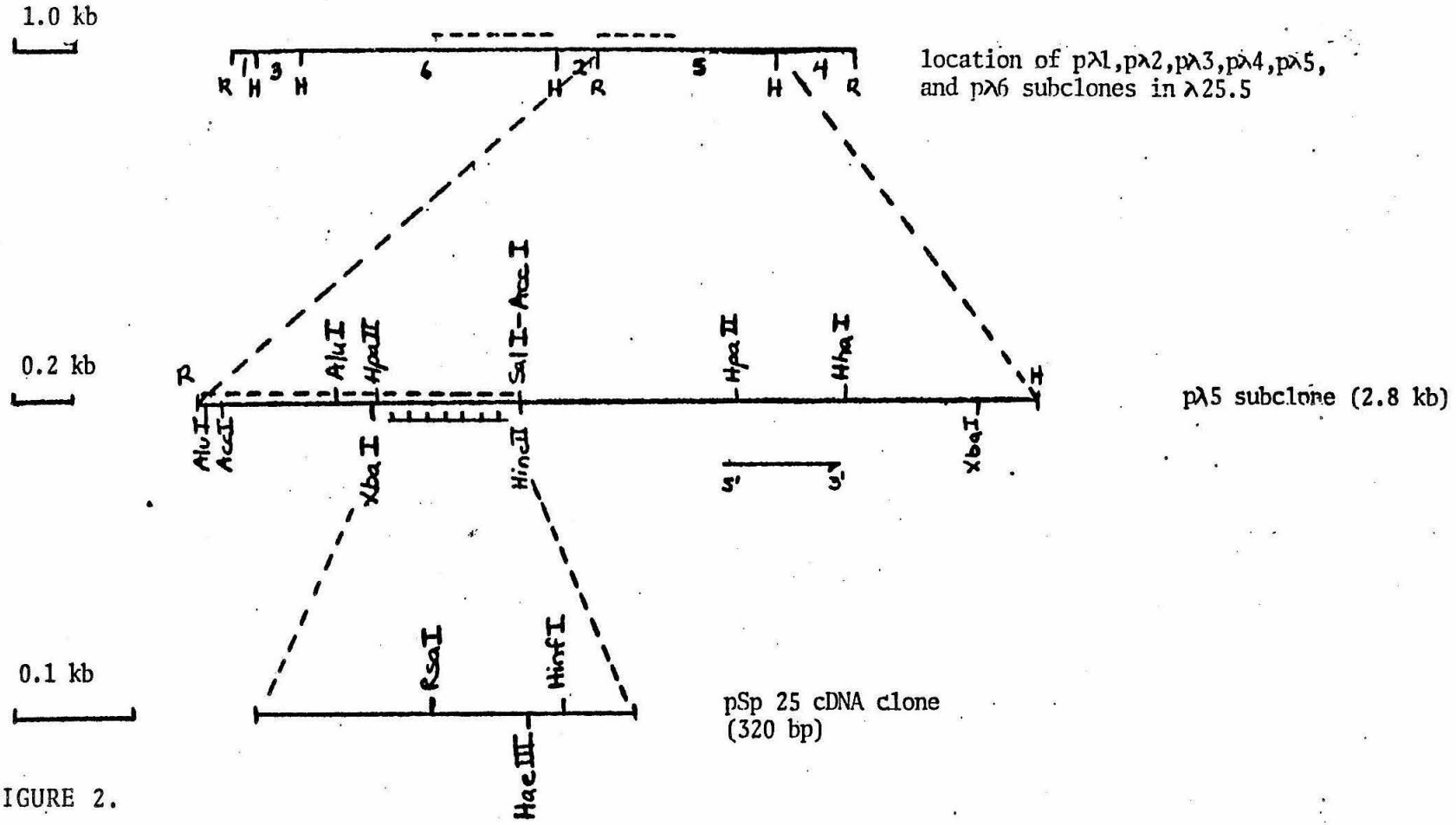

FIGURE 2.

---------- Fragments that hybridize to 1.5 kb RNA. Top figure: All 6 subclones were nick-translated and used individualy to probe blots of pluteus sea urchin poly A$^+$ RNA. Positives were noted with only the pλ5 and pλ6 subclones. Middle figure: Five fragments were, as before, used to probe blots of pluteus sea urchin poly A$^+$ RNA. Positives were noted with the two left-most fragments, the Eco RI-Hpa II and the Hpa II-Hinc II.

.... Location of cDNA. The pSp 25 cDNA clone was nick-translated and used to probe a blot of a gel containing five fragments from a Hpa II-Hinc II-Hha I digest. The band that hybridized corresponds to the Hpa II-Hinc II fragment as noted.

5' ——— 3' Direction of transcription on pλ5.

THE CONTACT RESISTIVITIES OF AMORPHOUS Fe-W DIFFUSION BARRIERS ON N^+ AND P^+ SILICON

Eric Ting-Shan Pan
Electrical Engineering Department
California Institute of Technology
Pasadena, California 91125

Abstract

Contact resistivities and barrier heights have been measured for contacts of amorphous Fe-W on n- and p-type silicon. The test-patterns for determining contact resistivity conform to the Transmission Line Model (TLM) [1]. The contact resistivity values of the n^+ Si/FeW/Ag and the p^+ Si/FeW/Ag ohmic contact systems were in the order of 10^{-7} and 10^{-6} $\Omega \cdot cm^2$ respectively and remained constant after annealing up to 500°C, 30 min. For barrier height measurements, circular Schottky-diodes with different radii were used. The barrier height of FeW on n-Si was determined from the forward I-V characteristics. The barrier height ϕ_B = (0.62 ± 0.03)V was measured for the as-deposited metallization, and ϕ_B = (0.65 ± 0.05)V after 300°C, 30 min.

Introduction

Amorphous alloys, such as Fe_xW_{1-x}, have been suggested as contact materials to semiconductor devices. Previous studies have shown that transition metal nitrides (e.g. TiN, TaN, HfN), perform as reliable diffusion barriers in multilayered electrical contacts to silicon. Their failure which occurs at temperature range of 600°C to 800°C is mainly attributed to local defects and grain boundaries. Glassy metals, such as FeW, where the fast short circuit diffusion along grain boundaries is eliminated by the amorphous structure, offer an attractive alternative to their polycrystalline counterparts.

The electrical properties of the ohmic contacts are of major importance in determining the operation limitation of a device. Low contact resistivities are needed to obtain a low voltage drop at the ohmic contact operating at high current density levels. The contact resistivity is known to depend on the nature of the semiconductor material, its doping level, the nature of the contact metal and the interfacial cleanness. In multilayer structures, where a diffusion barrier is used to separate the semiconductor substrate from the actual contact metal [2], the electrical behavior of the contact is determined by the interface formed between the barrier layer and the semiconductors substrate. Transition metal nitrides have contact resistivities in the order of 10^{-5} $\Omega\cdot cm^2$ on n^+-Si [3] and 10^{-4} $\Omega\cdot cm^2$ on p^+-Si [4]. Typically, the contact resistivity values required for LSI devices and solar cells are $\sim 10^{-7}$ $\Omega\cdot cm^2$ and $\leq 10^{-3}$ $\Omega\cdot cm^2$ respectively. In order to have low values of

contact resistivity high doping concentration, low barrier height, or both must be used. In this experiment, the contact resistivities of amorphous FeW films were determined on heavily doped n^+- and p^+-Si (N_D, $N_A \sim 10^{20}$ cm^{-3}). Additionally, the Schottky barrier height of FeW was measured on n-type Si.

Experimental Procedures

Two kinds of samples with different geometry and patterns were used for the contact resistivity determination. Both conform the TLM.

The substrates of first test-pattern were n-type silicon wafers with a boron diffused p^+-layer. Patterns were defined by conventional photolithography. First, long mesas were defined in order to insulate the patterns from each other, by using a solution of HF:HNO_3:Acetic acid (1:9:2) for 10 seconds. The depth of the mesa was $\sim$ 6000 Å, ($\geq$ 3000 Å). The whole wafer was then covered by photoresist patterned in such a way that only the square contact pads on the mesa were open. Before the FeW deposition, the samples were etched in a 10% HF solution, and dried in N_2-gas flow. The contact metal (FeW and Ag) was deposited everywhere. Finally, the photoresist was removed (lift-off) with acetone in an ultrasonic bath, leaving the structure as shown in Fig. 1.

The substrates of the second type of test-patterns were p-type silicon wafers with a silicon oxide layer of thickness $\sim$ 4000 Å. The samples were prepared by conventional photolithographic methods. First is to open in the oxide layer the diffusion windows and second is to define the contact metallization patterns. The advantage of fabricating the samples in this way is to avoid lateral current spreading effects. Deposition and cleaning procedures were the same as before. In the

Ag-FeW-Si system, the Ag deposition followed a FeW co-sputter-deposition. The FeW and Ag layers were ∿ 1000 Å and ∿ 2000 to 3000 Å thick respectively. Finally, applying lift-off would leave a structure as shown in Fig. 2.

FeW was co-deposited from a composite Fe/W target in a magnetron RF sputtering system with a rotating substrate table. Sputtering was carried out at 15 mTorr total pressure of argon gas. Sputtering power was 300 W and the deposition rate was ∿ 200 Å/min. No d.c.-bias was applied to the substrate during the deposition.

Diode substrates for determining barrier heights were n-type silicon wafers with a silicon oxide layer of thickness ∿ 3000 Å. Diodes of different areas were patterned by conventional photolithography and lift-off technique. Contact metal (FeW) of thickness ∿ 3000 Å was deposited by co-sputtering. The back contact metal was made by a Ga-In-Sn compound.

Transmission Line Model

For the first test-pattern samples, the configuration for measurements, shown in Fig. 1, affords that the resistance between two nearest pads increases linearly with the pad distance. According to the TLM, from the resistance value R_c extrapolated to the zero pad distance (two times the contact resistance) and the sheet resistance, R_s, (the slope of resistance versus pad distance times the width of the pad, w) the contact resistivity ρ_c can be determined from the equation

$$\rho_c = w^2 R_c^2 / R_s \ .$$

The electrical measurements were repeated for twenty different patterns. The reproducibility was within 10%. The contact resistance and R_s were determined from those measurements using a least mean square fit.

For the second type of test-patterns, the configuration for measurement is shown in Fig. 2. A theoretical model which accounts for both the voltage drop beneath the contact width and the voltage drop along the contact length was applied. The expression for determining contact resistivity is [5]:

$$R_e = V_e/I_o = 2\frac{\rho_m}{\ell t}\ \frac{1}{\alpha\ \sinh(\alpha W)}\ ,$$

where $\alpha = \sqrt{\left(\frac{2\rho_m/\ell t}{2\sqrt{(\rho_s\rho_c)}\ \text{cotgh}\ (\sqrt{(\rho_s/\rho_c)}\ \ell)\ +\ \rho_s L}\right)}$; ρ_m is the metal stripe resistivity, $\Omega\cdot$cm; ρ_c is the contact resistivity, $\Omega\cdot cm^2$; $\rho_s(R_s)$ is the sheet resistance, $\Omega/\square$; ℓ is the metal stripe width, cm; L is the metal stripe separation, cm; t is the metal stripe thickness, cm; W is the metal stripe length, cm; I_o is the total current flowing between two metallic stripes (see Fig. 2), A; and V_e is the voltage drop appearing at the end of two metallic stripes (see Fig. 2), V.

By iteration the value of contact resistivity is obtained, which gives theoretical R_e equal to the experimental value. Actually, these values are very much in agreement with the ones that could be determined by using the simplified relation $\rho_c = w^2R_c^2/R_s$, as the metal resistivity was very low (R_s=0.12 $\Omega/\square$ for Ag + FeW).

Schottky Barrier Height

The forward current-voltage characteristics measurements were used to determine the barrier height of the FeW-Si contact. As the diodes used in this experiment have a high series resistance, the Norde method which is less sensitive to series resistance effect was applied. The values of barrier height were obtained from plotting [6]:

$$F(V,I) = \frac{V}{2} - \frac{(kT)}{q} \ln \frac{I}{AA^*T^2}$$

where AA^* is the effective Richardson constant (= 112 $A/cm^2/K^2$ for Si); k is the Boltzmann's constant; q is the charge; T is the temperature; V is the voltage; and I is the current.

The barrier height was calculated from the expression

$$\phi_B = F_o + V_o/2 - kT/q,$$

where F_o is the minimum at $V = V_o$.

Results

X-ray analyses show that amorphous Fe_xW_{1-x} films are obtained for $x \geq 0.3$. In our experiments the electrical contact properties were determined for layers having the approximate composition $Fe_{.45}W_{.55}$.

Electrical measurements indicate that the contact resistivities of amorphous $Fe_{.45}W_{.55}$ diffusion barriers on n^+ and p^+ silicon substrates are low. The results before and after heat treatments up to 500°C, 30 min are stated in Tables I and II for the second test-pattern.

The contact resistivity of FeW/Ag on p^+-Si (the first test-pattern) as-deposited was $\sim (1.4 \pm 0.4) \cdot 10^{-6}$ $\Omega \cdot cm^2$ which was within 50% of the values given in Table II for the other test-patterns. The contact resistivity of FeW on n^+-Si (first patterns) as-deposited was in the order of 10^{-6} $\Omega \cdot cm^2$.

The results of barrier height measurements for FeW-Si contact are presented in Table III. The heat treatment of 300°C for 30 min increased the barrier height. This was observed as a decrease in the diode forward current. In contrast, the reverse current unexpectively increased. This may be due to minute diffusion of iron into the depletion region and consequent increase in the recombination current.

Conclusion

The contact resistivity of amorphous FeW diffusion barriers on n^+ and p^+ silicon has been characterized. Test-patterns used to measure the contact resistivity conform the Transmission Line Model (TLM). The n^+-Si/FeW/Ag and the p^+-Si/FeW/Ag metallization systems show very low contact resistivities in the order of 10^{-6} to 10^{-7} $\Omega \cdot cm^2$ as-deposited. The values remained stable during vacuum annealing at 500°C for 30 min.

Barrier heights of n^+-Si/FeW contact of 0.62V and 0.65V for as-deposited and after a 300°C, 30 min vacuum annealing, respectively, were obtained. The thermal stability of the barrier height will be further investigated.

References

[1] H. H. Berger, Solid-State Electronics, 15, 145 (1972).

[2] M-A. Nicolet and M. Bartur, J. Vac. Sci. Technol. 19, 786 (1981).

[3] M. Mäenpää, I. Suni, M-A. Nicolet, F. Ho and P. Iles, in Proceedings of the 15th IEEE Photovoltaic Specialists Conference, Kissimmee, Florida (May 12-15, 1981), (IEEE, New York, 1981), p. 581.

[4] M. Finetti, personal communication (1982).

[5] M. Finetti, P. Ostoja, S. Solmi, and G. Soncini, Solid-State Electronics, 23, 255 (1979).

[6] H. Norde, J. Appl. Phys. 50, 5052 (1979).

TABLE I. $Ag/Fe_{.45}W_{.55}/N^+$ Si Contact System (Second Test-Pattern).

Temperature	Contact Resistivity	Sheet Resistance
As-Deposited	$(1 \pm 0.5)\ 10^{-7}\ \Omega\cdot cm^2$	$31.3 \pm 1\ \Omega/\square$
400°C, 30 min	$(2 \pm 1)\ 10^{-7}\ \Omega\cdot cm^2$	$33.4 \pm 1\ \Omega/\square$
500°C, 30 min	$(1 \pm 0.5)\ 10^{-7}\ \Omega\cdot cm^2$	$34.8 \pm 2\ \Omega/\square$

TABLE II. $Ag/Fe_{.45}W_{.55}/P^+$ Si Contact System (Second Test-Pattern).

Temperature	Contact Resistivity	Sheet Resistance
As-Deposited	$(2.8 \pm 0.8)\ 10^{-6}\ \Omega\cdot cm^2$	$42.7 \pm 0.3\ \Omega/\square$
400°C, 30 min	$(1.1 \pm 0.3)\ 10^{-6}\ \Omega\cdot cm^2$	$42.6 \pm 0.2\ \Omega/\square$
500°C, 30 min	$(1.1 \pm 0.3)\ 10^{-6}\ \Omega\cdot cm^2$	$42.2 \pm 0.2\ \Omega/\square$
600°C, 30 min	$(1.3 \pm 0.5)\ 10^{-6}\ \Omega\cdot cm^2$	$42.7 \pm 0.2\ \Omega/\square$

TABLE III. $Fe_{.45}W_{.55}$ Si Diode.

Temperature	Barrier Height
As-Deposited	0.62 ± .03V
300°C, 30 min	0.65 ± .05V

Figure Captions

Figure 1 A cross-section and a top view of the first test-pattern. The electrical measurements were always made between two nearest contact pads as shown.

Figure 2 A top view of the second test-pattern.

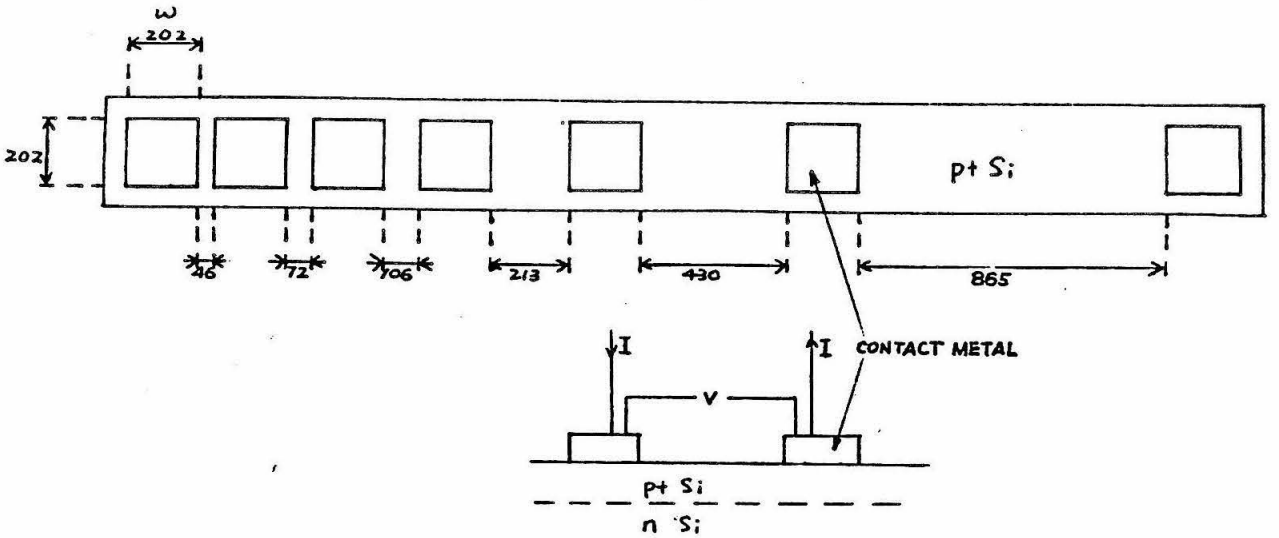

all dimensions are in μm

Figure 1

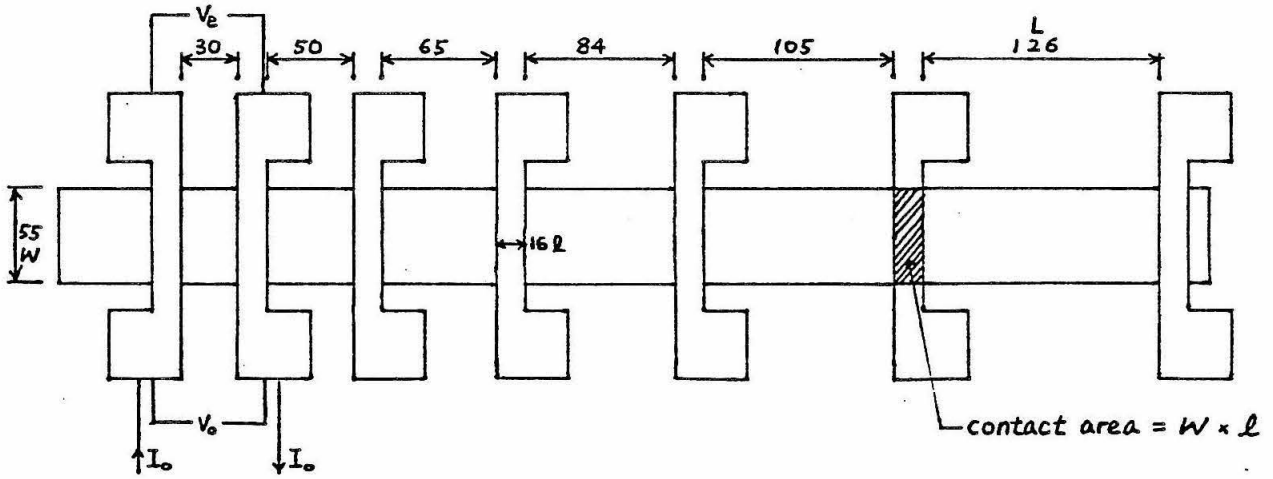

all dimensions are in μm

Figure 2

Steven D. Penn September 10, 1982

SURF PROJECT - FINAL REPORT

ABSTRACT: Investigation of the plasma oscillation in the sun's granules as detected with a spectrograph at Big Bear Solar Observatory, (BBSO). Spectral line shifting was photographed with a 35mm film camera for several hours, and a set of individual frames were stored on computer disk by means of a digitizer. These stored prints were then analyzed in great detail in order to fully reveal the true nature of these oscillations.

Granules are the uppermost layer of convection cells in the sun. When viewed through a spectrograph the cellular motion is revealed because the radial velocity causes Doppler shifting in the spectral lines. This effect is best seen in sharp dark lines such as Fe 5250A, (used for this experiment). Graphing the velocity fluctuations against time reveals the change to be the superposition of several different oscillations. The best documented of these periodic waves has a five minute period which has its origin in the supergranules, (Leighton, et al., 1961). According to the theory there is a wave nature to the plasma flow in the supergranules which results in a regular variation in velocity. Possibly similar patterns exist in both the granules and the super supergranules which would cause both the longer and shorter period oscillations that coexist with the five minute oscillation. To better resolve the characteristics of each separate oscillation, one may find the Fourier seriew which best represents the composite wave. The result yields the period of each of the contributing regular waves. By using spectral lines formed at different depths in the sun, one may conclude where

each of these different oscillations is created and thus what is its most likely source. (Ulrich, 1976)

My project reinvestigated these studies using modern computer methods. In the lightpath immediately above the slit of the spectrograph was placed a tube filled with iodine vapor. Because our spectrograph was tuned to the green, where a large number of iodine lines were to be found, the pictures contained a plethora of straight reference lines. At this point the planned computer analysis would begin. An interactive mobile cursor program would have allowed me, with the help of the digitizer, to specify boundaries for spectral lines and reference lines. Once these limits had been established a series of automated programs would take over. They would calculate the shift of every point on the spectral line with respect to the iodine line. Then the position of that point would be determined from a feature on the solar surface. All the points for each specific position would then be grouped together and a graph, of change in velocity versus time, would be drawn for each. Next, the correlation values for each point would be derived and this data, then, evaluated to find the best fit Fourier series. The results would then be printed out and a graph drawn of the Fourier series versus time. This process would be repeated for each of the 480 points along the slit to provide an accurate average value for the oscillations.

The results of these calculations are still pending due to a break in communications with the observatory computer system which has prevented the retrieval of the data. Shortly after the program writing for the second project got underway, the

activity was delayed for several days while a new disk system for the computer was installed. Later, I continued to input my programs with the assurance that the digitizer would soon be communicating with the new system. This link-up is essential to the recovery of my data. Dr. Patterson, the observatory's resident director, and Mr. Kumar, the computer programmer, have been working diligently on the problem, but no solution has yet been found. I have remained on at the observatory three extra weeks in order that this project would be able to be completed, but it has become apparent that goal will not be achieved during this summer. Without the digitizing function, the information can not be refined from its raw state. I will apply for a term job with the physics department with the aim of finishing this research. Once my results are attained I would like to submit a follow-up report so that the final result of my experiment may be known.

This research project was originally intended to learn more about the rare blue continuum flares which occur in very complex active regions on the solar surface. The sun was more active than expected this summer, when one considers that it was the third year after solar maximum. This activity produced a strong conviction in me that one of these infrequent, very energetic flares would very likely occur during the summer. Thus, I spent almost the entire summer carefully videotaping every bright flare which appeared (sixten in total). Each of these tapes were then reviewed several times to conclusively determine whether each was powerful enough to produce a continuum. When not processing flare data, I was busied by observing with or fixing the telescope and/or spectrograph which are in constant states of repair. These activities developed my skills until

I was able to make my equipment function well. My abilities in this practical half of research increased immensely, and as a result the data gathering became easier and more accurate. The experience of this first project provided me with invaluable knowledge in solar physics, optics, mechanics, and electronics. This knowledge I find difficult to document in this report, but I realize that it will remain with me for a very long time. Now BBSO has a flare spectrum system which can be put to much future use, and I have gained a great deal of practical learning to support my more theoretically-based education. Despite all this extensive preparation, as luck would have it, the one large flare which did occur this summer, did so at night.

I would like to thank Dr. Alan Patterson, Mr. Milan Mijic, Mr. Greg Burnett, and Mr. Pawan Kumar for their aid and advice. I would also like to thank the SURF committee for their generosity their patience, and their understanding.

SURF REPORT

Sponsor : Prof. M. Aschbacher
Fellow : Vipul Periwal

Project : Embeddings of SL(2,5) or A_5 as maximal subgroups in various linear groups.

Abstract : The main purpose of the work undertaken was to determine when the abovementioned groups are embedded as maximal subgroups in those finite groups in which the representations of these groups lie. The method used was to determine the character tables of SL(2,5) over fields of any characteristic, and to then attempt to determine if these representations were the restrictions of representations of larger groups, in which case, of course, SL(2,5) would not be maximal, as a subgroup in the group being considered. It was found that when the characteristic of the field, say p, is congruent to ±1(mod 5) then SL(2,5) is not maximal in Sp(4,p), where Sp(4,p) is the 4-dimensional symplectic group over a field of order p. In many cases, however, it was found that it was not possible to determine maximality of the embedding simply by examining the character tables.

Introduction : In setting up a theory of permutation representations of finite simple groups it is of interest to know which groups are maximal subgroups of these groups, since every transitive permutation representation of a group is equivalent to a representation on the cosets of some subgroup of the group. Hence maximal subgroups are related to indecomposable representations, and so are of interest.

The character tables provide information on the subgroups of the general linear groups where the representation of the group being considered may lie. The following lemmas (from [1]) are of great use .

Notation : Let n: G → GL(V) be an irreducible FG-representation, where G is a finite group, F a finite field and V a vector space over F with GL(V) the general linear group of the vector space, V.

Lemma 1 : Let K be a subfield of F, and s a generator of the Galois group of F over K. The following are equivalent :

i) n is defined over K

ii) $V = F \otimes_K U$ for some irreducible KG-submodule of V

iii) V is FG-isomorphic to V^s.

Lemma 2 : If V is absolutely irreducible as an FG-module and n is defined over a subfield K of F, then $V = F \otimes_K U$ for some absolutely irreducible KG-submodule U of V.

Lemma 3 : Let V be an absolutely irreducible FG-module defined over no proper subfield of F, and let a be an element of Aut(F), the automorphism group of F. Then

i) If V is isomorphic to V^{*a} then either a = 1 and G is a subgroup

of the subgroup of the general linear group of V which preserves some non-degenerate symmetric or skew symmetric form f, or a is an involution and G is a subgroup of the group preseving some unitary form.
ii) If G is a subgroup of O(V,f), where O(V,f) is the subgroup preserving f,a nondegenerate bilinear form, then $V \cong V^*$.
iii) If G is a subgroup of O(V,g) for some unitary form g, then the order of F is a square and V is isomorphic to V^{*a}, where a is the involutary automorphism of F.

Other results of this type that were of use and enabled the use of the character tables in this fashion are contained in [2]. It was already known that SL(2,5) was maximal in SL(2,p) where p is congruent to ±1(mod 5) (previous notation is still being used) or in $SL(2,p^2)$ where p congruent to ±2(mod 5), since all the subgroups of the groups SL(2,q), where q is a power of some prime, were already known (see [3], [4]).

Work : The complex character table of SL(2,5) was calculated with the aid of the complex character table of A_5 (see [5]). The characters not found in this manner were calculated using the orthogonality relations for complex irreducible characters and other information from Prof. Aschbacher about the dimensions of the remaining representations. (Later the complex character table of all the groups SL(2,q) [q as above] was found in [6].)

The characteristic 5 character table was obtained by using the description of the representations of the groups SL(2,p) over characteristic p in [7], and thus calculating the character values. The required knowledge of the theory of modular representations was obtained from the abovementioned sources and [8]. The characteristic 3 character table was obtained by noting that A_6 is isomorphic to PSL(2,9), where PSL(2,9) is the group SL(2,9) modulo its centre. Then on noting that A_5 is embedded in A_6 naturally, one obtains two 2-dimensional characters of SL(2,5) on lifting this embedding to SL(2,5) and SL(2,9). A result of Brauer and Nesbitt (in [8]) enables the taking over of the two 3-dimensional characters and the 6-dimensional character from the complex character table to the characteristic 3 character table. Then one needs just one character, using results from modular representation theory (references above) and that turns out to be the character obtained from the permutation character by subtracting the trivial character.

The characteristic 2 character table is easily obtained on noting the isomorphism between A_5 and SL(2,4), then using the results on the modular representations over characteristic p fields of the groups $SL(2,p^n)$ in the paper of Brauer and Nesbitt quoted above.

The character table over fields of characteristic other than 2,3 or 5, or equivalently, over characteristic not dividing the order of SL(2,5), which is 120, is easily obtained by using the results in [9] and certain information given by Professor Aschbacher. Since it is of interest to note the minimal field over which the corresponding representations are defined, for the use of the lemmas presented

earlier and referred to in [2], it was found that when the characteristic of the field, p, is congruent to ±1(mod 5) then the character table is defined over the field of order p, and all the representations are also defined over the same field; and when p is congruent to ±2(mod 5) then the field is of order p^2.

These character tables are given as follows :
Table 1 - The character table over the complex numbers and prime characteristic where the prime is larger than 5.
Table 2 - Over characteristic 5.
Table 3 - Over characteristic 3.
Table 4 - Over characteristic 2.

It then remains to determine when the embedding is as a maximal subgroup. First it remains to find which subgroups the embedding lies in. Problems start occuring at this point since the lemma one uses (Lemma 3, i) and ii)) is ambiguous on whether the subgroup is going to be symplectic or orthogonal. Indeed though it is often possible to write some of the irreducible representations as the tensor product of some of the other representations, often these other representations are defined over fields that are larger than the field of definition (minimal i.e.) of their tensor product and hence from just the character table it is not possible to determine whether the actual representation is symplectic or orthogonal. This limitation hampered investigations in quite a few cases.

The results obtained are now tabulated below with notes on the method by which they were obtained in parentheses.

Characteristic 2

All representations were faithful representations of A_5, i.e., all the representations of SL(2,5) into vector spaces over characteristic 2 fields have the centre as kernel. There are two 2-dimensional representations and one 4-dimensional representation. Since the 2-dimensional symplectic and special linear groups coincide, and there is an isomorphism between SL(2,4) and A_5, this case is of no interest since A_5 is not embedded as a proper subgroup. The 4-dimensional character may be written as the tensor product of the two 2-dimensional ones, but since the minimal field of definition of the representation corresponding to it is Z_2 itself, this is one of the cases as mentioned earlier where the character table does not help, especially since the degree of the character is 4 and hence there is no limitation on the group not being symplectic by reason of odd degree. Since S_6 and Sp(4,2) are isomorphic there is certainly an embedding of A_5 into Sp(4,2). However in this case the embedding is certainly not maximal since A_6 obviously contains A_5 and is maximal in S_6.

Characteristic 3

As discussed earlier it is known that SL(2,5) is a maximal subgroup of SL(2,9). Thus the two 2-dimensional representations are taken care of. The two 3-dimensional representations are not faithful and so we might as consider them as representations of A_5. They lie in the orthogonal group O(3,9) which has as a subgroup $\Omega(3,9)$, which is

isomorphic to A_6. The 6-dimensional representation is the tensor product of the 2-dimensional and 3-dimensional representations and their transpose representations. Its field of definition (minimal) is however Z_3 and hence we obtain no information from the character table. This representation is also faithful. I could obtain no more information about the maximality of SL(2,5) in this six-dimensional representation. However, the four-dimensional representation lies in $\Omega_-(4,3)$ since there is an isomorphism between this group and PSL(2,9) and it is known that SL(2,5) is faithfully embedded in SL(2,9) - the maximality remains undetermined however.

Characteristic 5

The group O(5,5) has A_5 embedded in it. Since $\Omega(5,5)$ and PSp(4,5) are isomorphic, it is felt that the 4-dimensional representation probably lies in the group Sp(4,5), but I have been unable to prove that it cannot lie in the groups $O_\pm(4,5)$. Also I was unable to determine maximality since it was not found possible to find the required character tables of other groups SL(2,5) was embedded in, over characteristic 5. The 2-dimensional representation was trivial, of course. The 3-dimensional representation lies in $\Omega(3,5)$ which is isomorphic to PSL(2,5) and hence the embedding is just an isomorphism and hence of no interest.

Characteristic p (where p is a prime larger than 5)

The maximality of SL(2,5) in SL(2,p) for $p \equiv \pm 1 \pmod 5$ and in $SL(2,p^2)$ for $p \equiv \pm 2 \pmod 5$ has already been mentioned. We have already stated a result for $p \equiv \pm 1 \pmod 5$ regarding the non-maximality of SL(2,5) in Sp(4,p). Since PSL(2,p) and $\Omega(3,p)$ are isomorphic we note that A_5 is maximal in $\Omega(3,p)$ for $p \equiv \pm 1 \pmod 5$. For $p \equiv \pm 1 \pmod 5$, we also have that SL(2,5) is embedded in Sp(6,p) and that A_5 is embedded in $O_\pm(4,p)$. For $p \equiv \pm 2 \pmod 5$ in neither of the immediately preceding representations can we decide on the basis of the character table that the groups involved are symplectic or orthogonal. Further it was not possible to conclude anything about the maximality of SL(2,5) in Sp(4,p) though it was found possible to eliminate the possibility of the group being embedded in $O_\pm(4,p)$.

Conclusions : It has already been mentioned that the approach employed was not suited for answering the questions that were desired answered. However some useful information was obtained. Indeed it is surprising (to me at least) that the character should contain so much information about the group in which the group being represented is being embedded. The work is by no means complete. The aim of trying to determine maximality for the case of SL(2,5) was to obtain some sort of general idea about the behaviour of the embeddings, to extend these results to the other finite simple groups. That aim is not yet completed. Lack of time and knowledge about the finite simple groups prevented me from trying out all the possible restrictions of characters of groups in which SL(2,5) or A_5 are embedded. It might be that on trying all the different restrictions, all the desired information on maximality will be available.

Acknowledgements : I would like to thank the SURF programme for this opportunity to do research and to try to determine if I could do independent work. I am deeply grateful to Prof. Aschbacher for all the time he spent explaining things to me and for the patience with which he treated my questions. I would also like to thank Mike Lewy for drawing my attention to several results that proved quite useful, and for several interesting conversations.

Bibliography :

1. Results supplied by Prof. Aschbacher.
2. Huppert,B. and N. Blackburn - Finite Groups II, Springer-Verlag, Berlin 1982.(Theorems 1.17,1.18,2.6,3.6,3.8,3.9,3.11)
3. Suzuki, M. - Group Theory I, Springer- Verlag, Berlin 1982.
4. Huppert, B. - Endliche Gruppen I, Springer-Verlag, Berlin 1967.
5. Isaacs, I. Martin - Character Theory of Finite Groups, Academic Press, New York 1976.(Appendix)
6. Dornhoff, L. - Group Representation Theory, Marcel Dekker, New York 1971.
7. Huppert and Blackburn, op. cit., pp.38 - 41.
8. Brauer, R. and C. Nesbitt - On the modular characters of groups, Ann. of Math.,vol. 42, 556-590 (1941).
9. Isaacs, op. cit.,Ch. 15.

General References :

Naimark and Stern - Theory of Group Representations
Kirillov - Elements of the Theory of Representations
Artin - Geometric Algebra
Notes from Ma 120 (unpublished) taught by Prof. Aschbacher in 1981-2.

TABLE 1

Conjugacy classes (labelled by order)

	1	2	3	6	4	5_1	10_1	5_2	10_2
X_1	1	1	1	1	1	1	1	1	1
X_2	4	4	1	1	0	-1	-1	-1	-1
X_3	5	5	-1	-1	1	0	0	0	0
X_4	3	3	0	0	-1	a_1	a_1	a_2	a_2
X_5	3	3	0	0	-1	a_2	a_2	a_1	a_1
X_6	2	-2	-1	1	0	t	-t	t^2-2	$2-t^2$
X_7	2	-2	-1	1	0	t^2-2	$2-t^2$	t	-t
X_8	4	-4	1	-1	0	-1	1	-1	1
X_9	6	-6	0	0	0	1	-1	1	-1

Let w be a primitive fifth root of unity. Let $t = w + w^{-1}$. Then t lies in the field of order p if p, the characteristic of the field (if not 0) is congruent to $\pm 1 \pmod 5$, and lies in the field of order p^2 otherwise. Define $a_1 = 1 + t$ and define $a_2 = t^2 - 1$.

TABLE 2 (Characteristic 5)

Conjugacy classes

	1	2	3	6	4	5_1	10_1	5_2	10_2
X_1	1	1	1	1	1	1	1	1	1
X_2	2	-2	0	-1	1	2	-2	2	-2
X_3	3	3	-1	0	0	3	3	3	3
X_4	4	-4	0	1	-1	-1	1	-1	1
X_5	5	5	1	-1	-1	0	0	0	0

TABLE 3 (Characteristic 3)

Conjugacy classes

	1	2	3	6	4	5_1	10_1	5_2	10_2
X_1	1	1	1	1	1	1	1	1	1
X_2	3	0	0	0	-1	a_1	a_1	a_2	a_2
X_3	3	0	0	0	-1	a_2	a_2	a_1	a_1
X_4	6	0	0	0	0	1	-1	1	-1
X_5	2	-2	2	-2	0	g	-g	d	-d
X_6	2	-2	2	-2	0	d	-d	g	-g
X_7	4	4	1	1	0	-1	-1	-1	-1

Here a_1 and a_2 are as in table 1. Since $3 \equiv -2 \pmod 5$, they lie in the field of order 9.

Let e be a generator of the multiplicative group of the field of order 9. Let s be such that

$\begin{pmatrix} s & v \\ ev & s \end{pmatrix}$ has order 10. Here v is an element of the field of order 9 such that $s^2 - ev^2 = 1$. Such an element exists (see Dornhoff, op. cit., Ch. 38). Then

$$g = s^2 + 1 \qquad \text{and} \qquad d = s^4 - s^2 - 1 .$$

TABLE 4 (Characteristic 2)

Conjugacy classes

	1	2	3	6	4	5_1	10_1	5_2	10_2
X_1	1	1	1	1	1	1	1	1	1
X_2	2	0	1	1	0	w	w	w^{-1}	w^{-1}
X_3	2	0	1	$\bar{1}$	0	w^{-1}	w^{-1}	w	w
X_4	4	0	1	1	0	1	1	1	1

Here w is a generator of the field of order 4 (i.e., a generator of the multiplicative group of the field.).

Modeling of Nonlinear Systems with Iterated Maps

William A. Polson
SURF Project Report
September, 1982
Advisor: Dr. Donald S. Cohen

Feigenbaum's recent theory of universality in nonlinear iterated maps[1] has been applied with some success in describing several nonlinear physical systems. The best example yet is the driven anharmonic electrical oscillator.[2] Both the qualitative and quantitative details of the transition from order (periodic motion) to chaos (aperiodic motion) for this circuit are exhibited by the simple map:

$X_{n+1} = \lambda \cdot X_n (1-X_n)$
Where λ is a parameter which reflects the magnitude of the nonlinearity.

Why should such a simple one dimensional difference map describe accurately a many dimensional differential system? My summer's work consisted of:
1.) extensive reading in the field of nonlinear dynamics to gain insight into this question.
2.) computer modeling of the electrical circuit. My intention here is to actually generate a map which describes the circuit, using the correct differential system as a start.
3.) collaboration with Ed Felten in the search for Feigenbaum-type bifurcation sequences in a five dimensional nonlinear system. Please refer to his SURF Report.

At the heart of this topic is the problem of constructing iterated maps to model differential systems. This is not the same thing as constructing difference equations from differential equations. A difference equation seeks to locally approximate the process of taking a derivative; an iterated map describes more global characteristics of the solution. Over the summer I've had some ideas on the appropriate way to do this. Among them are:
1.) the ways in which the parameters in the system and in the map are the same; more importantly, the ways in which they are not.
2.) the importance of the principle of confluence[3], which is the tendency of map solutions to stay near fixed points. This is essential in modeling both hysteresis and the phase relationships between different levels of bifurcation along the route to chaos.

As of now, the project is incomplete. The attempt to construct a map to describe the nonlinear circuit has not been successful. The set of five equations mentioned above has barely been scratched- more bifurcation sequences and a reason for their ordering is still to come. I shall have more to say about the ideas mentioned here, and hopefully some further progress to report, at the final seminar in October.

1.) Feigenbaum, "Universal Behavior in Nonlinear Systems," Los Alamos Science, Summer 1980.
2.) Testa, Perez, and Jeffries, "Evidence for Universal Chaotic Behavior of a Driven Nonlinear Oscillator," preprint 1982.
3.) Mandelbrot, "Fractal Aspects of $Z_{n+1} = \lambda \cdot Z_n (1-Z_n)$," Nonlinear Dynamics, N.Y. Academy of Sciences, 1980.

Synthesis of a Membrane Permeable Derivative of DNA-cleaving Molecule MPE

Vince Powers

ABSTRACT

Methidiumpropyl-EDTA (MPE) and anti-cancer drug bleomycin cleave DNA *in vitro*. However, bleomycin exhibits bactericidal effects, but MPE does not. The latter result is attributed to the highly polar nature of MPE, which prevents the passage of MPE through the cellular membrane. It is proposed that a triester of MPE could traverse the cellular membrane, be hydrolyzed enzmatically back to MPE, and then cleave the cellular DNA.

Synthesis of a Membrane Permeable Derivative of DNA-cleaving Molecule MPE

Vince Powers

Little is known about the mechanism of anti-cancer drugs. Whether these drugs react directly with cancer cellular DNA or else indirectly exert their effects at other locations is not clear. However, the fact that anticancer drug bleomycin cleaves DNA in the presence of Fe(II) and oxygen suggests that DNA cleavage may be an integral part of anticancer activity of bleomycin and other cancer drugs.

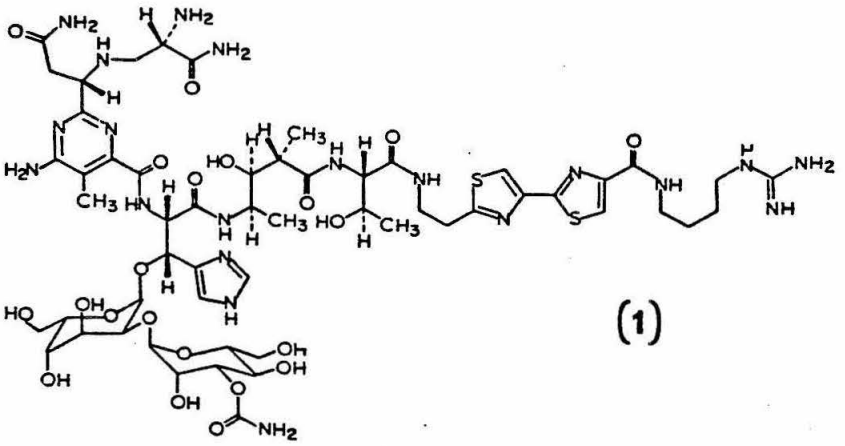

(1)

The structure of bleomycin (1) can be considered to be composed of three components: a DNA-binding group, a DNA-cleaving group, and a linking group which connects the first two. There is evidence that the binding group of (1) binds as an intercalator.[1] The cleaving component is known to chelate Fe(II) and in this form cleave DNA somewhat specifically[2] in the presence of oxygen. The reaction mechanism has not been elucidated.[3]

1. See refs. 1 and 2.
2. Bleomycin seems to react preferentially at guanines. See ref. 3.
3. Numerous cleavage products are observed. See ref. 3.

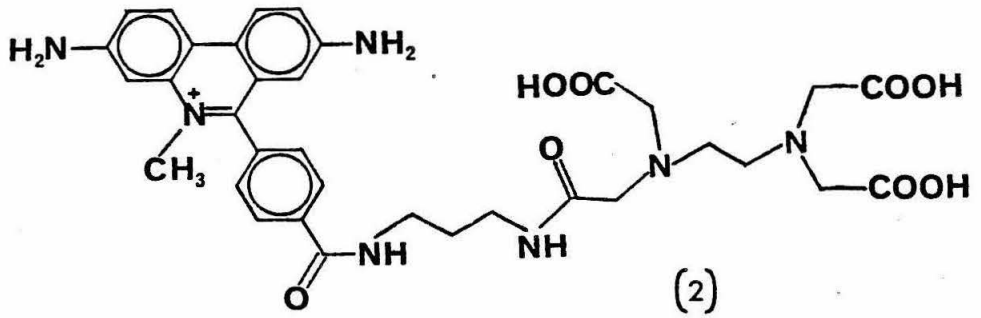

(2)

The DNA-cleaving molecule MPE (2) was designed by the Dervan group as a primitive model of bleomycin. It too consists of three components:

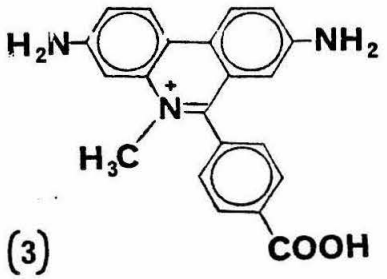

(3)

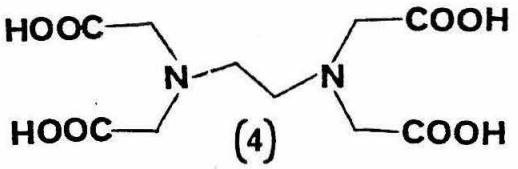

(4)

(5)

a DNA-binding group, methidium (3), a known DNA intercalator;[4] a DNA cleaving group, EDTA, which when chelated with Fe(II) cleaves DNA in the presence of oxygen; and a linker molecule, 1,3-diaminopropane. Like bleomycin, MPE binds to DNA and cleaves it in the presence of Fe(II) and oxygen, though not sequence specifically. Again, the mechanism is not known.

The *in vivo* characteristics of (1) and (2) differ significantly, however. (1) exhibits bactericidal effects,[5] whereas (2) does not.[6] It is likely that (2) does not even traverse the cellular membrane. The quaternary heterocyclic nitrogen, the EDTA nitrogens, and the carboxylic acid groups make MPE highly polar.

4. Methidium and ethidium are nearly identical in their properties. See ref. 4.
5. See ref. 3.
6. Recent experiments show that (2) may even enhance bacterial growth!

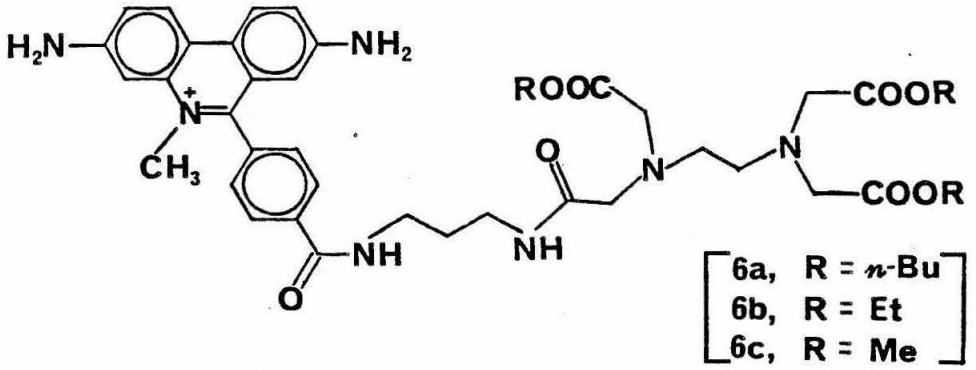

It is then postulated that a triester of MPE, which would no longer contain the carboxylic acid groups, could easily traverse a cellular membrane. Once inside the cell, the triester could then be converted enzymatically back to the triacid (2), chelate ambient Fe(II), and finally bind to and cleave the DNA. The likelihood of enzymatic hydrolysis of the triester is unknown.

Because of the considerable time and money necessary to make (3), we designed the following route for MPE-triester synthesis, in which step 2 could be perfected at the expense of inexpensive materials:[7]

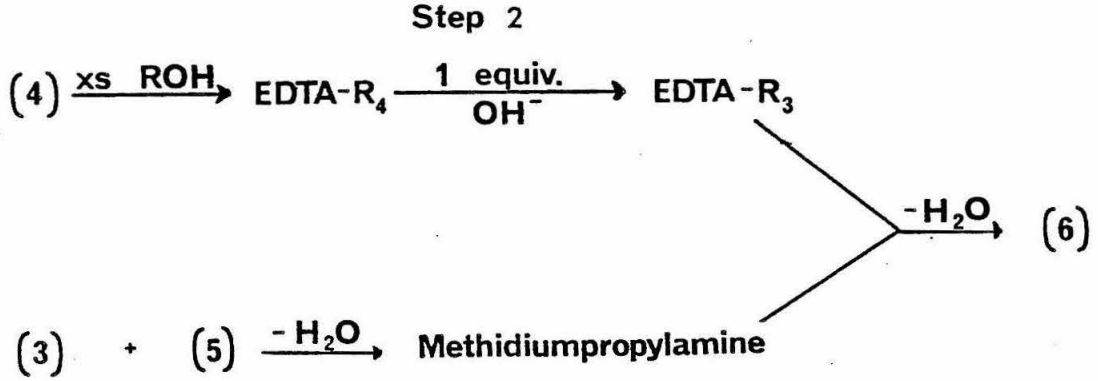

We decided further that the n-butyl triester of MPE, (6a), would be soluble in the membrane and would be a good molecule to start with. However, finding a solvent system for step 2 in which the reactants and intermediates are reasonably soluble and which gives triester in reasonable yield has proven difficult, so syntheses of (6b) and (6c) were begun instead. In these cases, step 2 goes easily. At the time of this writing attainment of these two compounds was about one week away. They would then be charactized and sent out to an outside lab to test for bactericidal effects. Synthesis of further triesters is presently under consideration.

7. For details of steps 3 and 4, see ref. 6; for those of steps 1 and 2, see ref. 5.

Referenses

1) Lerman, L. S.; J. Mol. Biol. **1961** 3, 18.
2) Waring, M.; J. Mol. Biol. **1970** 54, 247-279.
3) Burger, R. M.; Peisach, J.; and Horwitz, S. B.; Life Sciences **1981** 28, 715-727.
4) Ulman, A.; Gallucci, J.; Fisher, D.; and Ibers, J.A.; J. Am. Chem. Soc. **1981** 102, 6852-54.
5) Hertzberg, R. P.; and Dervan, P. B.; J. Am. Chem. Soc. **1982** 104, 313-15
6) Hay, R. W.; and Nolan, K. B.; J.C.S. Dalton Trans. **1975** 1348-51

DESIGN AND TESTING OF THERMAL CONTROL SYSTEMS

FOR A SPACE SHUTTLE PAYLOAD

SURF Project 1982

Research performed by Norman Princen under the supervision of Professor Thomas Caughey.

Abstract

Systems for keeping temperatures of a Space Shuttle payload between 5 and 30 degrees Celsius were designed and tested. The systems proved marginally adequate in keeping the payload within this temperature range. Improvements to the system are proposed for further testing and possible inclusion in an actual shuttle payload.

Introduction

Thermal considerations are important to the design of most experiment packages for space flight. Such payloads are subjected to temperatures ranging from -182 to 43 degrees Celsius. These temperatures must be modified in order to provide workable temperatures for experiments and hardware. The purpose of my SURF project was to design and test a system for controlling the temperatures of a Small Self Contained Payload (SSCP) for Space Shuttle flight. The temperatures must be kept between 5 and 30 degrees Celsius.

Presentation and Discussion of Results

In the design phase of the project, methods of heating, insulating, and cooling the payload were evaluated. Each method was evaluated in terms of cost effectiveness, space efficiency, weight efficiency, and most importantly, effectiveness in creating the desired thermal effects. It was decided that heating would be accomplished by using simple resistive wires driven by the payload battery supply. The battery supply will contain 2500 watt hours of power for a 170 hour mission. Insulation for the payload will consist of panels of polyurethane foam that have nearly the thermal conductivity of still air. To implement this insulation, aluminized mylar will be used to decrease radiative losses. Cooling of the payload will be accomplished through the choice of a special radiative coating which is applied to the insulating top cap of the SSCP can. By choosing a silver teflon coating, no other cooling devices should be needed for the payload. If the payload becomes too warm, vent shutters will open and fans will circulate the payload air past the top of the SSCP can to be cooled. The circulation fans are also used to maintain thermal uniformity by circulating air between cold and warm spots in the payload.

Before the testing phase of the project could begin, various equipment had to be built. A mock-up of the payload insulation jacket was constructed. The insulation thickness of this jacket was estimated to give a 30 degree Celsius temperature gradient across its walls with a 15 watt power

dissipation. A thermally isolated chamber was built in which to test the insulating jacket. It provides a means for heating and cooling the payload while tests are being run.

For the testing phase of the project, eleven temperature sensors were placed on various parts of the insulation jacket. Resistance heaters were mounted inside the jacket and could be set to run at various power dissipations. Circulation fans were also mounted in the jacket. The results of the experiments showed that a 15 watt power dissipation inside the insulating jacket produced a 15 degree Celsius increase in inside temperature. A further 5 degree Celsius increase was realized after the aluminized mylar was wrapped around the insulating jacket. Since the temperature on the exterior of the insulation jacket should not go below -15 degrees Celsius for a moderately cold shuttle orbit, this 20 degree temperature increase is barely adequate to maintain the 5 degree Celsius minimum temperature inside the payload. With a minimum power dissipation of 5 watts and the vent shutters open, a temperature of 30 degrees Celsius can be maintained on a hot orbit.

Conclusions

A feasible system of thermal control for the payload has been devised, but modifications should be made to expand the cold end of the temperature range to which the payload can be exposed. More insulation should be added to the insulating jacket in order to allow operation in a cold orbit condition. No modifications need to be made to the payload cooling system since it will handle a hot orbit condition.

FINAL SURF REPORT
RNA POLYMERASE RESEARCH FOR CARL PARKER

Doug Ruden
September 8, 1982

Abstract: RNA polymerase II and III from the yeast Saccharomyces cerevisiae and RNA polymerase II from Drosophila melanogaster were purified through a series of column chromatography steps. The purification scheme was optimized to yield an enzyme of high activity and purity. Antibodies will be made against the large subunits of both the Drosophila and yeast RNA polymerases. Once the antibodies are made, they will be used to screen expression libraries from yeast and Drosophila in order to identify the genes for these proteins.

Introduction: DNA dependent RNA polymerase is an enzyme which catalizes the polymerization of ribonucleotides into RNA chains from a DNA template according to the following reaction:

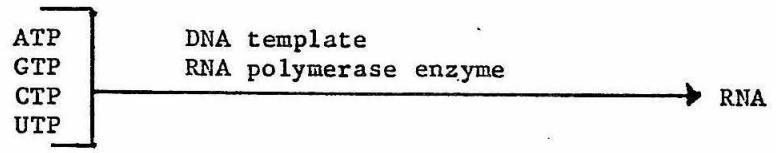

Eukaryotes, ie. organisms which have a cell nucleus, have three types of RNA polymerase. One type of RNA polymerase is responsible for the synthesis of each major class of RNA. RNA polymerase I transcribes only ribosomal DNA, while RNA polymerase II transcribes the genes for messenger RNA and RNA polymerase III synthesizes transfer and 5S RNA.

Eukaryotic RNA polymerase II is a large and complex enzyme which consists of two large (>100,000 daltons) and five to seven small (<50,000 daltons) polypeptide subunits. Compare this to a much more well known protein, hemoglobin, which consists of four polypeptide subunits, each about 14,000 daltons in size.

This summer, under the guidance of my advisor Professor Carl Parker, I have purified RNA polymerase II and III from whole cell extracts of yeast and RNA polymerase II from cultured cell extracts of Drosophila melanogaster. The purified protein can then be further characterized through a variety of procedures outlined in a later part of this paper.

Results: The first step in purifying yeast and Drosophila RNA polymerases is to make a cellular extract which contains an active RNA polymerase. In the case of yeast RNA polymerase, the following procedures are used. First, 6 to 8 liters of yeast cells are grown in a growth medium. These cells are then harvested by centrifugation and resuspended in a buffer solution containing DTT (dithiothreitol) to make them more susceptable to zymolyase treatment. Zymolyase, an enzyme which breaks carbohydrate bonds, is used to further degrade the cells' outer coat. After several wash steps, the cells are resuspended in a low-salt buffer to lyse them. The cytoplasmic material is separated from the nuclear material by centrifugation. Finally, two crude extracts are made by precipitating the proteins in the cytoplasmic and the nuclear fractions.

The Drosophila nuclear and cytoplasmic extracts are made in a similar manner using cultured cells, however, there is no need to pretreat the cells with DTT and zymolyase. In this case, RNA polymerase III is found in the cytoplasmic extract while I and II is in the nuclear extract. In yeast, however, RNA polymerase II is found in the cytoplasmic fraction, while I and III are found in the nuclear fraction.

The polymerases are purified from the crude extracts by running the extracts through a series of column chromatography steps. For example, to purify RNA polymerase II from Drosophila crude nuclear extract, it is necessary to chromatograph the material through five separate columns, employing four different resins. First, the crude extract is chromatographed through a DEAE (diethylaminoethyl) Cellulose column . DEAE Cellulose is a positively charged resin which binds the negatively charged amino acids in proteins. Next, the fractions containing RNA polymerase II from the first column are chromatographed through a DEAE Sephadex column. The third column is a phosphocellulose column; this resin is a cation exchanger which binds positively charged proteins. The main purpose of this phosphocellulose column is to concentrate the remaining protein from the previous two columns into a smaller, more convenient volume. The fourth column is an A5M sizing column which separates proteins according to mass. Finally, another phosphocellulose column is used to concentrate the protein obtained from the sizing column.

After performing the above chromatographic steps, the enzyme is denatured and electrophoresed on a standard denaturing polyacrylamide gel. This determines both the purity of the enzyme and gives an estimate of the various subunits' molecular weights.

Discussion and conclusions: The yields on each of the above columns varies between 30 to 50 percent. Therefore, after five columns, only two to three percent of the original activity is recovered. This low overall yield requires that one start with a large amount of material in order to purify an amount of enzyme sufficient for further characterization and study. Several modifications have been attempted in order to improve the chromatographic yields, but these modifications have made only marginal improvements. The chromatographically defined enzyme has been determined by polyacrylamide gel analysis to be of high purity. Furthermore, the subunit structure has been shown to be consistant with that of other RNA polymerase II preparations from yeast and Drosophila.

So far, I have purified an amount of Drosophila RNA polymerase II sufficient for antibody production in mice. Thus, in the next few weeks, I will isolate the the two large subunits of this enzyme and inject them into BALB C mice. During the coming school year, I plan to utilize a newly-developed expression vector system obtained from Ron Davis's lab at

Stanford. A library will be constructed using the expression vector and then screened with the pol II antibodies. These antigen-antibody complexes will be reacted with radioactive anti-mouse antibodies to identify those bacterial cells which posses the gene for these proteins.

Preliminary Studies of Mixed Cultures

Gregory D. Sayles
September 1982

ABSTRACT

Appropriate conditions were found for a possible cross-dominance in a continuous mixed culture of Escherichia coli and Saccharomyces cerevisiae were obtained from separate batch growth studies and from the literature. Other batch experiments showed growth inhibition of E. coli and S. cerevesiae due to the other's metabolic products, acetic acid and ethanol, respectively. Single species continuous experiments have shown that a cross-dominant system will exist and therefore a mixed culture coexistance is possible.

INTRODUCTION

Early work on the description of continuous microbial systems produced the Competitive Exclusion Principle[1]. It states that for two populations competing for a nutrient in continuous system, only one population will survive and the others will be wahsed out. This was later generalized to say that at most n populations can be supported by n rate limiting factors. So, for example, the coexistance of two populations in the presence of a single nutrient with inhibitors should be possible. For simplicity, let's consider a continuous dual population system where the only rate-limiting substrate is a nutrient. Then, the dynamic equations describing this system are:

$$\dot{x} = x\,[\,U(s) - D\,]$$

$$\dot{y} = y\,[\,V(s) - D\,]$$

$$\dot{s} = D\,[\,S - s\,] - xU(s)/X - yV(s)/Y$$

$$U(s) = Umax[\,s/(\,K + s\,)\,]$$

$$V(s) = Vmax\{\,s/(\,L + s\,)\,]$$

where x and y are biomass concentrations, U(s) and V(s) are growth

rates of the Monod form, Umax and Vmax are the maximum growth rates, X and Y are the yield coefficients, and K and L are substrate saturation coefficients of the two species, respectively. D is the dilution rate (the inlet flow rate divided by the reactor volume), s is the nutrient concentration, and S is nutrient concentration of the inlet flow. So, at steady-state U(s)=D and/or V(s)=D, i.e. the growth rate equals the dilution rate. If either population can not grow at the dilution rate, it will wash out of the reactor. When a dilution rate is established, the nutient concentration adjusts to the value that can be used by the most efficient species. The other species can no longer grow at the dilution rate at this nutrient concentration, so it washes out. However, if D, the reactor conditions, and the species are chosen such that U(s)=V(s), then coexistance may be possible. It is this situation we would like to consider (see figure 1).

Dilution rate (=growth rate) vs. nutrient concentratiom curves must be known for both species in order to establish a possible coexistance: If the curves cross, coexistance may be possible; If they do not cross, coexistance is impossible; since one will always dominate. Relative positions of the curves at high nutrient concentrations can be studied understanding that these portions of the curves are approaching D=maximum growth rate. Umax and Vmax are easily calculated from batch shaker flask experiments' biomass concentration vs. time curves. One possile way of finding trends in the curves (without actually experimentally determining them yet) at low nutrient concentrations is to compare the saturation coefficients. From the equations above, we see that, for s=K, U(s)=0.5Umax. Thus, if K and L are relatively small (we are concidering low nutrient concentrations), then the relative magnitudes of K and L will indicate the relative magnitudes of

U(s) and V(s) at low nutrient concentrations. Therefore continuous system experiments are unnecessary to indicate the presence of a possible co-existance point. However, the continuous flow experiments must be done to establish accurate D vs. s curves and verify the possibility of a coexistance point.

Assume now that we have found appropriate conditions for coexistance. Stephanopoulos[2] showed that the steady-state solutions of the above equations at the dilution rate of coexistance are unstable with respect to small perturbations. We wish to concider a system where in addition to the nutrient we have rate-limiting subrates such as growth inhbitors. Modifications in the equations above is necessary, but the cross-dominace features of the single substrate system should still be present, with the exception that now the system has at least two rate-limiting factors so that it can now support two populations. Therefore, we would now expect a stable coexistance at some dilution rate. My goals, then, were to establish the proper conditions to produce a cross-dominant system. I also wanted to investigate inhibition of the two populations by each other's secondary metabolite. And finally, I wanted to show the possibility of a stable coexistance of two populaions in a continuous flow system.

RESULTS

Shaker flask (batch growth) experiments were done with a defined growth medium separately for E. coli and S. cerevisiae. After inoculation into media filled flasks, periodic samples were taken from the flasks for population (biomass) concentration measurements. This was accomplished by measuring the sample's absorbance by a spectrophotometer at 660nm. PH was

controlled by periodic adjustment. From results of experiments at pH 4.5, temperature 30 degrees C and nutrient (glucose) concentration of 1.0g/l (see figure 2), maximum growth rates calculated for E. coli and S. cerevisiae were 0.31 and 0.42 per hour (to within roughly 5% error). Thus, conditions were discovered where S. cerevisiae grows faster than E. coli at a high glucose concentration. From the literature[4,5] saturation coefficients for E. coli and S. cerevisiae are 0.4μM and 0.6mM, respectively, at slightly different conditions than ours. But since the their magnitudes are 1000 times apart, the change in conditions should not alter their relative magnitudes by much. So, at low glucose concentrations, E. coli grows faster than S. cerevisiae. Therefore cross-dominance at these conditions is possible.

A preliminary study of possible inhibition of growth of one species by the other's secondary metabolite was positive with batch growth of E. coli with ethanol enriched media and S. cerevisiae with acetic acid enriched media decreasing the their maximum growth rates significantly. For example, Umax for E. coli grown with 0.2g/l ethanol is about 0.20 and that of S. cerevisiae g9own in 0.038g/l acetic acid is about 0.19 (within 5%). We are hoping, and there is some preliminary evidence to support this, in the continuous flow system, the inhibitor to the dominant species growth's concentration will be so low (because the other species' concentration is low) that it will not effect the cross-dominance previously predicted.

The continuous flow experiments are run in a continuous stirred tank reactor with temperature, pH, and inlet flow rate (dilution rate) control. Single species experiments to determine steady-state glucose concentrations vs. dilution rate curves for E. coli and S. cerevisiae were completed by

sampling the reactor periodically thereby determining glucose concentrations using a commercial enzyme kit. Steady-states were reached when consecutive samples yielded identical glucose measurements. The results are not too accurate but seem to show a crossing of D vs. s curves when they are compared (see figure 3). This would indicate that a steady-state coexistance is indeed possible. Further experiments will have to determine this quantitatively.

CONCLUSIONS

We have concluded that there is a good possibility of a steady-state stable coexistance of two microbial populations, with inhibition, in a continuous flow system. Ethanol has been shown to be a growth inhibitor for E. coli and acetic acid for S. cerevisiae, the two compounds being metabolic products,of the other. However, it is not clear how this will effect growth of the two species together in the same CSTR.

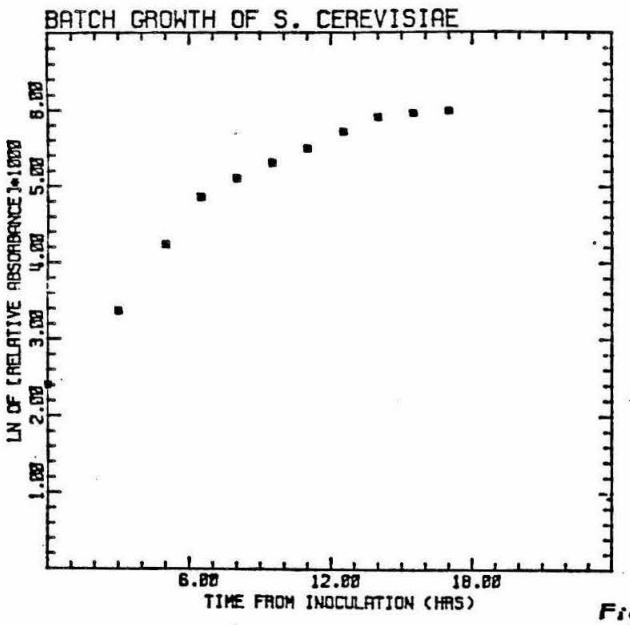

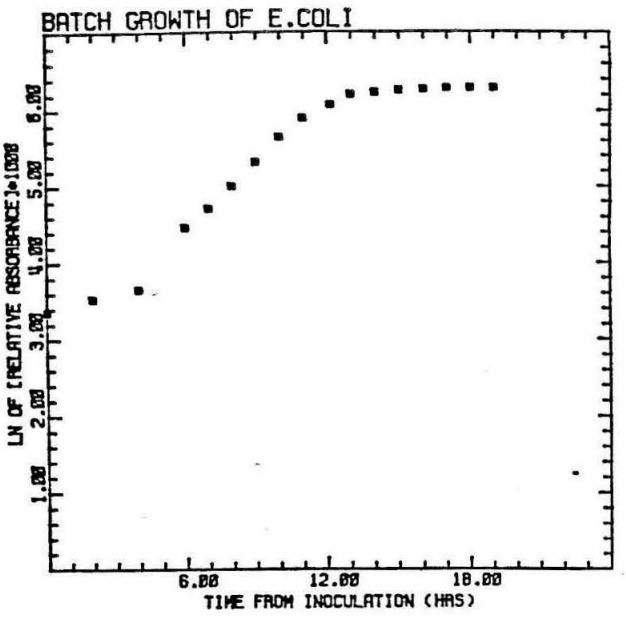

Figure 1

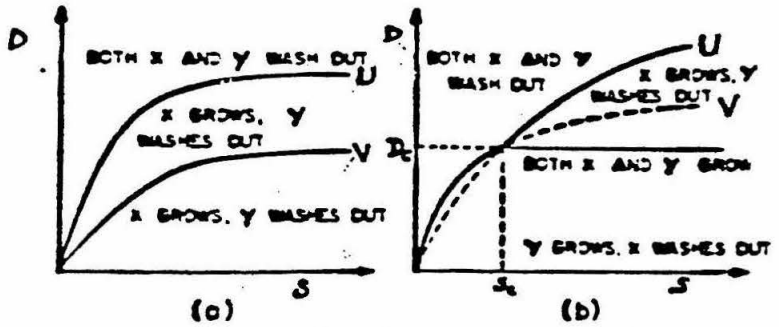

Fig 2. Operating diagrams for a chemostat in which two microbial populations grow competing for the same nutrient.

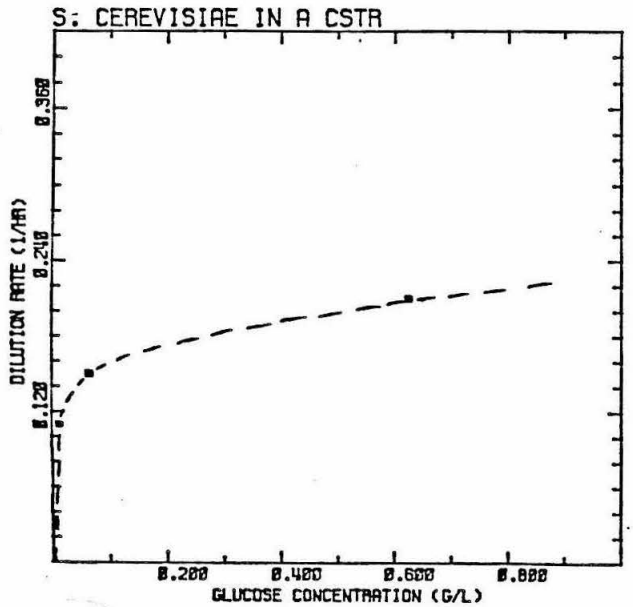

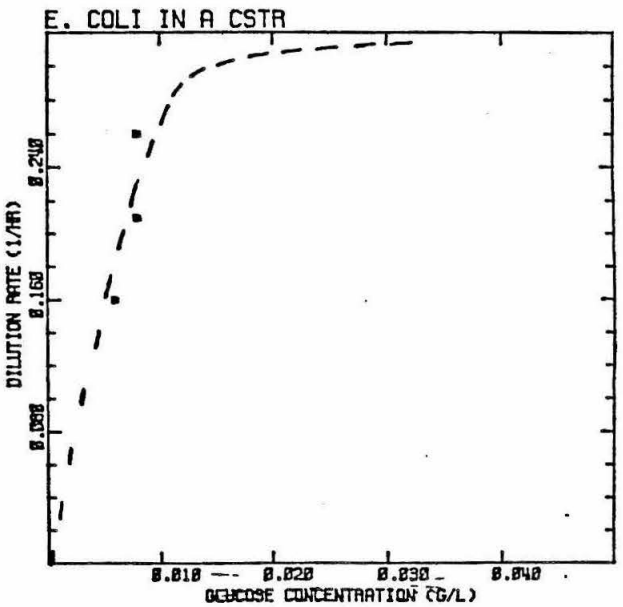

Figure 3

REFERENCES

1. Hardin, G. (1960). "Science", 131, 1292.

2. Stephanopoulos, G., Fredrickson, A., Aris, R. (1979). "Growth of Competing Microbial Populations in CSTR with Periodic Varying Inputs". "AICHE J." 25, 863.

3. Shehata, T. E., Marr, A. G. (1971). "Effect of Nutrient Concentration on the Growth of Escherichia coli". "J. of Bacteriology", July, 210.

4. Leuenberger, H. G. W. (1971). "Cultivation of Saccharomyces cerevisiae in Continuous Culture(I)". "Arch. Mikrobiol.," 79, 176.

BIBLIOGRAPPHY

1. Davison, B. H. (1981). "Experimental Studies of Stable Coexistance of Mixed Cultures".

2. Hansen, S. R., Hubbell, S. P. (1980). "Single Nutrient Microbial Competition: Quantitative Agreement Between Experimental and Theoretically Forecast Outcomes". "Science", 207, 1491.

3. Powell, E. O. (1958). "Criteria for the growth of Contaminants and Mutants in Continuous Culture". "J. Gen. Microbiology", 18, 259.

DIFFUSION LIMITED UNIDIRECTIONAL CRYSTAL GROWTH FROM SOLUTION

SURF Project 1982

Research performed by Darrell Schlom under the supervision of Professor David S. Wood.

Abstract

The goal of this research is to make a crystal growth experiment to be flown aboard the Space Shuttle. Crystal growth calculations were performed using a simplified diffusion equation. These calculations indicated that a crystal growth cell 3" in length would be adequate to simulate an "infinite" solute source for a five day growth period with 35 degrees Celsius supercooling of a potassium dihydrogen phosphate (KDP) crystal and solution contained in an isothermal growth cell. A 3"x2"x1/8" crystal growth cell was designed and constructed.

Introduction

Crystallization from solution is a process involving a simultaneous mass and heat transport between a crystal surface and the surrounding fluid, causing a reduction in the density of the fluid. Consequently, in the presence of gravity, a growing crystal is usually surrounded by a rising convection current (5). It has been suspected that growth in a microgravity environment, which greatly reduces these convection currents, might produce a superior quality crystal. The only crystal growth from solution experiment performed in space to date was done by Dr. Ichiro Miyagawa of the University of Alabama (2). His experiment was performed aboard Skylab-4. Parts of his space grown crystals were of excellent quality and other parts showed highly regular, elongated tubular voids. Crystals grown under the same conditions on earth showed much less regularity in defect structure.

The Student Space Organization (SSO) at Caltech has purchased two five cubic foot self contained payloads ("Getaway Specials") from NASA. My work this summer has been on the continuing development of a crystal growth experiment to be flown on or shortly after STS 11 in December 1983 in the second of these SSO payloads.

The goals of this experiment are to determine whether crystals grown in a convectionless environment in space are indeed superior to ones grown on the earth under otherwise equivalent conditions, and to see how closely the observed growth follows the predictions of a model of crystal growth dynamics proposed by Dr. W.R. Wilcox (4). His growth model predicts the unidirectional growth rate, and concentration profile for the unidirectional growth of a single crystal face in a solution (free of thermal gradients) which is being cooled at a constant rate.

Presentation and Discussion of Results

The growth of a single crystal face in an isothermal cell was decided upon in order to perform an experiment that could be compared to theory. Such an experiment can be directly compared to Dr. Wilcox's theory (4). His theory requires the growth characteristics of the crystal (potassium dihydrogen phosphate) to be known. I have been able to obtain data on most of the required characteristics, however, I have not been able to find experimental data on the interface kinetics of potassium dihydrogen phosphate (KDP). Consequently, detailed theoretical predictions cannot be performed. Calculations using a simplified differential equation (one that neglects the convective term and interface kinetics) have indicated that about 5 days of growth with a 35 degrees Celsius supercooling will result in 1mm of space-grown crystal. These simplified calculations also indicate that a 3" layer of solution above the growing crystal face is sufficient to simulate an infinite body of solution above the growing surface in a diffusion limited mass transfer environment.

Potassium dihydrogen phosphate (KDP) was selected as the crystal to be grown because it is labile, it can be greatly supercooled before it spontaneously nucleates, and it is commercially important. Unfortunately, it is corrosive to many common construcion materials. Many materials were tested in order to find suitable construction materials compatible with KDP. Titanium, 316 stainless steel, phosphor bronze, Teflon, and Tedlar were found to be compatible for long periods of time. Hard anodized aluminum was slowly attacked by KDP (though far slower than bare aluminum).

Because of its ease of machining and inexpensive nature, hard anodized aluminum was selected as the construction material for the crystal growth cell prototype.

From the theoretical calculations described above and the isothermal temperature profile desired, a 3"x2"x1/8" crystal growth cell (inside dimensions) was designed. A 1/8" thick cell was chosen so that thermal uniformity within 1/100 of a degree Celsius could be maintained while cooling the cell at a rate of 1/2 degree Celsius per hour (6).

A possible experiment sequence is as follows. Initially the crystal will be mounted in the growth cell with its (100) or (101) crystallographic face exposed. Once the payload is in orbit, a hot saturated solution will be introduced into the growth cell, covering the exposed KDP crystal face. As soon as the fluid motion of the input solution is damped out by viscous forces, the growth cell will be slowly cooled (less than 1/2 degree Celcius per hour) down to a few degrees above ambient temperature. After a few days of growth, the solution will be expelled from the crystal growth cell and replaced by oil. This will prevent further growth or dissolution of the space-grown crystal.

This experimental sequence entails many mechanical obstacles. Adequate methods of bringing the crystal and solution together at the beginning of the experiment, and of isolating the crystal from the solution at the conclusion of the experiment must be developed. Stringent temperature control of the cell must be exercised throughout the experiment. Measurements of the concentration profile, temperature profile, growth rate, and convection rate should be made and recorded during the experiment. It is important to measure the convection rate in order to show that the experiment was really diffusion limited crystal growth from solution.

In order to test alternative methods of crystal-solution contact and separation, two prototype crystal growth cells have been constructed. These cells allow for the testing of a sliding barrier between the crystal and solution, a plunger forcing out the solution, expanding gasketing to allow for the changes in solution volume with temperature, carbon flakes as a method of flow visualization, and other unforseen problems.

Conclusion

Simplified crystal growth modeling calculations indicate that a semi-quantitative crystal growth experiment is plausible theoretically, although there are still many mechanical problems to overcome. Further calculations are needed to establish the sensitivity required for measurement of temperature, concentration, and growth rate. Tests of the prototype growth cells will result in the modification of current experiment alternatives. Although definite answers to the many aspects of the crystal growth experiment are far off, we have begun to understand the problems that we are trying to overcome.

Acknowledgements

I would like to thank Dr. Paul J. Shlichta of JPL for his unceasing advice and for the continued use of his laboratory facilities; Dr. David S. Wood for his detailed and understandable explanations, simplified crystal growth models, and encouragement; Dr. Brad Sturtevant for his qualitative explanations and continued interest; Dr. George R. Rossman for his enthusiastic suggestions, chemical know-how, and the use of his laboratory facilities and radiation source; Dr. Jane G. Raymond for her friendly advice and loans of needed equipment; Fred MacDonald and Elmer Szombathy for their many machining tips; Connie Bennit for her dedication to and crucial help with this experiment; and to Great Western Inorganics for their $10,000 donation paying for the SSO's second payload canister (which this experiment will fly in).

REFERENCES

1. W.R. Wilcox, Preparation and Properties of Solid State Materials, Vol.2, Dekker, New York, 1976.

2. I. Miyagawa, Final Report: Investigation of Crystal Growth from Solutions, NASA, 1975.

3. Wok, Burton, N. Cabrera, F.C. Frank. The Growth of Crystals and the Equilibrium Structure of their Surfaces, Phil. Trans. Royal Society of London, A.243, pp. 299-358, 1951.

4. W.R. Wilcox, Computer Simulation of Growth of Thick Layers from Solutions of Finite Solute Concentration without Convection, Journal of Crystal Growth, Vol. 56, pp. 690-698, 1982.

5. P. S. Chen, P. J. Shlichta, W. R. Wilcox, and R. A. Lefever, Convection Phenomena During the Growth of Sodium Chlorate Crystals from Solution, Journal of Crystal Growth, Vol. 47, pp. 43-60, 1979.

6. P.J. Shlichta, Third Semiannual Report: Crystal Growth in a Spaceflight Environment, JPL, 1980.

Kelley Scott
20 September 1982

Visualization for Three-Dimensional Turbulent Jet Flow

Abstract

Several attempts have been made to find some means of revealing the three-dimensional structure of turbulent jet flow. In order to obtain more information about the flow's characteristic structures, Prof. P. Dimotakis suggested a new approach; using special scanning techniques and laser induced fluorescent (LIF) dye, we may arrive at a three-dimentional representation of the flow.

Introduction

When a thin sheet of laser light intersects jet flow labelled with LIF dye, the areas in which jet fluid exist fluoresce brightly in proportion to the dye's concentration. It is possible for a camera to capture the progress of the flow and its mechanisms for entrainment of the high- and low-speed fluids. In the cross-sectional views these mixing structures appear as slices of vortices. Mixing of the two fluids takes place in these vortices, which grow in size as the flow moves farther downstream. More and more of the surrounding fluid is entrained until the two fluids are no longer distinct.

By filming a series of parallel cross-sections of jet flow, a general idea of the overall structure should be readily visible. The three-dimensional view can be reconstructed from the succession of two-dimensional cuts. The goal of the project is to examine the entirety of the flow in this fashion and produce a more complete representation of turbulent structures as they evolve in three dimensions. The information gained from this project may be applied to understanding turbulent processes and their effects. Mixing and chemical reaction mechanisms, and jet noise are two examples of such processes.

Presentation and Discussion of Results

When passed through a combination of spherical and cylindrical lenses, a beam of laser light becomes a thin sheet of light. A stepping motor to which a small mirror is attached causes this sheet to be reflected over a small angle in steps of 1.8 . The motor receives pulses from the shutter system of a high speed movie camera. The frequency of stepping is determined by the framing rate, and the direction of the motor shaft reverses at every sixteenth step. Finally, a large cylindrical lens collimates the sixteen reflected sheets upwards into a glass panelled tank. A jet reservoir is centered above this tank. Fluid forced through the jet exit into the tank fluid is intersected in planes mostly parallel to the camera's film plane by the sweeping sheets of light. The camera photographs a single cross-section per frame.

The results so far appear to be good. With the aid of Dimitris Papantoniou, a graduate student in Aeronautics, films were taken of flows with different jet exit velocities. The first film shows the development of a flow with half the exit velocity of the second. Both runs were performed with a jet plenum having an exit diameter of one inch. A balance of structure size and movement with a good portion of downstream flow in the camera's view is achieved with this exit size.

More films will be taken using a larger jet exit. The structures produced with a 3" jet are very large and slow mi ing, so the scanning method will most likely give very detailed coverage of the flow. From these films I hope to produce some type of model of three-dimensional turbulent jet flow.

Conclusions

The scanning method differs from any other in that it allows us to examine thoroughly three-dimensional turbulent flow, rather than just a tiny portion of it. The flow visualization techniques used in this project result in a good representation of the overall structure. The general character of the flow is apparent on film when using the scanning method. This method can be used with different flow rates, and in the future will be adjusted to cover the same areas more extensively using smaller stepping angles.

Acknowledgements

Dimitris Papantoniou, filming and set-up.

Dan Lang, electronics.

Manooch Koochesfahani, trouble shooting.

Werner Dahm, optics and filming.

References

P. Dimotakis, private communication, 1981, 1982.

D Papantoniou, private communication, 1982.

The Neural Control of Birdsong
SURF Report by Dean Shibata
September, 1982

ABSTRACT:

In order to access the requirement for interhemispheric communication in song production, the anterior commissure was sectioned. The operation resulted in a maintenance of normal song for two to three weeks, after which a dramatic deterioration was observed. The nature of respiratory modulation during vocalizations was examined by implanting recording electrodes in motor centers of the medulla. Preliminary results suggest a control of respiratory activity at the level of the forebrain nucleus HVc.

My work for the past two summers in the laboratory of Mark Konishi has concentrated on investigating the anatomy and physiology surrounding the neural control of bird vocalizations. While the study of birdsong was formerly the domain of ethologists, the discovery of an unusual neural system of discrete nuclei governing its control (1) has led neurobiologists to use the song system as a model for answering the question of how brain pathways are organized to cope with the learning and coordination of a complex motor task. I have attempted to characterize several aspects of the functioning and interactions of the system through a series of experiments involving electrical stimulation, neuronal and nerve recording, nuclei lesioning, nerve sectioning, and song analysis. As much of this summer`s work is built directly upon the results of the previous summer, it will often be necessary to describe the two research periods as a single effort.

The majority of the summer was devoted to investigating the nature of the system`s lateralization along with the more general issue of the coordination of the two sides. The system`s lateralization at the hemispheric level (2) is of interest because it resembles the language centers of the human

brain. Prior anatomical studies indicated an absence of contralateral projections between the high-level nuclei in the forebrain, yet physiological studies (3) demonstrated a high degree of coordination in the electrical activities of the two sides. Thus it was suspected that yet undiscovered pathways might be utilized to govern the observed coordinated activity. This hypothesis was tested by sectioning the anterior commissure (analaogous to the corpus collosum), thereby severing any interhemispheric communication.

The surprising result was that the post-operative song remained intact for two to three weeks, but then deteriorated into a grossly simplified structure consisting of repetitions of distorted elements. One interpretation of this result which is consistent with the above-mentioned, seemingly contradictory anatomical and physiological observations is that the coordination of the two sides is achieved through an internal feedback mechanism. Thus, no direct interhemispheric communication is required for song production, yet the motor programs governing the two sides can be sychronized by having access to the other's output. When this feedback is denied, the song gradually deteriorates, just as human speech begins to "slur" with the loss of auditory feedback which accompanies deafening (For the particular bird, Poephila guttata, used for these experiments, auditory feedback is not required for song production). An effort to investigate this hypothesis by recording directly from the anterior commissure during natural song has thus far been unsuccessful. Further work directed towards the identification of any pathways utilized for the proposed feedback system is currently underway.

A second area of inquiry was the manner in which respiration is regulated during vocalizations. From work of the previous summer, it was observed that the electrical stimulation of the high-level forebrain nucleus, HVc, often resulted in aberrant vocalizations which appeared to consist of

respiratory "song pulsing" in the absence of coordinated syringeal activity. The hypothesis that respiration might be modulated or "gated" at the level of HVc is currently being examined by recording from respiratory centers and motor nuclei in the medulla during both HVc-evoked and natural vocalizations.

REFERENCES:

1) Nottebohm, F., Stokes, T.M. and Leonard, C.M. (1976). Central control of song in the canary, Serinus canarius. J. Comp. Neurol. 165, 457-486

2) Nottebohm, F. (1979). Origins and mechanisms in the establishment of cerebral dominance. In "Handbook of Behavioral Neurobiology" (M.S. Gazzangia, ed.) pp. 295-344, Plenum, New York

3) McCasland, J.S. and Konishi, M. (in press)

SURF REPORT

JEN SHU

SUPERCRITICAL EXTRACTION OF COAL

Abstract

Supercritical extraction of coal is a study of coal liquefaction. S.C.E. method is by using a solvent above its critical temperature and high pressure to discover those hydrocarbons and related compounds from coal. A series of experiments by using aromatic compounds as solvents has been done. It shows that larger molecules appeared to have greater solubilizing effects.

Introduction

Supercritical extraction process is based on improved mass transfer. A supercritical fluid has low density and viscosity. Therefore the mass transfer through the pore structure of coal is easier. The experimental work involved (1) S.C.E. of aromatic series, and (2) analyses of products by using N.M.R. spectroscopy, gas chromatography and sulfur analysis. The solubility parameter, combined with the second virial coefficient concept, provides more understanding about the nature of S.C.E. of coal.

Presentation and Discussion of Results

Theoretical Approach:

(1) The solubility parameter.

$$\Delta H \text{ mix} = \nu(\delta_1 - \delta_2)^2 \qquad \Delta G \text{ mix} = \Delta H \text{ mix} - T\Delta S \text{ mix}$$

In order to get the minimum of ΔG mix, the solubility parameter δ_1 should be equal to δ_2. Therefore, a good solvent should have a solubility parameter close to the solute. Coal has an average δ around 10. A solvent with a solubility parameter close to that of the coal will have a maximum extraction of coal.

(2) The second virial coefficient.

Rowlinson and Richardson made an approximation.

$$B_{12} = \frac{1}{2}(B_{11} + B_{22})$$

$$\ln\left(\frac{C_2}{C_o}\right) = \frac{(\nu_2 - B_{22}) - B_{11}}{\nu}$$

B_{12} = second virial coefficient of coal and solvent

ν = molar volume of mixture

For the same value of ν, a solvent with a more negative B_{11} can extract more material. Larger $-B_{11}$ means larger and heavier the compound.

Experimental Work:

(1) S.C.E. of aromatic series. The S.C.E. process is operated at 350°C, 2000 psia. The solvents are in fluid region under such temperature and pressure. The aromatic compounds that have been used are benzene, toluene, ethylbenzene, xylenes, mesitylene, and isopropyl benzene. Generally more extraction results as the $-B_{11}$ of aromatic compounds increases.

(2) Analyses of products. The N.M.R. spectroscopy and gas chromatography of the products show that there are indeed coal extract not from the solvents. Also, the S.C.E. process is a physical reaction. The sulfur analysis shows sulfur content of coal is pretty constant throughout the extraction process.

Conclusions

When aromatic compounds were used as supercritical solvents:

(1) $-B_{11}$ larger means larger extraction (which also implies larger molecular weight means larger extraction).

(2) No significant sulfur removal.

(3) Coal extracts are different by using different solvents.

Bibliography

1. Robert T. Fedors. A Method for Estimating Both the Solubility Parameters and Molar Volumes of Liquids.
2. Josef Chrastil. Solubility of Solids and Liquids in Supercritical Gases.
3. Harris, E. C. Fuel 58, 599 (1979).
4. Kiebler. Ind. Eng. Chem. 32, 1389 (1940).
5. Rowlinson and Richardson. Adv. Chem. Phys. 2, 85 (1959).

SURF REPORT

SEPTEMBER 8, 1982

NAME: ERIC SINN

TITLE OF PROJECT: REGULATION OF DNA REPLICATION

ABSTRACT:

This paper describes the characterization of a temperature-sensitive (ts) plasmid, pJN75, which exhibits normal copy number at the permissive temperature (30°C) but has an abnormally high copy number and a lethal effect at the nonpermissive temperature (42° C). By sequencing, we have located the cause of this phenotype to a transition mutation 398 basepairs upstream from the origin. This region encodes the primer and serves as a promoter for RNA I. Experiments have indicated that the mutated primer, not the promoter is responsible for the mutant phenotype.

INTRODUCTION:

Plasmids are extrachromosomal, autonomously replicating DNA's found in most bacteria. Unlike virulent episomal elements, plasmids can ensure their replication without disrupting or dominating host replication mechanisms. Usually the smaller plasmids are maintained at approximately 30 copies per cell. Maintenance of constant copy number per cell over many generations requires precise regulation of plasmid replication. The study of plasmid replication control is a direct method for elucidating the mechanism for the regulation of DNA replication.

Conrad, Campbell and Moser have found that a plasmid -encoded RNA, RNA I, could funtion as a negative regulator of plasmid replication (1,2). RNA I is a small RNA, around 100 bases long. It is a trans-acting, replicon specific repressor of plasmid replication. RNA I inhibits plasmid replication by interacting with the RNA primer. As copy number increases so does the cellular level of RNA I. Once a critical concentration of RNA I is achieved, plasmid replication is inhibited. During growth and division the inhibitor is diluted and plasmid replication is allowed.

We are currently working on a ts plasmid of E. coli which exhibits normal plasmid copy number at 30° C but shows an abnormally high plasmid copy number at 42° C. Prolonged incubation of cells carrying the mutant plasmid, pJN75, at 42°C is lethal to the cells. Cells containing the homologous wild type plasmid, pJN70, exhibit normal viability and plasmid copy number at this temperature.

RESULTS:

By DNA sequencing we have been able to locate the mutation to a single base pair change 23 base pairs upstream from the beginning of the RNA I transcript. Since one strand of DNA in this region serves as the promoter for RNA I while the complementary strand encodes the RNA primer, we were not sure if the mutation affected the RNA I promoter or the primer RNA. To find the cause of the ts phenotype I have inserted a piece of DNA containing the promoter and the coding sequence of RNA I from a wildtype plasmid into the ts plasmid. If the high copy number ts phenotype of pJN75 is caused by a defective RNA I promoter, the cloned sequence will complement the defect by providing the cell with a wild-type RNA I and the mutant phenotype will be suppressed. If the mutant phenotype is not suppressed by wild-type RNA I, then the mutation affects a cis-acting funtion, probably the RNA primer. My insert failed to suppress the mutant phenotype indicating that the mutated primer is the cause of the temperature sensitive high copy number characteristic.

To eliminate the possibility that the failure of my insert to suppress the mutant phenotype is due to an experimental artifact (e.g. failure of the insert to be transcribed) I repeated the complementation experiment using a different method. Both pJN70 and pJN75 contain the gene for ampicillin resistance (Amp). I excised the Amp gene from pJN70 and inserted a chloramphenicol resistance (Cm) gene in its place; the new plasmid was named pCm70. I transformed cells containing pJN75 with pCm70 and cells containing pCm70 with pJN75. Cells with two populations of plasmids were selected for by requiring growth in the presence of both ampicillin and chloramphenicol. Primer mutations are expected to be dominant while RNA I mutations are recessive as discussed in the last paragraph. Cells with both pJN75 and pCm70 were temperature sensitive. This confirms the results from my previous experiment indicating that it is an altered primer which is responsible for the temperature sensitive phenotype.

CONCLUSIONS:

1. A transition mutation (C to T) at a position 398 base pairs upstream from the origin is responsible for the temperature sensitive high copy number phenotype of pJN75.

2. Although the mutation lies in a location that both encodes the primer of the plasmid and functions as the promoter for the RNA I, a mutated primer seems to be resposible for the mutant phenotype.

BIBLIOGRAPHY:

1. Conrad, S. E., and Campbell, J. L. (1979). Role of Plasmid Coded RNA and Ribonuclease III in Plasmid DNA Replication. Cell 18, 61-67.

2. Moser, D. R., and Campbell, J. L. (1982). A Plasmid-Encoded RNA, RNA I, Determines Plasmid Copy Number and Incompatibility Properties. Submitted J. Bacteriol.

VLBI Observations of the Galactic Center

Paul J. Ste.Marie

SURF fellow

Marshall H. Cohen

Sponsor

ABSTRACT

The compact radio source at the Galactic Center was observed at 3.8 and 13 cm. The 3.8 cm data show a symmetric Gaussian structure 15.3 milliarc-seconds in diameter with a total flux of 0.86 Janskys. The 13 cm data failed to produce any useful results, due to defective tapes.

VLBI Observations of the Galactic Center

Paul J. Ste.Marie

SURF fellow

Marshall H. Cohen

Sponsor

1. Introduction

The compact source at the Galactic Center (G0.0) is particularly intriguing because it may be a weak but close (and thus visible) version of the giant compact sources in quasars and active galaxies.[1] Its study offers hope of understanding the energy mechanism in the larger, more powerful sources.

The diameter of G0.0 varies as the square of the wavelength, which is usually interpreted as due to scattering in a dense plasma cloud near the Galactic Center.[2] Its flux is variable as seen with the VLA and the Greenbank interferometer,[3] and there is a suspicion that its size is variable at 3.8 cm.[4]

The objectives of this experiment are to get a good measure of the visibility function of G0.0 at 3.8 cm, and an estimate of the diameter at 13 cm, in order to:

1. Compare the visibility function at 3.8 cm on the Goldstone-Owens Valley baseline to the ones measured in 1976 and 1978 for variations.
2. Check the square law relation with the 3.8 and 13 cm data.
3. Look carefully at the 3.8 cm visibility data, especially the closure phase, to see if it could be a symmetric Gaussian.
4. Seek an unresolved core, as reported at 3.8 cm.[5]

2. Results of Observations

On 19-20 July 1982, the Galactic Center was observed for ~6 hours using the Goldstone-Owens Valley-Hat Creek interferometer, at both 3.8 and 13.0 cm. The 13 cm data from 20 July were lost due to defective tapes. The remaining data were split up for reduction and calibration. The 19 July data were reduced by Andy Berkin, and I reduced and calibrated the 20 July 3.8 cm data. Differences in the results are pointed out as they occur.

2.1 Data reduction

The data was reduced using the standard VLBI techniques. In brief, the videotapes from each station were played back on the VLBI correlator, which corrected for the time offsets at each station and calculated the cross-correlation function from the data. The correlator recorded these data points onto standard 9-track magnetic tape.

The output tapes produced by the correlator were then transferred onto a DEC VAX-11/780 computer. Then the program PHASOR was used to fit interference fringes and

1. Brown, R. L., *et al. Astrophysical Journal* 83, 1594, 1978.
2. Backer, D. C. *Astrophysical Journal Letters* 222, L9, 1978.
3. Brown, R. L., *et al. Ap. J.* 250, 155, 1981.
4. Lo, K. Y., *et al. Ap. J.* 249, 504, 1981.
5. Kellermann, K. I., *et al. Ap. J. Letters* 214, L61, 1977.

produce the raw correlation data. This data consists merely of correlation sums and is uncalibrated.

2.2 Calibration

To calibrate the data, it is necessary to have measures of two parameters:

- T_{sys}, the system temperature. This is the total power output at the antenna, measured in degrees Kelvin.
- T_a, the antenna temperature. This is the portion of T_{sys} that is from the source radiation.

T_a is defined[6] by the equation:

$$T_a = \frac{A_{eff} S}{2k} = \frac{\eta \pi r^2 S}{2k}$$

where

A_{eff} ≡ effective area of antenna
k ≡ Boltzmann's constant
S ≡ total flux of source
η ≡ antenna efficiency
r ≡ radius of antenna

which makes it possible to derive T_a from the antenna gain, which is fairly well known at its peak value.

Unfortunately, the gain varies by ~20% with zenith angle at 3.8 cm. This curve has been derived for Owens Valley[7] but is unknown for Goldstone and Hat Creek. Thus NRAO 530 was used as a calibration source and assumed to be a unresolved point source. Gain curves were then derived for the two stations that fit the NRAO 530 data to a straight, flat line at 4.5 Jy. (1 Jy ≡ 10^{-26} W $Hz^{-1}m^{-2}$)

The Owens Valley-Hat Creek baseline had to be given a baseline factor of 1.363, instead of 1.239, which may be due to misalignment of the filters at the two stations. The crossing point at ~3.5 hours in the *uv*-plane was used as a check of the consistency of the data, which held to within 10%. The closure phases are auto-calibrating[8] and thus are unaffected by the calibration.

2.3 Model fitting and Results

A least-squares gradient search procedure was used to fit a model to the calibrated data. The results were:

1. Total flux of source is 0.86 Jy.
2. Source diameter is 15.3 milliarcseconds.
3. Closure phase is approximately zero. (The 19 July data show a small positive offset of approximately 1 σ fairly consistently.)
4. Data are consistent with a symmetric Gaussian.

3. Conclusions

From the observations, several new conclusions may be drawn. The closure phase seems to indicate that the source is symmetric, although the 19 July data reduced by Berkin are inconsistent with this conclusion. The diameter of the source deviates from the square law,[9] and the total flux was slightly lower (~15%) then expected. This may

6. Carleton, N. *Methods of Experimental Physics* 12C, (New York City: Academic Press, Inc.) 1974.
7. Shaffer, D. internal memo, June 1981.
8. Cohen, M. H., *et al. Ap. J.* 201, 80, 1975.

indicate variability with time.[10] No evidence was found of an unresolved core.

Bibliography

[1] Brown, R. L., Lo, K. Y., and Johnston, K. J. *Astrophysical Journal* 83, 1594, 1978.

[2] Lo, K. Y., Cohen, M. H., Readhead, A. C. S., and Backer, D. C. *Astrophysical Journal* 249, 504, 1981.

[3] Backer, D. C. *Astrophysical Journal Letters* 222, L9, 1978.

[4] Brown, R. L., Johnston, K. J., and Lo, K. Y. *Astrophysical Journal* 250, 155, 1981.

[5] Kellermann, K. I., Shaffer, D. B., Clark, B. G., and Geldzahler, B. J. *Astrophysical Journal Letters* 214, L61, 1977.

[6] Carleton, N. *Methods of Experimental Physics* 12C, (New York City: Academic Press, Inc.) 1974.

[7] Shaffer, D. internal memo, June 1981.

[8] Cohen, M. H., Moffet, A. T., Romney, J. D., Schlizzi, R. T., Schafer, D. B., Kellerman, K. I., Purcell, G. H., Grove, G., Swenson, G. W. Jr., Yen, J. L., Pauling-Toth, I. I. K., Preuss, E., Witzel, A., Graham, D., and Rinehart, R. *Astrophysical Journal* 201, 80, 1975.

9. Backer, *op cit.*

10. Brown, *et al.*, *op cit.*, 1981.

SURF Final Report

preliminary version

September 17, 1982

A Study of Airborne Transportation in the Santa Barbara County Area

by

Lee Sunderlin

working with

Dr. F. H. Shair

A Study of Airborne Transportation in the Santa Barbara County Area

Introduction

The coastal areas in and around Santa Barbara County are a good example of a land breeze / sea breeze system. Greater heating of the air over land during the daytime causes colder and denser air to flow in and displace it, resulting in a sea breeze during the daytime. The opposite effect causes a land breeze at night.

This study involved the release of a tracer gas (SF_6, Sulfur Hexafluoride) offshore during the morning and early afternoon while a sea breeze was starting. The tracer was subsequently tracked to determine its behavior under several influences. These influences include the diurnal wind patterns mentioned above, the convergence zone where the sea breezes from the west coast and the south coast of the county meet, and the effect of mountains in the path of the winds. (see map)

The data from this study has value as a purely local analysis of air flow patterns. Normal pollution from industry, automobile traffic, oil wells, and airplane traffic (much of it from Vandenberg Air Force Base) is a problem. The possibility of mishaps at Vandenberg or on an oil rig, which would release a sudden plume of pollutants from a point source as this study did, also exists.

This possibility will become more serious in the future, as a space shuttle launching facility is completed at Vandenberg, and as new oil fields are developed. As a 1978 air quality impact report stated, "Future studies in Santa Barbara County would benefit greatly from improved knowledge and documentation of local windfields and pollutant transport patterns."[1]

This study also has more general value as a study of coastal air transport. This field is poorly characterized, because of the lack of meteorological data from offshore areas and the complexity of wind patterns near a land / sea interface. The data gained in this study will be of value in future models of this system.

Experimental Procedure

The release system for this study consisted of six cylinders of compressed SF_6 linked in parallel to a flow meter set to release 80 lbs / hour. The release lasted from 0715 to 1340 Pacific Daylight Time on September 8, 1982. The total amount of tracer released was about 440 lbs.

Air samples were collected by two different methods.

---

[1] "Updating and Analysis of Air Quality Impacts of Regional Transportation Plans for Santa Barbara County," prepared for the Santa Barbara County-Cities Area Planning Council by Environmental Research and Technology, Inc., June, 1978.

One was by use of automatic samplers left at specific sites. These stationary samplers took one sample continuously during each hour. They ran for 12 hours; most sites had three samplers to provide 36-hour coverage.

The other sample collection method was by automobile traverses. Samples were taken out the window of a car at specific points on several highways.

The samples were analyzed by means of electron capture gas chromatography. This method is accurate to within 20% on concentrations down to 10 parts per trillion (ppt), and can detect concentrations as low as 1 ppt. Portable gas chromatographs, accurate to within about 50%, were used in the field to help track the tracer and determine traverse routes.

Results and Conclusions

As of September 17, final analysis of the data from this test is still in progress. A completed final report will be made as soon as possible.

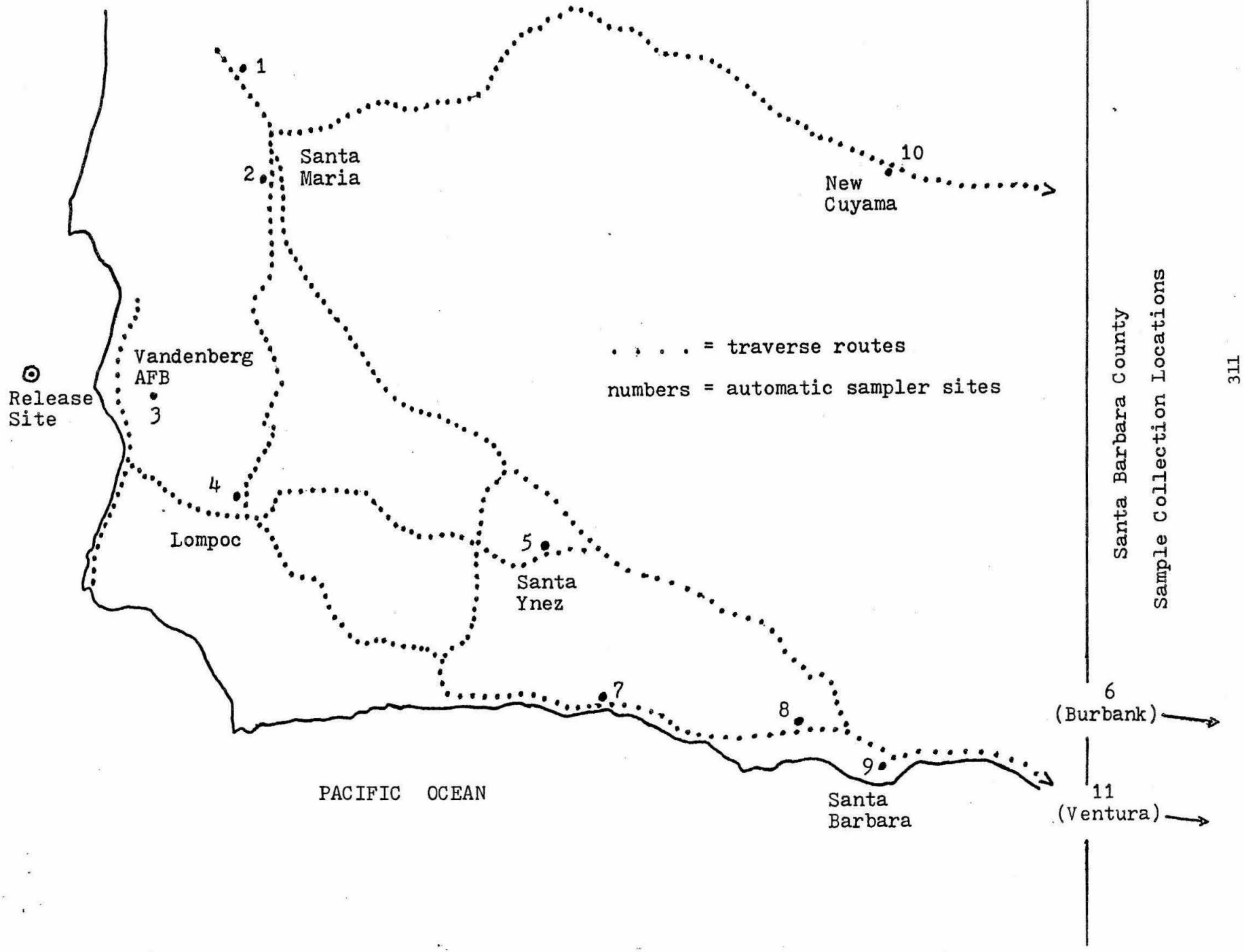
1
Santa
Maria
2
10
New
Cuyama
Vandenberg
AFB
3
Release
Site
. . . . = traverse routes
numbers = automatic sampler sites
4
Lompoc
5
Santa
Ynez
7
8
6
(Burbank)
9
PACIFIC OCEAN
Santa
Barbara
11
(Ventura)
Santa Barbara County
Sample Collection Locations

Santa Barbara County
Wind Patterns
and Topography

Interhelical DNA-DNA Crosslinking in Intact T7 Bacteriophage

Investigator: Eliza L. Sutton
Advisor: Peter B. Dervan
September 3, 1982

The higher order structure of packaged viral DNA can be studied using interhelical crosslinking reagents. DNA crosslinked in intact T7 has been treated with enzymes to yield fragments of unique length, each unambiguously labelled on one end. The locations of the crosslinks, plotted, will give a nearest neighbors map of T7 DNA.

The higher order structure of nucleic acids packaged in phage presents an interesting and unsolved problem. Attempts to elucidate the packaged nucleic acid structure of viruses by X-ray diffraction studies have failed to give any definitive structure, due to the large size and dense packing of the DNA. These studies have, however, indicated that the packaging is ordered and regular (1) and that it seems to be arranged around an axis parallel (1) or perpendicular (2,3) to the axis of the virus. Examination of mildly disrupted bacteriophage by electron microscopy has shown DNA extruding as rings or spirals. From these studies, several models have been proposed, including a ball of string (4), a simple solenoid (1,4), and a coil of coils (2,3). However, until recently no precise, interpretable method has been available for determining the packaged structure of viral nucleic acid.

Recently the Dervan group at Caltech designed and synthesized a reagent (5) that covalently links adjoining DNA helices within intact bacteriophage. The crosslinking reagent, bis(monoazidomethidium)octaoxahexacosanediamine (BAMO), is nucleic acid specific, bifunctional, water soluble, chemically inert, and photoactivatable. BAMO's span of ~40Å is sufficient to link two neighboring helices. The plan of action has been

developed for use of this reagent to crosslink DNA in intact phage, measure the location of the crosslinks, and plot the data to construct a nearest neighbors map of interhelical contact points. The purpose of this summer's research was to finalize the protocol and to begin constructing a nearest neighbors map towards eventual determination of nucleic acid structure of T7.

The methodology is as follows. Whole T7 phage were incubated in the dark with BAMO, some of which entered the phage head and became intercalated in two neighboring helices of DNA. After photolysis to bind the linker molecule in place, the phage heads were burst open. The DNA was cut once in the middle by BstEII, a restriction endonuclease. T4 polymerase was used to excise $\sim 10^2$ nucleotides from one strand of each of the four ends with its 3'→5' exonuclease action. (The entire genome is 39,936 base pairs long.) Addition of dATP, dCTP, dGTP, and biotinylated dUTP (6) resulted in 5'→3' polymerization along the single strand template ends with incorporation of the biotin-labelled dUTP. Incubation with a second restriction endonuclease, BglI, resulted in two more cuts of the DNA. The structures of interest at this point were crosses consisting of two pieces of DNA linked at one point. Each of the four possible pieces (from three endonuclease cuts) had one unambiguously biotin-labelled end. Avidin covalently attached to polymethacrylate spheres (7) were incubated with the DNA; biotin binds strongly to avidin, resulting in this case in cross structures with two ends labelled with spheres visible under the electron microscope. Since each fragment of DNA was a unique length and direction was unambiguous (because of the spheres), the placement of the link between the two fragments can be measured without ambiguity. Each cross then gives a point on the nearest neighbor map.

Double end labelled crosses originally composed less than

one percent of the DNA examined under the electron microscope, making the search for data points prohibitively time-consuming. This summer gel electrophoresis was introduced into the protocol as a means of efficiently separating the cross-linked DNA from uncrossed or over-crossed DNA. The level of crosses seen has improved significantly, up to about 40% of the DNA examined.

With the protocol finalized and preparation of cross-rich samples possible, a nearest neighbors map for T7 might be compiled in less than a year. Work on this problem will continue through the school year.

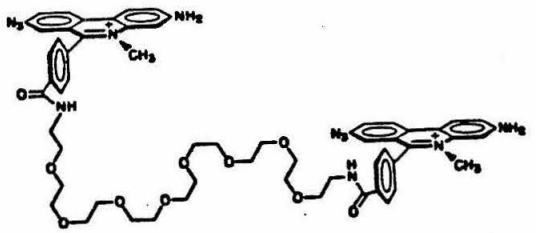

BAMO

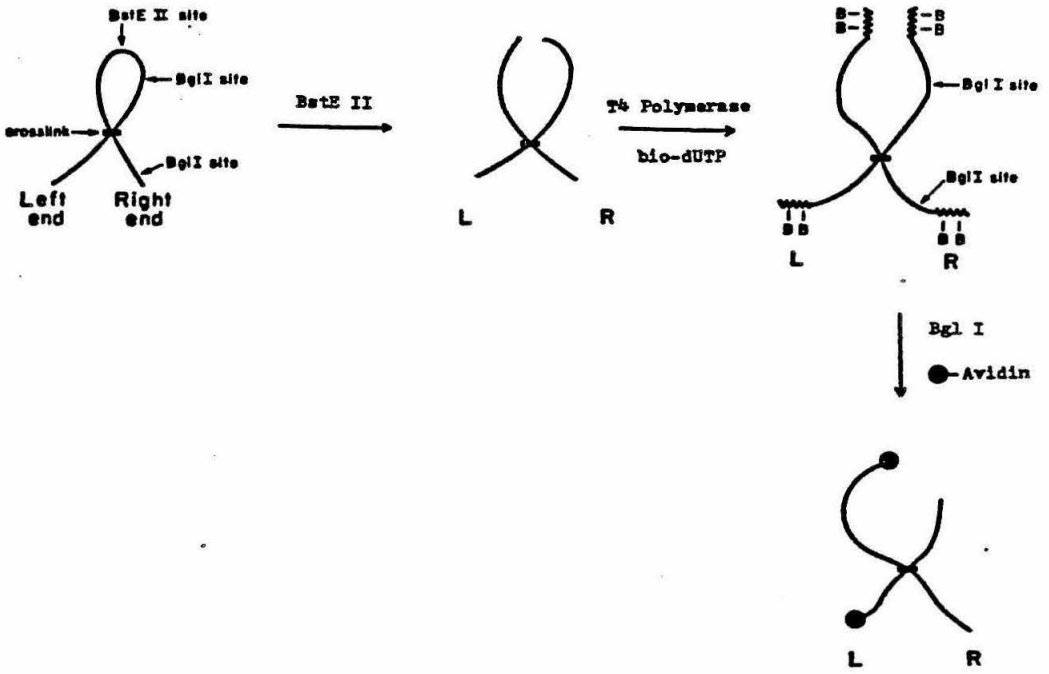

References:

(1) Earnshaw, W.C. and Harrison, S.C. (1977) Nature, 268, 598-602.

(2) Kosturko, L.D., Hogan, M., and Dattagupta, N. (1979) Cell, 16, 515-522.

(3) Kilkson, R., and Maestre, M.F. (1962) Nature, 195, 494-495.

(4) Richards, K.E., Williams, R.C., and Calendar, R. (1973) J. Mol. Biol., 78, 255-259.

(5) Mitchell, M.A., and Dervan, P.B. (1982) J. Amer. Chem. Soc., in press.

(6) Langer, P.R., Waldrop, A.A., and Ward, D.C. (1981) Proc. Nat. Acad. Sci. USA, 78, 6633-6637.

(7) Manning, J.E., Hershey, N.D., Broker, T.R., Pellegrini, M., Mitchell, H.K., and Davidson, N. (1975) Chromosoma, 53, 107-117.

Mount St. Helens & Fluid Flows

9/8/82

Matthew J. Swass

Abstract: Current debate in geology centers around volcanic eruptions and the mechanisms responsible for them. Current models include gravity driven flows, potential flows and fluid jets. Maps of the Mount St. Helens destruction lend support to the fluid jet model. A small scale laboratory apparatus is being made to explore this idea further.

The May 18th, 1980 eruption of mount St. Helens has sparked some debate in the geological community as to the nature of volcanic eruptions. The most simple models seek to describe the event as being merely a gravity driven landslide of material.[1] A slightly more sophisticated model is the potential flow, in which material is ejected upwards from the volcano's vent and then evenly dispersed about it.[2] The most sophisticated models describe eruptions in terms of multiphase fluid jets. The fluid jet is caused by a"vapor flash," in which the pressure on a large reservoir of superheated liquid is suddenly lowered. This causes the liquid to boil explosively, which is a common cause of industrial accidents. The expansion of material from a high pressure reservoir to a low pressure one under steady state conditions is well understood.[3] However, volcanic blasts are of too short a duration for steady state conditions to develop. The resulting flow is called a transient jet. Due to limits in analytic methods, no theory for these transient jets exists. The purpose of the present project is to construct and operate a small scale laboratory "volcano," which will be used to explore some of the aspects of transient multiphase jets.

The Blast at Mount St. Helens was investigated by Dr. Susan Kieffer of the United States Geological Survey. Dr. Kieffer is a co-investigator on this project. Her work indicates that the eruption, or blast, involved a considerable transfer of momentum.[4,5] Nearly three cubic kilometers of material was displaced, all of it to the north of the volcano. Furthermore, trees over a 500 Sq. km. area to the north of the volcano were blown down as well. The gravity flow model is inadequate to describe these effects, and the potential flow model is strongly contradicted as well—it does not predict a net momentum transfer.

Opponents of the fluid jet model cite as counter—evidence the fact that observers near the volcano heard no blast, and that only a dull rumble was heard.[6] This is cited in spite of the fact that a distinct blast was heard in far away regions, like Vancouver, Canada.

One aspect of our work has been to study the formation of a shock front ahead of a transient jet. Using a high speed spark-gap photography system, we were able to capture the formation of a compression wave ahead of our transient gas jets. These compression waves develop into shock waves at some distance from the nozzle or orifice in question.

An important aspect of our work is the role played by solids in our liquid reservoir. Solids compose a major portion of the liquid reservoir in a volcano. For example, the "liquid" reservoir in Mt.St. Helens is estimated to be only 15% water by volume. Solids serve three functions:

1) Granular solids would provide nucleation sites to drive the phase change.
2) The solid would provide the specific heat to drive the reaction
3) A solid would also simulate the mass loading in a multiphase jet.

In accordance with criteria 2), a solid that would provide a high relative heat capacity to vaporize the host liquid. Hence, aluminum powder was selected for the mass loading portion of these experiments because it has a higher heat capacity and density than does glass.

Because Aluminum powder is very dangerous to work with, and also because pressure differences are a fundamental parameter in the experiments, a large vacuum tank is being prepared for to fire the multiphase transient jet into. Unfortunately, as of this writing, not all the parts of this apparatus have been delivered by the manufacturers. However, a large part of the heavy construction is done, and the apparatus can be readily assembled when the parts are completed.

The scale of the experiments is one ten thousandth. On this scale, the vent on the experimental apparatus is one centimeter wide, and the fluid reservoir is ten centimeters in diameter. A 1 meter boulder on this scale is 100 microns across. An aluminum foil diaphragm is placed over the orifice to the reservoir. As the pressure in the high pressure reservoir is increased, the diaphragm bulges outwards onto a pair of razor blades and eventually ruptures. The liquid/solid mixture is then free to 'flash' into a solid-liquid-gaseous jet, which expands outwards into the vacuum tank. In these experiments, Freon 13 is used as the propellant liquid, because of its ideal thermodynamic properties, its chemical inertness and its low surface tension- the host liquid has to wet ten to one hundred micron diameter granules. The resulting jet is to be captured with a high sensitivity Schlieren photography system, and the pictures are analyzed for qualitative features.

Conclusion: Better understanding of transient jets will permit geologists to better predict volcanic blasts and define the hazard zones associated with them.Other models of eruptions are too contrived and have too many adjustable parameters to do this. Other applications of this work relate to the ignition of solid rocket boosters, as well as some astronomical events like geomagnetic storms, volcanic bursts on Io, the moon of Jupiter, and interstellar radio jets.

Bibliography

1) Private communication with Dr. B. Sturtevant, 8/8/82

2) Malin, M.C, and Sheridan, M.F. "Computer -Assisted Mapping of Pyroclastic Surges," Science, 8/13/82 pp.637-9

3) See for example Liepmann,H.W. and Roshko,A. Elements of Gasdynamics, GALCIT Aeronautical Series, New York: J.W.Wiley & Sons, 1957

4) Kieffer, S.W. "Blast Dynamics at Mt. St. Helens on 18 May 1980." Nature, 6/18/81 pp.568-570

5) " " " " "The Blast at Mt. St. Helens:What Happened?" Engineering and Science, California Institute of Technology, 9/81

6) Decker,R.B. &Decker,B. "The Eruption of Mount St. Helens," Scientific American, March 1981.

7) Sturtevant, B. "The Fluid Mechanics of Volcanic Eruptions Transient Jets of Multiphase Fluids." NSF Proposal for Research, 8/16/82

The Author would like to thank Mr. George Lundgren, Mr. George Wilson and Mr. Howard McDonald of the Aeronautics Machine Shop for their advice and aid in constructing experiments this summer.

CHRIS THOMPSON

No Report Submitted

HAROLD WEISER

No Report Submitted

The reaction $\pi^- p \rightarrow \pi^{\pm} K^{\mp} K^0 X$

Julian West

Observations of the D(1285) and the E(1440) cited by Dr. Jean Dickey in the reaction $\pi^- p \rightarrow \pi^{\pm} K^{\mp} K^0$ were studied. An attempt was made to duplicate Dr. Dickey's findings at a beam momentum of 100 GeV/c and to find similar signals at 175 GeV/c.

My research this summer was performed under the sponsorship of Professor Geoffrey Fox and the more direct guidance of Dr. Stuart Stampke. It was an effort to redo some of the analysis of a high-energy physics experiment run at Fermilab a few years ago. In particular, we were searching for D(1285) and E(1440) mesons from the reaction $\pi^- p \rightarrow \pi^{\pm} K^{\mp} K^0$. In this report, I shall discuss my summer's work in roughly chronological order. Thus, I begin with a general discussion of the experiment before discussing my efforts to duplicate the graphs in Jean Dickey's paper. I then discuss attempts to copy the raw data from tape to disk, and conclude with my study of the two "Cerenkov counters" included in the apparatus. This last should be considered the most important part of the project.

The protons for the reaction were supplied by a stationary liquid hydrogen target, while the pions came from a fixed momentum beam. The e xperiment was run at three different beam momenta: 50 GeV/c, 100 GeV/c and 175 GeV/c. Data was collected by a number of proportional wire chambers and two Cerenkov counters downstream of the hydrogen target.

I began my work with data which had already undergone preliminary analysis. The particle tracks, for example, had been reconstructed from the PWC data, and

charges had been ascribed to each particle. I also had the necessary software, in the form of a fortran programme. This programme analysed the data further, determining the species of each particle and making a number of further cuts based on the topology of the reaction, the momenta of the particles, and the like. It then produced a series of histograms which were to plot physically interesting properties which we wanted to study, such as the mass of a system of particles.

The programme as it initially existed was meant to duplicate the graphs in a recent paper by Jean Dickey written at Caltech, in which she claimed to observe both D and E mesons. We discovered, however, a number of differences between our code and the published paper. Even accounting for these, the plots turned out similar to, but slightly different from, the graphs in the paper. In most cases, the alleged signals were not as strong as the published claims. This can perhaps best be seen in the graphs shown in figure 1. This is a $KK\pi$ mass distribution with a δ cut (mass(KK) ≤ 1.04), and shows both the D and E signals clearly in the paper. Figure 1 compares the graph from the paper to one obtained using revised Cerenkov cuts to be discussed later in this report.

Eventually, we decided that our output was sufficiently close to the paper, and that further experimentation of this kind would not produce significantly better results. We thus changed the immediate direction of our efforts. It was decided that the programme could be run significantly more quickly if the data were saved on disk rather than on tape. I thus set about trying to write a useful subset of the events to disk. Unfortunately, this proved to be a more difficult task than it first appeared, since there were a number of errors in the code, and we lost rather a lot of time to this effort during the middle part of the summer.

This job was successfully completed, however, and we were able to proceed all the more quickly for its having been done. The main thrust of my work for the rest of the summer was to understand the analysis performed by the "Cerenkov counters" and make reasonable decisions based on this analysis.

The Cerenkov counters were used to determine the species of each particle. Each counter was a large chamber filled with a dielectric. When a particle travels faster

than the speed of light in a medium, it emits a faint blue light known as Cerenkov radiation. This was detected by an array of mirrors and phototubes at the back of the otherwise dark chambers.

Since we know the path and momentum of every particle passing through the Cerenkov counters, we can assume that the event was a $\pi\pi K$ and then calculate how much light we would expect to see in each mirror. If one of the particles was assumed to be a kaon instead of a pion, we would expect less light, or no light at all, since a kaon of the same momentum travels more slowly.

Using Poisson statistics, we can compare the expected value from each prediction to the actual observed value. A series of subroutines in the main programme carried out these calculations for several hypotheses and returned the likelihood, or the log of the calculated probability, in each case. Decisions about whether or not to include an event, and if so as what, were based on cuts made on the difference between two likelihoods.

It seems clear that these likelihood differences are somewhat important, yet we had surprisingly little understanding of how they actually behaved. I put some study into this, and obtained a degree of understanding. We then tried a few jobs using new Cerenkov cuts of our own devising. Jean Dickey had requrired the momentum of each particle to be between 6 and 45 GeV/c, in order to maximize the sensitivity of the Cerenkov counters. She had required $L(\pi\pi K^0) - l(K\pi K^0) \geq 10$ for a pion and $L(\pi\pi K^0) - L(K\pi K^0) \leq -2$ for a kaon. These figures were derived by testing the counters on known kaons and known pions.

We tried two variations on this, with moderate success. We first tried requiring momenta $\gtrless 6$, $\Delta L < 0$ for a kaon (actually a relaxed cut which Dr. Dickey had used), and $\Delta L \geq 1$ for a pion. It was this effort which resulted in the graphs included with this paper. The second variation, at Dr. Fox's suggestion, relaxed the pion cuts entirely, requiring both $\Delta L < -1$ and momentum between 6 and 50 for a kaon, and calling all other particles pions regardless of momentum.

In general, our efforts can be said to have failed. While we did not observe any overwhelmingly strong signals, neither did we prove that such signals were not hid-

den somewhere in the data. It is not clear that the fault rests entirely with us, however, since if there is a signal it is undoubtedly weak, and any form of analysis with the Cerenkov counters appears to be suspect due to the nature of the analysis and the efficiency of the counters. It also appears that the signals get weaker at higher beam momentum; thus the 175 GeV/c data is not so good as the 100 GeV/c data. The best data of all, the 50 GeV/c data, is unfortunately rather limited in quantity. Although the 175 GeV/c findings are not inconsistent with Jean Dickey's claims at 100 GeV/c, we found no truly convincing evidence of signals.

Bibliography

Particle Identification in the Multiparticle Spectrometer by William C. Danchi

Observations of the D and E mesons and possible three-kaon enhancements in $\pi^-p \rightarrow K^0K^*\pi^*X$, $K^0K^+K^-X$ at 50 and 100 GeV/c by J. O. Dickey, G. Fox, S. R. Stampke *et al.*

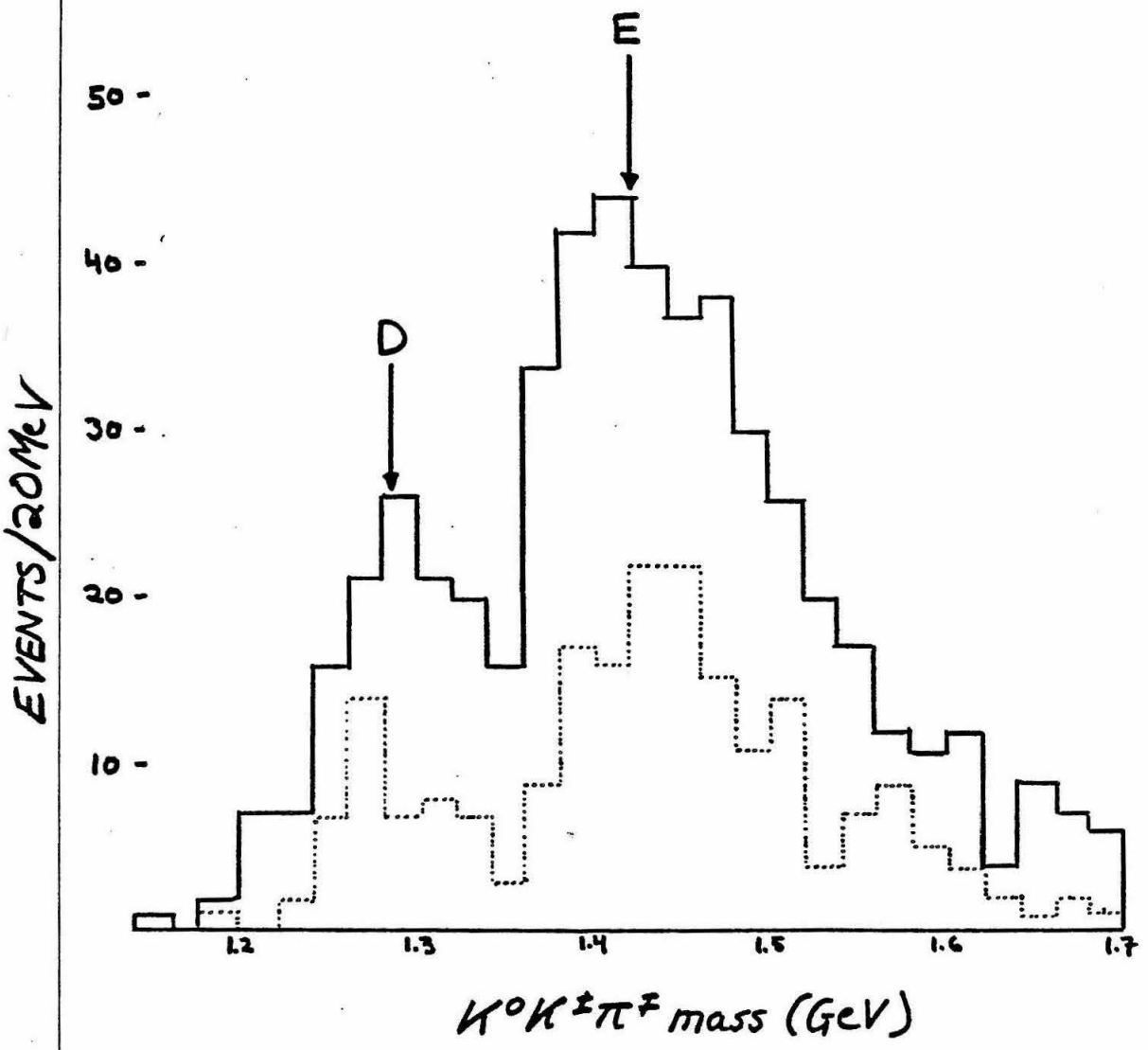

figure 1. δ cut from paper (dotted line) compared with our plot (total of all momenta). Our graph has a similar, though less pronounced, structure.

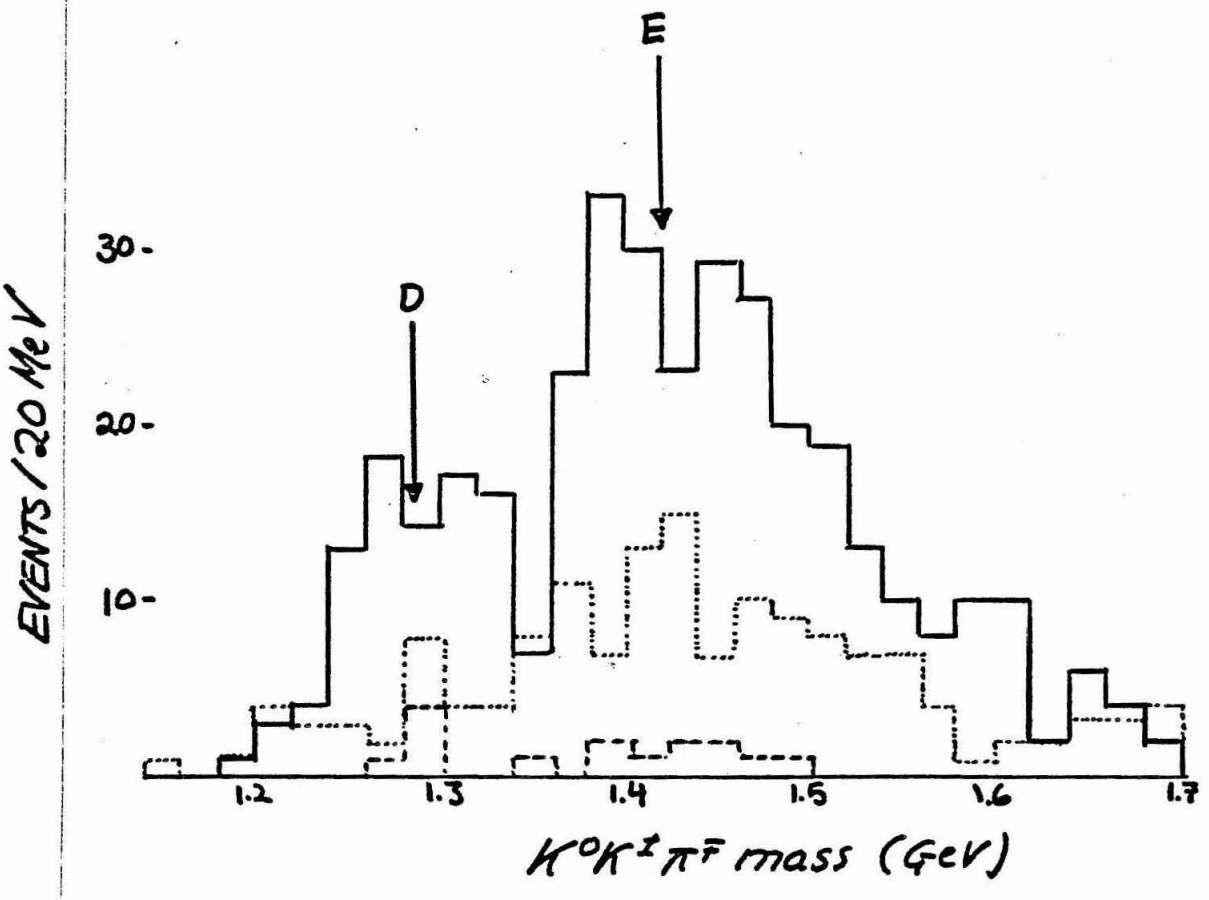

figure 2. Comparison of δ cut histogram for 50 GeV/c (dashed line), 100 GeV/c (solid) and 175 GeV/c (dotted), showing poorer resolution at higher momentum.

INFRARED PHOTOMETRY OF CEPHEID VARIABLE STARS

Frederick Wieland

Dept. of Physics, California Institute of Technology

ABSTRACT

Infrared light curves for twenty-five Galactic Cepheid variable stars are constructed from nearly three thousand photometric observations with the Mount Wilson 24 inch telescope. The observations were conducted in the near infrared J (1.2 μm), H (1.6 μm), and K (2.2 μm) bandpasses and are compared with the corresponding visual light curves (Schaltenbrand and Tammann, 1970). It is found that the amplitude of the infrared curves are substantially smaller than that in the visual, indicating that the effects of compositional differences and temperature variations within Cepheids are dramatically reduced in the infrared.

INTRODUCTION

Cepheids are variable stars with the useful property that their intrinsic brightness is known to increase with their period of pulsation. They were first discovered in the Small Magellanic Cloud by Miss Henrietta Leavitt of Harvard University early in this century, and, as they can be detected in galaxies within our Local Group, they are useful for determining the extragalactic distance scale. This distance scale, in turn, is used to calibrate distances to further galaxies, enabling us to determine the age of the universe.

Unfortunately, the calibration and application of the Cepheid Period-Luminosity relation, which has until now been done at visual wavelengths, has been under dispute. The argument centers on three principle reasons for uncertainty in the Period-Luminosity relation: (1) unknown interstellar and extragalactic absorption, which make objects appear more distant than they actually are; (2) composition differences in the atmospheres of Cepheids formed in galaxies with different chemical histories; (3) correction for temperature variations within the cycle of one Cepheid.

In the near infrared, these considerations are appreciably diminished. For example, the interstellar extinction at H (1.6 μm) is lower than at B (0.44 μm) by a factor of 6 (Savage and Mathis, 1979). The work undertaken at the Mount Wilson 24 inch telescope this summer has been a measurement of the near infrared light curves of Galactic Cepheid variables, in order to determine the near infrared Period-Luminosity relation by studying the ratio of infrared to visual brightness amplitudes and the phasing relationship of maximum light. This paper reports on photometric observations of twenty-five Galactic Cepheids at the J (1.2 μm), H (1.6 μm) and K(2.2 μm) infrared bandpasses. These data will be combined with a smaller set of observations taken by the infrared group at the University of Toronto. Ultimately, we hope to calibrate the infrared Period-Luminosity relation, which will be used to find the extragalactic distance scale in our Local Group, forming a determination of the age of the universe.

OBSERVATIONS

The data presented here were taken with the Mount Wilson 24 inch telescope from 12 June through 15 August 1982. The observations were made at bandpasses centered at 1.2, 1.6, and 2.2 microns. These three wavelengths are transmitted through the atmosphere with only minor attenuation; outside these wavelengths, atmospheric water vapor and carbon dioxide absorb most of the infrared photons.

The system consisted of a nitrogen cooled InSb infrared detector, with a filter wheel to define wavelength intervals, and a chopping mirror which caused the detector to alternatively view the source and blank sky. The signal passed through a lock-in amplifier which abstracted the source signal from the infrared background radiation, sending the output to an analog/digital pulse converter, finally being counted with a standard pulse counter.

With each star the pulses were counted for forty seconds, yielding a signal to noise ratio of better than 30:1 in most cases. Initially, a visual detector was used simultaneously with the infrared; however, visual signal to noise ratio of 10:1 after 160 second integrations led to its abandonment. Consequently, only infrared lightcurves in three wavelengths (1.2, 1.6, and 2.2 μm) were measured; parameters for the corresponding visual curves were obtained from Schaltenbrand and Tammann (1970).

On each night of observation a number of infrared standard stars were measured. Their coordinates and magnitudes were obtained from the Caltech standard list (Elias, et. al., 1982). Since the standard stars do not vary from night to night, their measured magnitudes were used to determine the instrumental sensitivity and the infrared extinction per air mass. The extinction correction was then applied to each Cepheid observed to obtain its magnitude.

DISCUSSION

The light curves for each of the twenty-five Cepheids are given in the accompanying figures, along with their visual maximum

and minimum magnitudes. Preceding the light curves are three figures comparing the amplitude of the infrared curves with the amplitude of the visual curves as a function of period. The infrared amplitudes were determined by eye; in each case, a mean curve was drawn through the data points and the amplitude was measured. In practice, the curve would be Fourier analyzed with the various coefficients determined by the method of least squares. This technique will be applied when these data are combined with that from the University of Toronto.

It can be seen in each case that the amplitude increases with the period. In addition, the infrared amplitudes are all smaller than the visual. Moreover, the scatter in the visual data is much greater than in any of the three infrared wavelengths. The reduced scattering and amplitude is due to the fact that longer wavelengths are less sensitive to compositional and temperature effects; in the visual, the high temperature dependence of the blackbody curve produces the higher amplitudes with resultant larger scatter in the amplitude/period graph.

Quantitative estimates of the phase relationship among the various wavelengths will have to wait until the curves are Fourier analyzed. However, for those stars with excellent phase coverage (YZ Sgr, U Sgr, S Sge) it can be seen, again by inspection, that the minimum of bandpass J seems to lag that of H and K by about 0.1 cycle. This fact is useful for those constructing models of Cepheid atmospheres and interiors.

CONCLUSION

The advantages of calibrating the Cepheid Period-Luminosity relation in the infrared rather than the visual have been shown. The infrared light curves have a smaller amplitude than the visual and consequently the amplitude/period relation has less scatter. This advantage combined with the reduced attenuation will make the Period-Luminosity relation in the infrared more accurate than in

the visual, thus allowing a more accurate determination of distance outside the Galaxy.

BIBLIOGRAPHY

Elias, J.H., et. al., Astron. J., 87, 1029 (1982)

McGonegal, R., et. al., Ap. J., 257, L33 (1982)

Savage, B.D., and Mathis, J.S., Ann. Rev. Astr. Ap., 17, 73 (1979)

Schaltenbrand, R. and Tammann, G.A., Astr. Astrophys. Suppl. 4, 265 (1970)

FIGURES

Figures A-C: Shown are the amplitudes of the visual light curve and one of the three infrared light curves plotted against the period. Note the lower scatter in the infrared compared to the visual. Not plotted is star SV Vul, with a period of 45.103 days, a visual amplitude of 1.036 mag., a J (1.2 μm) amplitude of 0.44 mag., and both an H (1.6 μm) and K (2.2 μm) amplitude of 0.38 mag.

Figures 1-25: Shown are the light curves for each Cepheid in each of the three wavelengths (1.2, 1.6, and 2.2 μm). V-max and v-min are the corresponding visual (0.55 μm) maximum and minimum magnitudes for the star. The phase is plotted up to 1.60; the points from phase 1.0 to phase 1.6 are the points from phase 0 to phase 0.6 duplicated for ease of seeing. (Figures 1-25 have not been included in the book, but copies may be obtained in Room 207 Thomas, Caltech.)

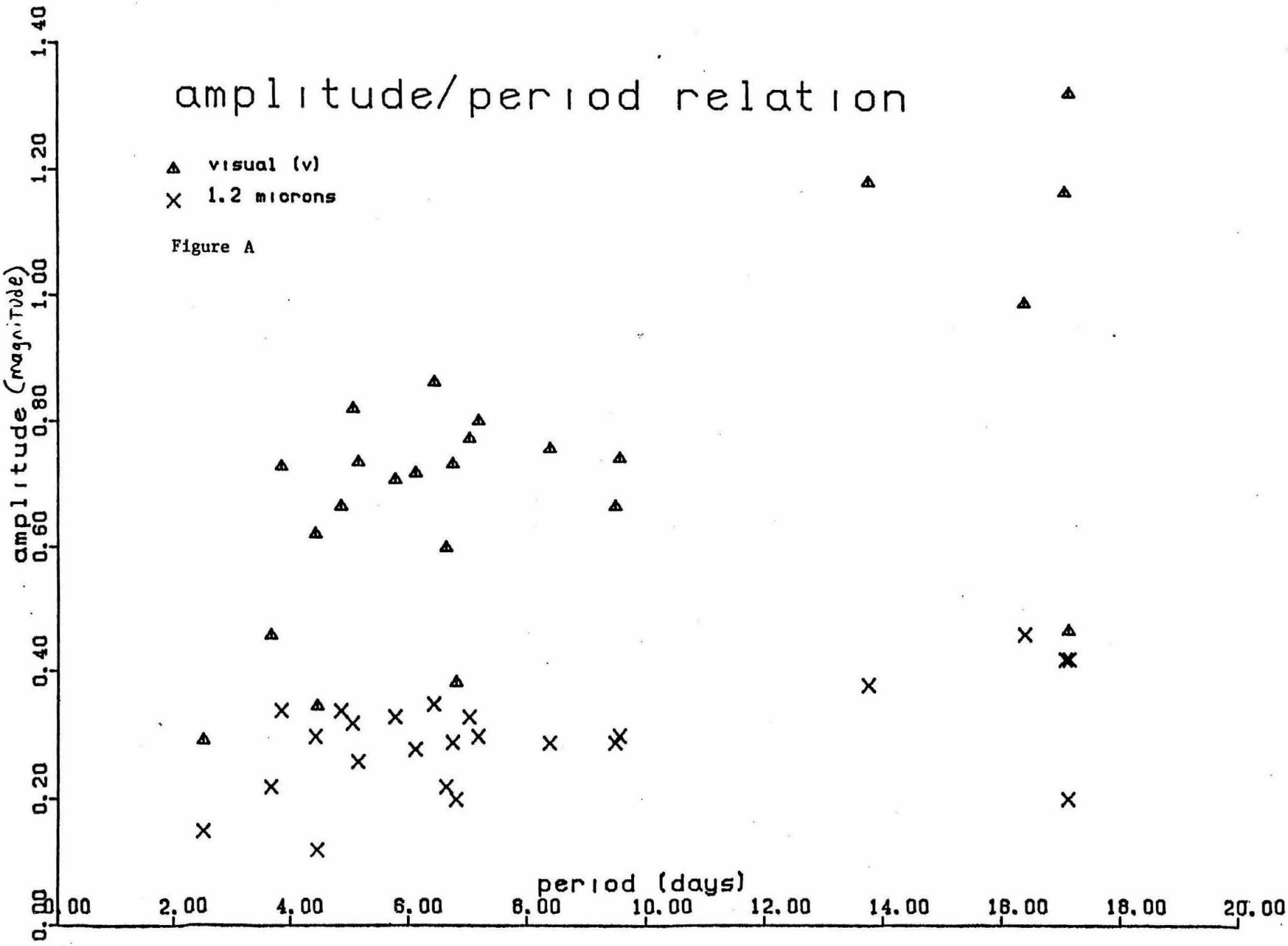
amplitude/period relation
visual (v)
1.2 microns
amplitude (magnitude)
period (days)
0.00
0.20
0.40
0.60
0.80
1.00
1.20
1.40
2.00
4.00
6.00
8.00
10.00
12.00
14.00
16.00
18.00
20.00

Figure A

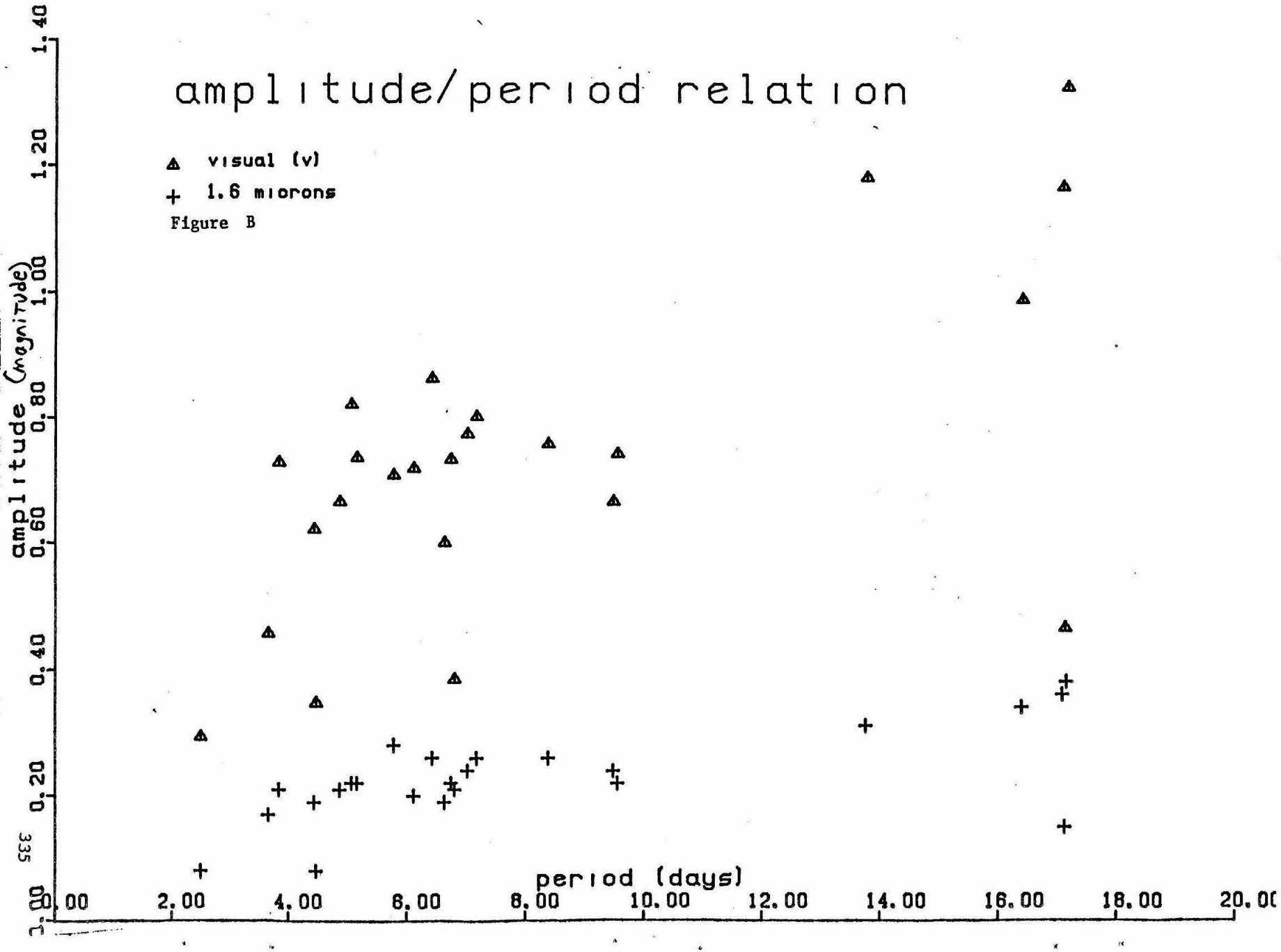
amplitude/period relation
visual (v)
1.6 microns
amplitude (magnitude)
period (days)
0.00
0.20
0.40
0.60
0.80
1.00
1.20
1.40
2.00
4.00
6.00
8.00
10.00
12.00
14.00
16.00
18.00
20.00

Figure B

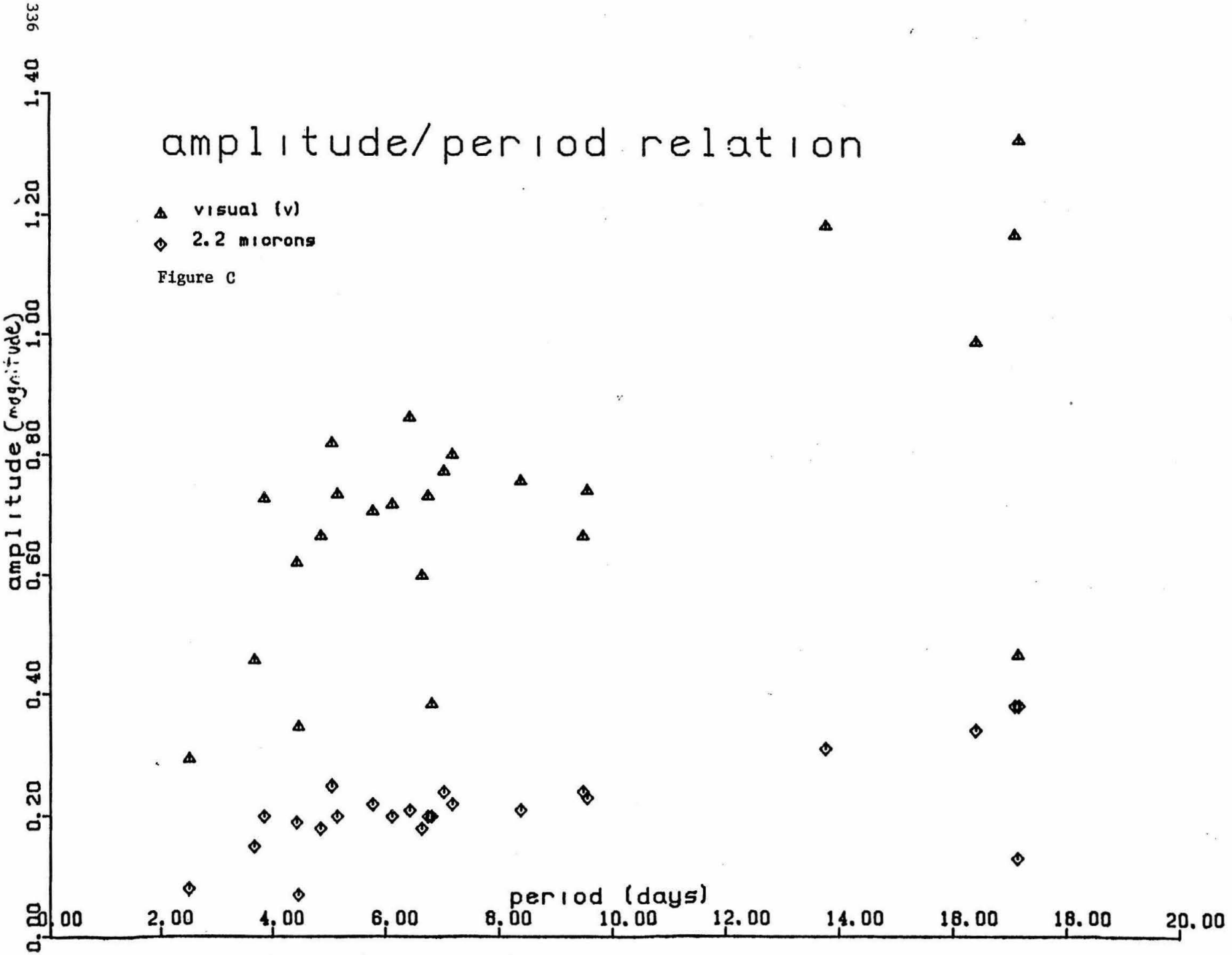
amplitude/period relation
visual (v)
2.2 microns
amplitude (magnitude)
period (days)
0.00
0.20
0.40
0.60
0.80
1.00
1.20
1.40
2.00
4.00
6.00
8.00
10.00
12.00
14.00
16.00
18.00
20.00

Figure C

WALTER WUENSCH

No Report Submitted

THE PRODUCTION OF REVERTANT BETA-LACTAMASE UNDER VARIOUS CONDITIONS

SURF Fellow: Minami Yoda SURF Sponsor: Dr. J. H. Richards

In SURF Program from June 21 to August 27, 1982.

ABSTRACT

The main purpose of this project was to isolate and characterize a mutant form of the enzyme beta-lactamase with serine instead of threonine at the 70th position. Unfortunately, we had trouble producing the mutated enzyme in large quantities. We did, however, study the stability of the enzyme, and its production under various conditions on a small scale.

INTRODUCTION

In recent years, much research has been done on the enzyme beta-lactamse, which hydrolyzes beta-lactam such as penicillin, a cephalosporin and [illegible]. The enzyme is encoded on the plasmid pBR322 (originally obtained from Salmonella) in E. coli strain LS1 (1), and is believed to be one of the major mechanisms for penicillin resistance in Gram-negative bacteria such as E. coli and Salmonella. Recently, Gloria Dalbadie-McFarland, a member of Dr. Richards' group, succeeded in making a strain of E. coli LS1 which produced a beta-lactamase with a ser-thr dyad inverted at the active site (ser 70→thr, thr 71→ser) (2). The enzyme was rendered catalytically inactive

by this inversion. This mutant strain partially reverted to the wild type by changing back from thr 70½ ser, producing a revertant strain with a resistance to ampicillin between that of the mutant and the wild type. Although it was not produced in as great quantity as the wild type enzyme, the revertant enzyme was catalytically active. We had hoped to isolate some of the revertant enzyme, determine its binding constants to various antibiotics such as penicillin and cephalosporin, and sequence its amino acids to verify the DNA sequence obtained by Gloria Dalbadie-McFarland.

PRESENTATION AND DISCUSSION OF RESULTS

To isolate the enzyme, the cells were grown up in a medium containing either 20 mg tetracycline or 5 mg ampicillin per liter. After 12-18 hours of growth at 37°C, the cells were centrifuged, washed, and suspended first in a sucrose/EDTA solution, and then in cold water to extract the protein excreted into the periplasmic space (3). The enzyme is then exclusive of ~~precipitated~~ with 60% w/v $(NH_4)_2SO_4$, put on a gradient column (buffer gradient 25 to 200 mM TEACl⁻ pH 7.25), and then on a sizing column for the final purification (3). The activity was assayed by measuring A_{240} of the binding between the enzyme and penicillin (4). The total amount of protein present was determined by measuring the A_{281}.

For some undertermined reason, we were unable to get any enzyme from our large-scale growths (12 l), even though we varied the time of growth from 12-17 hours, and added protease inhibitors like PMSF (phenyl methane sulfonyl fluoride) and Na_2EDTA. We did, however, get activity from our 1 liter

growths, and were able to investigate the influence of various compounds on the activity produced, and the stability of the mutated enzyme. All the 1 liter growths were harvested after approximately 16 hours, and under normal conditions (20 mg/l tetracycline), produced about 4×10^{-4} mcats total. In the presence of 5 mg/l ampicillin instead of the tetracycline, the cells yielded about 10^{-3} mcats total, and in the presence of 300 micrograms/l PMSF and 0.5 mg/l Na_2EDTA yielded about 5×10^{-4} mcats total.

The enzyme stability studies were less conclusive. The revertant enzyme seems to show a sharp drop in activity in the first couple days (from 4.71×10^{-4} mcats to 1.12×10^{-4} mcats total in the first 8 days), and then its activity seems to stabilize (at 1.24×10^{-4} mcats total after another 8 days). The addition of 2 mg/100 ml of PMSF helped limit the loss in activity (5.34×10^{-4} mcats total after 8 days, 3.48×10^{-4} mcats after 16). The assays are accurate to within a factor of two.

CONCLUSIONS

From our small-scale studies on the growth of the revertants, it seems that growing the revertants on 5 mg/l ampicillin, 300 micrograms/l PMSF, and 0.5 g/l Na_2EDTA will yield the maximum amount of beta-lactamase, and that the addition of 2 mg/l PMSF to the crude extract will help preserve the activity. The revertant enzyme is much less stable than the wild type one, which is stable for months, and this observation is interesting, considering that the

only difference between serine and threonine at the 70th position is a methyl group. While we were unable to obtain large quantites of the revertant enzyme, our small-scale studies did turn up some very interesting data.

BIBLIOGRAPHY

1. Sutcliffe, J. Gregor (1978) Proc. Natl. Acad. Sci. USA 75, 3737-3741.

2. Dalbadie-McFarland, G. et al. Proc. Natl. Acad. Sci. USA in press.

3. Fisher, Jed et al. (1980) Biochemistry 19, 2895-2901.

4. Melling, J., & Scott, G. K. (1972) Biochemistry 130, 55-62.

SURF REPORT

1982

Sung J. Yoo

Abstract: Gap junctions which are responsible for intercellular communication couple cells electrically and chemically. The characteristic of electrical coupling has been extensively used to investigate the gap junction using microelectrodes. But this method has some drawbacks; notably it requires time and experience. Therefore it is more desirable to have some other simple and convenient method. Dye transfer has been used for this purpose. Using liposomes as a delivery system, dyes were introduced into cells, which are then allowed to make contact with other cells. Theoretically one can use a cell-sorter to measure the dye transfer between two cells.

Introduction: Studies on the gap junction are primarily done by measuring a current though microelectrodes impaling two cells in contact. Statistical studies are difficult since one must test cells one by one. In addition, we don't exactly know to what extent the electrical coupling of cells represents actual cellular communication. Therefore, it is more desirable to have some other way which can actually show the exchange of cellular materials through gap junctions. Radioactive metabolites, rescue of deficient cells, and dye transfer have been used for this purpose. Dye should meet the following requirements for our purpose:

1. It should not be toxic to cells.
2. It should not interfere with the synthesis and formation of gap junctions.
3. It should be easily detectable at low concentration.
4. It should be small enough to go through the gap junction but large enough to be impermeable to the cell membrane; unless it would leak out of cells and reenter into other cells. This can be misregistered as a dye transfer by the cell-sorter.

Microelectrodes have been used to inject dye into the cell directly. But this approach again has the same problems of impaling a microelectrode and impaling such a microelectrode into a cell could cause considerable strain to the cell.

To solve this problem, we have tried to use liposome as a dye delivery system. It has been shown that under certain conditions, liposomes and cell membranes fuse together releasing their contents into the cytoplasm (for review, see Papahadjopoulos et al., 1979[2] and Düzgünes et al., 1980[3]). This method causes little, if any, strain to cells and was supposed to be very easy to use.

Methods and Results: We decided to work with Novikoff hepatoma cells because they can be incubated in suspension culture, and are known to form junctions.

Weinstein et al. showed that 6-carboxyfluorescein was taken up by cells by liposome fusion, when Dioleyl lecithin was used for a formation of liposome. However, our initial experiments with 6-carboxyfluorescein and liposome system failed. We have found 6-CF is permeable to the cell membrane. During the time period of establishment of cells, a considerable amount of dye has been leaked out. Cells were incubated at 37°C in free dye concentration of 5 to 20 mM for 30 min to 2 hrs. All cells took up the dye. Therefore we have tested other dyes[5] (see Table I). At the present time, Primulin and its derivatives seem most promising because they do not enter the cell when they are incubated in free dye. Also, they are highly fluorescent at low concentration.

We also found a problem with liposome system. Initial experiments with liposome showed that cells did not take up the liposome contents well, probably because of failure of membranes to fuse with liposomes. Procion which is impermeable to cell membrane, was used to prove this. Since Procion yellow reacts with proteins, it remains in cells once it is introduced into the cell. Varying lipid composition of the liposome caused little or no effect on cell to liposomes fusion.

While worried about this, I read about a protein called synexin secreted by the adrenal medulla, which could promote the cell to liposome fusion. Hong et al. [6] showed that synexin increased cell membrane to liposome fusion by three to four fold. I am now preparing synexin and testing its activity.

Conclusion: At the present time, the work is incomplete, but the synexin and dyes seem to show promising results. But considerable work in liposome fusion remains to be done for our system to be successful.

Table I

Dye	Permeability	Toxicity	Detectability
Nile Blue A	-	-	-
Methylen Blue	-	-	-
6-CF	+	-	+
Acridene Orange	-	+	-
Primulin	-	-	+
Titan Yellow	-	-	+

Bibliography

1. Meyer, David J., S. Barbara Yancey, and Jean-Paul Revel. J. Cell. Biol. **91**, 505-523.

2. Papahadjopoulos, D., G. Poste, and W. J. Vail. 1979. Studies on membrane fusion with natural and model membrane. In Methods in Membrane Biology. E. Korn, ed. Plenum Press Vol. 10, 1-121.

3. Düzgünes, W., K. Hong, and D. Papahadjopoulos. 1980. Membrane fusion: the involvement of phospholipids, proteins, and calcium binding. In Calcium-Binding Proteins: Structure and Function. F. L. Siegel, E. Caratoli, R. H. Kretsinger, D. H. MacLennan, and R. H. Wasserman, eds. Elsevier/North-Holland Biomedical Press, Amsterdam, The Netherlands. 17-22.

4. Weistein, J. N., S. Yoshikami, P. Henkart, and W. A. Hagins. Science **195**, 489-491. Liposome-cell interaction: Transfer and intracellular release of a trapped fluorescent marker.

5. H. J. Collins. Biological stains. 8th ed., R. D. Lillie, ed. The Williams and Wilkins Co., Baltimore, 1969.

6. Hong, Keelung, Nejat Düzgünes, and Demetrios Papahadjopoulos. J. Biophy. **37**, 297-305. Modulation of membrane fusion by calcium binding proteins.

Magneto Optic Devices uses in Optical Signal Processing

Jeffrey Yu

Abstract:

Recent advances in Magneto Optic Device (MOD) technology has made it possible to use as a two dimensional electrically addressable Spatial Light Modulator (SLM). As a result the MOD can be used in place of an optical mask in an Optical Signal Processing system. Giving the extra flexibility because of its addressability.

Introduction:

I. Magneto-Optic Device (Fig. 1)

The MOD is basically a two dimensional 48 x 48 binary SLM. The binary data is stored on the device by magnetizing each pixel either parallel or anti parallel to the direction of light propagation. The resulting Faraday effect will then rotate the direction of linear polarization by $\pm\alpha$ degrees. (Amount of Faraday rotation) where α is strongly dependent on the material and its doping. In our case the material is Gallium Iron Garnet (GIG). Thus, by placing a polarizer in front of the MOD and an analyzer rotated at about 45° to each other the binary data can be read out (see Fig. 2).

The addressing of the MOD is done by simultaneously pulsing current of about 500 mA in both the x and y conductors of the appropriate pixel and at the same time biasing a coil set around the device with also about 500 mA (Fig. 3). Complete erasing is induced by driving the bias coil when 1A pulse in the opposite direction. This method has its definite advantage over the old method of using a magnetized needle to address each pixel by hand.

II. Experiments:

A. Magnetic Holography Experiment

In this experiment it was proposed to write on the device a a series of alternatingly light and dark lines. The Fourier image would then be studied with and without the polarizers. In addition to this reconstruction of the original stripe image will be attempted without polarizers.

B. Pattern Recognition Experiment

In this experiment it was proposed to write on the MOD a pattern (letters, for example) and create a Fourier Transform Hologram of the image. The MOD would then have more objects written on it and a classical two-dimensional convolution done with the hologram in an attempt to recongnize the original pattern.

C. Binary Optical Convolution Experiment

This was the original goal of the Surf and the experiment and its merits are discussed in the attached original Surf Proposal.

Results:

Most of the summer was spent building the drivers for the MOD. This was done using the Texas Instruments 75325 memory driver chip. The addressing can only be done one pixel at a time. With more electronics the MOD can be driven one row at a time. As a result using shift register type logic a data stream can be loaded and a time wise convolution done by methods described in experiment C. There is hope that the whole MOD system can be interfaced to the group's IBM personal computer.

A small portion of the time was spent building and testing the output stage for the binary convolution experiment. The only experiment done this summer was that of the Magnetic Holography. Inspection of the Fourier Image with polarizers showed that the DC component was polarized perpendicularly to that of the first order components. Research into the literature was done to explain this and a mathematical explanation was found in Reference 2.

Attempts to reconstruct the image without polarizers failed probably because of a lack of laser light. Literature research was also done into the origination of the Faraday and Kerr effects (Ref. 3)

Conclusions:

1. The uses of the MOD at the 48 x 48 scale is very limited. However, the present technology has brought the resolution up to 128 x 128. Eventual goals are to make MODs up to 1024 a side or even 2048 a side. If this is ever reached, it will make computer generated holograms implementable on the device making it extremely powerful in Optical Signal Processing.

2. The current and power requirements for the device make it very hard to use. As an example addresing a single row in parallel would require about 24 amps of total pulse current and 49 parallel driver networks.

3. The contrast & transmission coefficient between oppositely magnetized pixels must be improved in order to use most of the gray leveling schemes described in Ref. 4.

Acknowledgements

I would like to thank Dave Cox and Litton Data Systems for loaning us the Magneto Optic Device and for advice in building the device drivers.

Bibliography:

1. G. R. Pulliam, W. E. Ross, B. Mac Neal and R. R. Bailey, "Large Stable Magnetic Domains" submitted Magnetics and Magnetic Materials Conference in Atlanta Georgia, Nov. 16, 1981.

2. Reuben S. Mezrich, "Reconstruction Effects in Magnetic Holography" IEEE Transactions. on Magnetics, Vol. MAG-6 No. 3 p. 537, Sept. 1970.

3. Marvin J. Freiser, "A Survey of Magneto optic Effects" IEEE Transactions on Magnetics, Vol. MAG-4, No. 2 p. 152, June, 1968.

4. W. Ross, D. Psaltis, R. H. Anderson "2D Magneto-Optical Spatial Light for Signal Processing" Submitted 1982, Technical Symposium in Arlington, Virginia, May 1982.

MAGNETO OPTIC DEVICE

General Characteristics

Property	Comments
Switching Times	50-1000 usec for 512 x 512 array depending on refresh requirements
Power Requirement	1 watt at high frame rate
Uniformity	Good (1%)
Efficiency	10%
Contrast Radio	Display Applications 10-50 Optical Applications 1000
Pixel Size	25 um and up
Array Size	Chip = (1 to 5 cm)² mosiacs possible to (10 cm)²
Array Configuration	M x N where $1 \leq M$ and $N \leq 2048$
Gray Scale	Basically digital
Wavelength Dependent	Yes, both Faraday effect and absorption fall off as λ is increased.
Temperature Dependent	Yes, but compensatable over range of -100°C to +100°C
Physical Size and Weight	Active element small
Cost	Chip cost near IC cost of equivalent size.

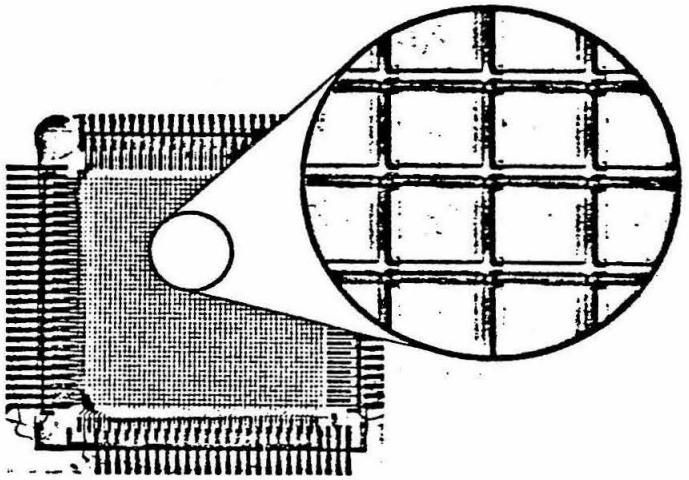

FIGURE 1

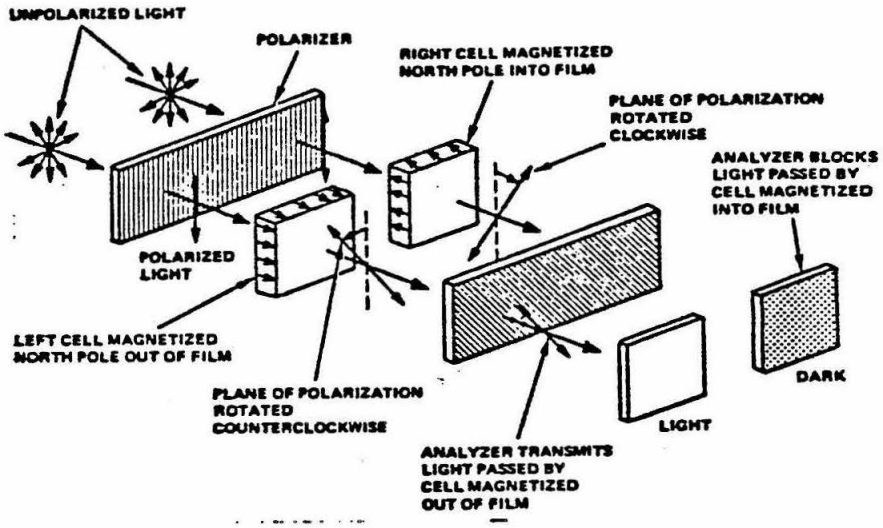

Figure 2. Operation of magneto-optic pixels

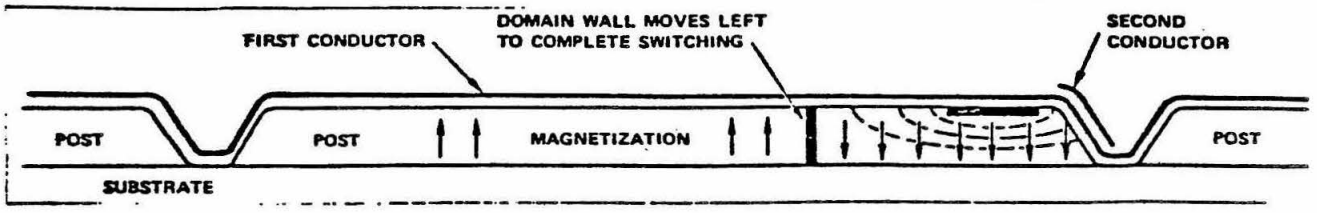

Figure 3. Post switching process [cross section of posts]

Accurate Optical Convolution by Binary Representation

Convolutions are an important aspect of optical pattern recognition and since this is easily implementable I will concentrate on doing convolutions with high accuracy. One of the major shortcomings of optical data processors is relatively low accuracy with which they perform computations. Usually this accuracy is limited by the dynamic range of the devices used as well as electronic noise present in the system. Current systems have a linear dynamic range of 30-40 db. This however can be increased by representing the optical signals in their binary representation. Sacrificing speed will then be traded for improved accuracy which I see as advantageous.

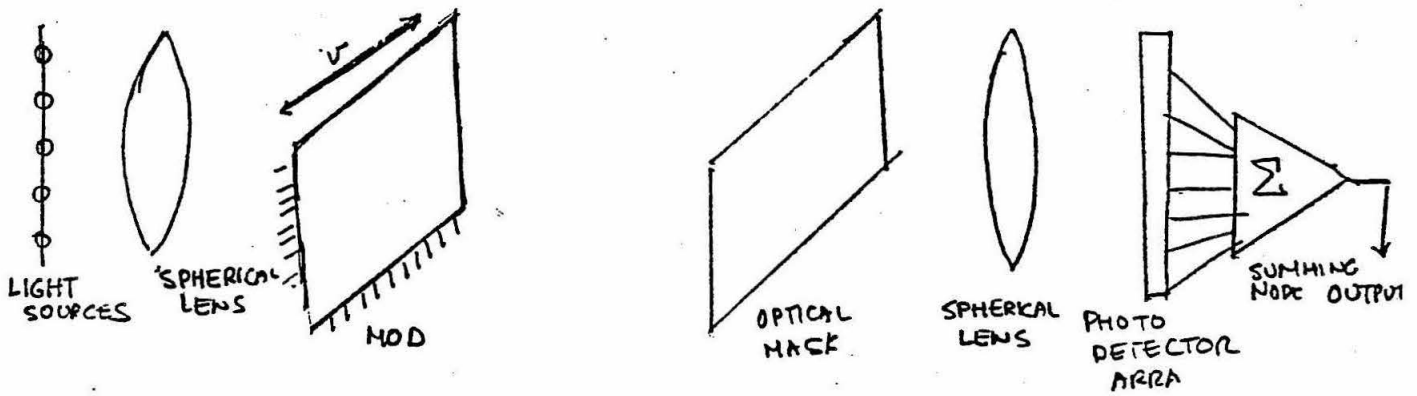

Because of the representation of the bits in the y direction it is necessary to do a binary multiplication in the ydirection as well as a convolution in the x direcion. However binary multiplication can be represented as a linear convolution of the two multiplicands. Thus to do the convolution with the binary representation it will be necessary to do a two dimensional convolution.

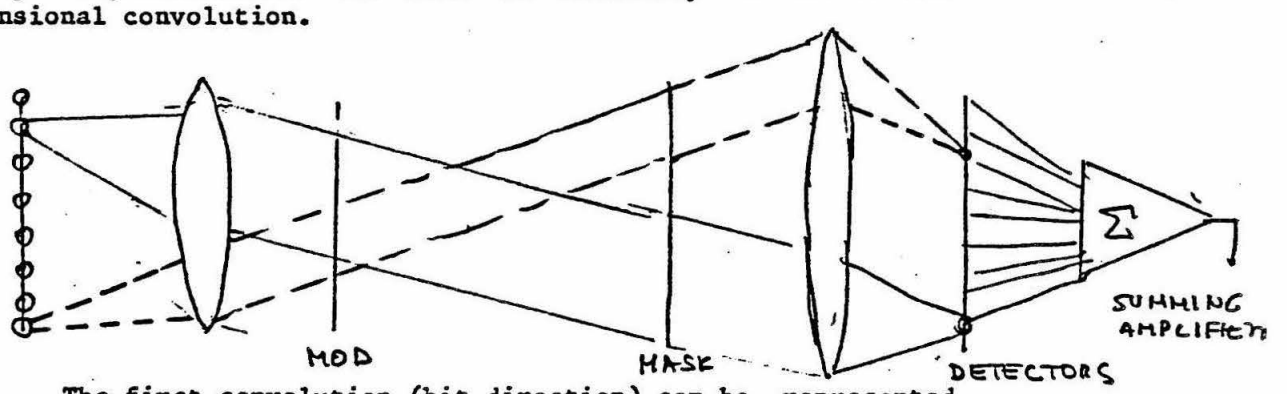

The first convolution (bit direction) can be represented by a side view of the optical system. Because there are only 8 bits (ie low space bandwidth product) the convolution can be done by shadow-casting.

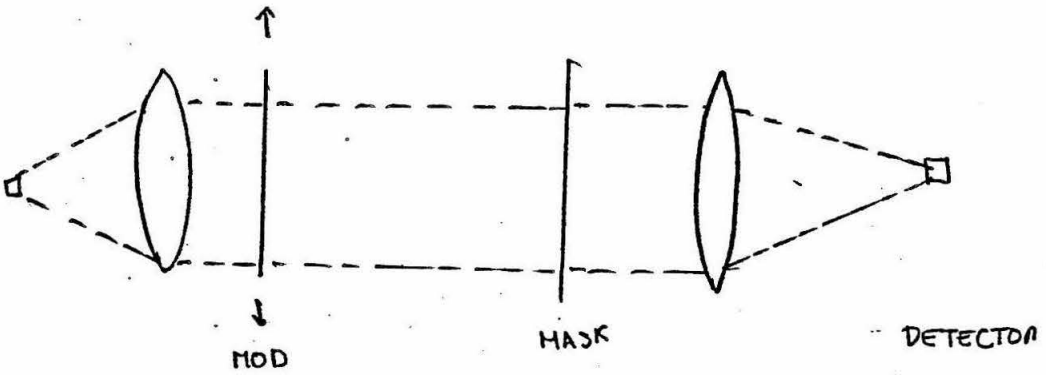

The convolution along the data direction can be represented by a top view of the optical system. Because the data has a high space bandwidth product it will be necessary to do the convolution by moving the input mask in the x direction. It can thus be represented by the following equation where v is the velocity at which the mask is being moved.

$$\int f(x-vt)\, g(x)\, dx$$

The impulse filter g(x) will be a magneto optic device (MOD) which is a magnetically adressable 50 x 50 array mask. The light appearing from the 2-D convolver will then be sensed by an array of phototransistors and converted to the corresponding analog signal.

CALIFORNIA INSTITUTE OF TECHNOLOGY

1982 SURF Seminar Series*
12:00-1:00 PM, Baxter Lecture Hall

Friday, June 18: M-A. Nicolet, Professor of Electrical Engineering

Title: Electrical Contacts in Integrated Circuits: The Weak Connection

Abstract: To the VLSI circuit designer, contacts and interconnects are mere lines, and not part of his concern. But metal films can react with the contacted substrate, and with each other, resulting in failures. As dimensions shrink, the problem becomes major. Solutions exist. Good solutions require understanding, too.

Friday, June 25: W. Whaling, Professor of Physics

Title: Laboratory Astrophysics

Abstract: The wonderful universality of physical laws permits us to draw conclusions about even the most distant astrophysical objects from experiments in the laboratory. I will give a brief overview of the active areas of nuclear, atomic, and molecular research inspired by astrophysics and discuss my work on atomic spectroscopy and the quanititative analysis of stellar spectra.

Wednesday, June 30: B. Sturtevant, Professor of Aeronautics

Title: Vapor Explosions and the Mt. St. Helens Blast

Abstract: Explosions that are caused by the rapid release of thermal or mechanical energy, rather than of chemical energy, are called physical explosions. The vapor explosion is an example of a physical explosion, in which very rapid boiling (or vaporization) occurs. Since physical explosions occur less frequently than chemical explosions, they are usually quite unexpected and seldom are adequate precautions taken. Some examples of vapor explosions, including the explosion of Mt. St. Helens, and current research directed at understanding the fluid flows that occur in these rapid events will be described.

* For more information, please contact Carolyn Merkel, ext. 4285.

Friday, July 9: H. Zirin, Professor of Astrophysics, Director of Big Bear Solar Observatory

Title: The Sunspot Cycle

Abstract: The 22 year sunspot cycle has persisted for centuries with great regularity, except through the Maunder Minimum. Small dipole fields associated with spots are processed into an overall solar dipole. The way in which this may happen, and the processes by which sunspots form will be discussed.

Friday, July 16 J-P. Revel, Albert Billings Ruddock Professor of Biology

Title: Cellular Communication: A Story of Imps and the Channels they Build

Abstract: The cells in the bodies of all multi-cellular organisms communicate with each other by direct channels. In animals these are characterized by clusters of Intra Membrane Particles (connexons) which form bridges between neighboring cells. Research on the structure of connexons and their roles will be discussed.

Wednesday, July 21: T. McDonough, Lecturer in Engineering

Title: How to Give a Seminar - I

Abstract: We will discuss how to give oral presentations including how to use visual aids.

Friday, July 23: D. Stevenson, Associate Professor of Planetary Science

Title: Core Physics

Abstract: The earth's outer core is a liquid iron alloy, consisting primarily of iron but containing other elements responsible for greatly reducing its melting point. The theoretical research to be discussed is an effort to understand the composition, temperature and dynamics of the innermost earth by an application of liquid theory to seismic and shock wave data.

Wednesday, July 28: T. McDonough, Lecturer in Engineering

Title: How to Give a Seminar - II

Friday, July 30: C. Barnes, Professor of Physics

Title: The Origin of the Elements - Nucleosynthesis

Abstract: Current astrophysical theory explains the origin of the chemical elements and their isotopes by postulating nuclear reactions during the formation of the universe, deep within evolving stars, and in the final explosion of stars. Laboratory measurements of the rates of these postulated nuclear reactions provide stringent tests of the theoretical models of nucleosynthesis.

Friday, August 6: T. Collins, Assistant Professor of Chemistry

Title: A Perspective of Oxidation Chemistry

Abstract: A personal view of the status quo of synthetic and mechanistic oxidation chemistry will be given. Special attention will be focused on subareas where opportunities for major original research contributions are thought to exist.

Friday, August 13: P. Dervan, Associate Professor of Chemistry

Title: Agents which Impair the Template Function of DNA

Abstract: Antibiotics and drugs may interfere with the synthesis of nucleic acids by directly interfering with the role of DNA as a template in replication and transcription. Research on how we study these small molecules, DNA complexes, will be discussed.

Friday, August 20: T.Y.T. Wu, Professor of Engineering Science

Title: Micro-organism Propulsion

Abstract: Viewing the self propulsion of motile protozoa and bacteria through a microscope, an observer invariably becomes impressed by the outstanding performance of these flagellates and ciliates. Their remarkably high specific speeds, in units of body lengths traversed in unit time, will be discussed from a mechano-physiological point of view. Also presented will be new understanding from our on-going research concerning the effects of microscopic slide boundaries on the flow field of central interest.

7/82

SURF LECTURES: HOW TO GIVE A SEMINAR

by Thomas R. McDonough

MAIN TECHNIQUES

1. Eye contact: Always look at the audience when possible.
2. Voice: SPEAK UP! (Unless there is a microphone.) Avoid a monotone.
3. Body language: Use occasional, smooth gestures; avoid stiffness and nervous, meaningless motions. Don't play with chalk, pen, pointer, etc. Don't lean on the table or blackboard.
4. Organization: Be sure to prepare an introduction and a conclusion. The conclusion should remind the audience of the most important points. Rehearse the introduction and conclusion thoroughly.
5. ENTHUSIASM! Create the impression that you are really interested in the subject. Remember Dr. George and Richard Feynman.
6. Visual aids: Use them if possible, plan their use carefully, and use them instead of notes. Face the audience whenever you can. Check out the room, light switch, blackboard, projector, microphone, pointer, etc. ahead of time. Run all your slides through the projector if possible, to verify that they are in correct order and not backwards or upside down. Make sure the projectionist knows the proper sequence and orientation of the slides. Use a pointer. Use color to simplify complex diagrams.

REFERENCES (with Caltech library number, when I have it)

Connolly: "Effective Technical Presentations" (PN 4121 C6, 1968)
Dietrich & Brooks: "Practical Speaking for the Technical Man" (PN 4121 D533, 1958)
Loney: "Briefing and Conference Techniques" (PN 4121 L645, 1959)
Mambert: "Presenting Technical Ideas, A Guide to Audience Communication"
Wilcox: "Oral Reporting in Business and Industry" (PN 4121 W385, 1967)
Springer, S.P., and Deutsch, G.: "Left Brain, Right Brain," W.H. Freeman, San Francisco, 1981 (quality paperback; this book helps you understand the mechanisms of the brain that you are trying to stimulate).
Walters, Barbara: "How to Talk With Practically Anybody About Practically Anything" (inexpensive paperback; possibly out of print; very good tips on the art of conversation).
Kodak: They publish several good paperback books on making slides and on running sophisticated slide shows (e.g., with multiple projectors and synchronized tape recordings). See any photo store.
Molloy, J.T.: "Dress for Success"; "The Woman's Dress for Success." (Well-researched studies of the best clothes to wear to impress others. Main conclusion: Wear dark gray or dark blue conservative suits. Both books are in quality paperback; the first is also in inexpensive paperback.)

TO LEARN MORE

Take Ch 90, Ge 102 or my E10; or join the JPL/Caltech Toastmasters Club. To visit the club, which meets at JPL, call me (795-0147). If you move out of this area, you can find the location of the nearest such club by writing to Toastmasters International, 2200 N. Grand Ave., P.O. Box 10400, Santa Ana, CA 92711.

Publications Which Have Been Initiated by SURF Projects

1. David M. Anderson, Richard H. Scheller, James W. Posakony, Linda B. McAllister, Steven G. Trabert, Clifford Beall, Roy J. Britten, Eric H. Davidson, "Repetitive Sequences of the Sea Urchin Genome Distribution of Members of Specific Repetitive Families", J. Mol. Biol. (1981) 145, 5-28.

2. Richard H. Scheller, David M. Anderson, James W. Posakony, Linda B. McAllister, Roy J. Britten, Eric H. Davidson, "Repetitive Sequences of the Sea Urchin Genome II. Subfamily Structure and Evolutionary Conservation", J. Mol. Biol. (1981) 149,15-39.

3. Richard H. Scheller, Linda B. McAllister, William R. Crain, Jr., David S. Durica, James W. Posakony, Terry L. Thomas, Roy J. Britten, Eric H. Davidson, "Organization and Expression of Multiple Actin Genes in the Sea Urchin", Molecular and Cellular Biology, July 1981, p. 609-628.

4. "Electrical Characteristics of Thin Ni_2Si, NiSi, and $NiSi_2$ Layers Grown on Silicon", paper presented by E. Colgan at the Electronic Materials Conference 1982, June 23-25, Colorado State University, Ft. Collins, CO. A manuscript is to be published in the Journal of Electronic Materials.